DISS. ETH No. 21158

Development of Novel Borate-Based Positive Electrode Materials for Rechargeable Lithium Batteries

A dissertation submitted to the

ETH ZURICH

for the degree of

Doctor of Sciences

presented by

Semih Afyon

M.Sc. Materials Science and Engineering, Koç University Istanbul

born on 11.11.1982

Turkish Citizen

accepted on the recommendation of

Prof. Dr. Reinhard Nesper, examiner

Prof. Dr. Maksym Kovalenko, co-examiner

2013

………Dedicated to My Family

Acknowledgements

First and foremost, I would like to thank Prof. Dr. Reinhard Nesper for giving me the opportunity to work under his guidance. I really appreciate the free research environment he provided in his group. I am also grateful to him for his constant support, scientific supervision, encouragement and many life lessons he taught to me.

I also want to thank Prof. Dr. Maksym Kovalenko for accepting the task to be my co-supervisor.

I would like to extend my gratitude to:

Christian Mensing, for his technical assistance and help in magnetic and thermal characterization of my samples.

Dr. Frank Krumeich, for electron microscopy characterization of various samples.

Dr. Michael Wörle, for crystal structure solutions and refinements and helpful discussions.

Dr. Barbara Hellermann, for her help in administrative issues.

I am also thankful to Dr. Dipan Kundu and Dr. Xiao-Jun Wang for their friendship and helpful discussions on electrode materials.

Furthermore, my sincere thanks to my labmates in H106, Michele Furlotti, Frederic Hilty and Adam Slabon for the nice working atmosphere. I would also like to thank the other past and present members of the Nesper-Group, Dr. Eduardo Cuervo-Reyes, Phillipp Reibisch, Florian Wachter, Martin Kortyba, Dr. Lilliana Viciu, Dr. Mihai Viciu, Dr. Sarah Russell, Matthias Herrmann, Dr. Tommy Kaspar, Dr. Yoann Patrice Mettan, Fabian von Rohr, Dr. Serhiy Budnyk, Dr. Jose Antonio Gonzalez Martinez, Dr. Anke Zürn, Dr. Rahul Fotedar, and Dr. Riccarda Caputo for small talks and the positive working environment.

I am also grateful to Prof. Dr. Mehmet Somer for his friendship and guidance prior to my Ph.D. studies.

Finally and most importantly, I want to thank my parents, sister, aunts and grandparents for their unconditional love and support throughout my whole life.

Abstract

The inevitable depletion of fossil fuels requires the generation of sustainable and clean energy from renewable sources. Due to the time-dependent occurrence of renewable energy sources, effective storage mechanisms have to be developed for large scale grid as well as for portable applications. As a way of energy storage, Li-ion batteries dominate the portable electronics market and full electric vehicles powered by Li-ion batteries have also become available in recent years. However, current cathode materials are still not capable enough to provide the high energy density demand required for the large scale implementation of rechargeable lithium batteries as energy storage mediums. The present work introduces novel positive electrode materials for rechargeable lithium batteries. Redox-active compounds, in which borate linking groups are supposed to induce a flexible linking of the former, are mainly investigated. If a safe and stable cycling is established, a number of the presented materials are projected to be possible candidates for next-generation rechargeable lithium batteries.

Nano h-$LiMnBO_3$ with an average particle size of ~ 20 nm has been synthesized by a sol-gel method for the first time. The nanoscopic material is obtained at temperatures of 350 ^{o}C and below, whereas the higher temperature synthesis above 500 ^{o}C results in the microcrystalline phases that have poorer electrochemical performance. In situ carbon coating of $LiMnBO_3$ particles by carbonization of propionic acid right during the synthesis of nano h-$LiMnBO_3$ (4.2 wt-% carbon) provides a conducting surface. Carbon particles partially cover the surfaces of nanorods and disperse among nano-crystallites enhancing the electronic transport in the electrode material. The sol-gel synthesized nano h-$LiMnBO_3$ yields a first discharge capacity of 136 mAh/g within a window of 4.7 – 1.7 V at C/20 rate. This is considerably higher than previously reported. Further improvements of the system are realized by preparing a composite electrode of

nano h-$LiMnBO_3$ with reduced graphite oxide (RGO) that delivers a high first discharge capacity of 145 mAh/g at C/20 rate and retaining a discharge capacity of 111 mAh/g at the 10th cycle. Similarly, nano-crystallites of $LiCoBO_3$ have been produced by a sol-gel method. The sol-gel synthesized $LiCoBO_3$ is further treated with RGO to obtain a composite material. The composite electrode gives a first charge capacity of ~ 55 mAh/g in a galvanostatic-potentiostatic protocol (within 4.7 - 2.0 V, at C/20 rate) demonstrating the electrochemical delithiation of $LiCoBO_3$. The enhanced electrochemical properties can be attributed to the intimate embedding of the nano-particles into the conductive reduced graphite oxide network. For $LiMnBO_3$ modifications and for $LiCoBO_3$, an increase of capacity is expected to be reached by further reduction of the particle size and size spread as well as by optimizing the conductive coating of the nano particles.

In Chapter 4, novel lithium-rich manganese borate compounds, which are synthesized by conventional solid state methods, are presented as candidate cathode materials for Li-ion batteries. Particularly, $Li_7Mn(BO_3)_3$ is interesting with a high theoretical capacity of ~ 479 mAh/g at an exchange of 5 Li per formula unit. The new phase crystallizes in the triclinic space group type *P*-1 (no. 2) with exclusively tetrahedral Mn^{2+} coordination that is an exceptional case among other related manganese oxides. $Li_7Mn(BO_3)_3$ has a network of MnO_4 tetrahedra and BO_3^{3-} units as important structural features. Though plain crystals of $Li_7Mn(BO_3)_3$ yield a negligible first discharge capacity of ~ 11 mAh/g due to the low electronic conductivity, a high first charge capacity of ~ 280 mAh/g (extraction of ca. 3 Li) and a first discharge capacity of ~ 154 mAh/g are attainable after nano-sizing and nano-carbon composite formation.

In the last chapter of this study, vanadate – borate glasses and glass ceramics are demonstrated as promising high capacity cathode materials for next-generation rechargeable lithium batteries. The synthesis method for glasses and glass ceramics is thought to be very simple and cost efficient. Vanadate – borate glass ceramics exhibit multi-phase lithium insertion reactions in the first discharge, whereas featureless charge/discharge curves without a multi-step behavior that indicates a homogeneous phase lithiation mechanism are obtained for vanadate – borate glasses from the first discharge to subsequent cycles. Especially, the electrochemical performances realized for new glassy composite electrodes of V_2O_5 – $LiBO_2$ with reduced graphite oxide are encouraging for the practical implementation of these composites as cathode materials. V_2O_5 – $LiBO_2$ glass composite electrodes retain discharge capacities in the range of ~ 300 mAh/g for 50 cycles. Comparable electrochemical performances for vanadate-based and other positive electrode materials are only available after lengthier and laborious approaches employing expensive techniques and educts.

A comprehensive result of this work is that materials, which are normally classified as insulators, can be utilized for electrochemical applications through proper modification and composite formation.

Kurzfassung

Nachhaltigkeit, Klimaveränderungen, umweltpolitische Randbedingungen und die unvermeidliche Abnahme fossiler Brennstoffe erfordern in Zukunft eine nachhaltige und saubere Energiegewinnung aus alternativen Quellen. Um die zeitlich schwankende Produktion aus diesen Quellen zu kompensieren, müssen effiziente Energiespeicher sowohl für Grossanlagen als auch für mobile Anwendungen entwickelt werden. Lithium-Ionen Batterien als Energiespeicher dominieren den Markt für mobile elektronische Geräte bereits heute und auch Fahrzeuge mit rein elektrischem Antrieb auf ihrer Basis sind bereits verfügbar. Zur Zeit sind jedoch die gängigen Kathodenmaterialien immer noch nicht leistungsfähig genug um die benötigten Energiedichten zu liefern, die für einen grossflächigen Einsatz von wiederaufladbaren Lithiumbatterien als Energiespeicher notwendig sind. Die vorliegende Arbeit untersuchtt neue Kathoden-Materialien für wiederaufladbare Lithiumbatterien vor. Falls sichere und stabile Ladezyklen erreicht werden können, sind einige dieser Materialien mögliche Kandidaten für die nächste Generation von wiederaufladbaren Lithiumbatterien. In dieser Arbeit werden Borat-basiert redoxaktive Verbindungen vorgestellt, in denen den Boratgruppen die Funktion flexibler Linkergruppen zukommt.

Zum ersten Mal wurde Nano-h-$LiMnBO_3$ mit einer mittleren Partikelgrösse von 20 nm mit einer Sol-Gel-Methode synthetisiert. Das nanoskopische Material wurde bei Temperaturen bis maximal 350 ^{o}C erhalten, während Hochtemperatursynthesen ab 500 ^{o}C zu mikrokristallinen Phasen führen, die deutlich schlechtere elektrochemische Eigenschaften zeigen. In situ-Beschichtung von $LiMnBO_3$-Partikeln mit Kohlenstoff durch Karbonisierung von Propionsäure während der Synthese von nano-h-$LiMnBO_3$ (4.2 gew.-% Kohlenstoff) führt zu einer leitenden Oberfläche. Die elektrische Leitfähigkeit wird durch Kohlenstoffpartikel erhöht, die teilweise die

Oberfläche der Nanostäbchen bedecken und zudem zwischen den Nanoteilchen verteilt sind. Sol-Gel-synthetisiertes Nano-h-$LiMnBO_3$ zeigt bei der ersten Entladung, mit einer C/20-Rate in einem Bereich von 4.7-1.7 V, eine Kapazität von 136 mAh/g. Diese ist deutlich höher als der früher berichtete Wert. Weitere Verbesserungen des Systems erreicht man, in dem man eine Komposit-Elektrode aus Nano-h-$LiMnBO_3$ mit reduziertem Graphitoxid (RGO) herstellt, die bei der ersten Entladung mit einer C/20-Rate eine beachtliche Kapazität von of 145 mAh/g zeigt und auch im zehnten Zyklus immer noch eine Entladekapazität von 111 mAh/g aufweist. Auf ähnliche Weise wurden Nanokristallite von $LiCoBO_3$ über das Sol-Gel-Verfahren hergestellt, welche mit RGO behandelt wurden, um ein leitfähiges Komposit-Material zu erhalten. Diese Komposit-Elektrode zeigt im ersten Entladezyklus eine Kapazität von etwa 55 mAh/g unter galvanostatisch-potentiostatischen Bedingungen (4.7 - 2.0 V, C/20-Rate), womit überhaupt zum ersten Mal eine elektrochemische Delithiierung von $LiCoBO_3$ gemessen werden konnte. Die verbesserten elektrochemischen Eigenschaften sind wahrscheinlich auf die Einbettung der Nanopartikel in das leitfähige reduzierte Graphitoxid-Netzwerk zurückzuführen. Bei weiterer Verkleinerung der Partikelgrösse bzw. einer schmaleren Teilchengrösse-Verteilung sowie einer Optimierung der leitfähigen Beschichtung kann für die Modifikationen von $LiMnBO_3$ und für $LiCoBO_3$ eine weitere Steigerung der Kapazität erwartet werden.

In Kapitel 4 werden neue lithium-reiche Manganborate als Kandidaten für Kathodenmaterialien in Lithium-Ionen Batterien vorgestellt, die mit konventionellen Festkörpersynthese-Methoden hergestellt wurden. Insbesondere $Li_7Mn(BO_3)_3$ ist mit einer theoretischen Kapazität von 479 mAh/g bei einem maximalen Austausch von 5 Li pro Formeleinheit sehr vielversprechend! Diese neue Verbindung kristallisiert in der triklinen Raumgruppe *P*-1 (Nr. 2) und enthält als Besonderheit gegenüber verwandten Oxiden, Mn^{2+} in ausschliesslich tetraedrischer Koordination. In $Li_7Mn(BO_3)_3$ bilden MnO_4-Tetraeder und BO_3^{3-}-Einheiten ein Netzwerk. Mikrokristalle von $Li_7Mn(BO_3)_3$ zeigen nur eine sehr geringe erste Entladekapazität von etwa 11 mAh/g, die auf die geringe elektrische Leitfähigkeit zurückzuführen sein dürfte. Jedoch erreichen Komposit-Elektroden aus Nanokristallen dieses Materials mit Kohlenstoffe bei der ersten Ladung bereits etwa 280 mAh/g (Extraktion von etwa 3 Li) und eine erste Entlade-Kapazität von immerhin beachtlichen 154 mAh/g.

Im letzten Kapitel der vorliegenden Arbeit wird gezeigt, dass Vanadat-Borat-Gläser und Glaskeramiken vielversprechende Kandidaten für Kathoden-Materialien mit hoher Kapazität in wiederaufladbaren Lithiumbatterien der nächsten Generation sind. Die Synthesemethoden für Gläser und Glaskeramiken sind sehr einfach und kosteneffizient. Bei der Entladung zeigen Vanadat-Borat-Glaskeramiken eine mehrstufige Lithiumeinlagerung, während die Vanadat-Borat-Gläser stufenlose, auf homogene Lithiierungsmechanismen hinweisende, Lade/Entlade-Zyklen zeigen. Besonders die für die neuen glasartigen V_2O_5–$LiBO_2$-Komposit-Elektroden mit RGO erreichten Werte sind sehr ermutigend im Hinblick auf die praktische Anwendbarkeit dieser Komposite als Kathodenmaterialien. Glas-Komposit-Elektroden von V_2O_5–$LiBO_2$ erreichen Kapazitäten im Bereich von 300 mAh/g über 50 Zyklen. Vergleichbare elektrochemische Werte können für Vanadat-basierte und andere Kathodenmaterialien nur nach sehr teuren und aufwändigen Prozessen erreicht werden. Die glasartigen Kathoden-Komposite haben durchaus das Potential Kathodenmaterialien für zukünftige Hochleistungsbatterien zu werden. Als übergreifendes Ergebnis konnte gezeigt werden, dass auch Stoffe, die üblicherweise als Isolatoren klassifiziert werden, so präpariert werden können, dass sie elektrochemisch nutzbar werden.

Abbreviations	
LIBs	Lithium-ion Batteries
EV	Electric Vehicles
PHEV	Plug-in Hybrid Electric Vehicles
DMC	Dimethyl Carbonate
EC	Ethylene carbonate
DEC	Diethyl carbonate
EMC	Ethyl methyl carbonate
PVDF	Polyvinylidene Fluoride
THF	Tetrahydrofuran
NMP	*N*-Methyl-2-pyrrolidone
PP	Polypropylene
PEO	Polyethylene oxide
XRD	X-ray Diffraction
TEM	Transmission Electron Microscopy
HRTEM	High Resolution Transmission Electron Microscopy
HAADF	High Angle Annular Dark Field
EELS	Electron Energy Loss Spectroscopy
SEM	Scanning Electron Microscopy
EDX	Energy Dispersive X-Ray
ED	Electron Diffraction
DTA	Differential Thermal Analysis
FTIR	Fourier Transform Infrared Spectroscopy
OCV	Open Circuit Voltage
SHE	Standard Hydrogen Electrode
CV	Cyclic Voltammetry
GITT	Galvanostatic Intermittent Titration Technique
SEI	Solid Electrolyte Interface

Table of Contents

List of Figures

Chapter 1

Introduction to Rechargeable Lithium Batteries

1.1 Energy Storage

Still the easiest way to access stored energy is to find it as wood or hydrocarbon fossil fuels. The processing and conversion of raw fossil fuels into other forms, like petrochemicals, has also been found very useful, and brought about legion of applications and countless scientific discoveries. However, wood and fossil fuels are not infinitely available on earth. With increasing energy demand in the modern era, the hydrocarbon sources are gradually depleted. The American geophysicist M. King Hubbert predicted the depletion of fossil fuels in 1956, denying the belief that new oil fields would be continuously found[1]. He proposed that fossil fuel production (or other natural resources) in a given region over time tends to follow a bell-shaped curve, reaching a peak point and gradually declining afterwards (**Fig. 1.1**).

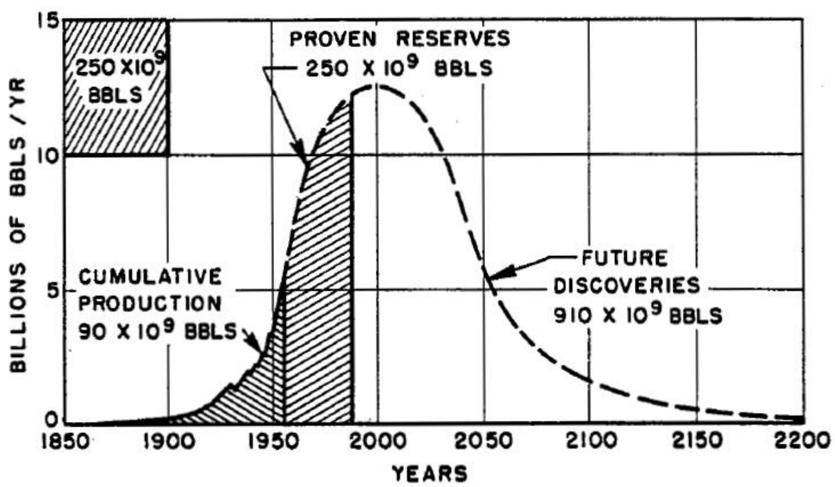

Figure 1.1 Ultimate world-wide crude-oil production projected by M. King Hubbert in his report "Nuclear Energy and The Fossil Fuels"[1].

The Hubbert peak theory was not taken seriously for decades, but gained popularity after a more correct estimation of the peak point and declines of oil production in the continental US in the early 1970s[2]. Thus, it is also expected that the fossil fuel production of the world will peak in near future, as the rate of new field discovery cannot keep up with the depletion rate of available resources. Growing population of the world and increasing energy demand of developing countries are to be considered as additional parameters that further degrade the long term sustainability of fossil fuels. In addition to the inevitable future depletion, the use of fossil fuels as the major source of energy has also potentially disastrous effects on the environment in terms of climate changes, pollution and global warming. Therefore, generation of sustainable and clean energy from alternative sources, such as solar, hydro, wind and tidal, becomes more and more important, and in recent years, the share of alternative sources in the total energy production has increased in developed countries (**Fig. 1.2**)[3].

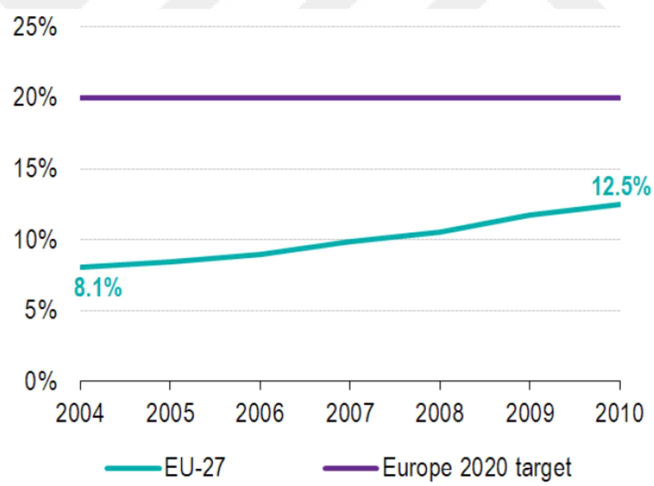

Figure 1.2 The percentage of renewable energy in total energy consumption for European Union (taken from [3]).

The generation of electricity by hydropower is one of the most widely used forms of renewable energy, where the large scale energy storage is also realized by pumping water to reservoirs at different heights. But, the loss of land, the unavailability of water and the damages to ecosystem could make increasing hydroelectricity disadvantageous in future. The sporadic nature of other renewable energy sources (for instance, solar electricity is not available when the sun does not shine) requires effective energy storage mechanisms different from using fossil fuels to supply electricity to grid. Currently, thermal stations producing electricity through the combustion of coal and crude oil are typically employed to power electrical grids, when renewable energy sources are not available or not sufficient to supply the demands.

In addition to large scale grid applications, there are also various portable applications that require effective energy storage. Among these applications, powering of portable electronics and vehicle propulsion make the electrochemical energy storage through batteries the most popular and extensively investigated choice compared to the other storage mechanisms. Though most of the automobiles on the roads are still powered by combustion engines, plug-in hybrid vehicles (PHEV) with rechargeable nickel-metal hydride batteries are also on the market for over a decade. PHEVs have both an electric motor and an internal combustion engine that are usually employed for short and long range driving, respectively. Since the introduction of PHEVs in 1997, the leading brand of hybrid vehicles has sold more than 4 million units worldwide as of April 30th 2012[4]. The limited range of PHEVs (~ < 100 km) when running on batteries alone have been extended to ~ 160 km for full electric vehicles (EV) that have become available in recent years[5-7]. EVs are solely powered by Li-ion batteries, and they don't have internal combustion engines. Owing to their high energy density, long cycle life and variable charge-discharge rates, rechargeable lithium batteries are preferred to power electric vehicles by car manufacturers[5-7]. However, the current technology and materials used in lithium batteries are still not sufficient to provide high practical energies that could increase the range of electric vehicles, and consequently, enable the large scale use of such vehicles with the elimination of range anxiety experienced by consumers. Bruce et al. predicted the driving ranges that could be supplied by future battery technologies (**Fig. 1.3**)[8].

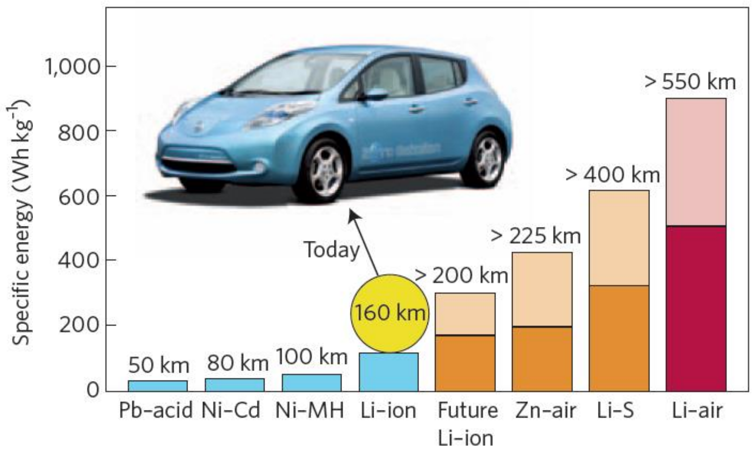

Figure 1.3 Practical specific energies and projected driving ranges for some rechargeable batteries, after Bruce et al.[8].

Although a minimal development in the field of Li-ion batteries is forecasted, the discovery of new electrode materials with high theoretical specific energies could lead to driving ranges beyond the presently anticipated value of ~ 200 km. The ultimate goal is to employ batteries like Li-air that can extend driving ranges to over 550 km, close to the ones provided by combustion engines. But, it should be noted that even for the current battery technologies, and specifically, for the rechargeable lithium batteries, several problems and barriers, such as cycle-life, high cost and safety characteristics, exist that should be overcome in order to realize a large scale application for electrical vehicles and grids.

1.2 Electrochemical Energy Storage and Battery Types

Electrical energy can be harvested in an electrochemical cell through spontaneous redox reactions. Electrochemical cells are categorized as galvanic cells and electrolytic cells depending on the spontaneity of the reaction. In an electrolytic cell, an externally applied current drives the reaction, and electricity is converted into chemical energy, whereas due to the difference in the chemical potential of two electrode materials, a chemical driving force occurs in a galvanic cell (battery). A simple galvanic cell (Daniell cell) is displayed in **Figure 1.4**.

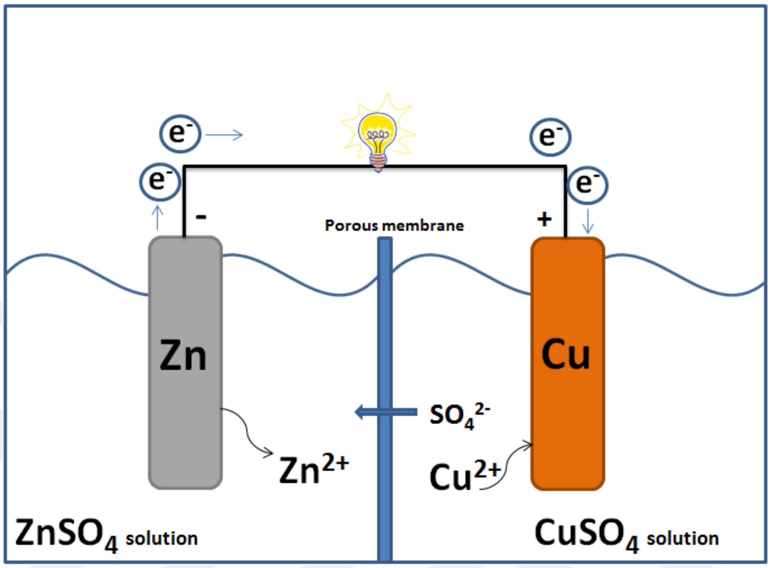

Figure 1.4 Schematic representation of a galvanic cell.

The galvanic cell consists of two half-cells that are made up by Cu and Zn metal electrodes. At the anode (negative pole), oxidation of zinc metal occurs, while Cu^{2+} species in the aqueous solution are reduced at the cathode (positive pole). The electrons formed at the anode flow through an external circuit to the cathode. Two half-cells are separated by a porous membrane and the charge balance is supplied by the movement of ions through the aqueous electrolyte. The corresponding half-cell reactions and the overall equation are given below:

$$Zn_{(s)} \rightarrow Zn^{2+}_{(aq)} + 2e^- \text{ (anode, oxidation)} \qquad 1.1$$

$$Cu^{2+}_{(aq)} + 2e^- \rightarrow Cu_{(s)} \text{ (cathode, reduction)} \qquad 1.2$$

$$Zn_{(s)} + Cu^{2+}_{(aq)} \rightarrow Zn^{2+}_{(aq)} + Cu_{(s)} \qquad 1.3$$

The chemical driving force for the electrochemical reaction can be expressed as the standard Gibbs free energy change per mole of reaction, ΔG_r^o, that is the difference between the standard Gibbs free energy of products and reactants. The standard electrode potential of half-cell at equilibrium is obtained by dividing -ΔG_r^o to z*F, where z is equal to the number of electrons transferred and F is the Faraday constant (~ 96500 C/mol).

$$E^o = \frac{-\Delta G_r^o}{zF} \qquad 1.4$$

Under non-standard conditions meaning the possible variations of pH, temperature and concentrations, the half-cell potential can be calculated by the Nernst equation, where R is the gas constant, T is the absolute temperature, F is the Faraday constant, a^i is the activities and v^i is the stoichiometric coefficients.

$$E = E^o - \frac{RT}{zF}\sum_i ln\, a_i^{v_i} \qquad 1.5$$

The voltage of the complete electrochemical cell is given by the difference between the positive electrode potential and the negative electrode potential. The standard hydrogen electrode (SHE) ($2H^+/H_2$, 0 V, at T = 25 ^oC) is used as the reference electrode to form a basis of comparison with other electrode reactions. Thus, the theoretical cell voltage for $Zn \,|\, Zn^{2+} \,\|\, Cu^{2+} \,|\, Cu$ can be calculated as +0.34 V − (−0.76 V) = 1.10 V.

$$\Delta E_{cell}^o = E_{cathode}^o - E_{anode}^o \qquad 1.6$$

Batteries can be categorized based on the reversibility of the electrochemical reactions and the initial charge/discharge states:

a) Primary Batteries: The term "primary battery" is generally used to describe non-rechargeable batteries. Primary batteries are ready for immediate use, delivering energy once connected to an electric device. They can be used for a one complete discharge as electrochemical reactions in cells are not reversible. Initial costs are lower and shelf lives are longer compared to rechargeable batteries. They are also more readily available and widely used in various consumer electronics, such as flashlights, calculators, watches and remote controls. The most commonly used primary batteries and their corresponding practical working potentials, gravimetric and volumetric energy densities are given in **Table 1**.

Table 1: Most commonly used primary batteries.

Battery Type	Voltage (V)	Specific Energy (Wh/kg)	Energy Density (Wh/l)
Alkaline (Zn/MnO_2)	1.5	130-145	320-430
Silver-oxide (Zn/Ag_2O)	1.55	130-140	400-500
Zinc-air (Zn/O_2)	1.4	350-450	500-1700
Lithium (Li/MnO_2)	3.0	270-280	600-700

b) Secondary Batteries: Rechargeable batteries are also termed secondary batteries; their electrochemical reactions are reversible. Though they elicit higher initial costs compared to primary batteries, they become cheaper in the long-term, if convenient cycling numbers and inexpensive charging are achieved. Despite of having very low energy densities, lead-acid batteries are the oldest rechargeable batteries that are still commonly used to power the starters of combustion engines and for emergency power systems. Lithium battery systems are the most popular among secondary batteries with a still continuing progress both at the fundamental and applied research levels. They dominate the portable electronics market owing to their high energy densities. Most common and widely used rechargeable battery systems batteries with their practical working potentials, gravimetric and volumetric energy densities are listed in **Table 2**.

Table 2: Most commonly used secondary batteries.

Battery Type	**Voltage (V)**	**Specific Energy (Wh/kg)**	**Energy Density (Wh/l)**
Lead-acid (Pb/PbO_2)	2.1	30-40	60-100
Ni-Cd (NiOOH/Cd)	1.2	45-60	100-150
Ni-MH ($NiOOH/MH_x$)	1.2	50-80	170-250
Li-ion ($LiCoO_2/C$)	3.6	100-200	200-350

c) Reserve Batteries: This type includes both primary and secondary batteries, where the battery is not activated until it is needed. Thermal batteries with practical specific energies in the range of ~100 Wh/kg, such as Na/Na_xS[9-11] and ZEBRA ($Na/NiCl_2$)[12] that are activated by heat, are among the most well-known examples. For instance, Na/Na_xS thermal batteries operate at 300-350 ^oC and are activated mainly by sodium in the molten state[13]. The battery configuration can be formulated as liquid/solid ($NaAl_{11}O_{17}$ electrolyte)[14]/liquid, rather than the conventional solid/liquid (electrolyte)/solid battery setup. Thermal batteries are especially used in various weapon systems. By the segregation of active chemicals of the cell until needed so prolonging the lifetime, reserve batteries are suitable for medium to large scale energy storage applications. Flow batteries[15], which are also used for large scale energy storage, might be included in this category as well, since active redox ions in negative and positive electrolyte tanks are pumped into the electrochemical cell when needed.

1.3 Important Practical Parameters, Definitions and Concepts

Batteries are devices that transduce chemical energy into electrical energy, and vice versa, if electrochemical reactions are reversible. The potential difference between two electrodes immersed in an electrolyte and separated by a porous membrane allows electrical work with the passage of electrons through an external circuit, assuming a good electronic conductivity for electrodes and a good ionic conductivity for electrolyte. Some important practical parameters, concepts and equations that are used to describe and understand battery characteristics are stated here.

Cathode: The electrode with the more positive potential for a galvanic cell.

Anode: The electrode with the more negative potential for a galvanic cell.

Electrolyte: The medium for the transfer of ionic charges only. Usually, a liquid solution of non-aqueous organic solvent with lithium salts for rechargeable lithium batteries.

Separator: A porous ceramic or polymer separating half-cells of a battery, while allowing the transfer of ions. Separators prevent shortcut between electrodes but have no ion selectivity.

Cell, modules and packs: A cell containing electrodes, electrolyte, separator, wiring, and current collectors is the smallest unit of a large battery pack. Cells connected in series or parallel build up modules. Modules, again connected in series or parallel, form larger battery packs.

Cell voltage: The theoretical cell voltage (E^o) can be calculated from the Gibbs free energy change per mole of reaction, $\Delta G_r^{\ o}$ (Equation 1.4). If there are no loss mechanisms, the experimentally measured value (U^o) should be equal to the theoretical one.

Charge & Discharge: The battery produces electricity by spontaneous electrochemical reactions during discharge, while an external current is applied to reverse these reactions to charge the battery.

Current Density: The current density is the ratio of the total current (I) to the electrode area (A).

$$j(t) = \frac{I(t)}{A} \qquad 1.7$$

Charge capacity: The charge capacity (Ah) is the amount of charge delivered by a cell.

$$Q = \int_{t1}^{t2} I(t)dt \quad [Ah] \qquad 1.8$$

Specific capacity: The theoretical specific capacity is the total amount of charge per mass unit for the electro-active material. It depends on the molecular weight and the electrochemical reactions of the material, and often reported as mAh/g or Ah/kg. The practical value is found by dividing the total charge obtained to the total mass of the active material (or cell).

$$q_{th.} = \frac{zF}{\sum_i m_i} \quad [Ah/kg] \qquad 1.9$$

$$q = {}^{1}\!/_{m} \int_{t1}^{t2} I(t)dt \quad [Ah/kg] \qquad 1.10$$

Specific charge density: The ratio of charge to the volume of reactants gives the theoretical value, whereas the practical charge density is the total amount of obtained charge divided by the volume of the active material (or cell).

$$Q_{V\,th.} = \frac{zF}{\sum_i V_i} \quad [Ah/l] \qquad 1.11$$

$$Q_V = {}^{1}/_{V} \int_{t1}^{t2} I(t)dt \quad [Ah/l] \qquad 1.12$$

Specific energy: Specific energy values of an electrode material or a practical cell are usually reported in Wh/kg. Theoretical values can be obtained by multiplying specific capacities with the theoretical cell voltages. The practical specific energy is given by the ratio of the yield of total electrical energy to the total mass of the active material (or cell).

$$w_{th.} = \frac{zF\Delta E^{o}}{\sum_i m_i} \quad [Wh/kg] \qquad 1.13$$

$$w = {}^{1}/_{m} \int_{t1}^{t2} I(t)U(t)dt \quad [Wh/kg] \qquad 1.14$$

Specific energy density: Similar to the above described gravimetric energy measures, specific energy densities are obtained by the division of total electrical energy values to the volumetric values.

$$W_{V\,th.} = \frac{zF\Delta E^{o}}{\sum_i V_i} \quad [Wh/l] \qquad 1.15$$

$$W_V = {}^{1}/_{V} \int_{t1}^{t2} I(t)U(t)dt \quad [Wh/l] \qquad 1.16$$

Specific power and power density: Power (W) is obtained by the multiplication of current (A) and voltage (V) in an electrical device; specific power and power density are ratios of power values to mass and volume, respectively.

$$P = \frac{IU}{\sum_i m_i} \quad [W/kg] \qquad 1.9$$

$$P = \frac{IU}{\sum_i V_i} \quad [W/l] \qquad 1.10$$

Coulombic efficiency: The ratio of the charge capacity to the discharge capacity for a given cycle is defined as Coulombic efficiency.

Polarization: The polarization is the deviation of working potential from its theoretical value resulting in a difference between average charge and discharge voltages.

C-rates: C-rates are used to describe current rates that are employed to charge or discharge batteries. The amount of capacity, C, is usually taken as the theoretical specific charge capacity, and for instance, the rates of C, C/2 and C/10 correspond to the currents that should theoretically fully charge or discharge the battery in 1, 2 and 10 hours, respectively.

1.4 Electrochemical Characterization

In this study, the electrochemical properties of materials under investigation were usually analyzed through galvanostatic and cyclic voltammetry tests, which were performed in a two-electrode configuration by using BAT-SMALL potentiostat and ASTROL software package (both acquired from Astrol Electronic AG). All of the electrochemical data were obtained at room temperature. In this work, the potential values are referring to the Li^+/Li reference electrode.

Swagelok-type cells that are schematically illustrated in **Figure 1.5** were used to carry out the electrochemical measurements. The outer casing of the cell is stainless steel, whereas the inner parts, in contact with the electroactive materials, are made of titanium. The counter electrode is constructed from a lithium disk (ca. 1.5 cm diameter) prepared by using 0.75 mm-thick ribbon Li (Aldrich) that is placed on a titanium cylinder, which is pressed against the working electrode with a spring mechanism. The working electrode is made up from a film of active material (the material under study) containing conductive carbon and binder that is coated on titanium current collectors. A polypropylene (PP) (Celgard®) separator is positioned on top of the active material film, and a second silica separator soaked in liquid electrolyte is placed on the first separator. The construction of electrodes and complete cells were carried out in an argon filled glove-box.

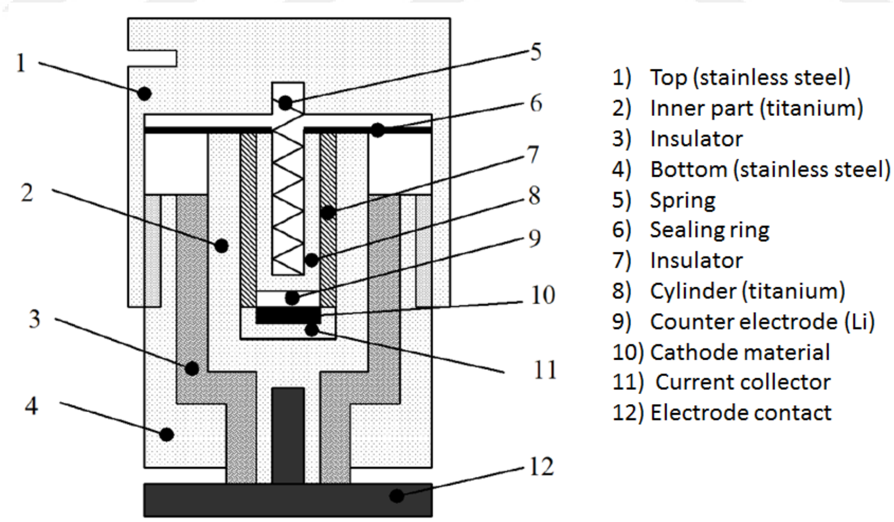

Figure 1.5 Schematic drawing of cells used for electrochemical characterization[16].

Cyclic voltammetry is usually applied as the first electrochemical characterization technique to get an initial idea about electrochemical processes in the study of new materials.

The potential of the electrochemical system is varied with a constant rate, which is called sweep rate (ν), through a chosen potential window. The potential window might be selected in accordance to similar systems considering the stability of electrolyte at the same time. In a CV-diagram or cyclic voltammogram, the measured current flow is plotted against the voltage. The curve above the zero line (anodic) is obtained with a positive sweep rate and denotes the oxidation or charge of a positive electrode material, whereas the negative curve (cathodic) designates the reduction and the discharge of a positive electrode material.

Galvanostatic cycling allows an insight into electrochemical processes and is apt to estimate the possible performance of materials under real working conditions. In a galvanostatic test, a constant current is applied between electrodes in a fixed potential window. Galvanostatic charge/discharge graphs are obtained by plotting the voltage against time or the state of charge. For a positive electrode material, the galvanostatic curve extending from the lower voltage limit (or the open-circuit voltage (OCV)) to the upper voltage limit designates the charge, whereas the discharge curve starts from the upper voltage limit (or OCV) and decreases down to the lower voltage limit. The delivered charge/discharge capacities are evaluated by comparing them to the theoretical specific capacities and corresponding data for related systems.

1.5 Rechargeable lithium batteries

The light weight of lithium (M = 6.94 g/mol and ρ = 0.53 g/cm^3) and the most negative potential among metals (-3.04 V vs. SHE) of the Li^+/Li redox couple motivated researchers to explore lithium metal anode based battery technologies with high energy densities. Primary battery technologies employing Li anodes, such as Li/MnO_2 and Li/$Ag_2V_4O_{11}$, which were commercialized in 1970s, are still popular and used in portable electronics like watches, calculators and medical defibrillators. The development of rechargeable lithium batteries was also continuing in parallel, and the concept of lithium insertion into layered structures, the reversible extraction of lithium afterwards and cycling of the electrode material at favorably high potentials and capacities were first shown for the layered structure TiS_2 (Li_xTiS_2)[17]. Many layered structures, such as MoS_3, MoO_3, V_2O_5 and $NbSe_3$, were similarly studied by various researchers afterwards[18-20]. In these configurations, batteries were assembled in charged states with pure metallic Li anodes and oxidized cathodic materials. The use of a lithiated positive electrode material was first demonstrated by Goodenough et al. in 1980s[21]. The layered-compounds, Li_xMO_2 (M = Co, Mn and Ni)[22-26], displayed working potentials of up to 4 V against Li^+/Li, and the employment of already lithiated positive electrode materials opened the door for the discovery of rechargeable Li-ion batteries on the discharged state without metallic lithium anodes.

For the early rechargeable lithium batteries, dendritic lithium growth on extensive cycling causing capacity losses, short-circuits and eventual explosion hazards, was a huge safety problem. This shortcoming was tried to be tackled with Li-alloy based anodes[27], but the capacity retention was found to be quite poor for such anode materials due to extreme volume changes leading to crumbling, cracks and contact losses. Another idea was the use of an insertion material for the anodic part as well[28-29], so that dendrite growth could be prevented by depositing Li in the ionic state at the anode. This concept that is called Li-ion or rocking-chair had contributions from various scientists eventually leading to the commercialization of the $C/LiCoO_2$ rocking-chair battery. **Figure 1.6** shows a schematic representation and operating principles of Li-ion battery.

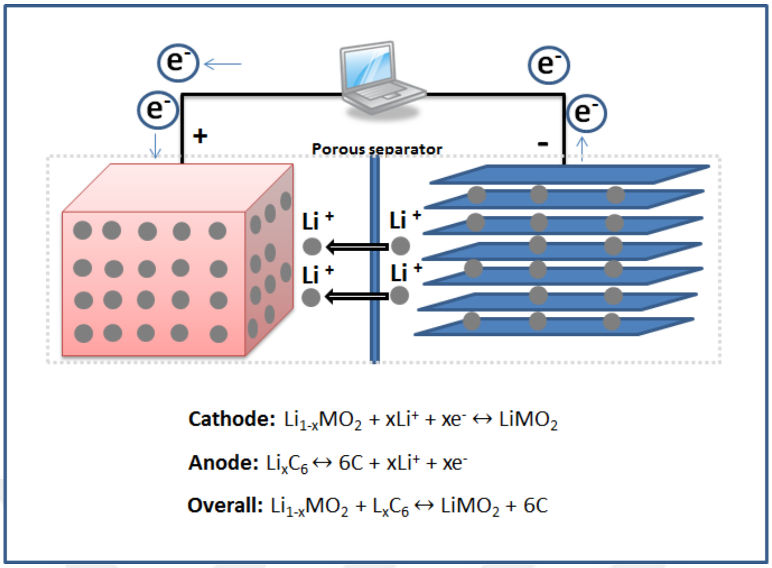

Figure 1.6 Schematic representation and operating principles of Li-ion battery.

A typical Li-ion battery consists of two electrode materials, into which lithium ions can be inserted back and forth in a reversible way. The electrochemical reaction proceeds with the oxidation of positive electrode material (e.g. Li_xMO_2) and the lithiation of negative electrode material (e.g. graphite) during charge. For the discharge process, lithium ions are extracted from the negative host and inserted back to the positive host. A solution of a lithium salt (e.g. $LiPF_6$) in an organic solvent (e.g. ethylene carbonate (EC):dimethyl carbonate (DMC) mixture) is usually selected as the electrolyte. In general, Li-ion batteries have the advantages of high energy density, long cycle life, no memory-effect and low self-discharge rates over conventional secondary batteries. Compared to the other rechargeable systems with aqueous electrolytes, the use of electrolytes is also minimized, since the organic electrolyte is not directly consumed during electrochemical reactions, which also allows practical uses in the form of very compact battery designs.

1.6 Materials for Li-ion and Li-batteries

1.6.1 Electrolytes

Electrolytes are media for the transfer of ions during the operation of batteries. In the case of rechargeable lithium batteries, Li^+ ions shuttle back and forth between positive and negative electrodes. The conventional electrolytes for Li-ion batteries consist of lithium salts (e.g. $LiPF_6$, $LiAsF_6$, $LiBF_4$, $LiClO_4$ and $LiCF_3SO_3$) dissolved in non-aqueous organic solvents (e.g. ethylene carbonate (EC), dimethyl carbonate (DMC) and 1,3-Dioxolane) or in mixtures of them. There are also continuing research efforts to develop safer, cheaper and more sustainable electrolyte systems. Some important requirements and parameters for electrolytes affecting the safe, practical and sustainable operation are listed below.

- Electrochemical stability in the potential window of the battery against cathode and anode materials.
- Low electronic conductivity ($< 10^{-10}$ S/cm)[30].
- Ionic conductivity in the range of 10^{-3} S/cm[30].
- Low cost and environmentally benign educts and products for the synthesis.
- Thermal stability and non-flammability up to 80-90 ^oC.

Type of electrolytes:

Organic Liquid Electrolytes: The most common electrolyte used in commercial Li-ion batteries, $LiPF_6$ dissolved in a mixture of ethylene carbonate (EC) with another carbonate (dimethyl carbonate (DMC), diethyl carbonate (DEC) or ethylmethyl carbonate (EMC)), falls under this category. Carbonate-based electrolytes are preferred for their ability to dissolve lithium salts, being fairly stable in a large potential of 4.7 – 1.0 V and forming protective SEI layers on graphitic anode materials[31-33]. However, their thermal stability, especially, in a battery comprising layered oxide cathodes and graphitic carbon anodes, have been considered to be problematic[34-35]. The use of additives as artificial SEI (solid electrolyte interface) formers, such as lithium bis(oxalato) borate[36], lithium difluoro(oxalato) borate[37], lithium tetrafluoro(oxalato) phosphate[38] and etc., have been proposed to stabilize such batteries. However, the costs of organic liquid electrolytes are very high even without any additives. The high cost of conventional carbonate-based electrolytes is also one of the main reasons for the search of alternative electrolyte systems.

Ionic Liquids: Ionic liquids, particularly those based on imidazolium cations, have also been explored as electrolytes for Li-ion batteries owing to their stability at high potentials (∼ 5.3 V vs. Li^+/Li)[39], their good thermal stability, high boiling points, non-flammability and their low volatility, which support a safe and sustainable operation especially at highly charged states and under thermal abuse conditions. The main drawbacks hindering the practical use of ionic liquid electrolytes are considered to be high viscosity, lack of protective SEI formation and very high prices.

Solid Electrolytes: Inorganic solid electrolytes and solid polymer electrolytes have been extensively investigated, since they provide additional advantages such as the elimination of the otherwise necessity for separators, usually better thermal and chemical stabilities, easy production and high availability of materials. Inorganic solid electrolytes have been mostly studied for thin-film lithium batteries, and lithium phosphorus oxynitride (LiPON)[40-41] and thio-LISICON ($Li_xA_{1-y}M_yS_4$, A = Si, Ge and M = P, Al, Zn, Ga, Sb)[42-43] materials have been usually selected for those investigations and applications. Even though good ionic conductivities in the range of ∼ 10^{-4} S/cm[42] were demonstrated for inorganic solid electrolytes, their use in larger scale batteries and long-term applications might be hindered because of contact losses on the electrode/electrolyte interface by the volume work with ongoing cycling.

Solid polymer electrolytes are usually based on polyethylene oxides (PEOs) consisting of lithium salts[44-46]. They are of low cost, nontoxic and easy to process providing many engineering benefits for Li-ion batteries, but the poor ion conduction in solid polymer electrolytes requiring higher operating temperatures (60-90 ^{o}C) is a drawback for many practical applications. This problem has been addressed and is still tackled by using hybrid systems containing additives, different lithium salts and different polymer backbones. There are commercial batteries in the market under the name, Li-ion polymer batteries, but in reality these systems mostly contain jellified polymers (e.g. PEO and PAN) with organic liquids, which is a compromise between carbonate-based electrolytes and solid polymer electrolytes.

1.6.2 Negative electrode materials

Early investigations on negative electrode materials for LIBs were triggered by the necessity of safer systems, as the use of elemental lithium anode for extensive cycling was an apparent safety risk with possible thermal runaway and explosion hazards of the battery. Most of the safety risks associated with the anode side of LIBs were circumvented by the employment of graphitic carbons as negative electrode materials, but the capacity was largely reduced as well. Thus, today, many researchers focus on the development of anode materials with high specific capacities and good cycling properties. Some other key parameters for anode materials are low cost, eco-friendliness, high energy density, etc., which are also valid and important for cathode materials. On one hand, the working potentials of negative electrode materials should be close to the reference (Li^+/Li) electrode potential in order to maximize the overall cell potential; on the other, a potential larger than 0.5 V above Li/Li^+ increases safety considerably, so that at the preset stage of knowledge, a compromise seems to be unavoidable.

1.6.2.1 Insertion materials

Widely used commercial anode materials for LIBs fall under the category of graphitic carbons that have the advantages of electrochemical stability, low cost, easy production and high availability. Graphitic carbon contains sp^2-hybridized C atoms arranged in hexagonal rings extending into two dimensional sheets (graphene layers). The interlayer distance of sheets is ~ 0.34 nm, and they are stacked as $(AB)_n$ (hexagonal graphite) or as $(ABC)_n$ arrangements. Li^+ ions can be intercalated into these layers forming Li_xC_6 with a maximum theoretical capacity of 372 mAh/g (x=1). During the insertion of Li^+ ions, different staging intermediates are formed in the potential range of ~ 200 mV – 50 mV (vs. Li^+/Li) as the stacking order of layers finally changes to an arrangement of ecliptic $(A)_n$ type[47]. On the initial discharge of a Li-ion battery with graphite anode, a solid electrolyte interface (SEI) at around ~ 700-800 mV is formed, that is generally composed of organic components and inorganic compounds, such as LiF, Li_2CO_3 and Li_2O[33, 48-49]. Although it causes an irreversible capacity loss in the first discharge, SEI layers passivate the graphite surfaces preventing further decomposition of the electrolyte and delamination of the anode. This provides a longer and safer operation of the battery. In addition to graphite, various soft and hard carbon materials, nano-forms of carbon as well as amorphous carbons have also been investigated as anode materials for Li-ion batteries. They were shown to provide capacities up to ~ 1000-1200 mAh/g[50-54]. These capacities beyond the theoretical capacity of graphite have been usually explained by the insertion and adsorption of Li^+ ions into defect sites and voids in addition to the intercalation process[54].

$Li_4Ti_5O_{12}$ and TiO_2 are other attractive insertion type negative electrode materials that have been widely studied. Lithium titanate based negative electrodes are currently used in plug-in electric vehicles owing to their excellent cycling stability and fast kinetics. Toshiba commercialized nano-based lithium titanate batteries under the product name, Super-Charge Ion Battery (SCiB™)[55], which were also chosen to power Mitsubishi's i-MiEV electric vehicle[5]. After 6000 cycles at a rate of 3C, more than 80 % of the initial capacity is claimed to be retained in Super-Charge Ion Battery (SCiB™)[55]. $Li_4Ti_5O_{12}$ is limited compared to carbon based anodes in terms of gravimetric energy density because of a potential of 1.55V vs. Li/Li^+ and a lower theoretical capacity of ~ 175 mAh/g[56-57]; however, nano lithium titanate offers excellent cycling stability and rate capability due to almost zero volume work during cycling and reduced or none electrolyte decomposition stemming from the higher working potential[56-59].

1.6.2.2 Conversion materials

The conversion reactions of transition-metal oxides (e.g. CoO, NiO, Co_3O_4, Fe_3O_4 [60-62]), nitrides (e.g. Cu_3N, Fe_3N, Co_3N [63-64]), phosphides (e.g. VP_4, FeP_2, MnP_4, CoP_3 [65-66]) and fluorides (e.g. FeF_3, FeF_2, CoF_2 [67-69]) with lithium have also been extensively investigated. Negative electrodes based on conversion reactions have been tried out for utilization in Li-ion batteries. Depending on the degree of lithiation, transition-metal particles can be formed and embedded on the respective binary lithium compound (e.g. Li_2O, Li_3N). Especially for transition-metal oxides, high capacities with reversible cycling have been demonstrated. Tarascon et al. showed reversible capacities in the range of 700-800 mAh/g up to 100 cycles for the nanoparticles of MO (M = Co, Cu, Fe and Ni)[62]. The lithiation/delithiation process was proposed to occur through the formation/decomposition of Li_2O (e.g. $CoO + 2Li \leftrightarrow Li_2O + Co$)[62]. Although excellent capacity retention and high capacities have been displayed for conversion-type anode materials, their practical use is limited due to large polarization between charge and discharge potential curves, high electrode potentials compared to graphitic carbons and instability for some of these materials under ambient conditions.

1.6.2.3 Lithium alloys

In order to tackle problems associated with the use of metallic lithium anodes, such as dendritic lithium growth with cycling and safety risks under thermal abuse conditions due to the low melting point of lithium, early research efforts have been devoted to the development of Li alloys as negative electrodes for Li-ion batteries. LiAl was one of the early explored alloys with a theoretical specific capacity of 790 mAh/g and a working potential of 0.3 V vs. Li^+/Li[27, 70]. Though the dendrite formation had been prevented through the use of a LiAl anode, later, it was found that the cycling stability became very poor due to extreme volume changes during lithiation/delithiation. In recent years, various alloys of lithium, Li_xM_y (M= Al, Ga, In, Si, Ge, Sn, Pb, Sb and Bi)[70-75], have been extensively studied as next generation anode materials, and especially, silicon based materials have gained particular attention owing to the very high theoretical capacity of $Li_{21}Si_5$ (~ 4008 mAh/g) and operating potentials below ~ 500 mV. But, similar to other lithium alloys, for silicon based anode materials, the capacity retention over multiple cycles has been found to be poor due to volume expansions up to ~ 400 % with lithiation[75-77]. Large volume changes under repeated lithiation/delithiation lead to the pulverization of the electrode and contact losses resulting in a poor cycling behavior. The continuous SEI formation with ongoing cycling has been suggested as another reason for the poor capacity retention[78]. Several approaches, namely, the employment of well-defined nanostructures and the application of functional coatings to counter the mechanical stress, have been used in order to improve the electrochemical performance of silicon based electrodes. For

Si nanowires directly grown on current collectors, Cui et al. achieved high capacities close to the theoretical value of $Li_{21}Si_5$ for a few cycles at a rate of C/20, and the capacity was retained at a level of 75 % for 10 cycles[75], and Huang et al. showed a capacity of 1326 mAh/g after 40 cycles for carbon coated Si nanowires[79]. The improved performance of Si nanowires compared to bulk and various nanostructured silicon anodes was attributed to the better electrical contact to current collector, efficient electron transport along the nanowire and facile relaxation of strain horizontally on the nanowire[75]. Hollow Si nanostructures were also demonstrated to perform at high capacities with good cycling stability. Park et al. fabricated hollow Si nanotube structures by using alumina templates[80]. These hollow structures delivered charge capacities of ∼ 3200 mAh/g at 1C rate, and the capacity was retained at a level of 89 % after 200 cycles[80]. In another investigation, a remarkable cycling stability has been accomplished via adding a mechanical constraining layer on hollow Si structures by Wu et al.[78]. Fairly high capacities of ∼2970 mAh/g and ∼1000 mAh/g at C/5 and 12C current rates, respectively, were obtained with up to 88 % capacity retention after 6000 cycles[78]. The long cycle life and enhanced electrochemical performances were ascribed to SiO_x coating layer on double walled Si nanotubes preventing large volume expansions and continuous SEI formation[78]. Although most of them don't get close to the cycling stability demonstrated by Wu et al., there have been many other investigations employing carbon[81-83] and metal-particle coatings (e.g. Ag, Fe, Cu and Co)[84-86] on silicon nanostructures. However, it should be noted that even at enhanced cycling stability and at high capacities, the practical use of silicon based anode materials is still rather challenging. Even if the volume expansion of silicon under lithiation could be limited to some extent, it would be still higher compared to graphitic anodes that might require the engineering of a cell with more space limiting the practical volumetric energy density. Furthermore, synthesis routes and approaches to form nanostructured composite silicon anode materials could be considered rather difficult, complicated and expensive for up-scaling and practical applications.

A selection of negative electrode materials that were previously described are listed in **Table 3** with their theoretical specific capacities and approximate potential windows, in which most of the capacities are obtained.

Table 3: Negative electrode materials for rechargeable lithium batteries.

Anode Material	Voltage (V)	Specific Capacity (Ah/kg)
LiC_6	0.05-0.5	372
$Li_4Ti_5O_{12}$	1.55	175
CoO	1.0-2.0	700-800
LiAl	0.3	790
$Li_{21}Si_5$	0.05-0.5	4008

1.6.3 Positive electrode materials

The working potential of a lithium battery is predominantly determined by the positive electrode (cathode), since widely used negative electrode (anode) materials have reduction potentials close to the reference (Li^+/Li) electrode potential. It may be asserted that today's applied and fundamental scientific investigations are mostly focused on positive electrode materials, especially those with high gravimetric and volumetric energy densities being usually targeted to enable the large scale employment of LIBs for energy storage applications. In addition, the impact of cathode materials on safe and sustainable operation of LIBs should also be considered. Thus, some key parameters that have to be kept in mind when choosing or studying a positive electrode material are listed below:

- High specific energy that might be provided by light weight, high operating voltage and utilization of more than one Li per formula unit.

- High volumetric energy density (a compromise with gravimetric density is necessary).
- Good electronic and ionic conductivity.
- Stability against electrolyte.
- Structural stability, reversibility of electrochemical reactions, and safety characteristics upon lithium extraction/insertion.
- Ease and up-scalability of synthesis method.
- Low toxicities and costs for precursors and products of the synthesis.

1.6.3.1 Layered lithium transition metal oxides

Until the introduction of safer and cheaper cathode materials, Li_xCoO_2 has been the primary choice as a positive electrode material since the commercialization of Li-ion batteries. $LiCoO_2$ adopts the α-$NaFeO_2$ structure (space group: $R\bar{3}m$) with a cubic closed packed arrangement of oxide ions and is as such, a special defective rocksalt structure having defects assembled in layers. Li^+ ions and Co^{3+} ions occupy octahedral sites and form alternating layers between closed-packed (111) planes of oxide ions (**Fig. 1.7**).

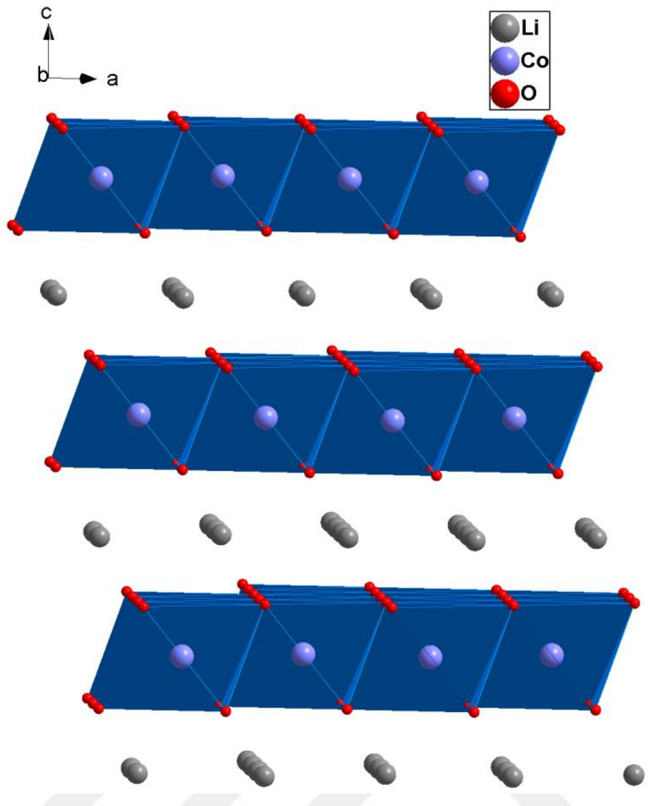

Figure 1.7 Projection of $LiCoO_2$ crystal structure along [010] direction.

Lithium ions can be reversibly inserted/deinserted into Li_xCoO_2 for $x \approx 0.5$ delivering practical capacities in the range of 140 mAh/g until 4.2 V vs. Li^+/Li[87-88]. The theoretical capacity of the material (~ 274 mAh/g) cannot be yielded over multiple cycles because of the instability of lithium poorer states leading to oxygen loss and electrolyte decomposition[87, 89-90]. The high cost of cobalt and safety problems when higher capacities are pursued led to the use and development of isostructural layered transition metal oxides (Li_xMO_2, M = Co, Mn and Ni) and their solid solutions. Out of this family of compounds, layered nickel-rich oxides ($Li[Ni_{1-x}M_x]O_2$[91-92] and NMC forms (e.g. $LiNi_{1/3}Co_{1/3}Mn_{1/3}O_2$))[93] gained particular interest owing to their high capacity, low cost and good cycling stability event at high current rates. The disadvantage of one metal center is compensated with others and vice versa in this class of materials. Ni, Co and Mn possess 2+, 3+ and 4+ oxidation states in $LiNi_{1/3}Co_{1/3}Mn_{1/3}O_2$, respectively[94]. The cobalt and nickel stabilize the layered structure against conversion to the spinel structure at high charge states, whereas the manganese reduces the overall cost. $Li_xNi_{1/3}Co_{1/3}Mn_{1/3}O_2$ has a quite small volume change upon cycling with ~ 1-2 % in the range of ~ $0 < x \leq 0.7$[95-96], and within the voltage window of 4.5 – 2.5 V. Yabuuchi et al. demonstrated a high capacity of 200 mAh/g at 18.3 mA/g for this compound[93]. Layered nickel-rich oxides like $Li[Ni_{0.80}Co_{0.15}Al_{0.05}]O_2$[97] and $Li[Ni_{0.8}Co_{0.1}Mn_{0.1}]O_2$[98] have also been extensively investigated yielding practical capacities in the range of ~ 200 mAh/g, but suffer largely from poor thermal properties as a result of oxygen release in highly delithiated state, again leading to severe thermal runaways and fire hazards[97, 99]. The best electrochemical performance for this family of phases, and possibly, for all layered transition metal oxide cathodes comes with the utilization of core-shell structures. In a more advanced form of this class, called concentration-gradient cathode materials, the concentration of transition metals are varied from the bulk to the surface to tune the electrochemical properties while minimizing the disparities of lattice parameters between the interfaces. The surface and shell are usually selected from the compounds that maximize the stability against electrolyte, while the core is constructed from high capacity materials (**Fig. 1.8**)[100].

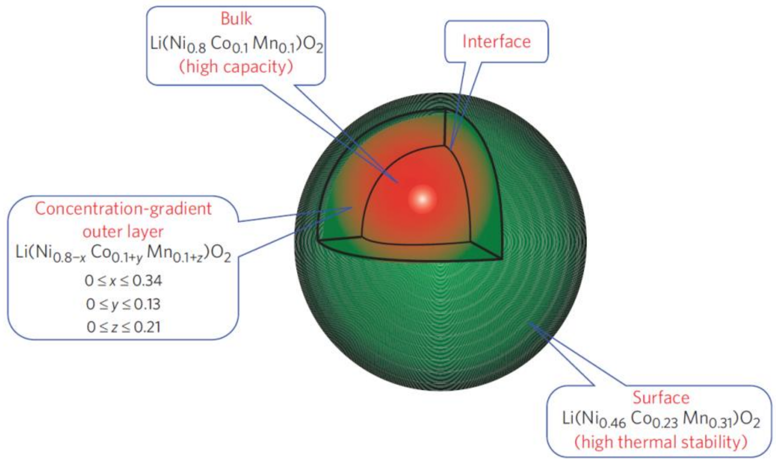

Figure 1.8 Schematic representation of core-shell, concentration gradient cathode material developed by Yang-Kook Sun et al. (taken from [100]).

Yang-Kook Sun et al. displayed a high capacity of 209 mAh/g under thermal abuse conditions (at 55 ^{o}C between 4.4 V and 3.0 V) for the concentration-gradient material $Li[Ni_{0.64}Co_{0.18}Mn_{0.18}]O_2$ with a core and surface of $Li[Ni_{0.8}Co_{0.1}Mn_{0.1}]O_2$ and $Li[Ni_{0.46}Co_{0.23}Mn_{0.31}]O_2$, respectively[100]. The capacity retention is quite remarkable, as ~ 96 % of initial capacities were preserved for 50 and 500 cycles at 55 ^{o}C and under ambient conditions, respectively[100]. In terms of electrochemical properties, core-shell compounds with a concentration-gradient are very promising cathode candidates for Li-ion batteries, however their quite complicated and possibly expensive syntheses is a main setback for large scale commercial implementations.

1.6.3.2 Materials with the spinel structure

$Li_xMn_2O_4$ is the predominant phase with a spinel structure that has been studied as a cathode material for Li-ion batteries. The compound is attractive by having the advantages of a high working potential (~ 4.1 V)[101], environmentally friendly and abundant elements and thermal stability at highly charged states. $Li_xMn_2O_4$ has a cubic spinel structure (space group: $Fd\bar{3}m$)

with Li^+ ions and $Mn^{3, 4+}$ ions occupying the tetrahedral and the octahedral sites, respectively, in the cubic-closed packed O^{2-} lattice (**Fig. 1.9**).

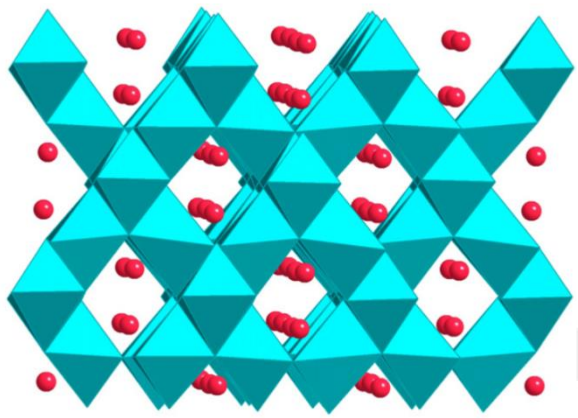

Figure 1.9 Crystal structure of spinel LiM_2O_4 (cyan: MO_6 octahedra, red: Li atoms), (taken from [102]).

For the nominal composition, $LiMn_2O_4$, the theoretical specific capacity is ~ 148 mAh/g, for one Li deinsertion/insertion into the structure, and practical capacities ca. ~ 120 mAh/g were displayed for the material with two close voltage plateaus at ~ 4.0 V and 4.1 V indicating an ordering reaction during lithiation/delithiation[101, 103-105]. Although a number of reasons causing cycling instability were suggested for lithium manganese oxide spinels[104, 106-109], the etching of the cathode material through a disproportionation reaction ($2Mn^{3+} \rightarrow Mn^{2+} + Mn^{4+}$) was found to be the main problem[107, 110]. Surface coatings and metal site doping were used to improve the cycling stability of $LiMn_2O_4$ in various investigations leading to another spinel structure material, $Li_xNi_{0.5}Mn_{1.5}O_4$[110-113]. For $Li_xNi_{0.5}Mn_{1.5}O_4$, a higher operating voltage of ~ 4.80 V vs. Li^+/Li is achieved due to the employment of high potential Ni^{2+}/Ni^{3+} redox couple[113-114]. The theoretical specific capacity is almost reachable practically for the compound even at a high rate of 2C, as it was shown by Xiao et al.[113] The cycling properties were also found to be better for $Li_xNi_{0.5}Mn_{1.5}O_4$ compared to $Li_xMn_2O_4$ without any major capacity losses over 200 cycles[113].

However, the working potential of $Li_xNi_{0.5}Mn_{1.5}O_4$ is close to the stability limit of carbonate electrolytes, which requires the development of alternative approaches, if this material is intended to be used in real-life applications.

1.6.3.3 Poly-anion based materials

1.6.3.3.1 Phosphates ($LiMPO_4$, M = Fe, Mn, Co, Ni)

Since the introduction of $LiFePO_4$ as a cathode material for Li-ion batteries in 1997 by Goodenough et al.[115], more than a thousand papers have been published in this field. The crystal structure of $LiFePO_4$ is of the olivine type, where lithium and iron ions reside in octahedral sites, and phosphorus occupies tetrahedral holes in a distorted hexagonal close-packed (hcp) oxygen array (**Fig. 1.10**). The crystal structure (space group: *P*nma) consists of FeO_6 and LiO_6 octahedra and phosphate groups forming a three dimensional network by edge and corner sharing.

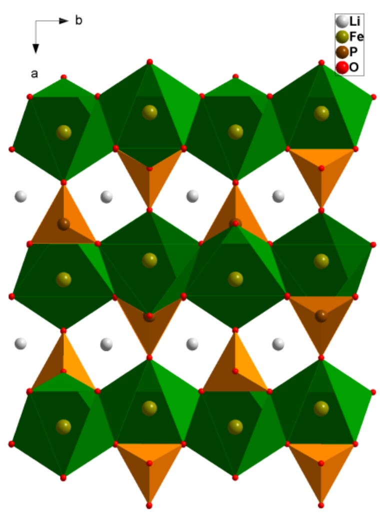

Figure 1.10 Projection of $LiFePO_4$ crystal structure along [001] direction

Early reports on $LiFePO_4$ did show poor electrochemical performance mostly due to the low electronic conductivity of the compound (~ 1 x 10^{-9} S/cm at room temperature)[116]. This problem was circumvented via employing nanoscopic forms and applying in-situ or ex-situ conductive coatings by various synthetic approaches, such as sol-gel, hydrothermal, polyol, spray-pyrolysis, ball-milling and etc.[117-123] Thereafter, the theoretical specific capacity of $LiFePO_4$ (~ 170 mAh/g) was practically obtained at a working potential of ~ 3.5 V by several research groups[116-117, 124-127]. $LiFePO_4$ is suitable for high power applications as well. As a benchmark in the field, Kang et al. showed specific capacities in the range of ~ 130 mAh/g at a very high current of 50C by employing $LiFePO_4$ particles with an ionically conductive lithium phosphate glass surface[125].

The mechanism of lihiation/delithiation of $LiFePO_4$ is normally described by a two phase reaction yielding a flat voltage profile in galvanostatic charge/discharge curves. The second phase obtained during the reaction is $FePO_4$ that has the same structure type as the lithiated form (*P*nma)[128]. Contrary to that, a solid solution behavior was also claimed by Yamada et. al at the extreme compositions of charge and discharge ($Li_{1-y}FePO_4$, y = 0.038 and Li_xFePO_4, x = 0.032)[129]. The relationship between the two-phase and solid-solution reactions remains controversial and it may depend on the size, metal site doping, and current rates[129-131]. Nevertheless, $LiFePO_4$ is currently the best choice as a positive electrode material and widely used in the energy storage systems of plug-in electric cars[5-7] with a great stability in charged and discharged states in most electrolyte systems, high rate capability with stable cycling, good safety characteristics even under thermal abuse, and low cost, abundance and environmentally friendliness of its elements. Electrochemical properties of other olivine-type cathode materials ($LiMPO_4$, M = Co, Ni, Mn) have been extensively investigated, too. For carbon coated nano-platelets of $LiMnPO_4$, a specific capacity of 168 mAh/g, close to the theoretical value, was demonstrated at C/50 rate with a flat voltage curve at 4.1 V[132]. For $LiCoPO_4$ and $LiNiPO_4$, high anodic upper voltage limits, ~ 4.8 V and ~ 5.1 V, respectively[133-134], reaching to the stability limit of carbonate electrolytes, are necessary to extract lithium from the compounds that results low charge/discharge capacities and poor cycling.

1.6.3.3.2 Pyrophosphates ($Li_2MP_2O_7$, M = Fe, Mn, Co)

The successful activation and use of olivine-type materials with low electronic conductivity and poor kinetics as cathode materials motivated research on similar poly-anionic materials. Two-lithium metal pyrophosphates ($Li_2MP_2O_7$, M = Co, Fe, Mn) with $P_2O_7^{4-}$ poly-anion groups have been studied as cathode materials for Li-ion batteries in recent years. For $Li_2FeP_2O_7$, synthesized by a conventional solid state reaction, Nishumura et al. realized one electron/lithium theoretical capacity of 110 mAh/g with an Fe^{2+}/Fe^{3+} redox plateau at ~ 3.5 V; there were no major capacity losses for 30 cycles between 2.5 and 4.5 V at a rate of C/20[135]. The extraction of the second Li from this structure was estimated to be around 5.2 V[136], but no detailed electrochemical study exists so far due the lack of electrolyte systems which are stable at so high voltages. Though very low capacities (~ 30 mAh/g) were obtained for $Li_2MnP_2O_7$[136] and $Li_2Mn_{0.8}Fe_{0.2}P_2O_7$[137], the potential for the Mn^{2+}/Mn^{3+} redox was estimated to be in the range of 4.2 – 4.5 V[136-137]. Kim et al. found the extraction of one Li from $Li_2CoP_2O_7$ to occur at a voltage plateau of ~ 4.8 V, and a charge capacity of ~ 160 mAh/g beyond the theoretical value (~ 110 mAh/g) stemming from partial electrolyte decomposition was realized for an upper voltage limit of 5.2 V[138]. The reversible capacity on discharge was found to be ~ 85 mAh/g[138]. The development of high-voltage stable electrolytes might be the key aspect for the practical applications of $Li_2MP_2O_7$ (M = Co, Fe, Mn) as high potential cathode materials, since the average working potentials are already on the stability limit of conventional electrolytes (~ 4.5 - 4.7 V) for one Li cycling, and the extraction of second Li is expected above 5 V.

1.6.3.3.3 Silicates (Li_2MSiO_4, M = Fe, Mn, Co)

Similar to phosphates and pyrophosphates, lithium transition metal silicates only show electrochemical activity, when conductive coatings are employed on nano-particles, as electronic conductivities for silicates were reported to be even lower than those of phosphates[139]. Also, in a similar way, the reversible cycling and charge/discharge capacities were found to be better for the iron compound compared to the cobalt and manganese isomorphs, especially for bulk materials. Most of the studies on Li_2MSiO_4 (M = Co, Fe, Mn) compounds have demonstrated the utilization of one Li per formula unit yielding specific capacities in the range of 130 -180 mAh/g at moderate current rates (0.2C-1C) below 4.5 V[139-143]. In recent reports, nano-particle composite materials, PEDOT/nano-Li_2MnSiO_4[144] and C/nano-Li_2FeSiO_4[145] were displayed to utilize more than one Li per formula unit, as specific capacities of 220 mAh/g and 293 mAh/g were delivered within 4.8-1.5 V and 4.5-1.5 V (~ 10 mA/g rates), respectively. However, high capacities were retained for only a few cycles, and much effort is still needed to practically use lithium transition metal silicates as positive electrode materials.

1.6.3.3.4 Fluorophosphates and fluorosulphates

Compounds containing fluoride ions are another class of cathode candidates that triggered extensive research efforts. As a result of the electron withdrawing F^- ions and the inductive effect of poly-anion groups, high working potentials were found for fluorophosphates and fluorosulphates. For instance, Tarascon et al. demonstrated $LiFeSO_4F$ polymorphs as cathode materials with good capacity retention yielding capacities ca. 130-150 mAh/g with voltage plateaus at ~ 3.6 V (tavorite phase)[146] and ~ 3.9 V (triplite phase)[147], which is the highest reported one for the Fe^{2+}/Fe^{3+} redox couple in oxidic compounds. Two of the early studied fluorophosphates are $LiVPO_4F$[148] and $Li_5V(PO_4)_2F_2$[149] with theoretical capacities of 156 mAh/g and 170 mAh/g, respectively. Baker et al. showed that $LiVPO_4F$ delivers its theoretical capacity at slow current rates with stable cycling, and charge/discharge curves indicate a two-phase reaction at an average discharge voltage of 4.2 V for V^{4+}/V^{3+} redox couple[148]. Other interesting cathode materials with fluoride ions are A_2MPO_4F fluorophosphates[150] $AMSO_4F$ fluorosulphates[151] (A = Na, Li; M = Fe, Mn, Co, Ni) and their solid solutions, which are under scrutiny in recent years.

1.6.3.3.5 Other poly-anion based materials

The phases with *Nasicon* structure ($A_xM_2(XO_4)_3$ (A = Li, Na, K and etc., M = Fe, Mn, Co, V and etc., X = P (the most abundant), S, Si, As, V, Mo))[152-157] are one of the first investigated polyanionic compounds for Li-ion batteries. The structure has a monoclinic symmetry and consists of MO_6 octahedra and XO_4 tetrahedra that are connected via corner sharing forming many void-like features. *Nasicon* compounds were first thought to be used as electrolytes in Na thermal batteries, but they were found to be not stable against elemental sodium in molten state[158-159]. An example of *Nasicon* type cathode materials is $Li_3V_2(PO_4)_3$; the extraction/insertion reactions for the first two lithium ions were found to be highly reversible and three two-phase plateaus were observed in galvanostatic cycling curves delivering specific capacities ca. 130 mAh/g[153]. Among numerous poly-anion and mixed poly-anion based compounds, $Li_9M_3(P_2O_7)_3(PO_4)_2$ (M = V, Mo)[160] and $A_xM(YO_3)(XO_4)$ (A = Li, Na, X = Si, As, P, Y = C, B; M = transition metal, and x = 0 to 3)[161] were also proposed as positive electrode materials for Li-ion and Na-ion batteries, which have been recently studied in many theoretical and experimental investigations.

1.6.3.4 Li-S and Li-O_2 batteries

Li-S and Li-O_2 batteries are considered to be the ultimate goals for rechargeable lithium batteries in order to accomplish driving ranges over 500 kilometers for plug-in electric cars and enable the large-scale use of energy storage systems based on rechargeable lithium batteries. Both of these battery systems employ metallic lithium anodes. Schematic representations of Li-S and Li-O_2 cells are displayed in **Figure 1.11**[8]. On discharge, lithium metal is oxidized releasing Li^+ ions into non-aqueous organic electrolytes, and through a series of electrochemical reactions, Li_2O_2 and Li_2S are formed as final discharge products for lithium-oxygen and lithium-sulphur batteries, respectively.

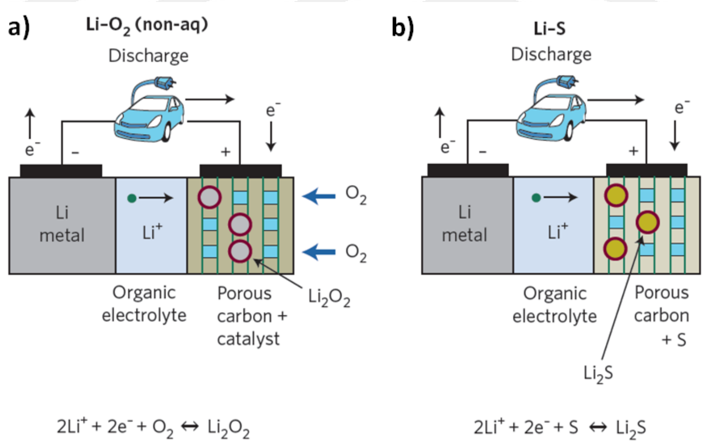

Figure 1.11 Schematic representation of a) Li-O_2 battery with non-aqueous electrolyte b) Li-S battery with non-aqueous electrolyte (taken from [8]).

The energy densities for Li-O_2 and Li-S batteries are quite high with theoretical values of 3505 Wh/kg and 2567 Wh/kg, respectively[8]. One of the best electrochemical results for Li-S batteries were obtained by Nazar et al., as reversible capacities up to 1320 mAh/g at ~ 2 V with moderate current rates were demonstrated for "a highly ordered nanostructured carbon–sulphur cathode", which had been produced by a melt-diffusion approach[162]. The good electrochemical performance was attributed to the carbon composite structure enhancing the conductivity and trapping the polysulphides formed during redox reactions[162]. These polysulphides normally dissolve into the organic electrolyte, cause active mass loss, and deposit on the anode side, which are considered as the main reasons, together with low electronic conductivity, for the poor electrochemical performance of sulphur as a cathode material; however, up to date, this problem is not completely alleviated, as the capacity fading with cycling still exists even for improved Li-S battery systems.

Early investigations on Li-O_2 batteries showed the reversible formation/decomposition of Li_2O_2 on a carbon scaffold by using organic carbonate–based electrolytes[163-164]. Also, a large potential difference for the formation/decomposition of Li_2O_2 has been observed. In more recent reports, ether-based electrolytes are mostly used[165-166], as the decomposition of carbonate-based electrolytes was found out on discharge[167]. Jung et al. claimed a lithium–air battery that operates over many cycles with a capacity of 5000 mAh g^{-1}_{carbon} at 500 mA g^{-1}_{carbon} rate (based on the mass of carbon)[166]. Improved performance of the system in terms of reduced polarization, stable cycling and high capacities was ascribed to the use of a stable electrolyte (a tetra(ethylene) glycol dimethyl ether–lithium triflate (TEGDME–$LiCF_3SO_3$)) and a better engineering of the cell by the authors[166]. Though the battery was denoted as Li-air, in reality $O_{2(g)}$ was used to form Li_2O_2, as many researchers do in order to exclude the non-oxygen components of air. This name confusion also indicates a problem that should be addressed, otherwise hindering the practical use of Li-O_2 batteries: normal air containing CO_2, water and nitrogen cannot be directly used for discharging a battery as it would lead to the irreversible formation of Li_2CO_3, LiOH, and lithium nitride. Furthermore, the reversible reactions in Li-O_2

batteries are still controversial, as some leading researchers in the field consider that even the ether-based electrolytes do not support the reversible formation/decomposition of Li_2O_2 at the cathode over multiple cycles. P. G. Bruce et al. have recently displayed the most convincing operation of the rechargeable Li-O_2 battery by using a nanoporous gold cathode (scaffold) instead of carbon and an electrolyte composed of 0.1 M $LiClO_4$ in dimethyl sulfoxide (DMSO)[168]. The capacity retention of 95 % after 100 cycles with an initial capacity of 300 mAh g^{-1}_{gold} (based on the mass of gold) was demonstrated, and the main source of capacity was proven to be the reversible formation/decomposition of Li_2O_2[168]. This study might be considered very important as a proof of concept, but many challenges and obstacles remain to be tackled for the practical application of Li-O_2 (or air) batteries.

The widely investigated and popular positive electrode materials with their average working potentials, specific capacities and energies, based on the reports that were previously stated, are summarized in **Table 4**.

Table 4: Positive electrode materials for rechargeable lithium batteries.

Cathode Material	Voltage (V)	Specific Capacity (Ah/kg)	Specific Energy (Wh/kg)
$LiCoO_2$	3.8-3.9	140	546
$LiNi_xCo_xMn_xO_2$	3.8-3.9	160-210	610-810
LiM_2O_4 (spinels)	4.1-4.8	120-148	492-650
$LiFePO_4$	3.4-3.5	160-170	580-595
$LiMnPO_4$	4.1	168	689
$Li_2FeP_2O_7$	3.5	110	385
$LiFeSO_4F$	3.6-3.9	130-150	470-510
Li-S	2.0-2.2	500-1320	1000-2640

Chapter 2

Nano $LiMnBO_3$, a High Capacity Cathode Material for Li-Ion Batteries

2.1 Introduction

Since their commercialization in the 1990s, Li-ion batteries are widely used as the primary choice for secondary batteries due to their outstanding energy density. By having the advantages of high voltage, high capacity, long cycle life and variable charge-discharge rates, Li-ion batteries dominate the portable electronics market and most recently, plug-in electric vehicles powered by Li-ion batteries have entered into the market[5-7]. The conventional Li-ion batteries have $LiMO_2$ (M = Co, Ni, Mn) cathodes and graphite based anodes. However, the use of such oxides as cathode materials is a setback for the large scale use of plug-in electric vehicles, when aspects like cost, energy density, and safety are considered. In order to address these problems, following the initial work of Goodenough et al.[115], olivine-type materials ($LiMPO_4$, M = Fe, Co, Ni, Mn) have been extensively investigated[118, 124, 126, 132-133]. Although PO_4^{3-} units are not electro-active, and thus detract from energy density, they introduce several advantages especially through a higher operating voltage due to the increased lattice potential, which also fixes oxygen atoms in the structure providing a chemical stability beyond $LiMO_2$ cathodes that act as strong oxidizing agents for organic electrolytes. For instance, $LiFePO_4$ operates at 3.5 V with a theoretical capacity of 170 mAh/g[169], and even though it suffers from poor ionic and electronic conductivity, the theoretical capacity is achievable for the material via nano-sizing and conductive (carbon) coatings[116, 118, 124, 126]. In addition, iron and manganese-based olivines have considerable advantages in costs. At present, many companies have started to produce and commercialize $LiFePO_4$ and its composites that are currently one of the preferred choices as the cathode material for plug-in electric cars. However, all current cathode materials are still not capable enough to satisfy the energy density demand required for the large scale use of electric vehicles. There is a need for cathode materials working at higher output voltages with higher practical capacities. Borates ($LiMBO_3$, M = Fe, Mn, Co) could be good alternatives to phosphates by having the lower weight BO_3^{3-} groups instead of PO_4^{3-}, but keeping the advantage of the linking anion group giving a higher operating voltage and enhanced structural stability. The idea was first introduced by Legagneur et al., but they were only able to extract 0.04 and 0.02 Li per formula unit for $LiFeBO_3$ and $LiMnBO_3$, respectively[170]. Recently, Yamada et al. achieved a high capacity of ~ 190 mAh/g at C/20 rate for $LiFeBO_3$ by carbon composite formation and avoiding the exposure of the material to air[171]. There are two phases of $LiMnBO_3$ that has a theoretical capacity of ~ 220 mAh/g[170, 172]. For the monoclinic phase, the electrochemical activity has been shown by Kim et al.; the material synthesized by a conventional solid state method and further treated by ball-milling and carbon coating delivers a second discharge capacity of 100 mAh/g at C/20[173]. For hexagonal-$LiMnBO_3$, most of the studies showed very low charge/discharge capacities so far[173-175]. Chen et al. claimed electrochemical activity for h-$LiMnBO_3$, but a charge/discharge capacity of only 75.5 mAh/g with a huge polarization at ~ C/40 rate was observed in the voltage window of 4.8 – 1.0 V[174]. The source of the capacity could be expected to be a conversion reaction rather than the lithiation/delithiation of h-$LiMnBO_3$ in the designated voltage range used in their study.

Similar to phosphates, lithium transition metal borates are considered to have intrinsically low ionic and electronic conductivity, which is believed to be the cause of the poor electrochemical performance of h-$LiMnBO_3$ so far[173-175]. Utilization of appropriate nano-particles can lead to diminish these effects and to aggravate charge/discharge capacities considerably. The use of nano-particles decreases the length of the diffusion paths for Li^+ ions and enhances electron hopping, thus, improving the electrochemical performance of the otherwise poorly conducting materials. Such materials have to be embedded in conductive matrices, which is generally done by conductive carbon coatings through various methods.

Here, the sol-gel synthesized nano-$LiMnBO_3$ modifications are reported as cathode materials for Li-ion batteries. Nano h-$LiMnBO_3$ is obtained at a temperature as low as 350 ^oC and consists of nano crystallites with an average size of ~ 20 nm. The composite electrode of nano h-$LiMnBO_3$ with reduced graphite oxide delivers a first discharge capacity of 145 mAh/g at C/20 rate, and it maintains a discharge capacity of 111 mAh/g at the 10th cycle. These are the best results reported so far for $LiMnBO_3$ to the best of our knowledge.

2.2 Experimental Section

2.2.1 Synthesis

Stable sols were obtained by dissolving stoichiometric amounts of $LiNO_3$, $Mn(NO_3)_2.(H_2O)_4$ and $B(OEt)_3$ in propionic acid. In a typical synthesis, 0.01 mol $LiNO_3$ and 0.01 mol $Mn(NO_3)_2.(H_2O)_4$ are dissolved in ~ 10 ml propionic acid at 80 ^oC for 3 hours, and similarly, 0.01 mol $B(OEt)_3$ in 30 ml propionic acid. After the salts are completely dissolved the two solutions are mixed and heated at 80 ^oC for an hour. 0.05 mol water are added for hydrolysis and a gel is obtained by evaporating the solvent at 80-100 ^oC. Annealing of the gel-powder at 350, 500, and 650 ^oC for 10 hours under reductive CO atmosphere yields nano h-$LiMnBO_3$, crystalline h-$LiMnBO_3$ and crystalline m-$LiMnBO_3$ (or a mixture of crystalline phases), respectively.

Graphite oxide was obtained from graphite by a modified Brodie method[176]. The composite material was obtained by ball-milling ~ 66.6 wt-% nano h-$LiMnBO_3$ with ~ 33.3 wt-% graphite oxide. To obtain reduced graphite oxide, the product was heated at 200-250 ^oC for 8 hours under nitrogen atmosphere. Combustion-infrared spectroscopy analysis (LECO instruments, ETH LOC Micro-Laboratory) confirmed a final carbon content of ~ 20 wt-% for the composite material.

2.2.2 Characterization

Powder X-ray diffraction patterns of the samples were recorded with a STOE Stadi P diffractometer equipped with a germanium monochromator and $CuK_{\alpha 1}$ radiation (operated at 40 kV, 35 mA). The average crystallite sizes of samples were calculated by the Scherrer equation: Crystallite size = 0.9 λ / ($\beta\cos\theta$), where λ is the wavelength of incident X-rays, β is the full width at the half maximum of the (111) peak for h-$LiMnBO_3$, and θ is the Bragg angle.

Scanning electron microscopy (SEM) analysis was done with a Zeiss Gemini 1530 operated at 1 kV. (Scanning) transmission electron microscopy ((S)TEM) analysis was carried out with a CM30ST (FEI; LaB_6 cathode) and a Tecnai F30 microscope (FEI; field emission gun), both operated at 300 kV, point resolution of ~ 2Å.

2.2.3 Electrochemical tests

For cathode fabrication, (70 wt-%) active material and (20 wt-%) conductive carbon (Super P® Li Timcal (or RGO) + in-situ carbon) were manually mixed and ball-milled for 1h afterwards to ensure proper mixing. Then, 10 wt-% PVDF binder was mixed, and a slurry of the mixture in 1:4, toluene:THF solution was prepared by ultrasonic dispersion. The slurry was cast on Ti current collectors and dried at 80 ^{o}C under vacuum. The final electrodes consisted of approximately 2-3 mg active material. Li metal anodes were prepared from a 0.75 mm-thick ribbon (Aldrich), and 1M solution of $Li[(C_2F_5)_3PF_3]$ in EC:DMC (1:1) (Merck, LF-30 SelectiLyte^{TM}) served as the electrolyte. Swagelok-type cells were constructed in an Ar filled glove-box. Galvanostatic tests were done in the voltage range of 4.7 – 1.7 V, and a potentiostatic step was applied at 4.7 V before discharging to 1.7 V. The cyclic voltammetry was carried out at a sweep rate of 0.05 mV/s within 4.7 -1.7 V.

2.3 Results and Discussion

Figure 2.1 shows the crystal structures of the two modifications of $LiMnBO_3$. The known structure[170] for the hexagonal phase (space group: *P*-6) (**Fig. 2.1a**) consists of MnO_5 square pyramids connected to each other via sharing of equatorial edges of the pyramids. Chains of MnO_5 polyhedra extend along the c-axis and are connected to each other by planar BO_3 units. Li atoms are in tetrahedral coordination, and the LiO_4 tetrahedra form chains parallel to those of the square pyramids along the c-axis. In the monoclinic phase[172] (space group: *C*12/c1) (**Fig. 2.1b**), MnO_5 has a trigonal bipyramidal geometry, and similarly forms polyhedral chains by edge sharing along the [-101] direction. Trigonal planar BO_3 groups connect three polyhedra chains via corner sharing, and Li atoms are tetrahedrally coordinated by O atoms. According to the previous theoretical work, the preferred diffusion path of Li^+ ions in both phases has a one dimension character parallel to the c-axis[173].

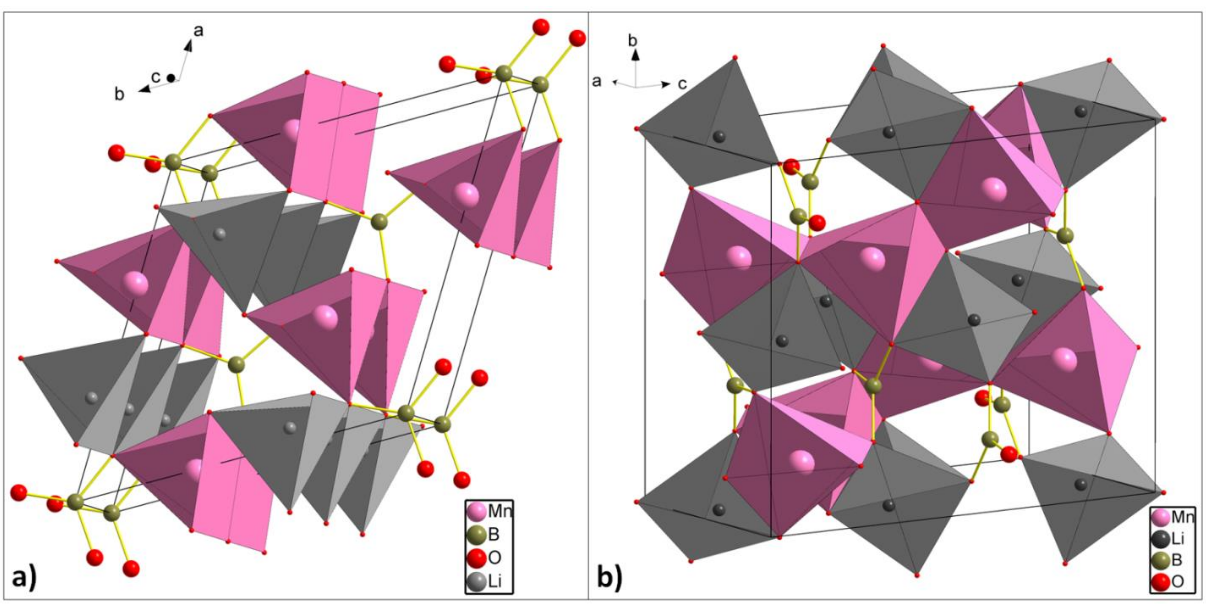

Figure 2.1 Crystal structures of $LiMnBO_3$: a) skew [001] view of the hexagonal phase, b) skew [100] view of the monoclinic phase.

In this work, different crystalline materials of $LiMnBO_3$ and nano h-$LiMnBO_3$ have been synthesized by a sol gel method, where stable sols were obtained starting from stoichiometric amounts of $LiNO_3$, $Mn(NO_3)_2.(H_2O)_4$ and $B(OEt)_3$ as precursors dissolved in propionic acid. By firing the gel-powder, obtained by evaporating the solution, under reductive CO atmosphere at 350, 500 and 650 ^oC, nano h-$LiMnBO_3$, crystalline h-$LiMnBO_3$ and crystalline m-$LiMnBO_3$ were produced, respectively. In situ carbon coating of $LiMnBO_3$ particles was also achieved by carbonization of propionic acid, though not in a homogeneous way, as revealed by transmission electron microscopy images (TEM, **Fig. 2.4**). By combustion-infrared spectroscopy analysis,we found 4.2, 4.3 and 2.9 wt-% carbon in the samples of nano h-$LiMnBO_3$, crystalline h-$LiMnBO_3$ and crystalline m-$LiMnBO_3$ samples, respectively. XRD powder patterns of the sol-gel synthesized $LiMnBO_3$ materials and the theoretical diffraction patterns are displayed in **Figure 2.2**. For both phases, all of the diffraction peaks can be matched to the theoretical patterns (ICSD 94318 and 200535), and residual diffraction peaks hinting impurities are not observed. In contrast to previous studies, where the hexagonal phase was obtained at a higher temperature than the monoclinic phase by solid state synthesis, we obtain nano h-$LiMnBO_3$ at a temperature as low as 350 ^oC. Annealing the gel-powder above 500 ^oC generates larger crystallites of h-$LiMnBO_3$, whereas annealing above 600 ^oC leads either to pure m-$LiMnBO_3$ or to a mixture of h-$LiMnBO_3$ and m-$LiMnBO_3$. Even though our studies do not reveal much about the thermodynamic stability of the phases, the reductive atmosphere used during the synthesis and the exothermic combustion reaction could be speculated as the driving force for the formation of h-$LiMnBO_3$ at a low temperature. Nevertheless, the synthesis of nano h-$LiMnBO_3$ at 350 ^oC is reproducible, and pure m-$LiMnBO_3$ was also synthesized to compare the electrochemical performances of two phases.

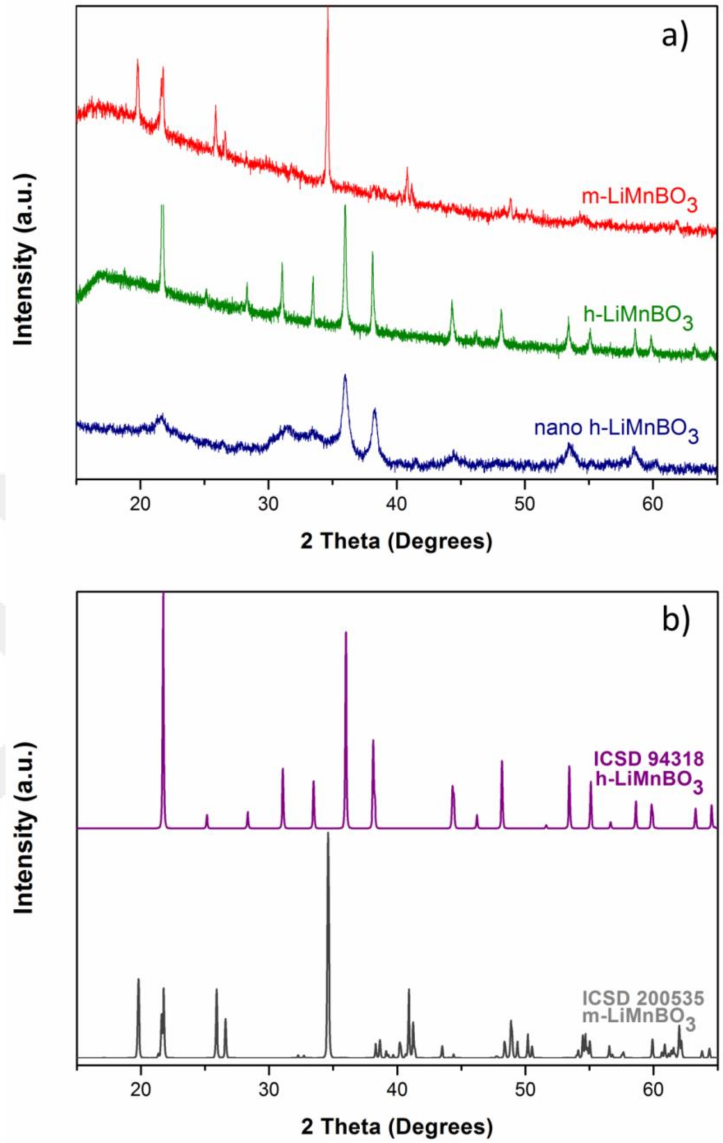

Figure 2.2 XRD powder patterns of $LiMnBO_3$: a) experimental, b) calculated.

Figure 2.3 shows scanning electron microscopy (SEM) images of the sol-gel synthesized $LiMnBO_3$ powders. Nano h-$LiMnBO_3$ (**Fig. 2.3a, 3b**) consists of nanorods and smaller rounder particles, and has an average particle size of ~ 20 nm that is calculated by the broadening of (111) diffraction peak. As the annealing temperature increases, the particles coalesce and grow bigger, leading to an increase of the average crystallite size for h-$LiMnBO_3$ (**Fig. 2.3c**), at 500 ^{o}C to ~ 120 nm.

The SEM image of the monoclinic $LiMnBO_3$ is shown in **Figure 2.3d**, and the shape of the particles is not very well defined. The crystallite size of m-$LiMnBO_3$ particles approximately ranges from 300 nm to 1 μ, but crystallites of 2-3 microns are also found.

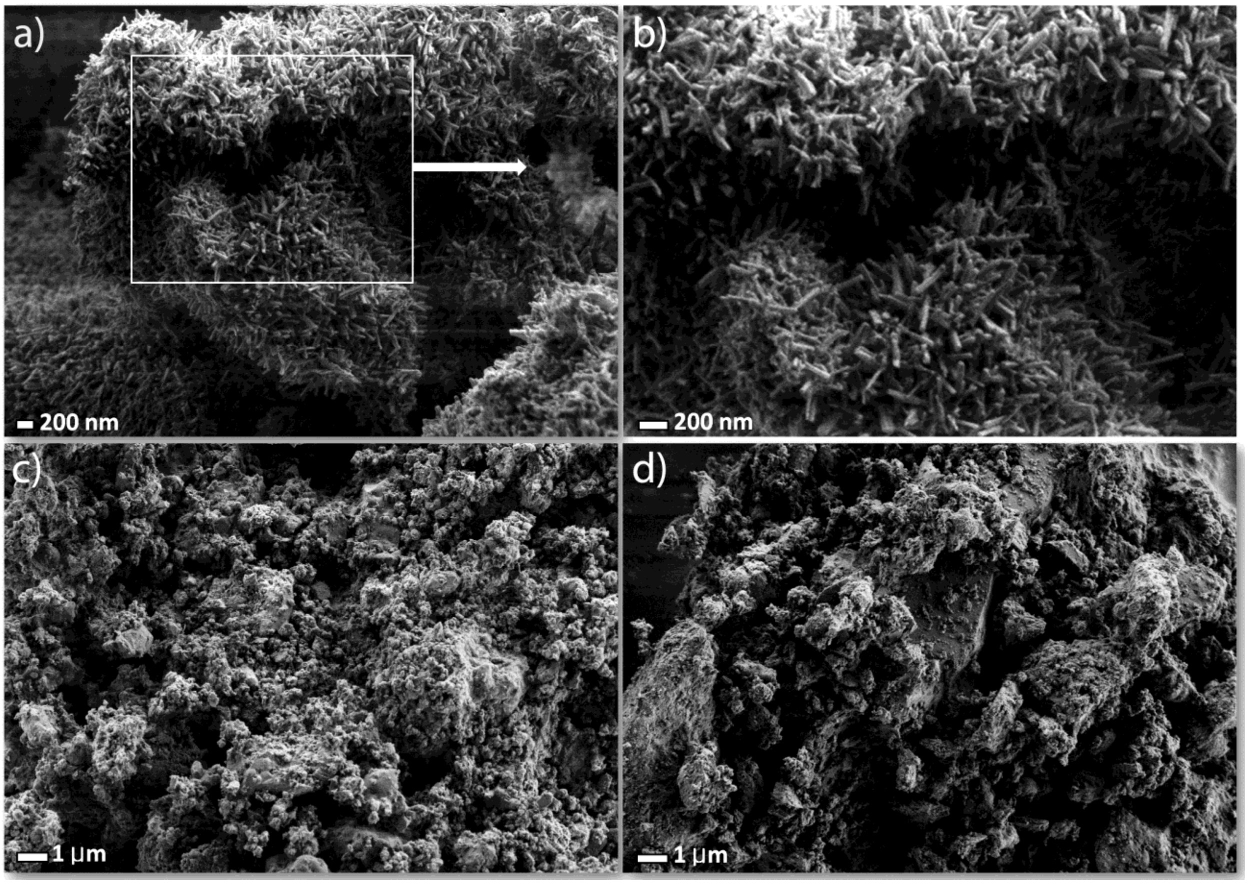

Figure 2.3 Scanning electron microscopy (SEM) images of a) nano h-$LiMnBO_3$, b) zoomed in image of the marked region in (a) indicating nanorods, c) crystalline h-$LiMnBO_3$, d) crystalline m-$LiMnBO_3$.

Transmission electron microscopy images (TEM) and the electron diffraction (ED) pattern of nano h-$LiMnBO_3$ are presented in **Figure 2.4**. The electron diffraction pattern (**Fig. 2.4a**) verifies the presence of nano h-$LiMnBO_3$ as the d-values derived from the pattern correspond to the theoretical plane distances of hexagonal $LiMnBO_3$. Nanorods of h-$LiMnBO_3$ with dimensions ranging from 20 to 35 nm in width and 50 to 80 nm in length are displayed in **Figure 2.4b**. The particles of nano h-$LiMnBO_3$ that are rounder and smaller in size can also be seen in **Figure 2.4b**, and more clearly in **Figure 2.4c**, on the tip of a nanorod. As stated before, there are

4.2 wt-% carbon in nano h-$LiMnBO_3$ powder. The presence of the carbon coating on the rim of particles is evident from **Figure 2.4c**. However, carbon particles do not cover the entire surfaces of the nano crystallites, but rather disperse among them, so that the conductive coating can still be enhanced. In addition, lattice fringes for the (110) planes of h-$LiMnBO_3$ are visible in high resolution images (**Fig. 2.4c**).

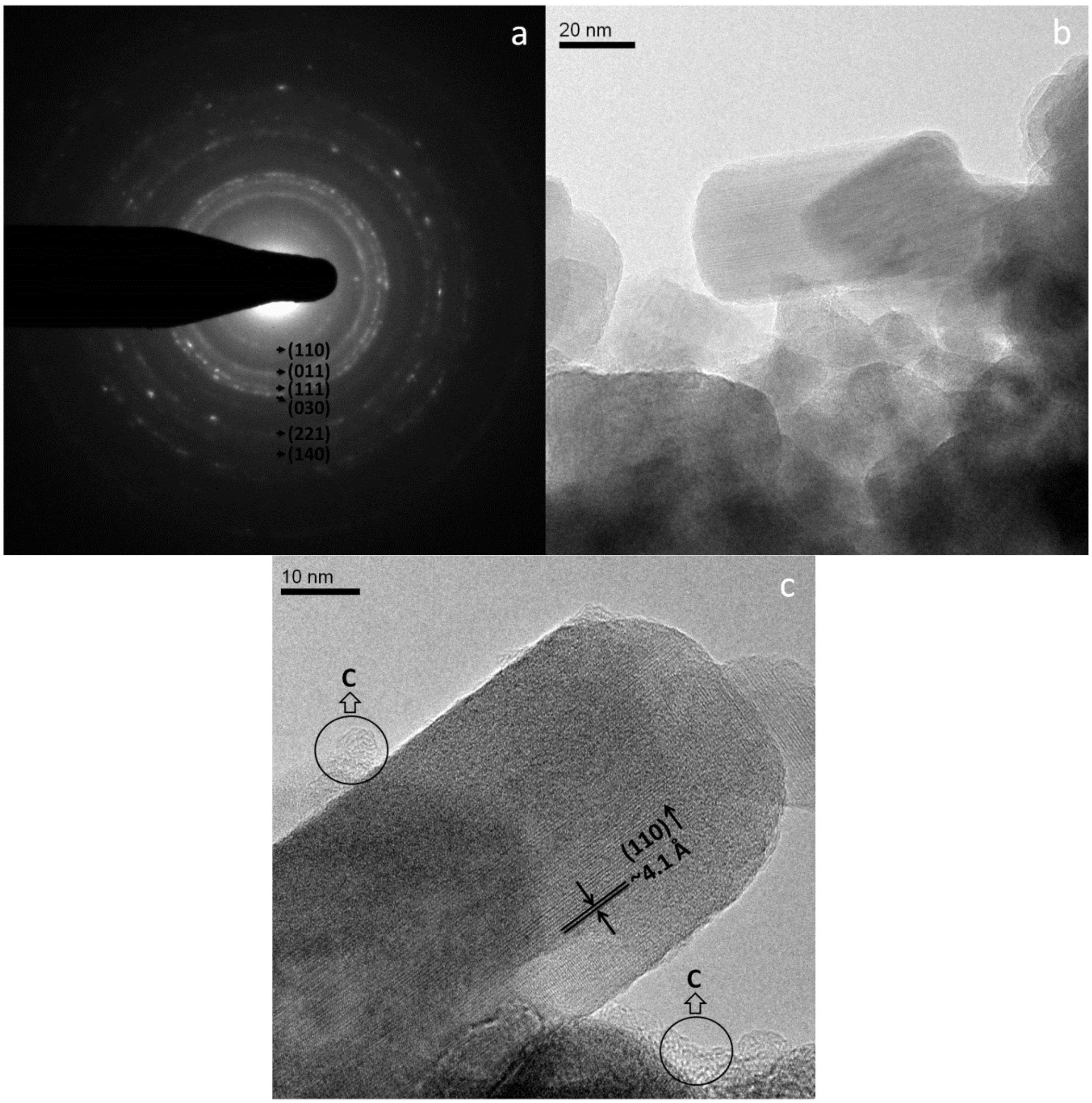

Figure 2.4 a) Electron diffraction (ED) pattern of nano h-$LiMnBO_3$ with identified diffraction rings, b) transmission electron microscopy image (TEM) of nano h-$LiMnBO_3$ showing nanocrystallites, c) transmission electron microscopy (TEM) image of nano h-$LiMnBO_3$ showing the presence of in-situ carbon particles and lattice fringes for the (110) planes of h-$LiMnBO_3$.

For the electrochemical characterization, electrodes consisting of approximately 2-3 mg active material on Ti current collectors were used as cathodes, and Li metal served as the anode. The working electrode was composed of (70 wt-%) active material, (20 wt-%) conductive carbon (Super P® + in-situ carbon) and (10 wt-%) PVDF binder. The electrolyte used for the electrochemical tests was 1M solution of $Li[(C_2F_5)_3PF_3]$ in EC:DMC (1:1) (LF-30 SelectiLyte™). This electrolyte is considered to be electrochemically stable in the voltage window of our interest[177]. Consequently, we do not expect a major capacity contribution from the oxidation of the electrolyte in the high voltage limit. The galvanostatic charge/discharge curves for nano h-$LiMnBO_3$, crystalline h-$LiMnBO_3$ and crystalline m-$LiMnBO_3$ are presented in **Figure 2.5**.

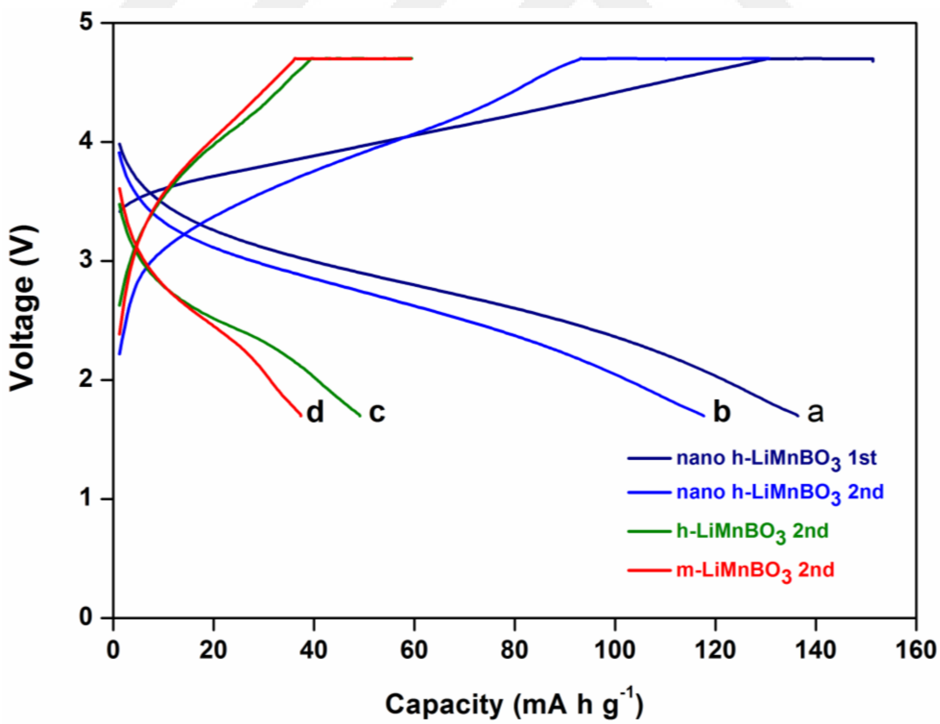

Figure 2.5 Charge/discharge curves for $LiMnBO_3$ samples within 4.7 – 1.7 V at C/20 rate (constant voltage at 4.7 V until the current <1mA/g): a) the first cycle of nano h-$LiMnBO_3$, b) the second cycle of nano h-$LiMnBO_3$, c) the second cycle of crystalline h-$LiMnBO_3$, d) the second cycle of crystalline m-$LiMnBO_3$.

The cells were cycled between 4.7 and 1.7 V in a combined galvanostatic-potentiostatic protocol. Galvanostatic (constant current) part was carried out at C/20 rate. The galvanostatic step in the charging process was followed by a potentiostatic step, where charging was carried out at the fixed upper voltage limit of 4.7 V, until the current dropped below 1mA/g. The first discharge capacity of nano h-$LiMnBO_3$ (~ 20 nm particles) is 136 mAh/g, and then drops to 118 mAh/g in the subsequent cycle. With increasing particle size, the hexagonal $LiMnBO_3$ (~120 nm particles) only delivers a second discharge capacity of 49 mAh/g, and the value for the monoclinic $LiMnBO_3$ (sub-micron particles) remains at only 38 mAh/g. Clearly, this finding shows that the particle size plays an important role for the electrochemical performance of $LiMnBO_3$ regardless of the phase in question. In the study of Kim et al., the second discharge capacity obtained for nano sized m-$LiMnBO_3$ (100 mAh/g) was higher than for micron sized h-$LiMnBO_3$ (10 mAh/g). In our study, nano h-$LiMnBO_3$ delivers the best specific capacity probably due to the reduced lengths of the diffusion paths for Li^+ ions and electrons.

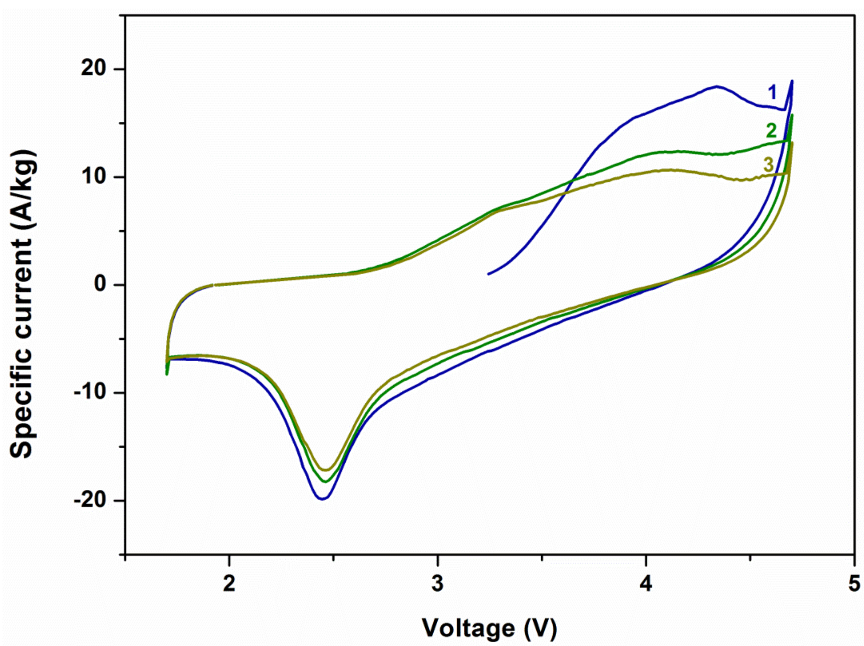

Figure 2.6 The cyclic voltammogram of nano h-$LiMnBO_3$ between 4.7 and 1.7 V at a scanning rate of 0.05 mV/s.

The cyclic voltammetry study for nano h-$LiMnBO_3$ shows very broad oxidation and reduction peaks with apparent polarization (**Fig. 2.6**). The overpotential has been reduced after the first cycle that could be explained by the partial amorphization of nano h-$LiMnBO_3$. In the second cycle, the oxidation has an onset of ~ 2.6 V, and the peak is at ~ 4.1 V (close to the predicted average voltage in a previous study[173]), whereas the reduction peak is at ~ 2.5 V, ranging from ~ 4.0 to 1.9 V. The peak intensities have dropped at each cycle that is consistent with the capacity loss observed in galvanostatic measurements.

Despite in situ carbon coating, cycling stability remains problematic. The drastic drop in the second discharge capacity could be due to not fully reversible delithiation/lithiation stemming from partially hindered ionic and electronic conductivity. In order to counter this problem and further increase the charge/discharge capacity, we designed a composite electrode of nano h-$LiMnBO_3$ mixed with reduced graphite oxide (RGO).

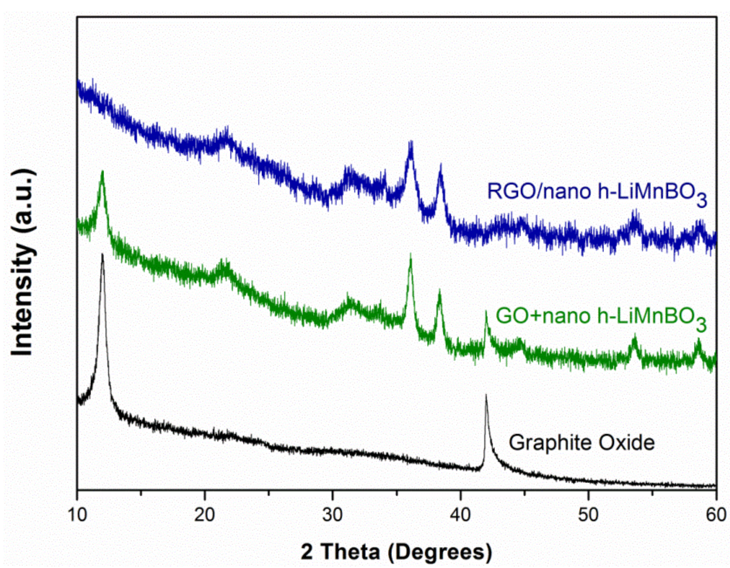

Figure 2.7 XRD powder patterns of graphite oxide (black), graphite oxide + nano h-$LiMnBO_3$ before heating (green), RGO / nano h-$LiMnBO_3$ composite (blue).

The composite electrode material was prepared by ball-milling nano h-$LiMnBO_3$ with graphite oxide and heating the product mixture at 200-250 ^{o}C for 8 hours under nitrogen atmosphere to ensure reduction. After ball-milling and heat treatment, no residual diffraction peaks from graphite oxide could be observed in the XRD powder pattern of the composite (**Fig. 2.7**) providing evidence for the reduction of graphite oxide to RGO, and the main diffraction peaks for nano h-$LiMnBO_3$ are not altered after the process showing that the phase was not decomposed or transformed. A TEM image of nano h-$LiMnBO_3$ coated with reduced graphite oxide (RGO) is shown in **Figure 2.8**. The interlayer distance, ~ 3.4 Å, of the coated material on nano h-$LiMnBO_3$ particles is close to the value for the (002) lattice spacing of graphite and indicates the presence of RGO on the surface. The TEM image also reveals that RGO does not only cover isolated particles, but rather forms a conductive network with embedded nano h-$LiMnBO_3$ particles.

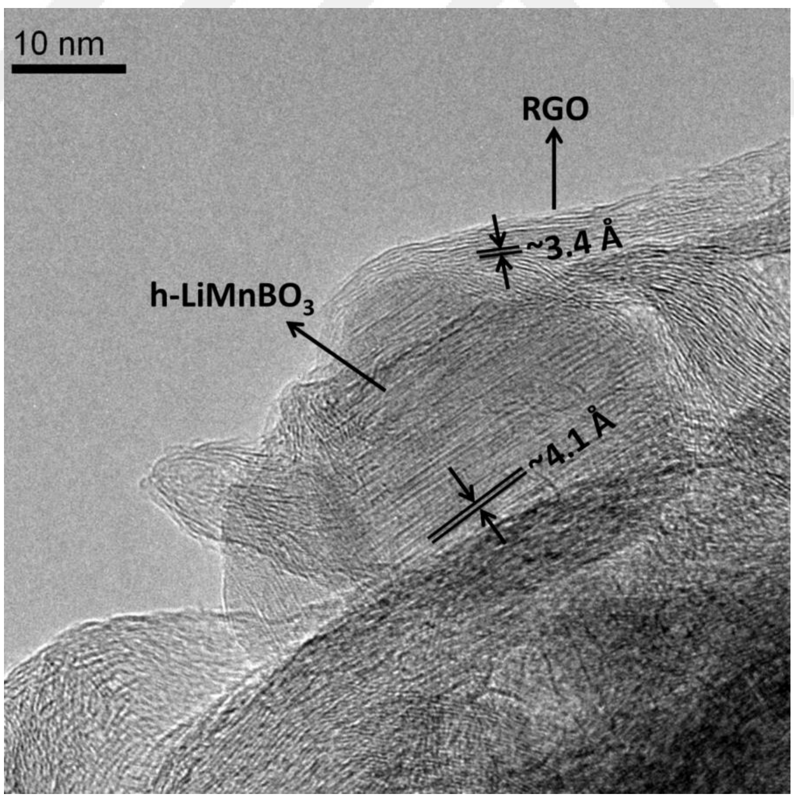

Figure 2.8 Transmission electron microscopy (TEM) image of nano h-$LiMnBO_3$ coated by reduced graphite oxide (RGO).

Figure 2.9 shows the first five charge/discharge curves for the composite RGO/nano h-$LiMnBO_3$ electrode within a window of 4.7 – 1.7 V at C/20 rate. Similar to the prior carbon-coated nano h-$LiMnBO_3$ electrode, the composite electrode approximately contained 20 wt-% conductive carbon (RGO + in-situ carbon), and no additional conductive carbon source, besides the reduced graphite oxide and the carbon resulting from the synthesis, was used for the electrochemical tests. For the RGO/nano h-$LiMnBO_3$ composite, the first discharge capacity increases to 145 mAh/g, and there is reversible cycling at the 10th cycle with a discharge capacity of 111 mAh/g.

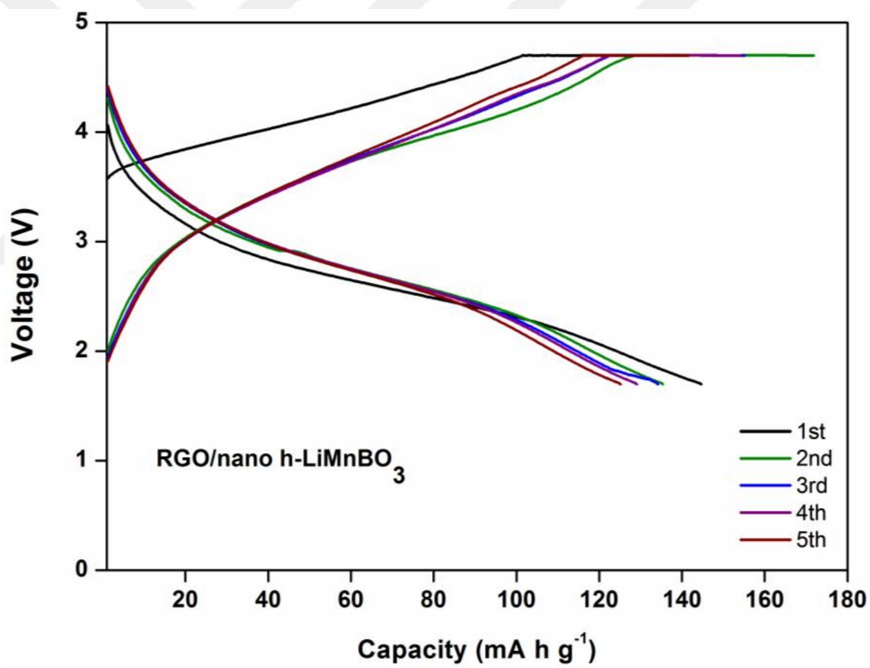

Figure 2.9 Charge/discharge curves of RGO/nano h-$LiMnBO_3$ within 4.7 – 1.7 V at C/20 rate (constant voltage at 4.7 V until the current <1mA/g) for the first five cycles.

Clearly, cycling properties as well as specific capacity are improved for the RGO/nano h-$LiMnBO_3$ composite compared to the prior described nano h-$LiMnBO_3$ electrode as illustrated in **Figure 2.10a**. The average discharge capacity loss is approximately 2.3 % per cycle for the RGO/nano h-$LiMnBO_3$ composite, whereas the value is 4.3 % for the plain nano h-$LiMnBO_3$.

The rate capability for the RGO / nano h-$LiMnBO_3$ is depicted in **Figure 2.10b**. The discharge capacities in the range of ~ 110, 102 and 77 mAh/g at the rates of C/10, C/5 and C/2 are obtained, respectively. The capacities decrease with increasing rate, but, yet, ~ 1/3 of the theoretical capacity is still delivered even at a rate of C/2. Considering the low ionic and electronic conducting nature of the material, this result is a significant improvement compared to the earlier work with various rates[174].

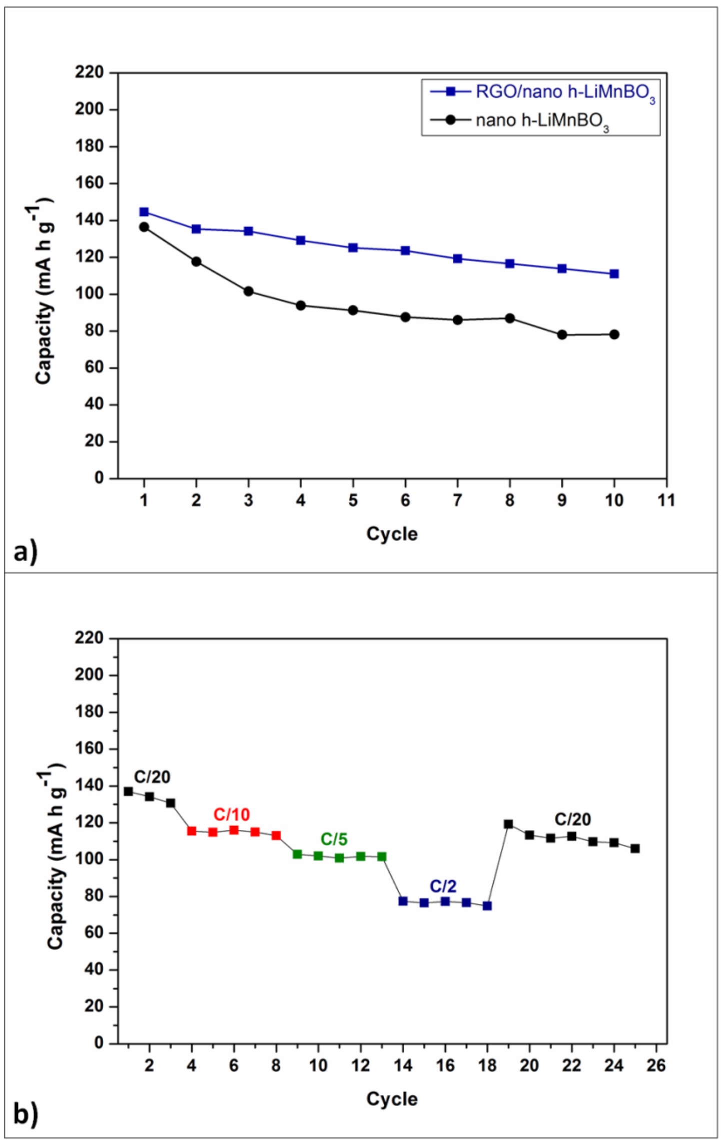

Figure 2.10 a) Discharge capacity vs. cycle number for nano h-$LiMnBO_3$ (black) and RGO/nano h-$LiMnBO_3$ (blue). b) Rate capability of RGO/nano h-$LiMnBO_3$. The cell was cycled within 4.7 -1.7 V at C/20, C/10, C/5 and C/2 rates (at room temperature); before discharging, the voltage was retained constant at 4.7 V till the current dropped below C/100.

The enhanced electrochemical properties for the RGO / nano h-$LiMnBO_3$ composite can be attributed to the covering and connecting of active nano h-$LiMnBO_3$ by RGO that is expected to facilitate electron and Li^+ ion transport. In addition, the RGO matrix may serve as a protective layer that can prevent the attack of by-products, such as HF, that might be formed during extensive cycling[178]. Furthermore, mechanical stability gained by the RGO network hinders capacity losses due to the pulverization and loss of interconnectivity during cycling.

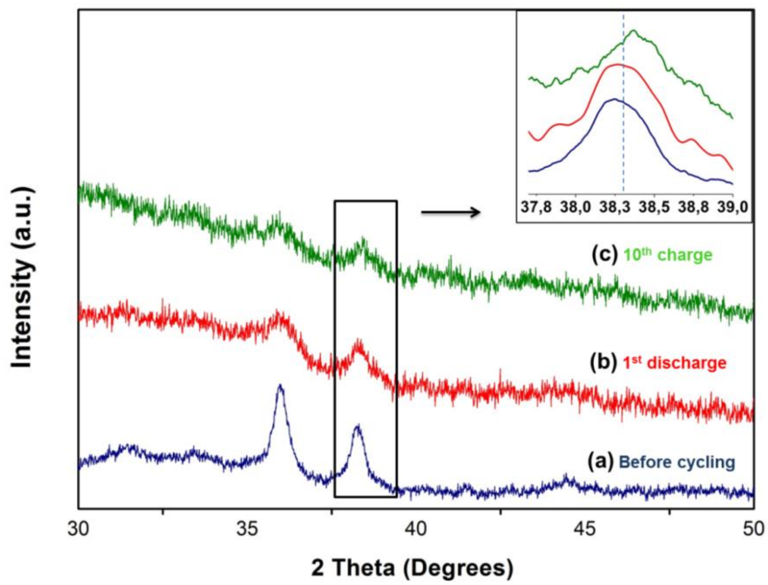

Figure 2.11 XRD powder patterns of the electrodes of nano h-$LiMnBO_3$ in the charged and discharged states: a) before cycling (blue), b) after first discharge to 1.7 V (red), c) after tenth charge to 4.7 V (green).

XRD powder patterns of the electrodes of nano h-$LiMnBO_3$ in the charged and discharged states are depicted in **Figure 2.11**. Even though it is hard to quantify the exact shift due to the broad diffraction peaks stemming from the nano nature of the compound, it can be seen that the major diffraction peaks slightly shift between charged and discharged states. As suggested by the broadening of diffraction peaks, particles become smaller on cycling. The sloping character of charge/discharge curves of nano h-$LiMnBO_3$ and the diffraction peak shifts without occurrence of new phases provide evidence for a solid solution lithiation/delithiation mechanism. Galvanostatic Intermittent Titration Technique (GITT) was applied as well to determine the thermodynamic voltage composition relation. **Figure 2.12** represents the relation of OCV (open circuit voltage) with composition (x in $Li_{1-x}MnBO_3$), obtained by plotting the steady state voltage at the end of each open circuit step. The sloping nature of the OCV profile further supports that the Li^+ extraction/insertion proceeds as a single phase reaction. This also allows the application of GITT for the determination of lithium diffusion coefficients.

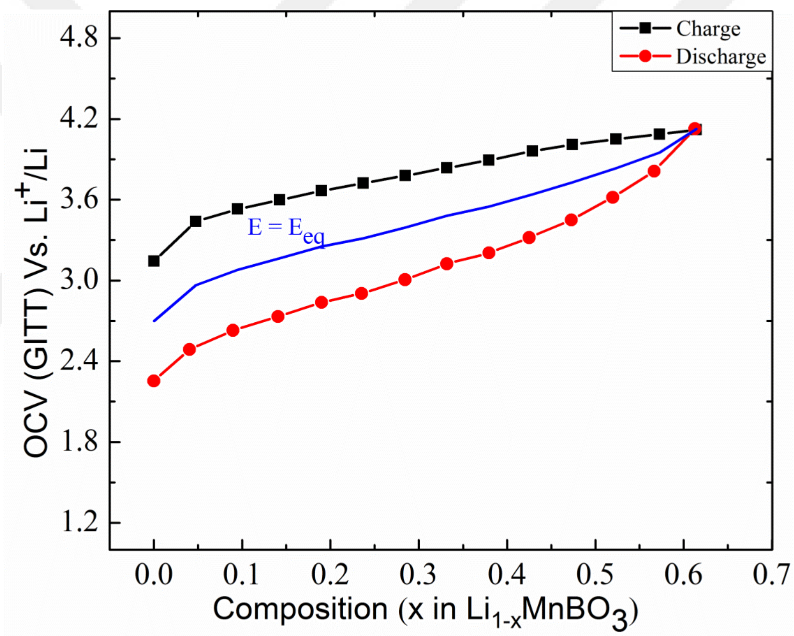

Figure 2.12 OCV (open circuit voltage, the steady state voltage at the end of each open circuit step in GITT measurement, during charge (black), during discharge (red), average (blue)) vs. composition (x in $Li_{1-x}MnBO_3$).

The Li^+ ion diffusion coefficients (D_{Li^+}) in Li_xMnBO_3 were calculated from the GITT data. In GITT method the transient voltage generated due to the application of a current pulse is monitored as a function of time. In our study, a galvanostatic section (charging or discharging) of 2 h at C/40 rate, followed by a 5 h open circuit step, was repeatedly applied until the charging (discharging) voltage reached 4.7 V (1.7 V) vs. Li^+/Li. **Figure 2.13** represents the potential vs.

composition profile obtained from GITT. As can be seen, about 0.6 Li^+ ions were extracted/inserted during the complete charging/discharging segment of the GITT measurement.

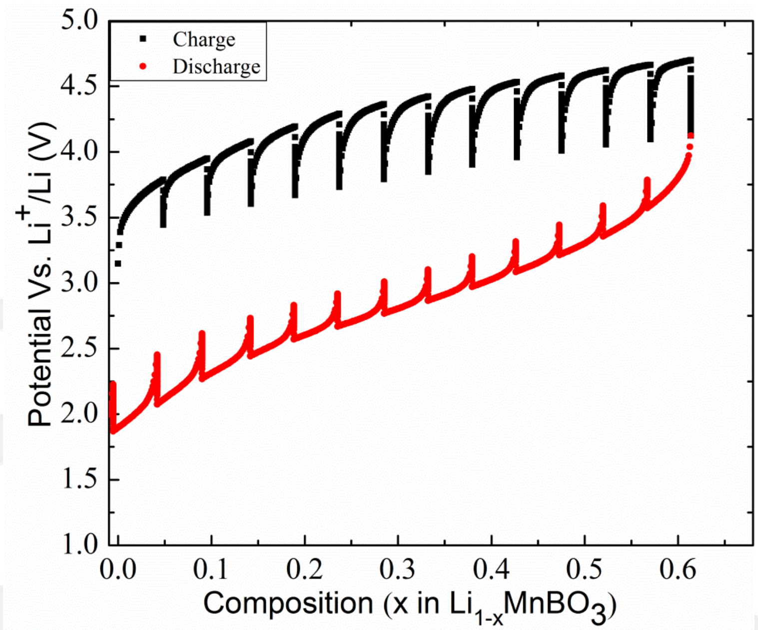

Figure 2.13 The potential vs. composition (x in $Li_{1-x}MnBO_3$) profile obtained from GITT.

As it was stated before, the relation of OCV (open circuit voltage) with composition (x in $Li_{1-x}MnBO_3$) indicates that the Li^+ extraction/insertion proceeds as a single phase reaction (**Fig. 2.12**) allowing the application of GITT for the determination of lithium diffusion coefficients, which were calculated by the following formula proposed by Weppner and Huggins[179-180].

$$D_{Li+}^{GITT} = 4/\pi\tau * [m_B V_M/M_B S]^2 [\Delta E_S/\Delta E_t]^2$$

In this equation τ is the constant current pulse time (2 h); m_B, V_M, and M_B are the mass, molar volume, and molar weight of the active material under investigation, respectively. S is the electrode-electrolyte interface area, and ΔE_S and ΔE_t are the changes in the steady state voltage and the overall cell voltage after the application of a current pulse in a single step GITT experiment, respectively. **Figure 2.14** shows the variation of the logarithmic value of lithium diffusion coefficient as a function of composition, as calculated from the GITT profile. The lithium diffusion coefficient values are higher during lithium insertion reaction than in the lithium removal process. Close to the stoichiometric composition of $LiMnBO_3$, lithium diffusion coefficient is ~10^{-11} cm^2/s, which is similar during lithium removal and insertion process.

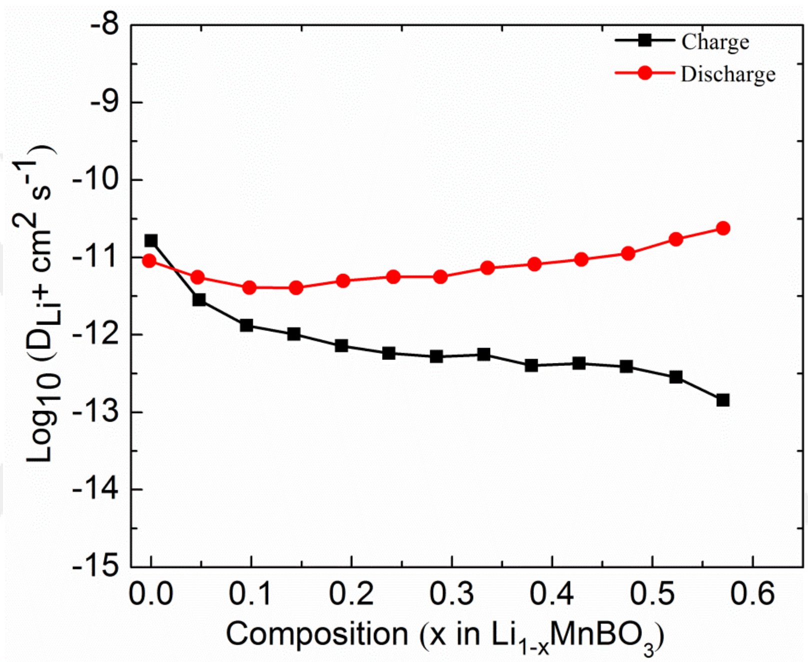

Figure 2.14 $Log_{10}D_{Li+}$ cm^2 s^{-1}vs. composition (x in $Li_{1-x}MnBO_3$).

Ongoing amorphization of $LiMnBO_3$ upon cycling may be one of the reasons for the capacity losses. The RGO coating and linkage of the particles decrease this problem by keeping the connectivity much better. However, even for the RGO coated samples, capacity fading is still noticeable that could be caused by several factors: Mn dissolution into the electrolyte might be one, as observed for cycling of Mn-oxides[181-182] and $LiMnPO_4$[183]; parts of the nanorods (35x80 nm, WxL) in our samples could still be too large for a fully reversible delithiation/lithiation considering the low ionic and electronic conductivity of the material; finally, unexpected SEI formation may increasingly separate active particles from the RGO network.

A performance close to the theoretical capacity and better cycling might be expected by utilizing even smaller particles of h-$LiMnBO_3$ combined with a more sophisticated coating and network formation process.

2.4 Conclusion

Hexagonal and monoclinic phases of $LiMnBO_3$ were synthesized by a sol-gel method. In situ carbon coating of $LiMnBO_3$ particles by carbonization of propionic acid was realized during the synthesis, leading to partially carbon covered active particles. Nano h-$LiMnBO_3$ with an average particle size of ~ 20 nm delivered a relatively high first discharge capacity of 136 mAh/g within 4.7 – 1.7 V at C/20 rate. The improved performance compared to older investigations is attributed to the small particle size and in situ carbon coating. Further improvement of capacity and cycling properties were achieved by employing a composite electrode of active material and reduced graphite oxide. The first discharge capacity increased to 145 mAh/g for the RGO / nano h-$LiMnBO_3$ composite, and most of the capacity was retained over multiple cycles. The enhanced properties were ascribed to the RGO matrix facilitating electron transport and acting as a protective layer. The advances made on $LiMnBO_3$ are encouraging not only for the use of borate based compounds but also other materials of low kinetics for use as high energy cathodes for Li-ion batteries. Further studies are still necessary to enhance cycling performance and reduce kinetic polarization. To our knowledge, these are the best results reported for $LiMnBO_3$ opening more room for improvement of the electrochemical performance of kinetically hindered electrode materials.

Chapter 3

$LiCoBO_3$ as a Cathode Material for Li-Ion Batteries

3.1 Introduction

Li-ion batteries remain as the primary choice in the portable electronics market. Plug-in electric vehicles powered by Li-ion batteries, possessing the advantages of high voltage, high capacity, long cycle life and variable charge-discharge rates compared to other secondary batteries, have also become available in recent years. $LiFePO_4$ could arguably be named as the most popular and primary choice among cathode materials for Li-ion batteries, when aspects like safety, cost and long cycle life are considered. Other cathode materials with poly-anion groups, PO_4^{3-}, SiO_4^{4-}, $P_2O_7^{4-}$ and BO_3^{3-} have also been extensively investigated[115, 138, 142, 170-171, 184-185]. Though the non-active (oligo-)anion groups restrict theoretical specific capacities of respective cathode materials because of their larger weights, they bring about other advantages, such as a better chemical stability and a higher operating voltage through the inductive effect. Among poly-anionic materials, borates are especially interesting to study because of their comparably lower molecular weights. In addition, there is lack of research on borate based cathode materials. While pure $LiFeBO_3$ and $LiMnBO_3$ were found to be electrochemically non-active in the pioneering work of Legagneur et al.[170], they have been shown to be possible high capacity cathode materials for Li-ion batteries in modified forms, e.g. by employing conductive carbon coatings and nano-sizing in recent studies[171, 173, 185]. Low ionic and electronic conductivities of borates were speculated as reasons for the poor electrochemical performance in the first place, and for $LiCoBO_3$, only 0.015 Li per formula unit could be extracted by Legagneur et al. in their study[170]. However, still, to the best of our knowledge, there are no results proving a reasonable electrochemical activity for $LiCoBO_3$ in Li-ion batteries. The cobalt system could be very attractive in terms of a higher expected operating voltage compared to manganese and iron borates, and with a theoretical capacity of ~ 215 mAh/g, it could result in a quite large specific energy as well. For instance, the redox potential of Co^{2+}/Co^{3+} is ca. 4.8 V vs. Li/Li^+ in $LiCoPO_4$[134], whereas the potential for Fe^{2+}/Fe^{3+} stays at ~ 3.5 V for the extensively studied olivine structure[115, 124, 186]. Likewise, higher operating voltages for the Co^{2+}/Co^{3+} redox couple compared to Fe^{2+}/Fe^{3+} and Mn^{2+}/Mn^{3+} were also reported in various poly-anionic cathode materials (Li_2MSiO_4, $Li_2MP_2O_7$, etc.)[134, 138, 142, 184].

Similar to the related borates and other poly-anionic cathode materials, the utilization of nano-particles of active materials and conductive coatings on the surfaces of these particles could be anticipated as important requirements in order to reach a reasonable electrochemical activity for $LiCoBO_3$, as it will be presented here. $LiCoBO_3$ is obtained by a sol-gel synthesis and appears as nano-crystallites with an average size of ~ 170 nm. The composite electrode of nano-$LiCoBO_3$ with reduced graphite oxide (RGO) is electrochemically active and delivers a first discharge capacity of 46 mAh/g within 4.7 – 2.0 V. The capacity is retained over multiple cycles as 87 % of the initial discharge capacity is still reachable at the 25th cycle.

3.2 Experimental Section

3.2.1 Synthesis

In order to obtain a stable sol, the stoichiometric amounts of $LiNO_3$ (0.01 mol) and $Co(NO_3)_2 .(H_2O)_6$ (0.01 mol) are dissolved in 11.5 ml propionic acid at 80 ^oC for 3 hours. In a similar way, 0.01 mol $B(OEt)_3$ is added into 29.5 ml propionic acid, and the same heating procedure is applied. After mixing the two solutions, the resulting solution is heated at 80 ^oC for an hour; thereafter, 1 ml of deionized water is added in order to induce hydrolysis. After evaporating the solvent at 100 ^oC for 24-72 hours, a purple gel powder is yielded. The gel powder is annealed at 600-650 ^oC for 10 hours under ambient atmosphere to obtain purple colored nano-$LiCoBO_3$ (**Fig. 3.1a**). For the solid state synthesis of $LiCoBO_3$, a mixture of Co_3O_4

and $LiBO_2$ (with 3:1 Li to Co mol ratio) is pressed into pellets and annealed at 800-850 ^oC for 10-15 hours under ambient atmosphere. Excess $LiBO_2$ is dissolved in water or ethanol, and the mixture is then filtered to obtain $LiBO_2$ free $LiCoBO_3$. It should also be noted that for both sol-gel and solid state syntheses, annealing processes were done in glassy carbon crucibles placed in quartz reaction tubes.

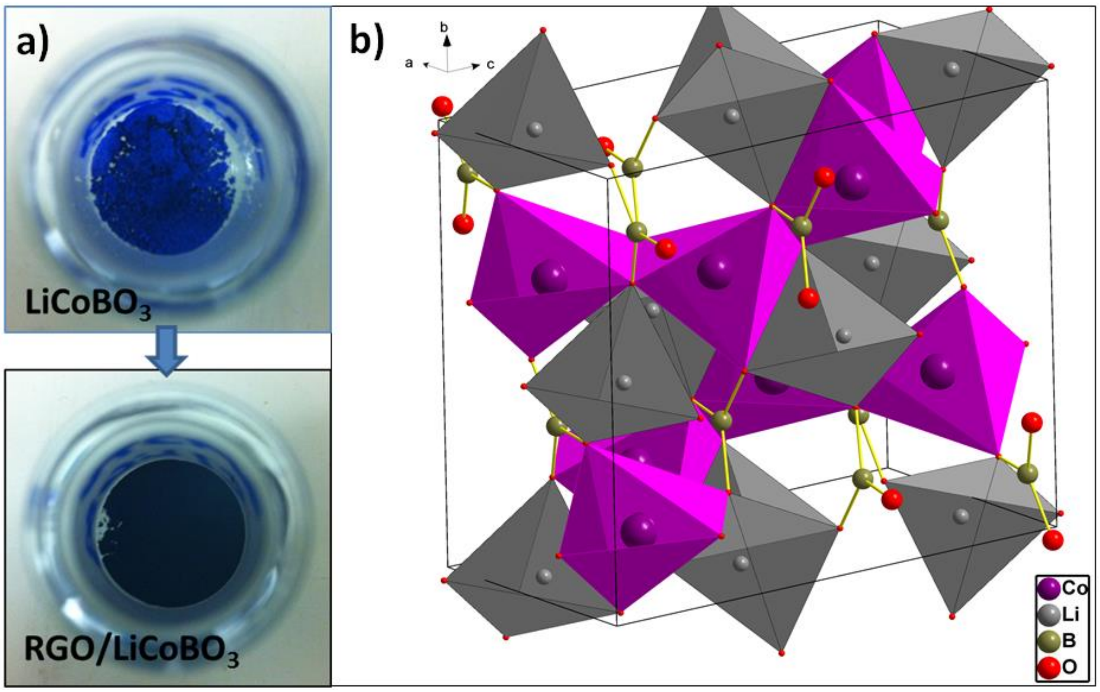

Figure 3.1 a) $LiCoBO_3$ synthetic products, (top) nano-$LiCoBO_3$, (bottom) RGO/nano-$LiCoBO_3$ composite. b) Crystal structure of $LiCoBO_3$ (skew [100] view).

The RGO/nano-$LiCoBO_3$ composite (**Fig. 3.1a)** was prepared by ball-milling ~ 66.6 wt-% nano-$LiCoBO_3$ with ~ 33.3 wt-% graphite oxide; then, this mixture was heated at 200-250 ^oC for 8 hours under nitrogen flow for the reduction of graphite oxide. The final carbon content was ~ 18 wt-% for the composite material as found by combustion-infrared spectroscopy analysis (LECO instruments, ETH LOC Micro-Laboratory).

3.2.2 Characterization

A STOE Stadi P diffractometer equipped with a germanium monochromator and $CuK_{\alpha1}$ radiation (operated at 40kV, 35 mA) was used to acquire powder X-ray diffraction patterns of the samples. The Scherrer equation was applied to calculate the average crystallite size: Crystallite size = 0.9 λ / ($\beta\cos\theta$) (λ = the wavelength of incident X-rays, β = the full width at the half maximum of the (004) peak for $LiCoBO_3$, and θ = the Bragg angle).

Scanning electron microscopy (SEM) analysis was carried out with a Zeiss Gemini 1530 operated at 1 kV. Transmission electron microscopy (TEM) was performed on a Tecnai F30 microscope (FEI, field emission gun), operated at 300 kV with a point resolution of ~ 2Å.

3.2.3 Electrochemical tests

For electrode fabrication of the solid state synthesis product and the sol-gel synthesized nano-$LiCoBO_3$, (70 wt-%) active material, (20 wt-%) conductive carbon (Super P® Li Timcal) and (10 wt-%) PVDF binder were manually mixed in an agate mortar to ensure proper mutual distributions. Similarly, for the preparation of RGO/nano-$LiCoBO_3$ composite electrode (90 wt-%) active material was mixed with (10 wt-%) PVDF binder. Then, a slurry of the mixture in 1:4 toluene:THF solution was prepared by ultrasonic dispersion. The slurry was cast on Ti current collectors and dried at 80 ^oC under vacuum. The current collectors had approximately 2-3 mg active material left on them after drying. A 0.75 mm-thick ribbon (Aldrich) of Li was used to prepare Li metal anodes. 1M solution of $Li[(C_2F_5)_3PF_3]$ in EC:DMC (1:1) (Merck, LF-30 SelectiLyte^{TM}) was the electrolyte used for galvanostatic and cyclic voltammetry tests. The electrochemical tests were performed with Swagelok type of cells that were constructed in an argon filled glove-box. Galvanostatic tests were carried out in the voltage range of 4.7 – 2.0 V with a potentiostatic step at 4.7 V until currents were below 2 mA/g, and also, within 5.0 – 2.0 V but without the aforementioned potentiostatic step. The applied current rates were C/20 and C/40 for charges and discharges, respectively. The cyclic voltammogram was obtained at a sweep rate of 0.05 mV/s in the potential range of 5.3 – 1.7 V.

3.3 Results and Discussion

The crystal structure of $LiCoBO_3$ is shown in **Figure 3.1b**. The reported structure for $LiCoBO_3$ has a monoclinic symmetry (space group: *C*12/c1) with a = 5.129(1) Å, b = 8.840(2) Å, c = 10.100(2) Å, β = 91.36(3)°, V = 457.81(37) $Å^3$. The structure contains trigonal bipyramidal CoO_5 which form chains by edge sharing along the [-101] direction. The polyhedra chains are connected to each other by trigonal planar BO_3 groups leading thus to a three dimensional oxidic framework. Li atoms are in tetrahedral coordination by O atoms, and LiO_4 tetrahedra are connected to CoO_5 polyhedra via corner sharing through BO_3 units.

Nano-$LiCoBO_3$ was realized by sol-gel synthesis with $LiNO_3$, $Co(NO_3)_2.(H_2O)_6$ and $B(OEt)_3$ as precursors dissolved in stoichiometric amounts in propionic acid. By annealing of the gel-powder under ambient atmosphere at 600-650 ^{o}C, a purple-colored powder of nano-$LiCoBO_3$ (**Fig. 3.1a**) was obtained. $LiCoBO_3$ was even obtained at an annealing temperature as low as 400 ^{o}C, but $Co_3(BO_3)_2$ and Co_3O_4 impurities were present. For the sol-gel synthesis of the hexagonal modification of $LiMnBO_3$ in nanoscopic form that was described in the previous chapter, a reductive CO atmosphere was necessary to ensure a high purity product. However, under reductive CO atmosphere, pure m-$LiCoBO_3$ cannot be obtained, as Co^{2+} was reduced to Co metal in our trials. Thus, quite differently from the nano h-$LiMnBO_3$ synthesis, firing the gel-powder under ambient atmosphere is essential to synthesize nano m-$LiCoBO_3$. The required ambient atmosphere and higher annealing temperatures cause a lack of in-situ carbon coating, which was present in the case of h-$LiMnBO_3$.

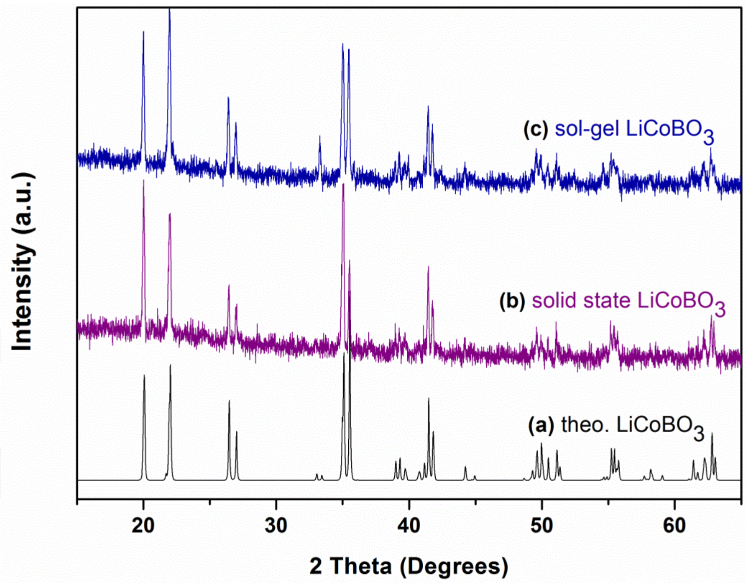

Figure 3.2 XRD powder patterns of $LiCoBO_3$: a) calculated b) the solid state synthesis product c) the sol-gel synthesis product obtained at 650 ^oC.

In order to compare the electrochemical performances of different synthetic products under similar electrochemical test conditions, m-$LiCoBO_3$ has also been synthesized via reaction of $LiBO_2$ and Co_3O_4 by conventional solid state synthesis. XRD powder patterns of the sol-gel synthesized $LiCoBO_3$, the solid state synthesis product and the theoretical diffraction pattern are displayed in **Figure 3.2**. The sample has a high purity, and the diffraction peaks can be matched to the theoretical pattern (ICSD 59346). The broadened diffraction peaks for the sol-gel synthesized $LiCoBO_3$ indicate the presence of nano-particles. The differences of intensities of the experimental XRD powder patterns to the theoretical pattern might be stemming from directional growths and preferred orientations in nano-crystallites (see electron microscopy data below).

The composite electrode material of nano-$LiCoBO_3$ was acquired by ball-milling the synthesis product with graphite oxide (produced by a modified Brodie method[176]) and heating the resulting mixture at 200-250 °C for 8 hours under nitrogen flow to reduce graphite oxide. **Figure 3.3** shows the XRD powder pattern of the composite material. No residual diffraction peaks from graphite oxide were observed after ball-milling and heat treatment. The diffraction peaks are broadened after this process indicating a size reduction, but the peak positions of nano-$LiCoBO_3$ are not shifted showing that lattice constants are not altered after the treatment.

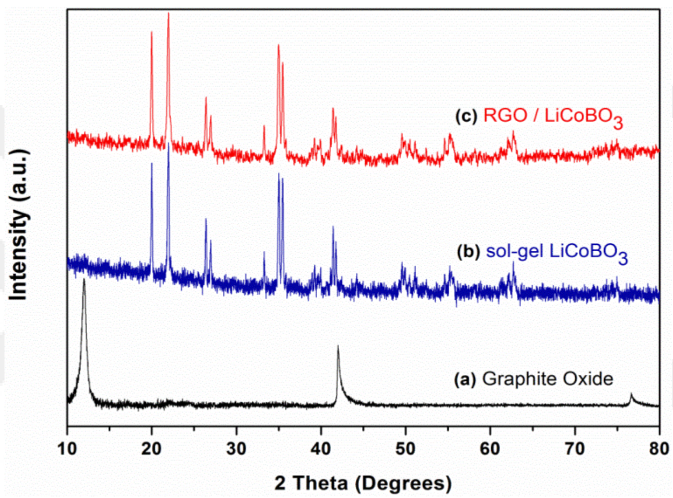

Figure 3.3 XRD powder patterns of a) graphite oxide, b) nano-$LiCoBO_3$, c) RGO/nano-$LiCoBO_3$ composite, indication to a complete delamination of RGO.

Figure 3.4 shows scanning electron microscopy (SEM) images of $LiCoBO_3$ samples. The sol-gel synthesized $LiCoBO_3$ starts to appear as nano-crystallites, when the gel-powder is annealed at 400 °C (**Fig. 3.4a**). The platelet particles coalesce, and larger agglomerates are formed, as the annealing temperature is increased to 650 °C (**Fig. 3.4b**) to ensure a high purity product. The agglomerates are spread and reduced in size after ball-milling and heat treatment to prepare the composite electrode material (**Fig. 3.4d**). Solid state synthesis yields micron-sized $LiCoBO_3$ particles with textured surfaces as it can be seen in SEM images (**Fig. 3.4c**).

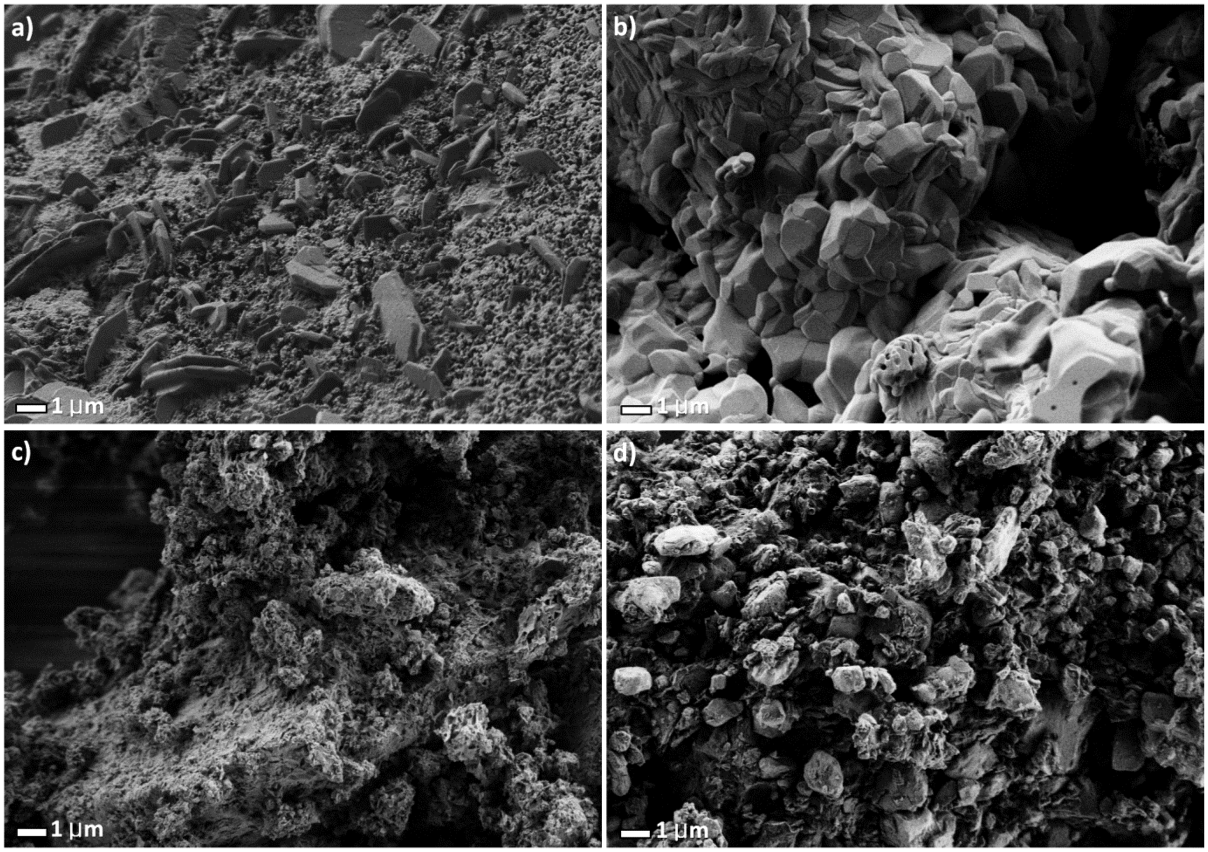

Figure 3.4 Scanning electron microscopy (SEM) images of the sol-gel synthesized $LiCoBO_3$ obtained at a) 400 ^oC , b) 650 ^oC, and SEM images of c) the solid state synthesis product, d) RGO/ nano-$LiCoBO_3$ composite.

Transmission electron microscopy images (TEM) of the sol-gel synthesized $LiCoBO_3$ and the composite material with RGO are displayed in **Figure 3.5**. The sol-gel synthesized $LiCoBO_3$ consists of micron-sized agglomerates (**Fig. 3.5a**) that are built by nano-crystallites (**Fig. 3.5b**) with an average size of ~ 170 nm (calculated by the broadening of (004) diffraction peak). The crystallinity of the particles is indicated by the observation of lattice fringes in high resolution images, e.g. the (020) planes of $LiCoBO_3$ (**Fig. 3.5c**). TEM images of the RGO/nano-$LiCoBO_3$ composite show the coverage of $LiCoBO_3$ agglomerates by RGO flakes (**Fig. 3.5d**) and the connection of crystallites through RGO (**Fig. 3.5e**). The network formation via reduced graphite oxide could be expected to provide an improved conductivity and mechanical stability within the composite electrode material. The interlayer distances, ~ 3.5 Å and ~ 4.2 Å , found for the coating material on nano-$LiCoBO_3$ provide evidence for the reduction of graphite oxide, as these values are close to the (002) lattice spacing of graphite (**Fig. 3.5f**).

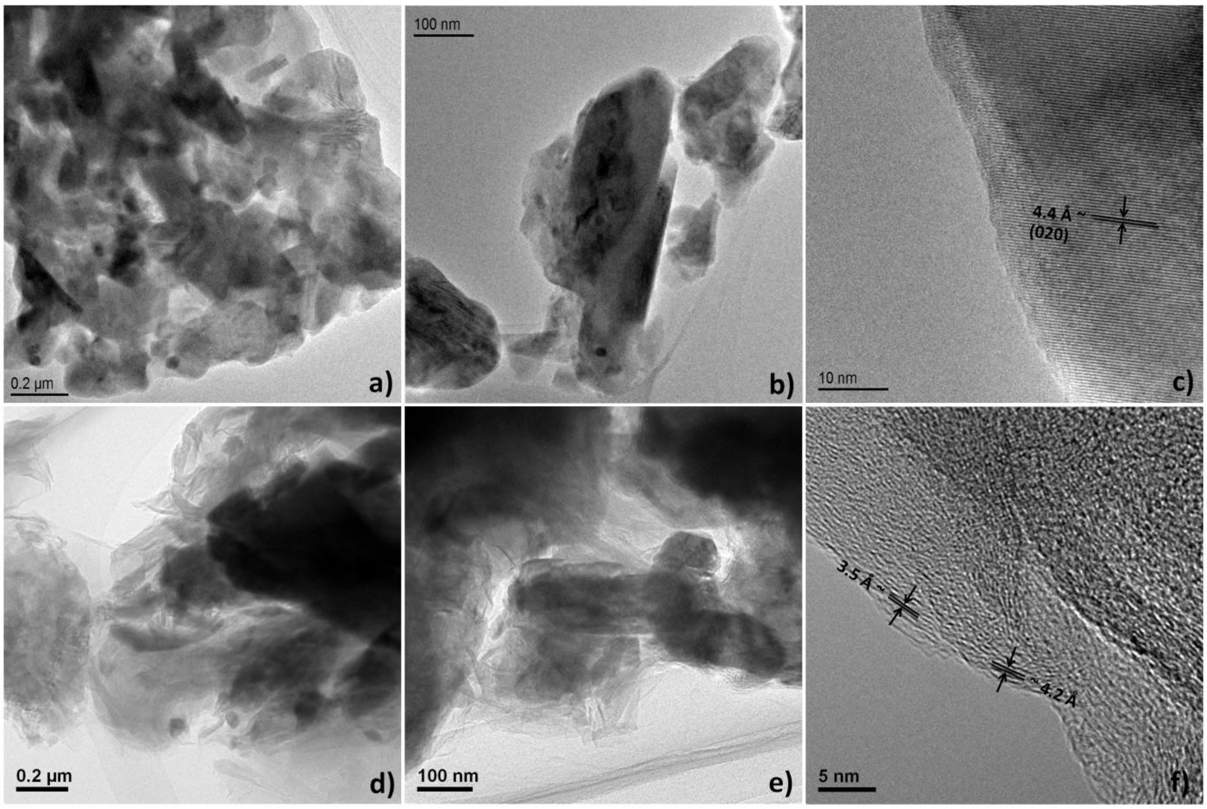

Figure 3.5 Transmission electron microscopy images (TEM) of the sol-gel synthesized $LiCoBO_3$ showing a) particle agglomerates, b) nano-crystallites, c) lattice fringes for the (020) planes, and TEM images of the RGO/nano-$LiCoBO_3$ composite displaying d) the coverage of agglomerates by RGO, e) the connection and coverage of nano-crystallites through RGO, f) RGO coating of $LiCoBO_3$.

Comparable to the findings of Legagneur et al.[170], micron-sized $LiCoBO_3$ synthesized by a solid state reaction is not electrochemically active. The potential (V) vs. time (h) plot for the cell cycled in a galvanostatic mode between 4.7 V and 2.0 V at C/20 rate is shown in **Figure 3.6**. The first discharge capacity is only ~ 3 mAh/g similar to the value found by Legagneur et al., and could be originating from side reactions rather than due to deinsertion/insertion of lithium.

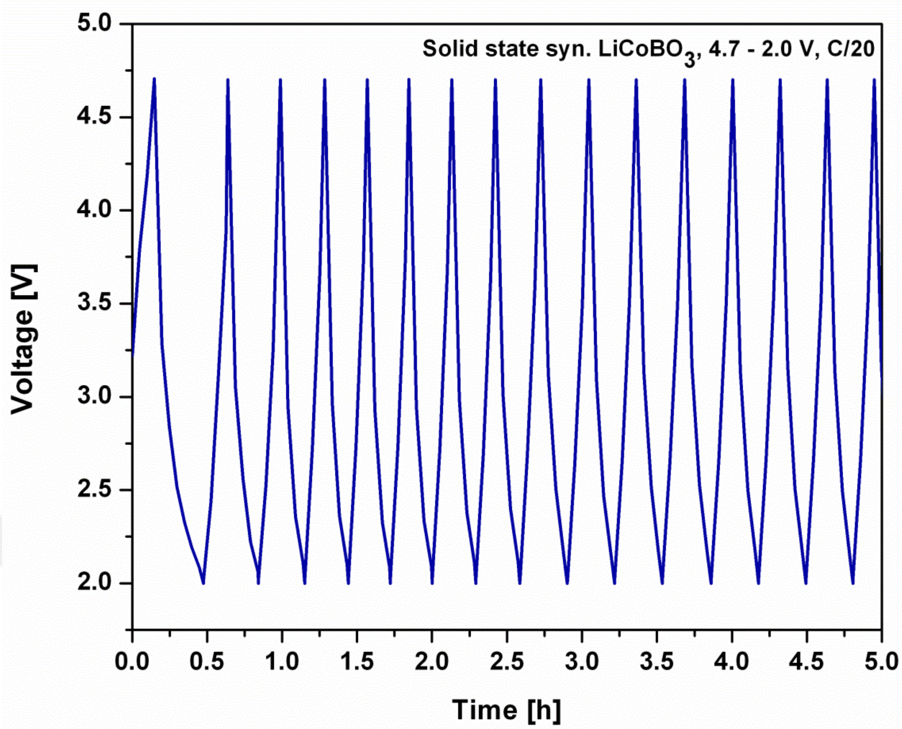

Figure 3.6 The potential (V) vs. time (h) plot for the solid state synthesized $LiCoBO_3$ cycled in a galvanostatic mode between 4.7 V and 2.0 V at C/20 rate.

The first five charge/discharge curves of the sol-gel synthesized nano-$LiCoBO_3$ are displayed in **Figure 3.7**. The cell was cycled within 4.7 – 1.7 V at C/20 rate. The working electrode was prepared with (70 wt-%) active material, (20 wt-%) conductive carbon (Super P®) and (10 wt-%) PVDF binder. An electrochemical activity can be claimed with a first charge capacity of 26 mAh/g pointing out the delithiation of the compound. The utilization of nano-particles successfully improves the electrochemical performance of $LiCoBO_3$ by decreasing the length of the diffusion paths for Li^+ ions and enhancing electron hopping. The first discharge capacity remains at 17 mAh/g and capacities drop at each cycle due to not fully reversible delithiation/lithiation arising from the still limited ionic and electronic conductivity.

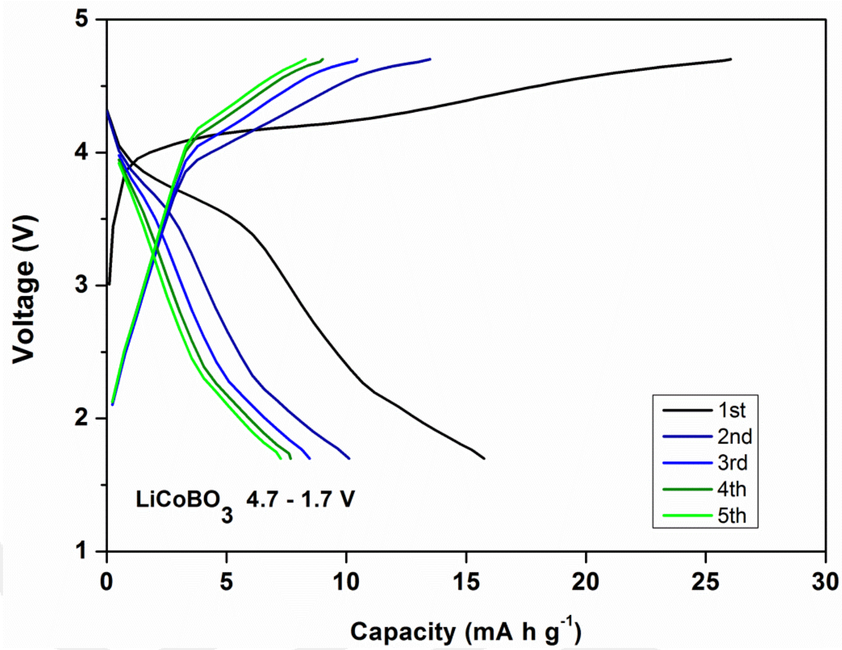

Figure 3.7 The first five charge/discharge curves of the sol-gel synthesized nano-$LiCoBO_3$ within a potential window of 4.7 – 1.7 V at C/20 rate.

As expected, charge/discharge capacities and cycling properties were improved for the RGO/nano-$LiCoBO_3$ composite electrode compared to the above described plain nano-$LiCoBO_3$ electrode. The composite electrode contained ~ 74 wt-% nano-$LiCoBO_3$, ~ 16 wt-% conductive carbon sourcing from the RGO and 10 wt-% PVDF; no additional carbon black was added. **Figure 3.8** shows the galvanostatic charge/discharge curves of the RGO/nano-$LiCoBO_3$ composite that were obtained in a combined galvanostatic-potentiostatic mode within 4.7 – 2.0 V. Galvanostatic (constant current) analysis was performed at a rate of C/20 and C/40 for charge and discharge, respectively. In the charging process, a potentiostatic step was applied at the upper voltage limit, 4.7 V, until the current dropped below 2 mA/g. The RGO/nano-$LiCoBO_3$ composite delivers a first charge capacity of ~ 55 mAh/g. The first discharge capacity is ~ 46 mAh/g, and the cycling is fairly stable with a discharge capacity of ~ 43 mAh/g at the 10^{th} cycle.

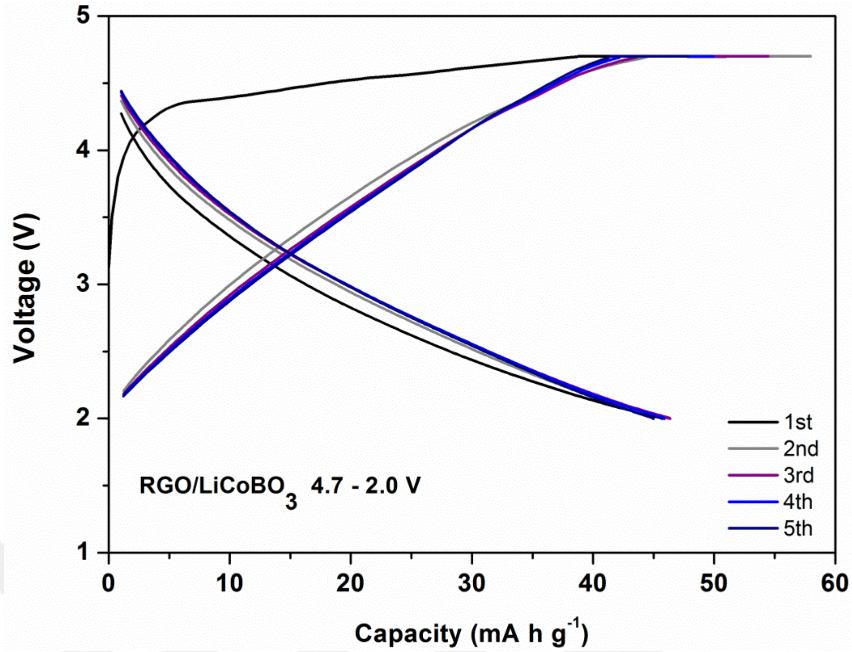

Figure 3.8 The galvanostatic charge/discharge curves of RGO/nano-$LiCoBO_3$ composite within 4.7 – 2.0 V at C/20 rate for charge (constant voltage at 4.7 V until the current < 2 mA/g), and at C/40 rate for discharge.

The average discharge capacity loss is only ~ 0.25 % per cycle for the first 25 cycles (**Fig. 3.9**). The improvements for the RGO/nano-$LiCoBO_3$ composite electrode can be linked to a number of reasons: 1. The reduced graphite oxide network can be expected to increase the reversible delithiation/lithiation by assisting Li^+ ion and electron transports. 2. The mechanical stability gained by the RGO network better prevents contact losses generally occurring through the amorphization of electrode material after multiple cycles. 3. The coverage of nano-$LiCoBO_3$ by the protective RGO layer may also limit the undesirable reactions with by-products that could be formed during cycling by electrolyte decomposition.

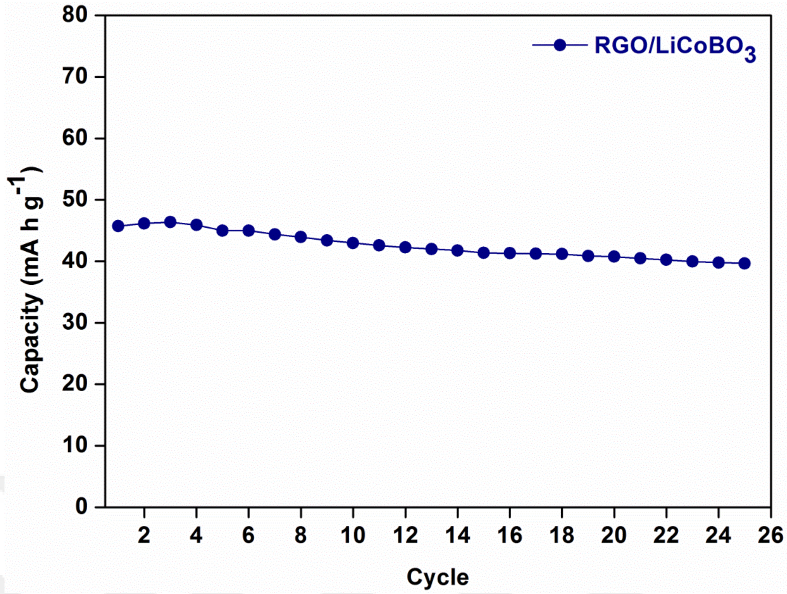

Figure 3.9 Discharge capacity vs. cycle number for RGO/nano-$LiCoBO_3$ composite.

As the upper voltage limit has been increased to 5.0 V in the charging process, the first charge and discharge capacities were elevated to ~ 83 mAh/g and ~ 64 mAh/g (**Fig. 3.10**), respectively, indicating that the delithiation of $LiCoBO_3$ is not complete at 4.7 V.

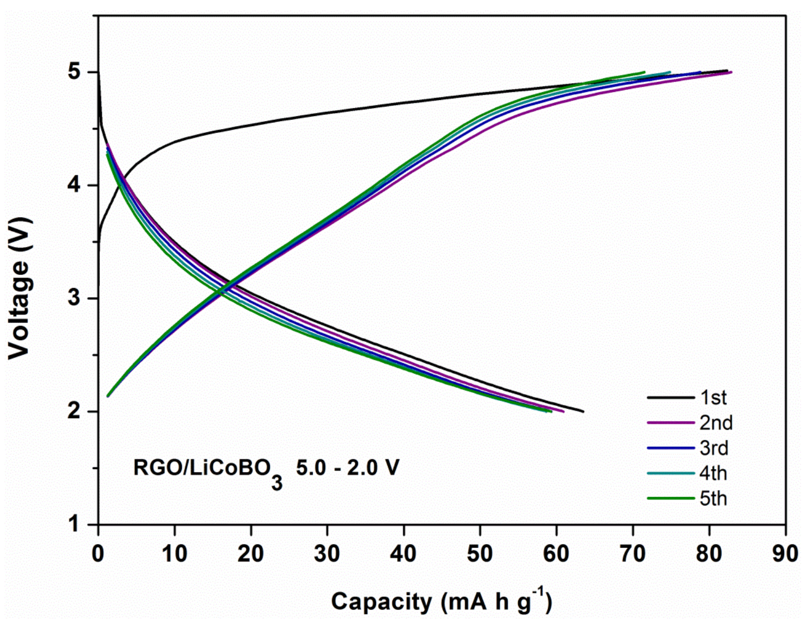

Figure 3.10 The first five charge/discharge curves of RGO/nano-$LiCoBO_3$ composite within 5.0 – 2.0 V at C/20 and C/40 rates for charge and discharge, respectively.

The coulombic efficiency drops with the higher voltage limit, and the reason for the higher charge capacity could be the oxidation of electrolyte, though the electrolyte (LF-30 SelectiLyte™) used in our study is expected to be electrochemically stable in the voltage window of 5.0 – 2.0 V[177]. For the galvanostatic measurement in this window, the average voltage for charge is found to be ~ 3.94 V, whereas the average discharge voltage is approximately 2.80 V for the 5th cycle. This huge polarization shows the poor kinetics in the system that is very similar to the cases of $LiFeBO_3$ and $LiMnBO_3$.

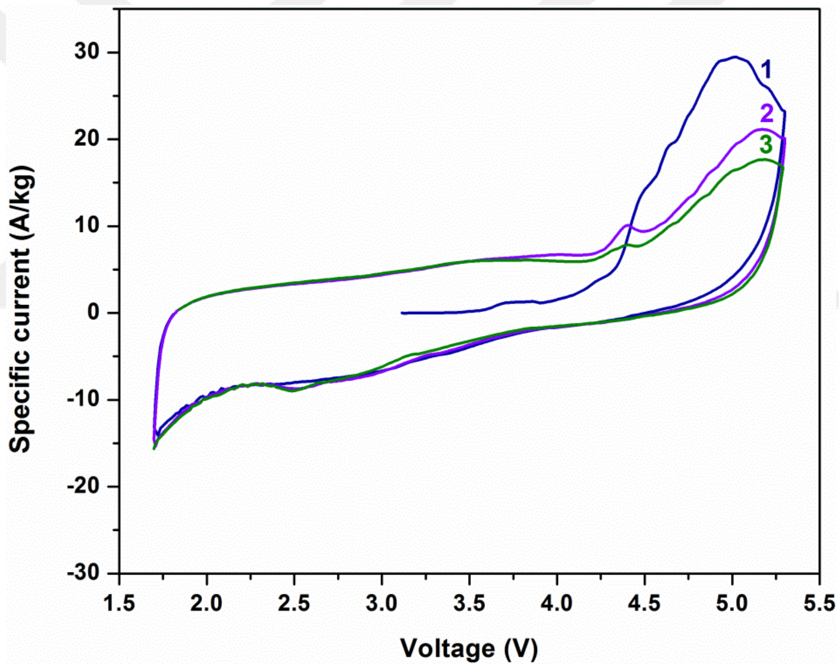

Figure 3.11 The cyclic voltammogram of RGO/nano-$LiCoBO_3$ composite between 5.3 and 1.7 V at a scanning rate of 0.05 mV/s.

The polarization is also found in cyclic voltammetry studies. The cyclic voltammogram of the RGO/nano-$LiCoBO_3$ composite is shown in **Figure 3.11** for the potential window, 5.3 – 1.7 V, at a scanning rate of 0.05 mV/s. Oxidation and reduction processes could be observed in a broad voltage range with better defined oxidation peaks. In the first cycle, the most distinct oxidation peak appears at ~ 5.0 V with an onset of ~ 4.2 V; the reduction process, which seems to be comparable with subsequent cycles, ranges from ~ 4.6 V to 1.7 V, and no well-defined effect could be seen. The oxidation starts at ~ 1.8 V in subsequent cycles, and two peaks at ~ 4.4 V and ~ 5.1 V are present that might be indicating to a structural change after the first charge. The overpotential is reduced after the first charge as the oxidation process is spread to a wider range in the second and third cycle; this reduction might be arising from the partial amorphization of crystalline electrode material.

Figure 3.12 illustrates the rate capability for the RGO/nano-$LiCoBO_3$ composite within 5.0 – 2.0 V. The discharge capacities are in the range of ~ 60, 35, 30 and 25 mAh/g for the rates of C/40, C/20, C/10 and C/5, respectively. With increasing rate, the capacities decrease, and only 70 % of the initial discharge capacity is retained at the 25th cycle at C/40 rate. Cycling properties and capacities with increasing rate could be considered as poor, but the results are still encouraging since the electrochemical activity for $LiCoBO_3$ is evidenced even for these relatively high rates.

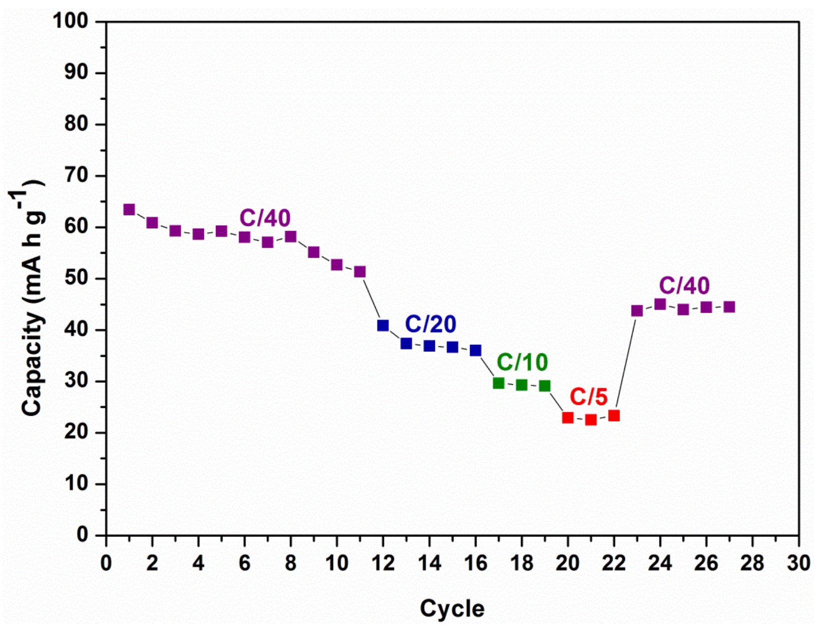

Figure 3.12 The rate capability of RGO/nano-$LiCoBO_3$ within 5.0 – 2.0 V at C/40, C/20, C/10 and C/5 rates (at room temperature).

XRD powder patterns of the electrodes of the RGO/nano-$LiCoBO_3$ in the charged and discharged states are displayed in **Figure 3.13**. A slight shift between charged and discharged states occurs, and the formation of new phases is not observed at various charged and discharged states. In comparison to the similar structural and electrochemical properties of m-$LiFeBO_3$[170-171] and m-$LiMnBO_3$[170, 173], together with the small shift of the diffraction peaks and the sloping nature of charge/discharge curves, a solid solution lithiation/delithiation mechanism could be predicted for $LiCoBO_3$. However, it should be noted that the ex-situ characterization of cycled electrodes is not sufficient to make definitive conclusions since only ~ 30 % of the theoretical capacity is achieved implying that most of the $LiCoBO_3$ particles are still not electrochemically activated that is likely to shadow the results. The unactivated blocks are visible in cycled electrodes of the RGO/nano-$LiCoBO_3$ composite (**Fig. 3.14**). Further investigations of this system might be necessary to better understand the electrochemical process.

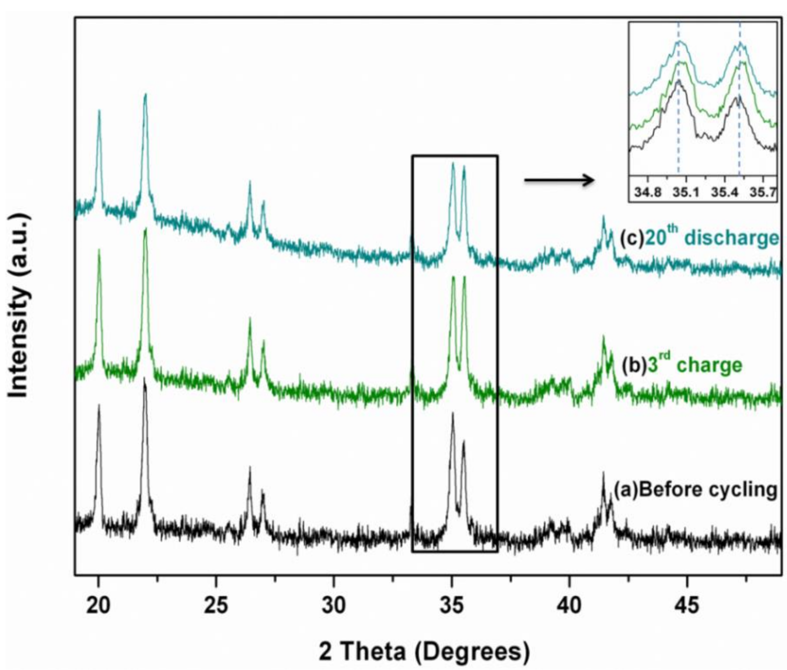

Figure 3.13 XRD powder patterns of the electrodes of RGO/nano-$LiCoBO_3$ composite in the charged and discharged states: a) before cycling (black), b) after third charge to 5.0 V (green), c) after twentieth discharge to 2.0 V (turquoise).

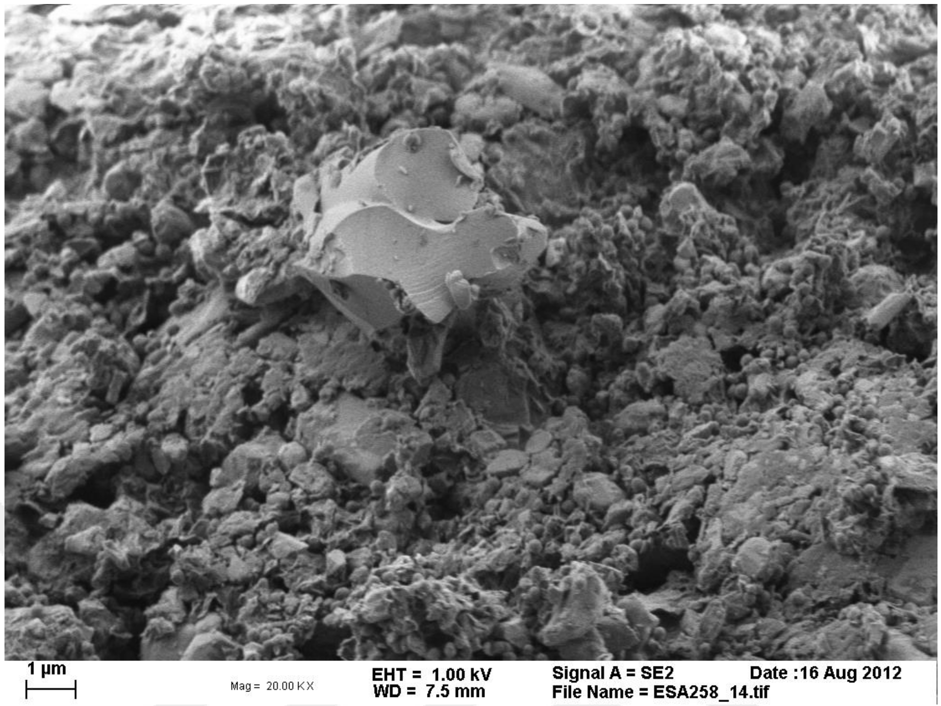

Figure 3.14 Scanning electron microscopy (SEM) image of the electrode of RGO/nano-$LiCoBO_3$ after 25 galvanostatic cycles showing the presence of unactivated $LiCoBO_3$ blocks.

Even though the electrochemical activity of $LiCoBO_3$ as a cathode material for Li-ion batteries is shown here, realized capacities are still low for practical applications and the kinetic polarization remains to be a problem. The utilization of nano-particles and RGO coating-network formation lower these problems, but the average particle size and the agglomerate of particles are still too large to reach values close to the theoretical capacity of $LiCoBO_3$. For h-$LiMnBO_3$, discharge capacities were doubled, when the average particle size decreased from ~ 120 nm to ~ 20 nm. A similar improvement might be expected for m-$LiCoBO_3$. Furthermore, the reduced graphite oxide network possibly enhances the long range conductivity within the electrode, but the sol-gel synthesized nano-$LiCoBO_3$ still lacks a proper conductive coating on the surface. If these problems could be solved by different synthetic routes yielding smaller particles and in-situ carbon coating, a better electrochemical performance might be accomplished. Besides, the metal site doping in $LiCoBO_3$ could also improve the overall performance by increasing the electronic conductivity or lowering the average voltage and kinetic polarization, as it was already demonstrated for several poly-anionic cathodes in previous investigations.

3.4 Conclusion

$LiCoBO_3$ was synthesized by a sol-gel method and consisted of nano-crystallites with an average size of ~ 170 nm forming micrometer-sized agglomerates. A composite electrode of $LiCoBO_3$ was obtained with reduced graphite oxide. The RGO/nano-$LiCoBO_3$ composite delivers a first discharge capacity of ~ 46 mAh/g in a galvanostatic-potentiostatic protocol within 4.7 – 2.0 V. The capacity retention is quite good with an average loss of ~ 0.25 % per cycle for the first 25 cycles. When the upper voltage limit was set to 5.0 V, the first charge and discharge capacities were increased to ~ 83 mAh/g and ~ 64 mAh/g, respectively, indicating that the delithiation of $LiCoBO_3$ is not complete at 4.7 V. The employment of smaller nano-particles with conductive coatings on their surfaces and the use of high-voltage stable electrolytes are expected to provide higher charge/discharge capacities and more stable cycling. Nevertheless, to the best of our knowledge, these are the best results obtained for $LiCoBO_3$ so far and set a reasonable example for the electrochemical activity of $LiCoBO_3$ in Li-ion batteries.

Chapter 4

Novel Li-rich Borate Compounds as High Capacity Cathode candidates for Li-ion Batteries

4.1 Introduction

For an increase of specific energies especially new cathode materials beyond to date known ones like $Li_x(Ni,Mn,Co)O_2$ (NMC), Li_xFePO_4 (LFP), etc.[38, 124, 183, 187] have to be developed, which utilize more than one Li per 100 atomic mass units. Presently employed $LiFePO_4$ is quite limited with a theoretical specific charge of 170 mAh/g. However, it exemplifies how transition metal ions can be bound efficiently into stable networks by linking through phosphate groups. Borate groups may fulfill a similar function but at a lower specific weight. In order to exchange more charge per mass unit, several oxidation state switches have to be realized, eventually reaching high oxidation states of the transition metal. Manganese is especially suited for this purpose. However, at high oxidation states monomeric units like the permanganate anion tend to form, which easily dissolve in the electrolyte and thus induce battery failure. Here, inert linker groups like BO_3 units may become part of a problem solution. The use of mono borates like $LiMBO_3$ (M = Fe, Mn, Co) as cathode materials for Li-ion batteries was first investigated by Legagneur et al. with little success due to low ionic and electronic conductivity of such compounds[170]. At the time, only 4% and 2% Li were extractable for $LiFeBO_3$ and $LiMnBO_3$, respectively[170]. Later, Yamada et al. obtained about 190 mAh/g at C/20 rate after enhancing electronic conductivity by carbon composite formation and by avoiding the exposure of the material to air[171]. This value is close to the theoretical specific capacity of $LiFeBO_3$. In previous chapters, we demonstrated a high capacity of 145 mAh/g within 4.7 – 1.7 V at C/20 rate for h-$LiMnBO_3$ by nano-sizing and employing a composite electrode utilizing reduced graphite oxide, and similarly, $LiCoBO_3$ has been activated as a cathode material for Li-ion batteries. Even though the theoretical capacities for lithium transition metal borates are larger than those of presently employed phosphates, especially that of $LiFePO_4$, capacities are still low compared to other systems such as Li-S[162, 188] and Li-O_2[8, 168]. For poly-anionic cathode systems, comparable specific capacities and energies could only be achieved with new electrode materials having properties such as light weight, high operating voltage, and utilizing more than one Li exchange per formula unit. Naturally occurring minerals might be used as blueprints for the search of such materials, and in our case, pinakiolites that have the general formula of $(Mg_x,Mn_y)_2Mn(BO_3)O_2$ were chosen as a starting point. Pinakiolite minerals were first tried to be electrochemically lithiated with no success. Consequently, we have further explored the Li_2O – MnO – B_2O_3 system with the hope of finding new lithium rich phases by replacing magnesium in oxoborate compounds with lithium. Further investigations in the system led to the new Li-rich compound $Li_7Mn(BO_3)_3$, which constitutes a colorless phase of very low electronic conductivity. Encouraging first electrochemical data became possible by nano-sizing and employing of a carbon composite electrode. $Li_7Mn(BO_3)_3$ possesses several prerequisites for a high energy density electrode material for Li-ion batteries: a high theoretical capacity of ~ 479 mAh/g at an exchange of 5 Li per formula unit. With an average cell potential higher than 3V against lithium metal, it is a highly interesting cathode candidate. A unique feature of the new compound containing Mn atoms in tetrahedral coordination may allow for a better stabilization of different oxidation states in the borate framework at large redox stress.

4.2 Experimental Section

4.2.1 Synthesis

Crystals of $Li_7Mn(BO_3)_3$ were synthesized from high purity Li_2O, MnO and B_2O_3 mixed in stoichiometric amounts and pressed into pellets in an Ar filled glove box. The pressed pellets were sealed in a niobium tube, transferred into a quartz tube and heated under slight vacuum at

850 ^oC for 24 hours. After cooling down to 700 ^oC at a rate of 10 $^oC/h$, the sample was quenched to room temperature. The compound was also obtained in an open system with stoichiometric amounts of Li_2CO_3, MnO and H_3BO_3 which were intensively mixed, pressed into pellets, placed in a semiclosed glassy carbon crucible, and annealed at 660 - 700 ^oC for 15 hours under reductive CO atmosphere. Successive cooling, grinding, mixing and re-annealing of the reaction product yields high purity $Li_7Mn(BO_3)_3$. A nano-composite electrode material was obtained by ball-milling of crystalline $Li_7Mn(BO_3)_3$ (75 wt%) with carbon black (Super P® Li Timcal) (25 wt%) under Ar atmosphere. The handling and electrode fabrication were carried out in a glove box, as the formation of $LiB(OH)_4$ occurs when this material is exposed to air for a few hours.

High temperature treatment of $Li_7Mn(BO_3)_3$ yields the lithium-poorer crystalline compound $Li_{4.14}Mn_{1.21}(BO_3)_3$. For the synthesis of $Li_{4.14}Mn_{1.21}(BO_3)_3$, starting materials, Li_2CO_3, MnO and H_3BO_3, were mixed and ground in an agate mortar with relative ratios of ~ 2.33Li: 0.33Mn: 1B, and thereafter the powder mixture was pressed into pellets. The pressed pellets were placed in a partially closed glassy carbon crucible and annealed at 850 ^oC for 24hours in a vacuumed quartz tube (ca. 2.0 x 10^{-1} mbar). Afterwards, the reaction tube was cooled down to 700 ^oC at a cooling rate of 10 $^oC/h$ and quenched to room temperature from 700 ^oC. The main products are colourless crystals of the title compound along with some impurity phases.

4.2.2 Characterization

For structure determination, a crystal of $Li_7Mn(BO_3)_3$ of suitable size (0.10 x 0.18 x 0.28 mm) was selected under a microscope using polarized light. Similarly, for $Li_{4.14}Mn_{1.21}(BO_3)_3$, a crystal with dimensions, 0.20 x 0.20 x 0.10 mm, was selected. Data sets were collected on a Bruker SMART CCD 1K area detector diffractometer using MoKα-radiation (0.73071 Å). As crystals are always twinned, the crystal structures had to be determined by multiple twin refinements. Further details for the solution and refinement of the structures are given in the **Appendix** (p. 180).

Powder X-ray diffraction patterns were obtained on a STOE Stadi P diffractometer equipped with a germanium monochromator and $CuK_{\alpha 1}$ radiation (operated at 40 kV, 35 mA).

The electrical conductivity of $Li_7Mn(BO_3)_3$ was measured between 310 K and 535 K using pressed pellets with a diameter of ~ 4-6 mm and a thickness of ~ 1 mm . The measurements were performed in an argon filled glove-box with custom made cells employing nickel contact electrodes for a 2-point measurement. The Arrhenius plot (ln(σ) vs. 1000/T) was used to derive the conductivity value at room temperature.

Scanning electron microscopy (SEM) analysis of the as-obtained samples were carried out with a Zeiss Gemini 1530 operated at 1 kV. (Scanning) transmission electron microscopy ((S)TEM) analysis was performed with a CM30ST (FEI; LaB_6 cathode) and a Tecnai F30 microscope (FEI; field emission gun), both operated at 300 kV, point resolution of ~ 2Å.

4.2.3 Electrochemical tests

Electrodes containing approximately (70 wt-%) active material, (20 wt-%) conductive carbon (Super P® Li Timcal) and (10 wt-%) PVDF binders were prepared from a slurry with NMP that was cast on Ti current collectors and dried at ~ 100-120 ^{o}C under vacuum. No additional carbon black, besides the carbon resulting from the composite formation, was used to prepare the electrodes of nano-composite $Li_7Mn(BO_3)_3$. The final electrodes consisted of approximately 6-7 mg active material. Li metal disks prepared from a 0.75 mm-thick ribbon (Aldrich) served as anode, and 1M solution of $Li[(C_2F_5)_3PF_3]$ in EC:DMC (1:1) (Merck, LF-30 SelectiLyte^{TM}) was used as the electrolyte, which is expected to be electrochemically stable within the voltage window (4.7 – 1.7 V) employed. Swagelok-type cells were assembled in an Ar filled glove-box. Galvanostatic measurements were carried out within 4.7 – 1.7 V at a rate of 10 mA/g. Also, voltage windows of 4.2 – 1.7 V and 5.3 – 1.7 V were explored at rates of 10 mA/g and 5 mA/g for charge and discharge, respectively. The cyclic voltammetry was done with a sweep rate of 0.05 mV/s between 4.7 and 1.7 V.

4.3 Results and Discussion

$Li_7Mn(BO_3)_3$ has been synthesized by reaction of Li_2O, MnO and B_2O_3 in exact stoichiometric amounts by conventional solid state synthesis. The colorless crystals are of triclinic symmetry (space group *P*-1 (no. 2), a = 8.3234(15) Å, b = 9.1952(17) Å, c = 11.248(2) Å, α = 71.495(4)°, β = 79.525(4)°, γ = 71.368(4)°, V = 770.5(2) Å^3). The atomic coordinates for $Li_7Mn(BO_3)_3$ are given in the **Appendix** (p. 182), along with the crystallographic data including bond lengths, positional and displacement parameters.

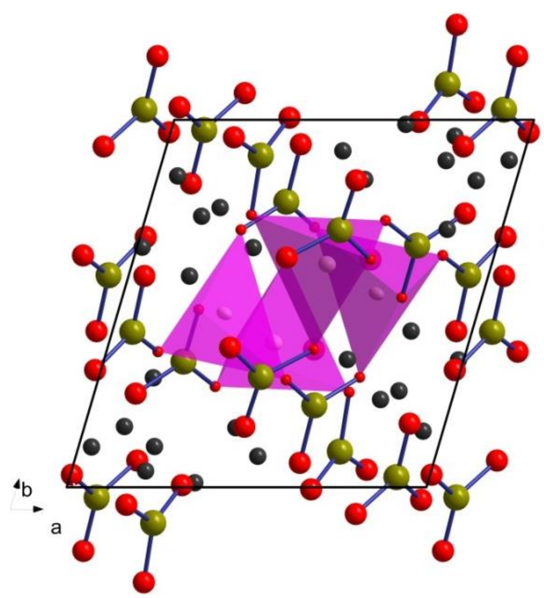

Figure 4.1 View of the crystal structure of $Li_7Mn(BO_3)_3$ along [001]. This corresponds to the direction of columns of MnO_4 tetrahedra pairs (pink) interconnected by BO_3^{3-} anions (boron - green, oxygen - red spheres, respectively).

The crystal structure of $Li_7Mn(BO_3)_3$ (**Fig. 4.1**) contains six crystallographically different BO_3^{3-} anions of which only one is exclusively linked to Li^+ cations. All other borate units are linked both, through Mn as well as through Li centers. All manganese atoms are tetrahedrally coordinated by oxygen centers of the BO_3^{3-} groups. The MnO_4-tetrahedra form columns extending along the crystallographic c-axis (**Fig. 4.2**) and are surrounded only by Li-atoms in their first coordination spheres. One of the BO_3^{3-} units connects two of the tetrahedra in pairs and another one links the tetrahedra pairs into the columns. Terminal BO_3^{3-} units provide the fourth oxygen atoms to the MnO_4-tetrahedra. To the best of our knowledge, the tetrahedral coordination of manganese at such low oxidation state is unique compared to other related Mn^{2+} oxide compounds. Typically MO_6 octahedra or MO_5 (M = Fe, Mn, Co in $LiMBO_3$) polyhedra with trigonal bipyramidal or square pyramidal geometry have been found in the hitherto known phases[170]. Furthermore, the tetrahedral coordination may help to stabilize the borate-manganate framework up to high oxidation states of the manganate centers.

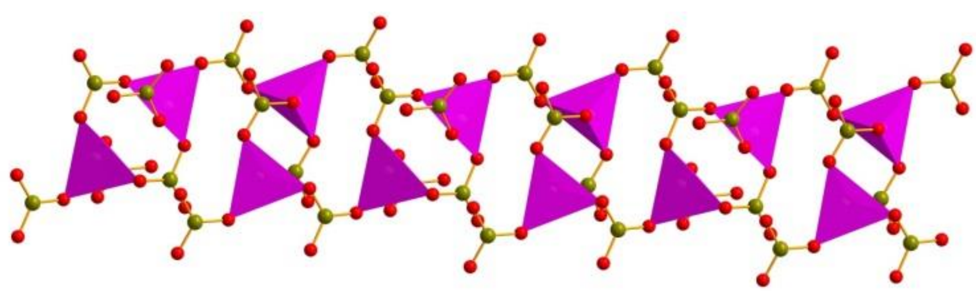

Figure 4.2 Columns of pairs of MnO_4 tetrahedra (pink) interconnected by BO_3^{3-} anions extending along the crystallographic c-axis (boron - green, oxygen - red spheres, respectively).

XRD powder patterns for $Li_7Mn(BO_3)_3$ are displayed in **Figure 4.3**. The samples are phase pure, and no trace reflections of impurities are observed. **Figure 4.3c** shows the XRD powder pattern of nano-composite material that is obtained by ball-milling of crystalline $Li_7Mn(BO_3)_3$ (75 wt%) with carbon black (Super P® Li Timcal) (25 wt%). The broadening of diffraction peaks indicates the nano-sizing of the pristine micron sized particles. This finding is supported by electron microscopy images.

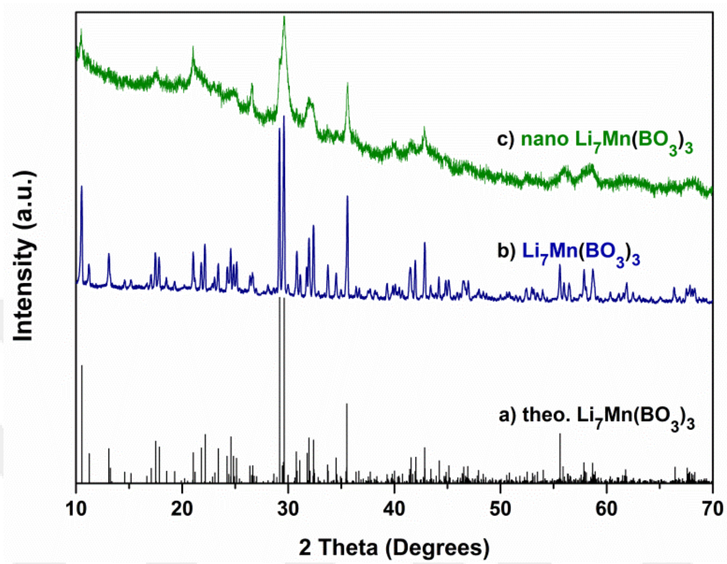

Figure 4.3 XRD powder patterns for $Li_7Mn(BO_3)_3$: a) theoretical, b) crystalline, c) nano-composite.

$Li_7Mn(BO_3)_3$ synthesized by conventional solid state synthesis occurs mainly in form of micron sized (4-5 µ) crystallites, but the existence of sub-micron particles can be found in scanning electron microscopy (SEM) images as well (**Fig. 4.4a**). After ball-milling with carbon black, the crystallite size has been reduced to 50-200 nm **(Fig. 4.4d)**. Nano-carbon particles disperse very well among nano-crystallites (**Fig. 4.4d, 4e**) and are embedded on the surfaces of particle agglomerates (**Fig. 4.4b, 4c**) possibly enhancing the short and long range conductivity within the composite electrode. The presence of nano-carbon on the rim of particles is also evident from the transmission electron microscopy images (**Fig. 4.4d, 4e, 4f**).

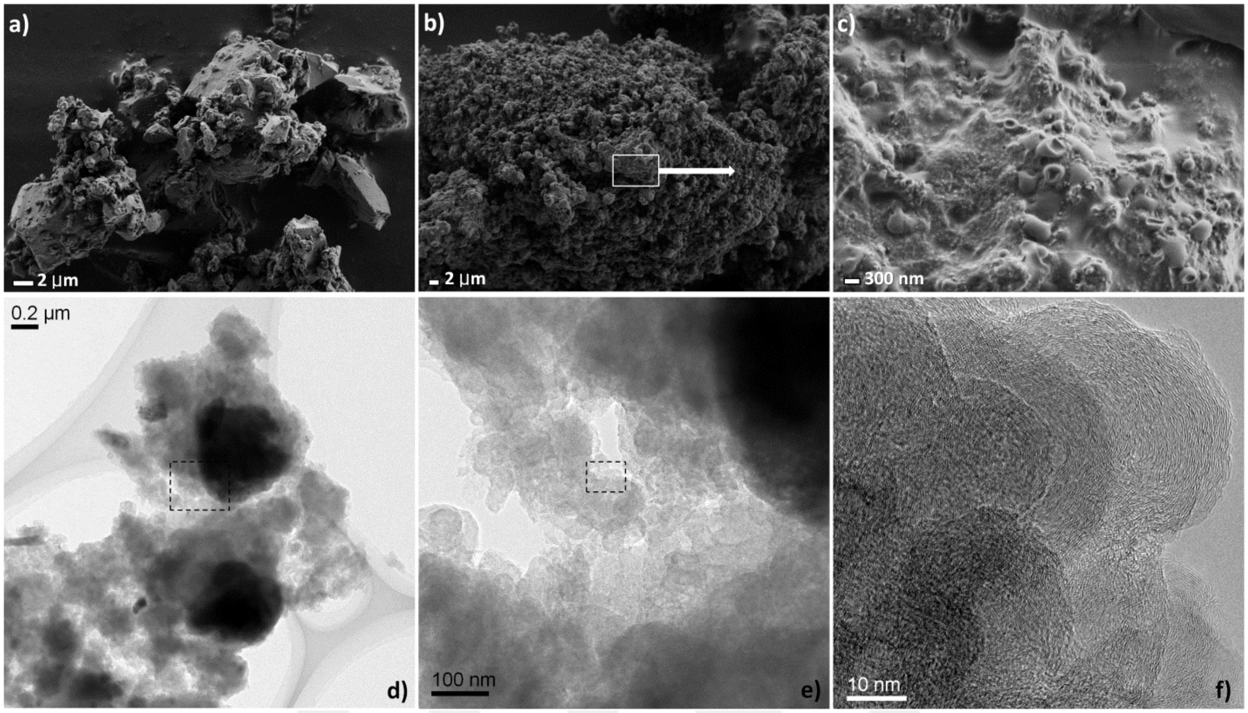

Figure 4.4 Scanning electron microscopy (SEM) images of a) crystalline $Li_7Mn(BO_3)_3$, b) nano-composite of $Li_7Mn(BO_3)_3$, c) magnified image of the marked region in (b) indicating carbon on the surface of particle agglomerates. Transmission electron microscopy (TEM) images of d) nano-composite of $Li_7Mn(BO_3)_3$, e) & f) zoomed in image of the marked region in (d) showing the carbon black coverage of nano-crystallites.

Like related borates, $Li_7Mn(BO_3)_3$ has an intrinsically low electronic conductivity (~10^{-11} S/cm) at room temperature (**Fig. 4.5**), which is also indicated by its colorless crystals. Consequently, pure $Li_7Mn(BO_3)_3$ is hardly electrochemically active with a first discharge capacity of ~ 11 mAh/g within a potential window of 4.7 – 1.7 V at 10 mA/g rate (**Fig. 4.6**). This low practical capacity with obvious polarization is traced back to the poor conductivity. In order to gain a reasonable electrochemical activity, the utilization of nano particles and conductive coatings are pivotal prerequisites, similar to the cases of $LiMPO_4$ and $LiMBO_3$ (M = Fe, Mn, Co), where such composites have been proven successful for activating the materials[124, 127, 132, 171, 173, 183, 185-186]. Quite frequently "nanoization" has been found to sufficiently increase the electrochemical performance of such poorly conducting materials.

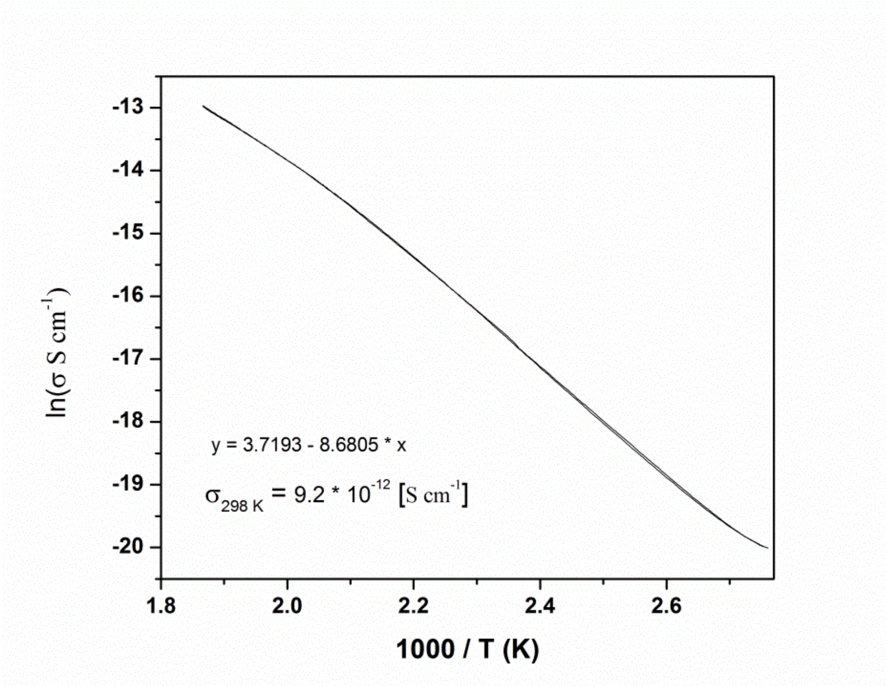

Figure 4.5 Conductivity vs. temperature (ln(σ) vs. 1000/T) for crystalline $Li_7Mn(BO_3)_3$.

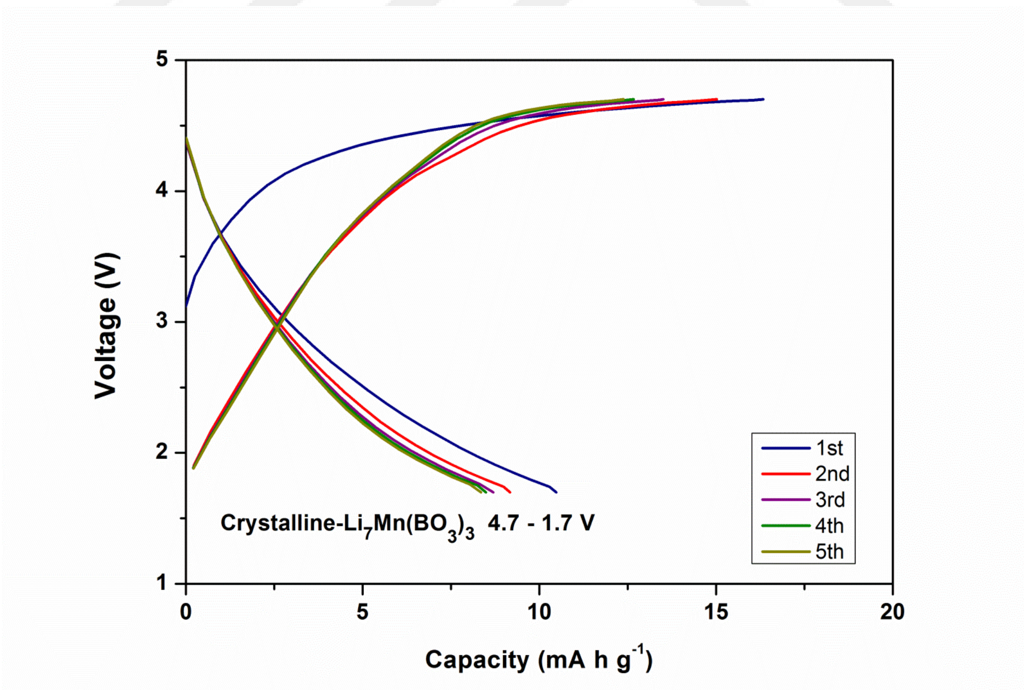

Figure 4.6 Charge/discharge curves of crystalline $Li_7Mn(BO_3)_3$ within 4.7 – 1.7 V at 10 mA/g rate for the first five cycles.

Comparable to related compounds, like $LiMnBO_3$ and $LiFePO_4$, the practical capacities were only reached, and the polarization was widely diminished after preparing and employing a nano-composite electrode of $Li_7Mn(BO_3)_3$. The first galvanostatic charge/discharge curve for the nano-composite is presented in **Figure 4.7a**. The cell was cycled between 4.7 and 1.7 V at a rate of 10 mA/g and it delivers a first charge capacity of ~ 280 mAh/g corresponding to a specific energy of ~ 1135 Wh kg^{-1} and an extraction of ca. 3 Li per formula unit. The first discharge capacity is ~ 154 mAh/g and charge/discharge capacities are reversible in subsequent cycles with a capacity of ~ 108 mAh/g at the 5^{th} cycle (**Fig. 4.7b**). At present, the average discharge capacity loss is approximately 2.5 % per cycle for the first 25 cycles (**Fig. 4.7c**). The cyclic voltammogram of the $Li_7Mn(BO_3)_3$ nano-composite is shown in **Figure 4.7d** for a potential window between 4.7 and 1.7 V at a scanning rate of 0.05 mV/s. Broad oxidation and reduction peaks with polarization appear. The oxidation region in the first cycle can be interpreted as three distinct effects at ~ 3.0 V and ~ 4.4 V, and a broad oxidation process from ~ 3.3 to 4.1 V. The reduction starts at ~ 4.3 V, and two reduction effects at ~ 3.6 V and ~ 2.2 V can be clearly seen. The voltammogram enters into a smooth behavior in the subsequent cycles, and only, the reduction effect at ~ 2.2 V remains distinct. The peak intensities for oxidation and reduction have decreased at each cycle which is consistent with the capacity loss in galvanostatic measurements; however, the peak positions approximately remain unchanged which may be interpreted as reversible lithiation/delithiation mechanisms.

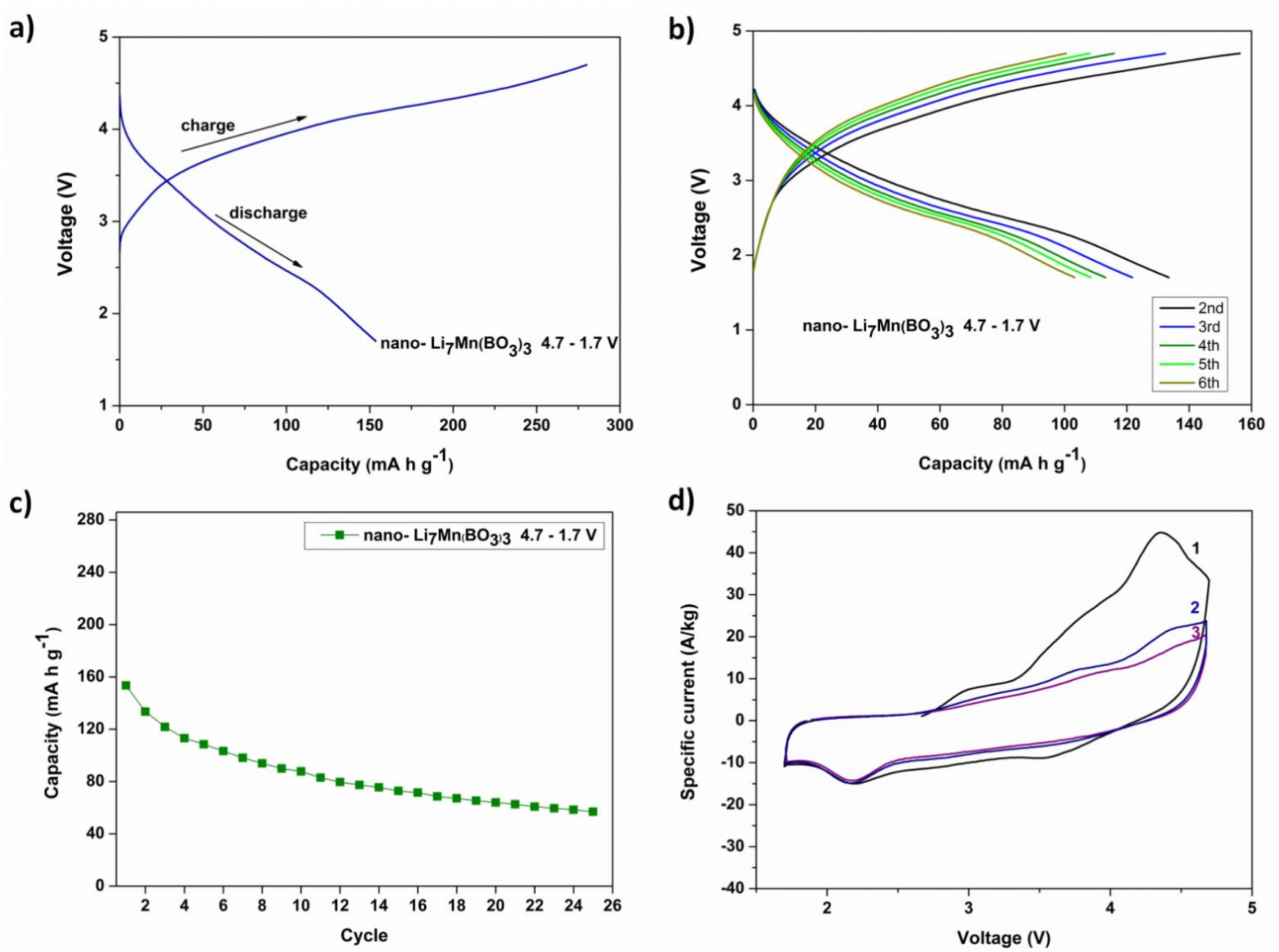

Figure 4.7 Electrochemical tests for the nano-composite of $Li_7Mn(BO_3)_3$: a) the first charge/discharge curve within 4.7 – 1.7 V at 10 mA/g rate, b) subsequent charge/discharge curves, c) discharge capacity vs. cycle number, d) cyclic voltammogram between 4.7 and 1.7 V at a scanning rate of 0.05 mV/s.

The reason for the irreversible capacity loss may have several sources like amorphization of the electrode material, the formation of electrochemically inactive phases, contact losses due to volume work and SEI formation. XRD powder patterns of the electrodes of the $Li_7Mn(BO_3)_3$ nano-composite, cycled within 4.7-1.7 V, in the charged and discharged states provide evidence for the amorphization during cycling as suggested by the broadening of diffraction peaks **(Fig.**

4.8). However, formation of new phases or shifts of diffraction peaks between charged and discharged states were not found, but only amorphous cycling products.

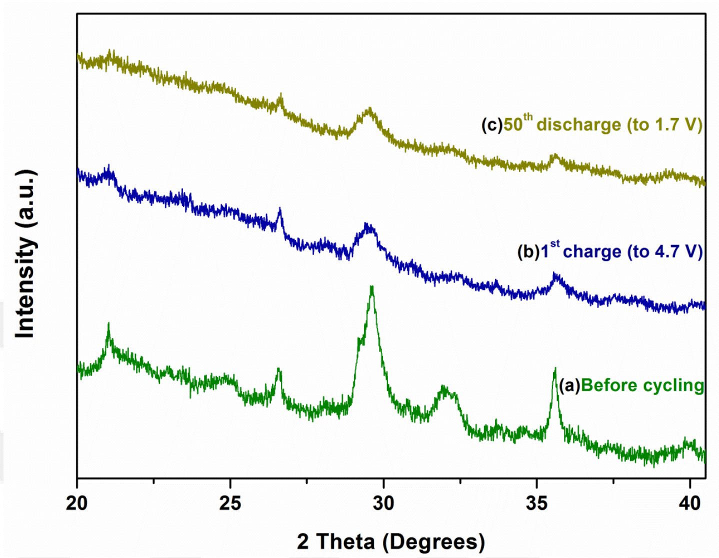

Figure 4.8 XRD powder patterns of the electrodes of $Li_7Mn(BO_3)_3$ nano-composite in the charged and discharged states: a) before cycling (green), b) after first charge to 4.7 V (blue), c) after fiftieth discharge to 1.7 V (dark yellow).

In order to further investigate the stability upon lithium extraction, different upper voltage limits have also been applied. Stopping the charge at 4.2 V instead of 4.7 V considerably improved the cycling stability of $Li_7Mn(BO_3)_3$ nano-composite, and the first charge capacity is ~ 181 mAh/g corresponding to an extraction of ca. 2 Li at a rate of 10 mA/g , and a capacity of ~ 117 mAh/g is obtained for discharging to 1.7 V at 5 mA/g rate (**Fig. 4.9a**). There is reversible cycling at the 25th cycle with a discharge capacity of ~ 73 mAh/g. More of the theoretical capacity is achievable in the first cycle for charging up to 5.3 V (a first charge capacity of ~ 366 mAh/g, corresponding to an extraction of ca. 4 Li (**Fig. 4.9b**)). However, the cycling stability is much poorer in comparison to galvanostatic measurements with the narrower potential windows of 4.7 - 1.7 V and 4.2 - 1.7 V (**Fig. 4.9c**).

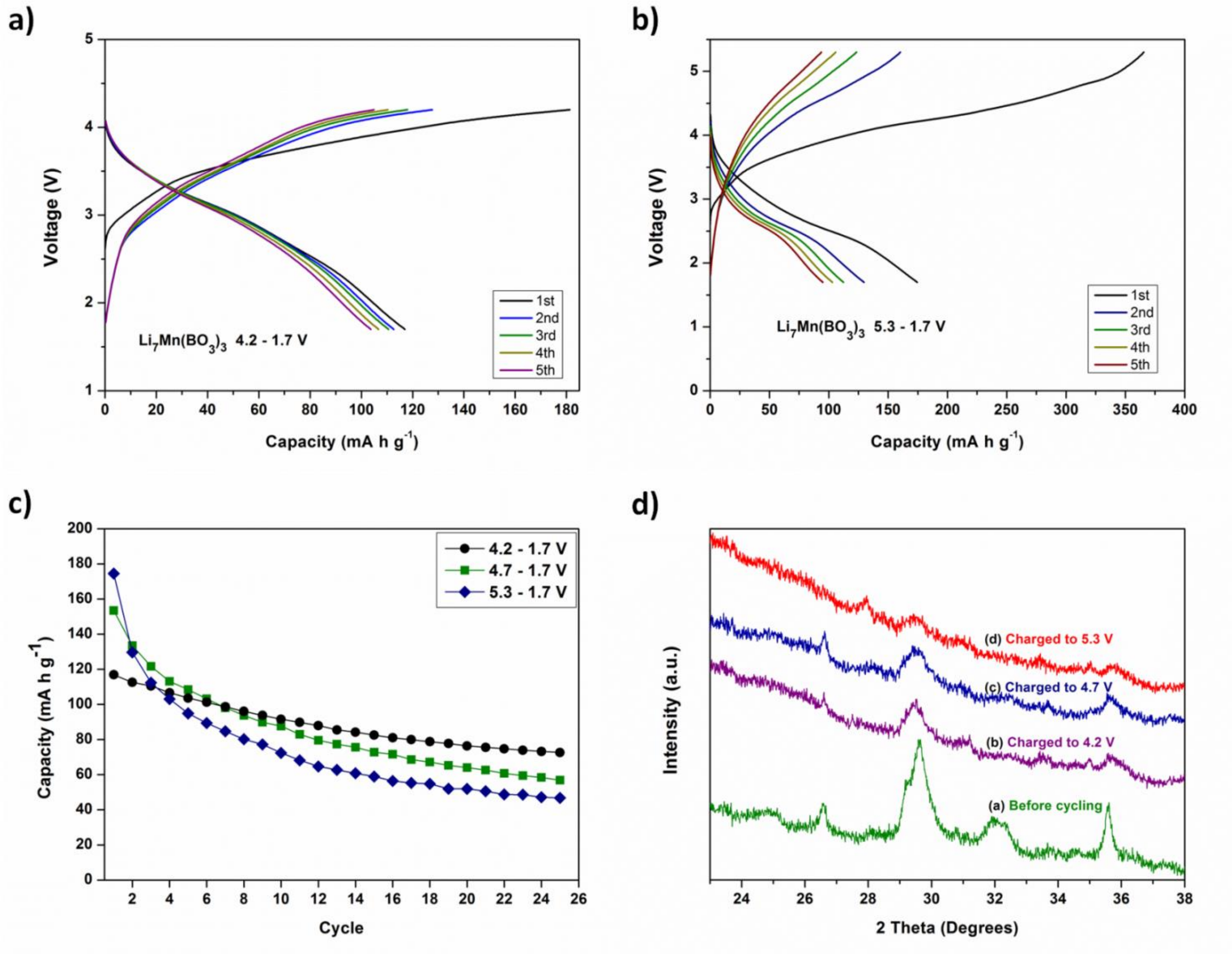

Figure 4.9 Investigations for the nano-composite of $Li_7Mn(BO_3)_3$ at different voltage ranges: a) the first five charge/discharge curves within 4.2 – 1.7 V at 10 mA/g charge rate, b) the first five charge/discharge curves within 5.3 – 1.7 V at 10 mA/g charge rate, c) discharge capacity vs. cycle number for designated voltage ranges , d) XRD powder patterns of the electrodes of $Li_7Mn(BO_3)_3$ nano-composite after the first charge: before cycling (green), charged to 4.2 V (purple), charged to 4.7 V (blue), charged to 5.3 V (red).

Better cycling stability for the narrow voltage window can be explained by a reduced stress with the extraction of less lithium from the structure that would result in relatively smaller amorphization of the electrode material. Furthermore, the phase stability and reversible formation of the original phase, $Li_7Mn(BO_3)_3$, during discharge might not be realized after more than 3 Li extraction, as high oxidation states of $Mn^{5,\ 6+}$ could become soluble, enter the electrolyte and cause in this way a loss of capacity. When the $Li_7Mn(BO_3)_3$ nano-composite is charged to 5.3 V, a new diffraction peak ($2\Theta = \sim 27.95^o$) not belonging to the original phase appears (**Fig. 4.9d**), and the main diffraction peaks get much broader or completely disappear showing increased amorphization and thus the breakdown of the phase. Also, the electrolyte stability might be an issue above 5.0 V; unwanted SEI formation and side reactions by the oxidation of electrolyte could be the causes of irreversible capacity losses and problematic cycling. In comparison, for XRD powder patterns of the electrodes charged to 4.2 and 4.7 V, no impurity peaks show up. Besides, no significant shifts of major diffraction peaks are observed but the amorphous part of the electrode material increases. Further investigations will be necessary to understand the detailed processes that appear during cycling. But, still, more sophisticated coating and network formation processes might be able to reduce irreversible losses and capacity fading. Also, a higher specific capacity may be achieved by employing even smaller nano-particles.

One could argue that the compound completely deteriorates during the first charge for upper voltage limits (> 4.2 V), however, in the meantime more and more conversion reactions have been reported, which work quite reversibly. Necessarily, conversion reactions must lead to first order phase transitions which destroy crystal structures. At low temperatures the formation of new structures cannot be expected but amorphous states should result. Ultimately, an amorphous electrode material is the final goal because that allows for optimal redox kinetics provided that reasonable conductivities can be guaranteed and dissolution in the electrolyte suppressed. Consequently, glassy materials have been targeted and investigated in this work as well.

$Li_{7-x}Mn_{1+y}(BO_3)_3$ ($0 \leq x \leq 2.86$ and $0 \leq y \leq 0.21$)

Annealing of pure $Li_7Mn(BO_3)_3$ at 850 °C (40 hours under CO atmosphere) leads to the decomposition of this phase, and another new lithium rich phase of manganese borate is obtained (**Fig. 4.10**).

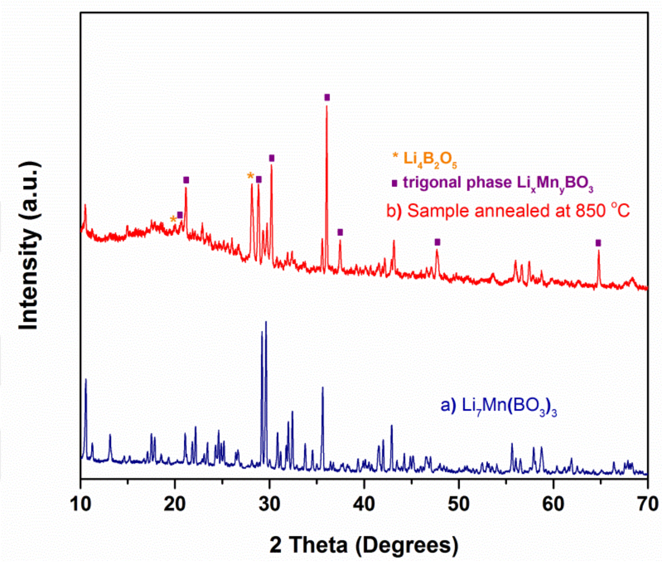

Figure 4.10 XRD powder pattern of a pure $Li_7Mn(BO_3)_3$ sample annealed at 850 °C under CO for 40 hours indicating the decomposition and the formation of a new phase.

This new phase is also yielded by a reaction of Li_2CO_3, MnO and H_3BO_3 in stoichiometric amounts comparable to the synthesis of $Li_7Mn(BO_3)_3$ with a similar procedure, except the annealing temperature is increased from 700 °C to 850 °C. The colourless crystals of the new compound, $Li_{4.14}Mn_{1.21}(BO_3)_3$, are obtained at the end of the process along with impurity ($Li_4B_2O_5$ and MnO) (**Fig. 4.11**). Suitably sized single crystals were selected, and a data set was obtained on a Bruker Smart Platform diffractometer equipped with a CCD-detector. The crystals of this compound turned out to be multiple twins, too. Further details for the solution, refinement and crystallographic data including bond lengths, positional and displacement parameters are given in the **Appendix** (p. 184).

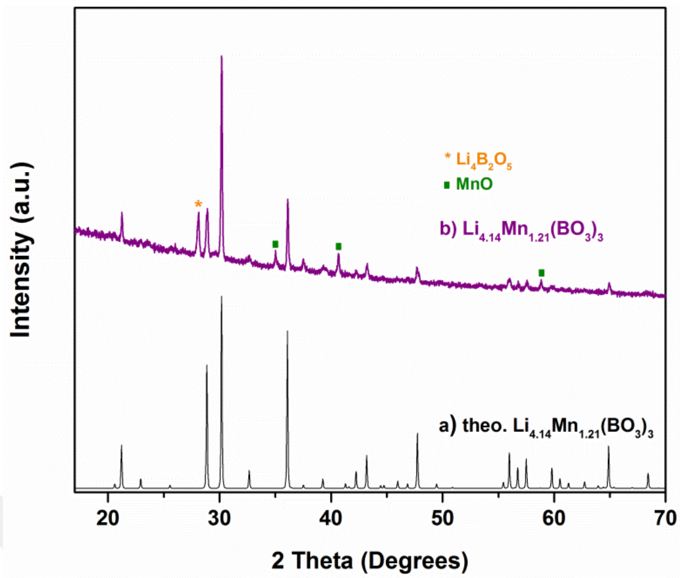

Figure 4.11 XRD powder patterns for $Li_{4.14}Mn_{1.21}(BO_3)_3$: a) theoretical, b) solid-state reaction product.

The crystal structure of $Li_{4.14}Mn_{1.21}(BO_3)_3$ which is distinctly different from $Li_7Mn(BO_3)_3$ is shown in **Figure 4.12**.

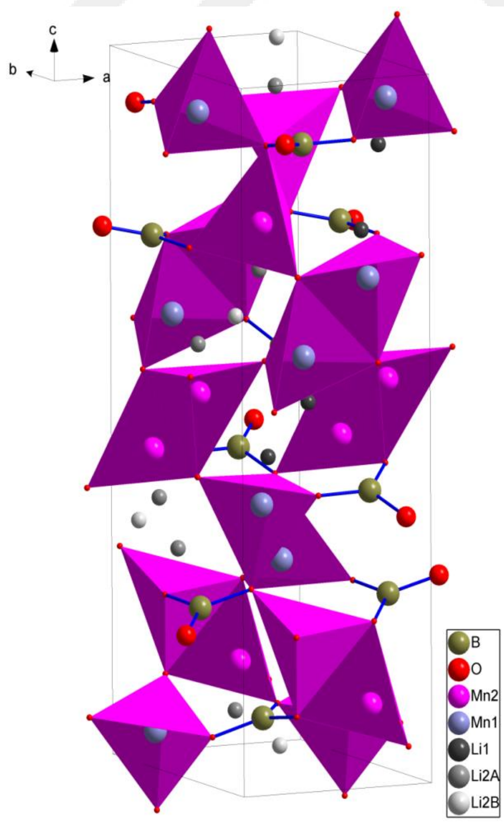

Figure 4.12 The crystal structure of $Li_{4.14}Mn_{1.21}(BO_3)_3$ (skew [010] wiew).

The new lithium manganese borate compound crystallizes in the trigonal space group $P3_112$ (No.151) (a = 4.9741(3) Å, c = 17.7511(19) Å). There is disorder on all metal sites and mixed occupation. Similar to the structure of $Li_7Mn(BO_3)_3$, manganese atoms are in tetrahedral coordination. MnO_4 tetrahedra and BO_3^{3-} units are also important structural features for $Li_{4.14}Mn_{1.21}(BO_3)_3$. Two tetrahedra formed by crystallographically different Mn atoms are connected to each other by corner sharing, whereas the tetrahedra of the same sites are linked via edge sharing. BO_3^{3-} units connect MnO_4 tetrahedra along the c-axis and the chains of polyhedra are formed along this direction. The pseudo helical chains leave voids in the structure that can be seen in a view along [001] (**Fig. 4.13**).

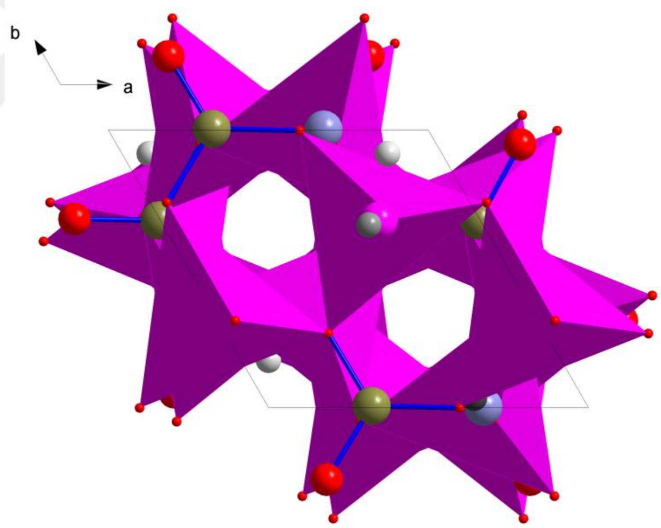

Figure 4.13 View of the crystal structure of $Li_{4.14}Mn_{1.21}(BO_3)_3$ along the [001]-direction.

It should be noted here that due to twinning, disorder and Li-ion mobility a unique and precise determination of the composition is not possible. Especially the lithium content is associated with a fairly large standard deviation. Therefore, further investigations in order to explore phase width and structure variations are still necessary. It should be also noted that lithium borates, manganese oxides, and also carbon, originating from the reaction crucible, are always present in the reaction products, preventing reliable information from other characterization techniques. Nevertheless, the electrochemical properties of $Li_{4.14}Mn_{1.21}(BO_3)_3$ are still worth investigating because of a theoretical capacity of ~ 354 mAh/g for ~ 3.57 Li exchange per formula unit.

A working electrode of this new compound was prepared with ~ (70 wt-%) active material, (20 wt-%) conductive carbon (Super P® Timcal) and (10 wt-%) PVDF. $Li_{4.14}Mn_{1.21}(BO_3)_3$ crystals were tried to be separated from impurities under an optical microscope, but the presence of lithium borates in the active material part could not be totally prevented due to the similar appearance of colorless compounds. Cells constructed with such electrodes were tested in a galvanostatic mode between 4.7 V and 1.7 V at a rate of 10 mA/g.

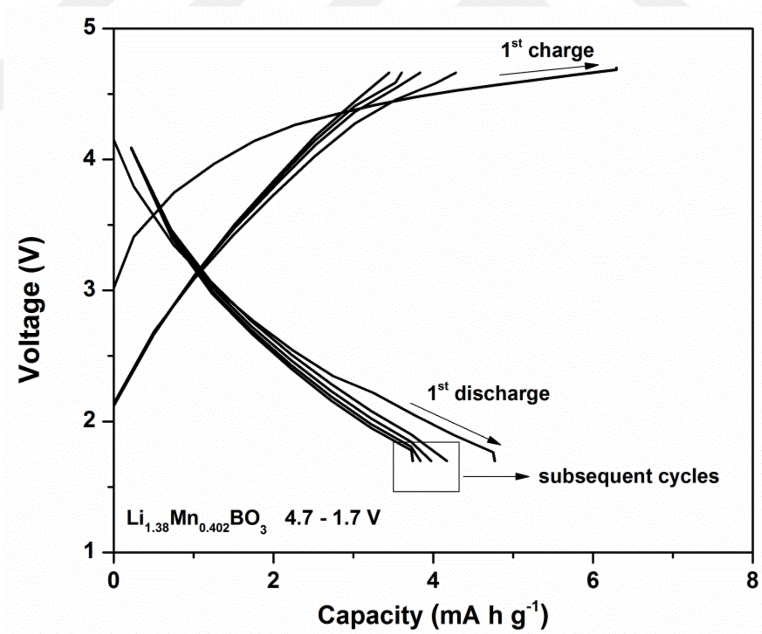

Figure 4.14 The first five charge/discharge curves of $Li_{4.14}Mn_{1.21}(BO_3)_3$ within 4.7 – 1.7 V at 10 mA/g rate.

The first five charge/discharge curves of $Li_{4.14}Mn_{1.21}(BO_3)_3$ are illustrated in **Figure 4.14.** Noisy charge/discharge curves reaching very limited capacities, even less than those of the other studied non-modified borate compounds, are obtained. For the first charge and discharge capacities, only ~ 6 mAh/g and ~ 5 mAh/g were achieved, respectively that might be originating from side reactions rather than an extraction/insertion of lithium into the title compound. These values are even lower than those obtained for micro-crystalline $Li_7Mn(BO_3)_3$.

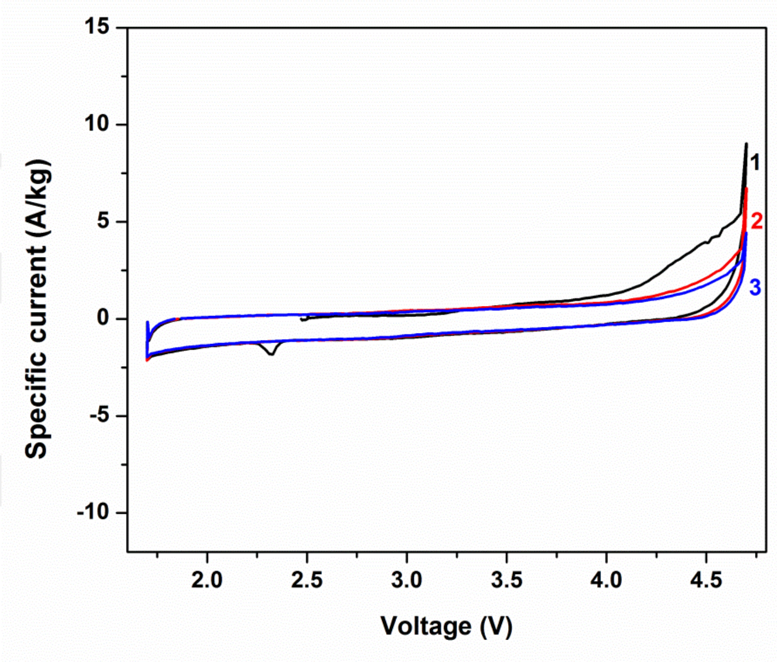

Figure 4.15 The cyclic voltammogram of $Li_{4.14}Mn_{1.21}(BO_3)_3$ between 4.7 and 1.7 V at a scanning rate of 0.05 mV/s.

Cyclic voltammetry tests were also done, and the cyclic voltammogram of $Li_{4.14}Mn_{1.21}(BO_3)_3$ is displayed in **Figure 4.15**. No well-defined oxidation-reduction processes that would indicate delithiation/lithiation of the compound are seen in the potential window, 4.7 – 1.7 V at a scanning rate of 0.05 mV/s. Hence, under such conditions no reasonable electrochemical activity can be evidenced for $Li_{4.14}Mn_{1.21}(BO_3)_3$ as a cathode material. Similar to the cases of $LiMnBO_3$, $LiCoBO_3$ and $Li_7Mn(BO_3)_3$, which were effectively activated through the utilization of nano-particles and conductive coatings, $Li_{4.14}Mn_{1.21}(BO_3)_3$ should also show a reasonable electrochemical activity by circumventing the problems related to poor kinetics. Up to now, the phase pure compound cannot be synthesized and so the impurities and side phases are expected to bring additional issues, which make an appropriate analysis difficult, even if the nano-conductive composite formation would be achieved. Consequently, the principal focus of future research on $Li_{4.14}Mn_{1.21}(BO_3)_3$ should be the determination of the compositional phase width by synthesizing a pure phase material.

4.4. Conclusion

Novel lithium rich manganese borate compounds have been attained, and their electrochemical properties as cathode materials for Li-ion batteries have been investigated. $Li_7Mn(BO_3)_3$ exhibits exclusively tetrahedral Mn^{2+} coordination, being an exceptional case among other related oxides. Both $Li_7Mn(BO_3)_3$ and $Li_{4.14}Mn_{1.21}(BO_3)_3$ comprise a network of MnO_4 tetrahedra and BO_3^{3-} units as characteristic structural features. No reasonable electrochemical activity could be claimed for $Li_{4.14}Mn_{1.21}(BO_3)_3$, as the crystalline material delivered very low first charge and discharge capacities of only ~ 6 mAh/g and ~ 5 mAh/g, respectively. While micron sized crystals of $Li_7Mn(BO_3)_3$ yielded a negligible first discharge capacity of ~ 11 mAh/g, a high first charge capacity of ~ 280 mAh/g (extraction of ca. 3 Li) and a first discharge capacity of ~ 154 mAh/g were obtained after nano-sizing and nano-carbon composite formation. The nano-composite electrode cycles reversibly, but the cycling stability is an issue that should get further attention in future. Better electrochemical performance and cycling stability might be realized by exploring new synthetic approaches that may give smaller nano-particles, optimizing conductive coatings of particles, and investigating the structural changes and stabilities during lithiation/delithiation for the new electrode material. It should be noted that many of today's attractive cathode oxides went through such stages of research taking decades in past, e.g. $LiFePO_4$ and $Li(Mn,Co,Ni)O_2$, but are in application these days.

Chapter 5

Vanadate – Borate Glasses and Glass Ceramics as High Capacity Cathode Materials for Rechargeable Lithium Batteries

5.1 Introduction

Layered oxides, vanadium pentoxide (V_2O_5)[189] and molybdenum trioxide (MoO_3)[190], are one of the earliest studied materials as high capacity cathode materials for lithium batteries. MoO_3 could intercalate 1.5 Li per formula unit without a major change in the main structure, but the low average voltage and slow kinetics in this system make it unfavorable as a cathode material[190-192]. On the other hand, due to the many stable oxidation states of vanadium, vanadate-based electrodes are interesting alternatives for current cathode materials. Consequently, there has been extensive research on vanadates as a cathode materials synthesized by various methods resulting different morphologies, compositions and properties. The research on vanadium oxides may be divided into two branches as vanadium pentoxide gels and crystalline vanadium oxides.

Vanadium pentoxide gels are usually synthesized by condensation from vanadate (V) solutions with or without redox reactions and can be described by the general formula of $H_xV_4O_{10}.nH_2O$[193-198]. The structure of gels are claimed to contain a double layer structure formed by VO_6 octahedra[199], different than the single layered pyramidal of V_2O_5. Depending on the drying method and on resulting morphology the gels are further classified as xerogels and aerogels[194, 196-197]. Xerogels are obtained by conventional evaporation, and they usually have higher water contents but lower stacking distances and smaller surface areas compared to aerogels[197-198, 200-201]. By keeping the parent gel structure via drying under supercritical conditions, aerogels with higher surface areas and better electrochemical performances are achieved[193-196]. With the use of thin film electrodes and slow rates, the insertion of up to 5.8 and 4 Li per formula unit of V_2O_5 were demonstrated for aerogels[195, 202] and xerogels[196-197, 200-201], respectively. For the lithiation mechanism of the xerogel, by a steady decrease of the voltage with lithium insertion in the discharge curve and the reduction of V^{5+} to lower oxidation states, a single phase process was claimed[195, 198]. However, the reactions of aerogels with lithium as well as with other polyvalent (Mg^{2+}, Al^{3+}) cations are not very well understood, as many researchers assert that the oxidation state of vanadium does not change accordingly to the amount of guest cations and obtained capacities[198, 202-204]. The high amount of lithium insertion that was stated for such thin film samples decreases to ca. 2-3 Li per V_2O_5, when standard electrodes and higher rates are used[200, 205-206]. The capacity fading during cycling is a big obstacle for the practical use of vanadium pentoxide gels[195-196, 200, 206]. This problem occurs in a similar way to other vanadium oxide systems that will be discussed later.

Crystalline vanadium oxides, such as V_2O_5 ($Li_xV_2O_5$)[207-210], LiV_3O_8[211-212], δ-$M_xV_4O_{10}$[213], V_6O_{13}[214-215] and VO_2[216-217], synthesized via various methods have been extensively investigated as positive electrode materials for lithium batteries, and the literature is legion. Here, we will mainly focus on V_2O_5 ($Li_xV_2O_5$). The crystal structure of V_2O_5 is shown in **Figure 5.1**.

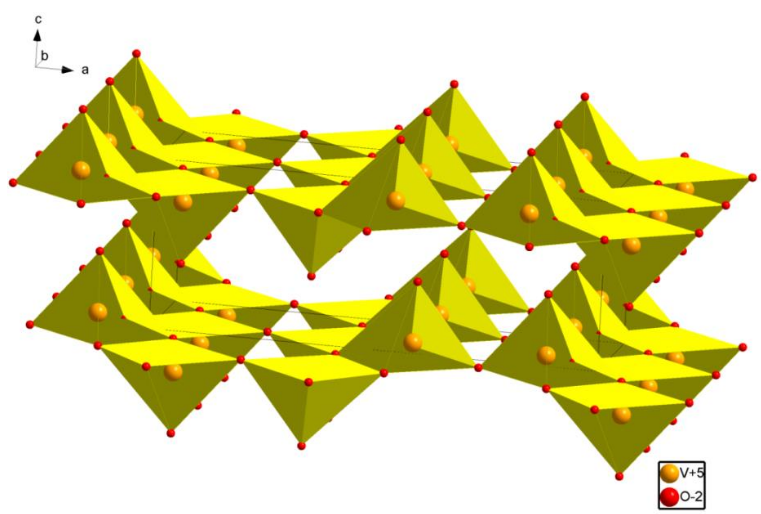

Figure 5.1 Crystal structure of V_2O_5: skew [010] view showing VO_5 layers.

VO_5 square pyramids are present with four long V - O bonds forming the basal plane and a shorter bond to the upper corner representing the vanadyl group. VO_5 square pyramids extend along b-axis via edge and corner sharing. Such polyhedra chains with alternating up and down directed tips are connected to each other by corner sharing and extend to the layered structure of V_2O_5. On insertion smaller amounts of lithium into V_2O_5, several structural transitions occur, but VO_5 square pyramids and polyhedra chains remain as characteristic structural figures[210].

V_2O_5 transforms into several $Li_xV_2O_5$ phases depending on the amount of lithium inserted, α- ($x < 0.01$), ε- ($0.35 < x < 0.7$), δ- ($x = 1$), γ- ($1 < x < 2$) and ω- ($x = 3$)[210]. The phases that are formed up to the intercalation of one Li per formula unit of V_2O_5 (α-, ε-, δ-$Li_xV_2O_5$) are not significantly different from the initial structure with only a puckering of VO_5 layers. They can be cycled in a reversible way with a theoretical capacity of ~ 147 mAh/g. An irreversible phase transformation arises with insertion of more than 0.5 Li per V, and γ-$Li_xV_2O_5$ is formed that can be cycled without structural transformation for $0 \leq x \leq 2$ and yielding a theoretical capacity of ~ 294 mAh/g.

Upon deep discharge to voltages below 1.9 V, another irreversible transition occurs to ω-$Li_xV_2O_5$ at insertion of 3 Li[210]. With this, a large theoretical capacity of ~ 440 mAh/g is reached that is almost three times larger than that of many conventional cathode materials. ω-$Li_xV_2O_5$ cycles as a single solid solution in subsequent charge/discharge curves with an irreversible capacity loss in the first charge since all of the inserted lithium atoms cannot be extracted from the host structure (~ 0.4 Li per formula unit of $Li_3V_2O_5$ remain unexchanged)[210]. The capacity retention is again a huge problem as half of the capacity vanishes within the first ten cycles for the unaltered V_2O_5 even at very low current rates (10 mA/g)[218].

Bulk V_2O_5 is also considered to be kinetically limited by low ionic and electronic conductivity as it was shown that the increase of current density leads to markedly reduced practical capacities[218-219]. In order to address these problems, many different approaches have been tried by various research groups. Whittingham et al. employed nanorods of V_2O_5 that were synthesized by annealing xerogels under O_2 atmosphere, and obtained a stable capacity at ca. 300 mAh/g but only for the first 10 cycles[220-221]. The enhanced performance of this material was attributed mainly to high surface area, shorter Li diffusion lengths and facilitation of strain relaxation[220-221]. Porous monodisperse V_2O_5 microspheres were tested by Wang et al. in the voltage window of 2.05 – 4.0 V, and an initial discharge capacity of 276 mAh/g was realized with a capacity fading rate of 0.38 % per cycle[222]. Composite electrodes with carbon and conducting polymers were also tried. V_2O_5/polypyrrole-composite cathode prepared by Kim et al. delivered an initial discharge capacity of ~ 425 mAh/g that decreased to ~ 250 mAh/g during the 10th cycle[223]. For a nano-V_2O_5/PEDOT composite film electrode, Song et al. reported specific capacities of ~ 262, 239, 186 and 141 mAh/g at 0.1C, 1C, 10C and 100C rates within 4.0 – 1.8 V, respectively[224]. Numerous other investigations employing nano-particles and composite electrodes can be found in the literature[225-228].

Irreversible phase transformations and volume work leading to amorphization as well as loss of low valence state metal ions into the electrolyte accompany most high capacity materials during cycling. This is also exemplified in chapters 2 and 4 for the manganese-based electrode materials. That is why we have here chosen redox-active glasses and glass ceramics as targets for more stable cathode materials. There are a few research reports on V_2O_5 – P_2O_5 glasses as cathode materials[229-231]. P_2O_5 is a classical glass network former that assembles cross-linked macromolecular chains enhancing glass formation. Glasses are solids lacking a long range atomic order with translational symmetry that goes into a molten state by heating above the glass transition temperature. Sakurai et al. reported a first discharge capacity of 500 mAh/g within 4.0 – 1.0 V for the V_2O_5 – P_2O_5 glass cathode[231]. The cathode material functions as a single phase without any visible plateau, but the capacity on the first charge already drops to 350 mAh/g, and cycling properties are not very remarkable for the large potential window. It has been also suggested that the source of irreversible capacity obtained in the first discharge could be the formation of Li_3PO_4, which is inactive and cannot be further cycled[232]. Nevertheless, the well-known hygroscopic nature of P_2O_5 also makes this system unattractive for practical applications. Even a small amount (few ppm) of water was reported to change the physical properties of phosphate glasses markedly[233-237].

We have chosen borate-based glasses of V_2O_5 in order to explore vitreous redox-active systems pursuing the goal of utilizing many oxidation states of vanadium to the highest possible extent and fixing the vanadate group by a network former to enhance cycling stability.

For borate based binary, ternary, quaternary V_2O_5 glass systems, there had been research on vibrational, mechanical, thermal and electrical properties[238-243]. The use of V_2O_5 – B_2O_3 glass as an electrode material for secondary batteries is mentioned in a few older patents grosso modo with other glasses[230, 244], but no electrochemical study exploring their actual utilization exists in literature, yet. Furthermore, to the best of our knowledge, there has been no research on V_2O_5 – $LiBO_2$ glasses (Li_2O – B_2O_3 – V_2O_5 system) and their composites as positive electrode materials, so far. Here, we report on glass ceramics obtained in the V_2O_5 – B_2O_3 system, V_2O_5 – $LiBO_2$ glasses and their composites as cathode materials for rechargeable lithium batteries for the first time. The synthesis method of glasses and glass ceramics is very simple and cost efficient.

Comparable cathode materials delivering similar capacities and specific energies are only obtainable by laborious synthetic methods and using expensive techniques and educts.

5.2 Experimental Section

5.2.1 Synthesis

95:5, 90:10, 85:15, 80:20, 75:25, 70:30 wt-% V_2O_5 : B_2O_3 glass ceramics are obtained with a glass forming procedure. V_2O_5 (99.2 %, Alfa Aesar) and B_2O_3 (99.9 % Alfa Aesar) analytical pure grade powders in corresponding amounts (e.g. 4g V_2O_5 and 1g B_2O_3 for 80:20 wt-% V_2O_5 : B_2O_3 glass ceramics) are thoroughly mixed and ground in an agate mortar, and thereafter, the mixtures are placed in Pt crucibles. The crucibles are heated in a muffle furnace at 850-900 ^oC, and homogeneous melts are obtained after 1 hour of heat treatment. Then, melts are quenched in air between Cu plates yielding V_2O_5 – B_2O_3 glass ceramics. The ceramics are pulverized in a mortar in order to perform analytical measurements and to prepare electrode composites. A typical product is shown in **Figure 5.2a**.

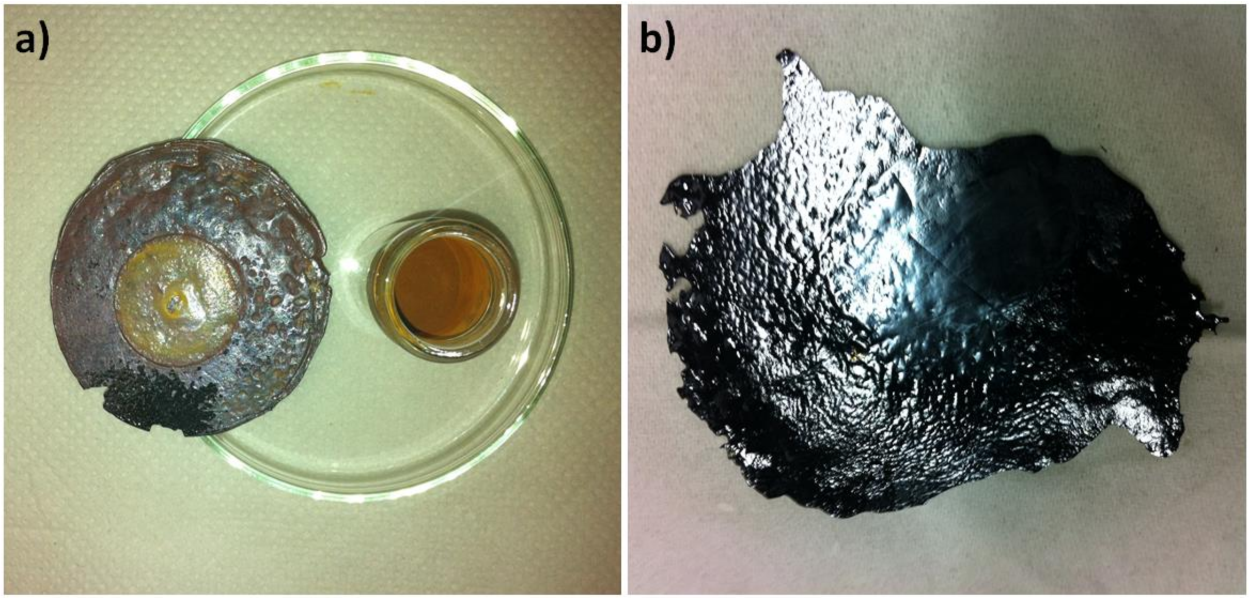

Figure 5.2: Typical synthetic products: a) V_2O_5 – B_2O_3 glass ceramics b) V_2O_5 – $LiBO_2$ glasses.

Reduced graphite oxide (RGO) and Super P® composite electrodes of 85:15 wt-% V_2O_5 : B_2O_3 glass ceramics are prepared by ball-milling the active material with ~ 33.3 wt-% graphite oxide and ~ 25 wt-% Super P® Li Timcal, respectively. For the RGO composite, the ball-milled product is further treated by heating at 200 ^oC for 8 hours under nitrogen in order to reduce graphite oxide.

With the above described synthesis procedure 80-20 wt-% V_2O_5 – $LiBO_2$ and 80-5-15 wt-% V_2O_5 – NiO – $LiBO_2$ glasses are synthesized by quenching from 900 ^oC to room temperature. A typical glass disk is shown in **Figure 5.2b**. The produced disks are pulverized in an agate mortar for further characterizations. The composites with reduced graphite oxide are also similarly produced by ball-milling ~ 66.6 wt-% active material with ~ 33.3 wt-% graphite oxide that is followed by the heat treatment for the reduction. The carbon contents of the RGO composites are found to be ~ 18 wt-% by combustion-infrared spectroscopy analysis (LECO instruments, ETH LOC Micro-Laboratory).

5.2.2 Characterization

Differential thermal analysis (DTA) was performed with a NETZSCH STA 409 C/CD. Samples were planted in Pt crucibles, and heating/cooling curves between room temperature and 930 ^oC were obtained under air flow.

Powder X-ray diffraction patterns of the samples were acquired with a STOE Stadi P diffractometer equipped with a germanium monochromator and $CuK_{\alpha 1}$ radiation (40 kV, 35 mA).

Magnetic measurements were carried out with a SQUID magnetometer (MPMS 5S, Quantum Design) between 300 and 2 K under constant field strength.

FT-IR spectra were recorded with a Thermo Scientific Nicolet iS10 Smart iTR.

Scanning electron microscopy (SEM) analysis of samples were carried out with a Zeiss Gemini 1530 operated at 1 kV. (Scanning) transmission electron microscopy ((S) TEM) analysis was performed with a CM30ST (FEI; LaB_6 cathode) and a Tecnai F30 microscope (FEI; field emission gun), both operated at 300 kV, point resolution of ~ 2Å. The F30 microscope is equipped with a high-angle annular dark field detector (HAADF STEM), an energy-dispersive X-ray spectrometer (EDXS; EDAX) and an electron energy-loss spectrometer (EELS; Gatan).

5.2.3 Electrochemical tests

For electrode fabrication of composite materials with RGO, no additional carbon black was used, and (90 wt-%) composite powder was thoroughly mixed with (10 wt-%) PVDF binder in an agate mortar. The mixture was ultrasonically dispersed in 1:4 toluene:THF solution. The resulting slurry was cast on Ti current collectors and dried at 80 ^{o}C under vacuum. The dried electrodes had approximately 5 mg electrochemically active material. The plain electrodes without any carbon resulting from the composite were constructed in the same way, but the initial powder mixture was prepared with (70 wt-%) active material, (20 wt-%) conductive carbon (Super P® Li Timcal) and (10 wt-%) PVDF binder. Li metal anodes were prepared from a 0.75 mm-thick ribbon (Aldrich), and 1M solution of $LiPF_6$ in EC:DMC (1:1) (Merck, LP-30 SelectiLyte™) served as the electrolyte. Swagelok type cells were built in an Ar filled glove-box. Galvanostatic measurements were performed in the voltage range of 1.5 – 4.0 V at a usual rate of 50 mA/g. Rate capability tests were done with ~ 10 cycle blocks at varying rates 50, 100, 200, 400 mA/g, and then again 50 mA/g; the rates were successively altered after a charging section. Cyclic voltammetry studies were carried out at a sweep rate of 0.1 mV/s within 1.5 – 4.0 V; first cycles were made up from discharge to 1.5 V.

5.3 Results & Discussion

5.3.1 V_2O_5 – B_2O_3 glass ceramics

Glass ceramics are acquired by a controlled crystallization from glass forming melts. They are composed of nano-crystalline phases embedded in an amorphous matrix. In our samples, physical and electrochemical properties of the glass ceramics are predominantly due to the crystalline phase, its composition and its crystallite size.

Here, glass ceramics of V_2O_5 were prepared with the network former, B_2O_3. XRD powder patterns of 95:5, 90:10, 85:15, 80:20, 75:25, 70:30 wt-% V_2O_5 : B_2O_3 glass ceramics that were produced by melting the precursor mixtures at 850 ^oC, and then quenching the melts to room temperature are illustrated in **Figure 5.3**. The only crystalline phase that can be observed is V_2O_5 (Scherbinaite), and a high background indicates the presence of the amorphous part. The diffraction peaks for V_2O_5 are broadened in V_2O_5 – B_2O_3 glass ceramics compared to pure V_2O_5, which was also melted at 850 ^oC and quenched in air for reasons of comparison.

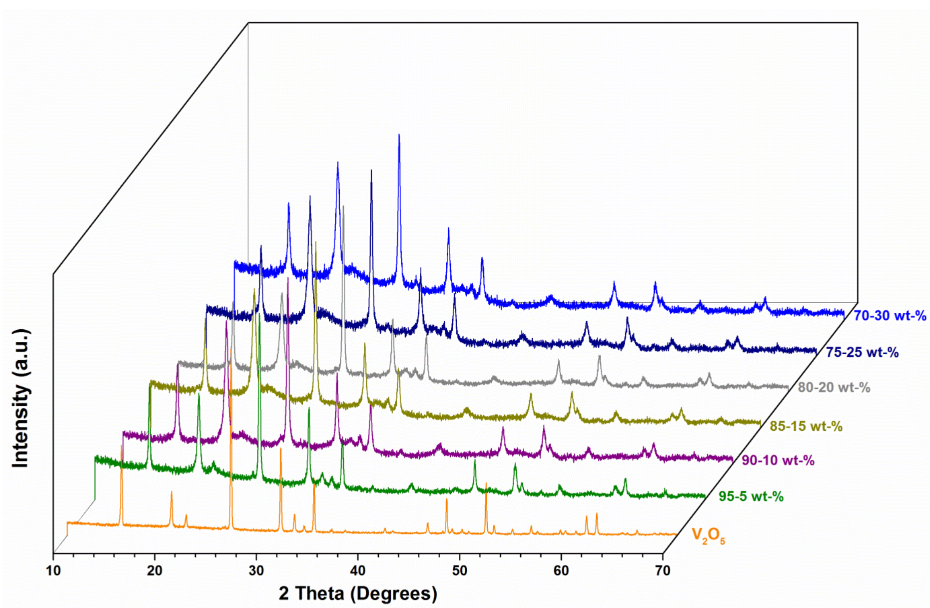

Figure 5.3: XRD powder patterns of 95:5, 90:10, 85:15, 80:20, 75:25, 70:30 wt-% V_2O_5 : B_2O_3 glass ceramics.

The average crystallite sizes of V_2O_5 in the series were estimated with the Scherrer equation: crystallite size = 0.9 λ / ($\beta\cos\theta$), where λ is the wavelength of incident X-rays, β is the full width at the half maximum of the (001) reflection and θ is the Bragg angle. The values are given in **Table 5.1**. However, it should be noted that these results do not deliver precise values, as the Scherrer formula considers only one diffraction peak, and the effect of strain broadening is not taken into account. Therefore, they are not exact, but show the trend well within the series.

Table 5.1: The average V_2O_5 crystallite size for V_2O_5 – B_2O_3 glass ceramics

wt-% B_2O_3	V_2O_5 size (nm)
30	26.9
25	29.9
20	29.9
15	28.8
10	33.6
5	53.8

It can be seen that B_2O_3 amounts of $\geq$ 10 wt-% result in smaller V_2O_5 crystallites. The glass ceramics with 5 wt-% B_2O_3 has significantly larger but still smaller V_2O_5 crystallites compared to quenched pure V_2O_5. The smaller size of V_2O_5 particles in the glass ceramics can be explained by the slower growth kinetics in the amorphous B_2O_3 matrix preventing the growth of V_2O_5 crystallites into larger particles.

Electron microscopy investigations also proved the presence of V_2O_5 nano-crystallites and amorphous regions. **Figure 5.4** displays scanning electron microscopy (SEM) images of 85 wt-% V_2O_5 – 15 wt-% B_2O_3 glass ceramics that are representative for the series. After grinding, the material mostly appears as in form of micron-sized particles with a porous morphology at times, and an unspecific geometry (**Fig. 5.4a)**. The porous structure of some particles is clearly seen in **Figure 5.4b**. The presence of some platelet crystals is also visible. These are thought to form and grow larger at slower crystallization, when the quenching rate was not high enough (**Fig. 5.4c & 4d)**.

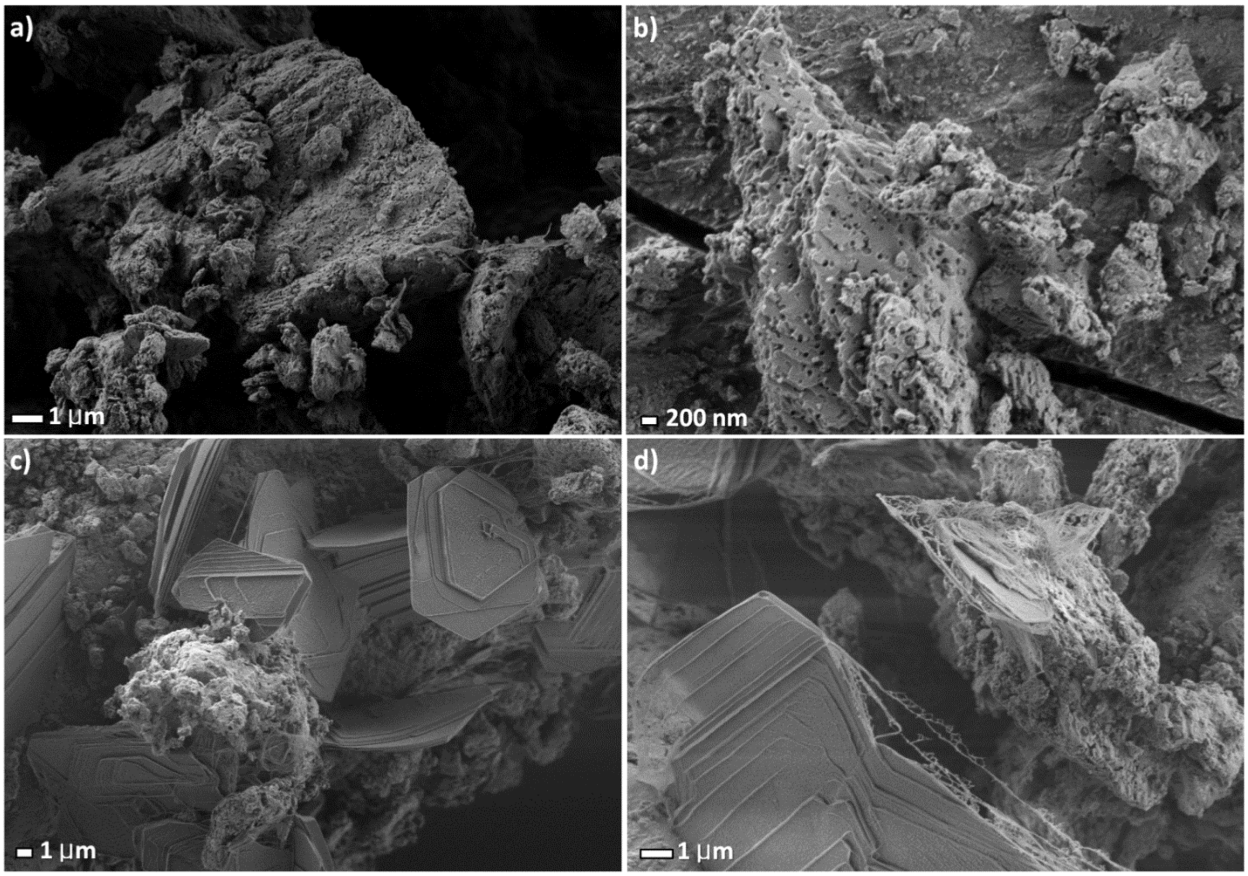

Figure 5.4: Scanning electron microscopy (SEM) images of 85:15 wt-% V_2O_5 : B_2O_3 glass ceramics displaying a) a general view of particles, b) the porous structure, c) & d) the larger platelet crystals.

Transmission electron microscopy images (TEM) of 85:15 wt-% V_2O_5 : B_2O_3 glass ceramics are shown in **Figures 5.5 and 5.6**. Micron-sized particle agglomerates are made of crystalline and amorphous regions, and the agglomerates look like micron-sized sponges (**Fig. 5.5a & 5.5b**). The crystalline part has two constituents that are V_2O_5 nano-crystallites embedded in the amorphous matrix and separated V_2O_5 nano-crystallites. Embedded nano-crystallites are smaller in dimension, and their sizes, ca. 20 – 40nm, are close to the value estimated by the broadening of diffraction peaks (**Fig. 5.5c**). A separate nano-platelet with dimensions of ~ 50 nm width and ~ 230 nm length is displayed in **Figure 5.5a** at the bottom of the agglomerate. Lattice fringes corresponding to the (001) planes of V_2O_5 (spacing of ~ 4.4 Å) can be observed in the magnified regions (**Fig. 5.5c & 5.5d**). An amorphous part of the glass ceramics is depicted in **Figure 5.6** more noticeably. Pores in the amorphous region are clearly visible, and this part of the material is found to be mesoporous with pore sizes in the range of ~ 50 nm.

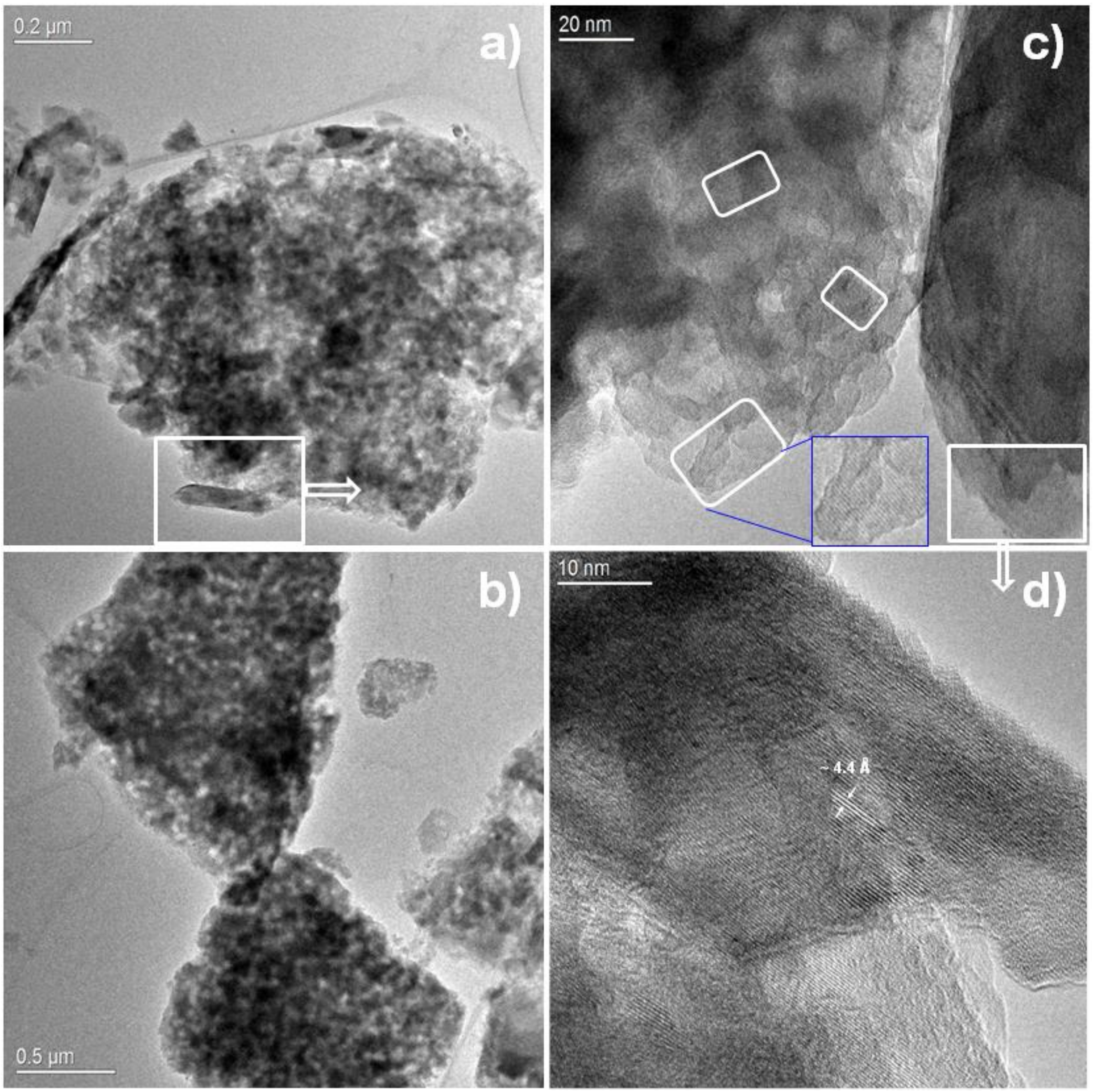

Figure 5.5 Transmission electron microscopy images (TEM) of 85:15 wt-% V_2O_5 : B_2O_3 glass ceramics showing a) an agglomerate with amorphous and crystalline parts, b) an overview of micron-size agglomerates, c) zoomed in image of the marked region in (a) indicating nano-crytallites in an amorphous matrix, d) lattice fringes for the (001) planes of V_2O_5.

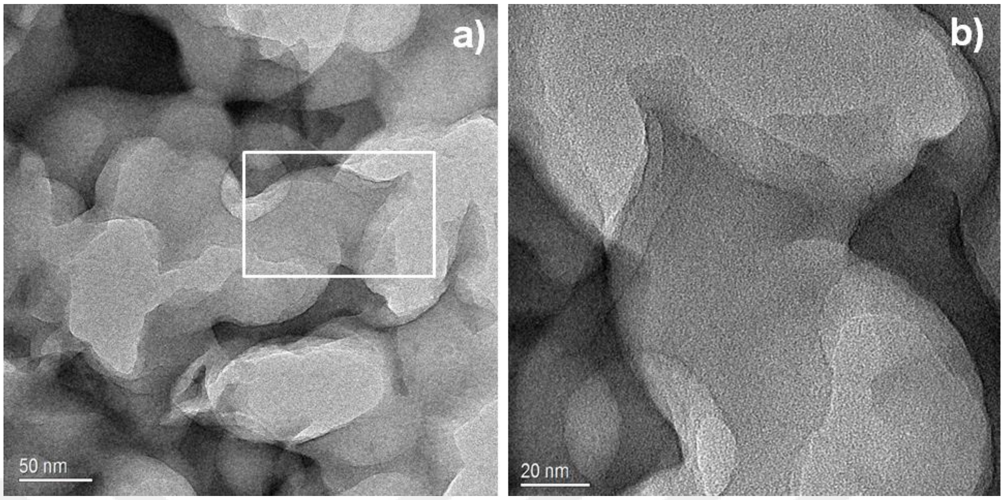

Figure 5.6 Transmission electron microscopy (TEM) image of 85:15 wt-% V_2O_5 : B_2O_3 glass ceramics showing amorphous regions and mesopores.

The presence of vanadium on the center and on the rim of particles is proven by the energy dispersive X-ray (EDX) and electron energy loss spectroscopy (EELS) spectra, respectively (**Fig. 5.7**). Boron (~ 200 eV) could not be detected due to the background.

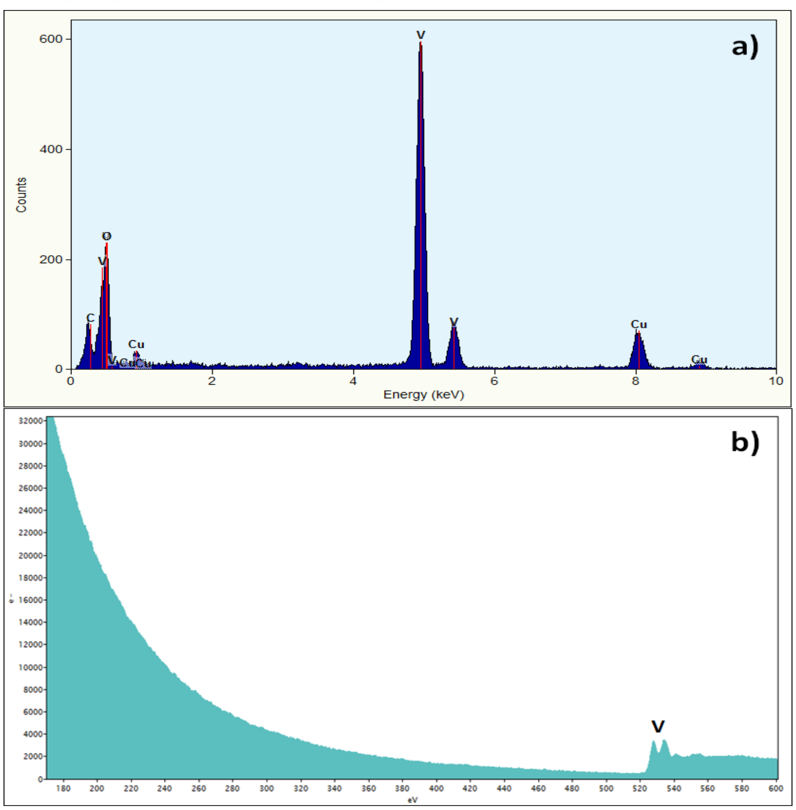

Figure 5.7 a) EDX spectrum from the agglomerates in Figure 5a, b) EELS spectrum from Figure 5c.

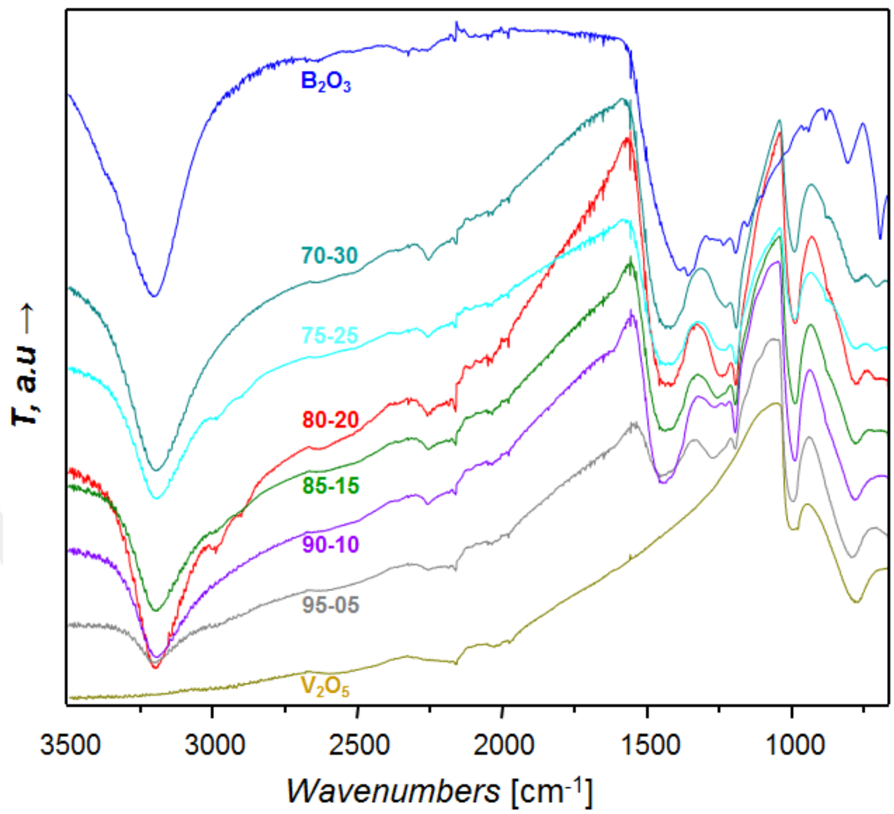

Figure 5.8 Infrared (IR) spectra of 95:5, 90:10, 85:15, 80:20, 75:25, 70:30 wt-% V_2O_5 : B_2O_3 glass ceramics, and V_2O_5 and B_2O_3 precursors.

Infrared (IR) spectra of the V_2O_5 – B_2O_3 glass ceramics series are given in **Figure 5.8**. The main bands observed for V_2O_5 are at ca. 1020 cm^{-1} from the stretching of V = O in the VO_5 square pyramids, and at ca. 820-830 cm^{-1} due to vibrations of V – O – V chains[243, 245]. These bands are shifted to ~ 1010 cm^{-1} and ~ 799 cm^{-1}, respectively in the IR spectra of glass ceramics. Similar shifts were also found for various glass systems of vanadium pentoxide[243, 245-246], and show reduction of bond force constants by the interaction with network forming groups. The bands observed between 1200 and 1600 cm^{-1} are related to the asymmetric stretching modes of BO_3 trigonal units[245, 247]. The broad peak at ca. 3200 cm^{-1} is attributed to water groups and shows the hygroscopic nature of the V_2O_5 – B_2O_3 glass ceramics and a possible formation of boric acid with air exposure. The band observed at 806 cm^{-1}, which is attributed to the bending vibrations of boroxol rings in B_2O_3[246], cannot be clearly detected in the spectra of the V_2O_5 – B_2O_3 glass ceramics series. This might either be indicating to the absence of boroxol ring formation in these systems or the band became too weak to be detected in the presence of V – O – V modes at the same region of the spectrum. Nevertheless, the presence and effects of borate groups and the partial glass formation in V_2O_5 – B_2O_3 materials that we investigate are verified here by vibrational spectroscopy, which were not obviously revealed by previous characterization methods.

Electrochemical investigations

In line with the finding that favourable V_2O_5 nano-crystallites can be produced with B_2O_3 quantities of $\geq$ 10 wt-%, but higher quantities of electrochemically inactive network former would limit the specific capacities and cause a more hygroscopic nature, a ratio of 85:15 wt-% V_2O_5 : B_2O_3 ceramics was chosen to be focused on for further electrochemical investigations. In order to compare the electrochemical performance of the glass ceramics and the commercial V_2O_5 powder, from which it was produced, cells of both materials with a working electrode composition of 70 (wt-%) active material, (20 wt-%) conductive carbon (Super P®) and (10 wt-%) PVDF were tested in a galvanostatic protocol. The cells were first discharged to 1.5 V and then charged to 4.0 V at a constant current rate of 50 mA/g. The first ten charge/discharge curves of 85:15 wt-% V_2O_5 : B_2O_3 glass ceramics are displayed in **Figure 5.9**. The first discharge curve and the subsequent cycles of V_2O_5 – B_2O_3 glass ceramics are comparable to the lithium intercalation behavior of V_2O_5 (**Fig. 5.10**).

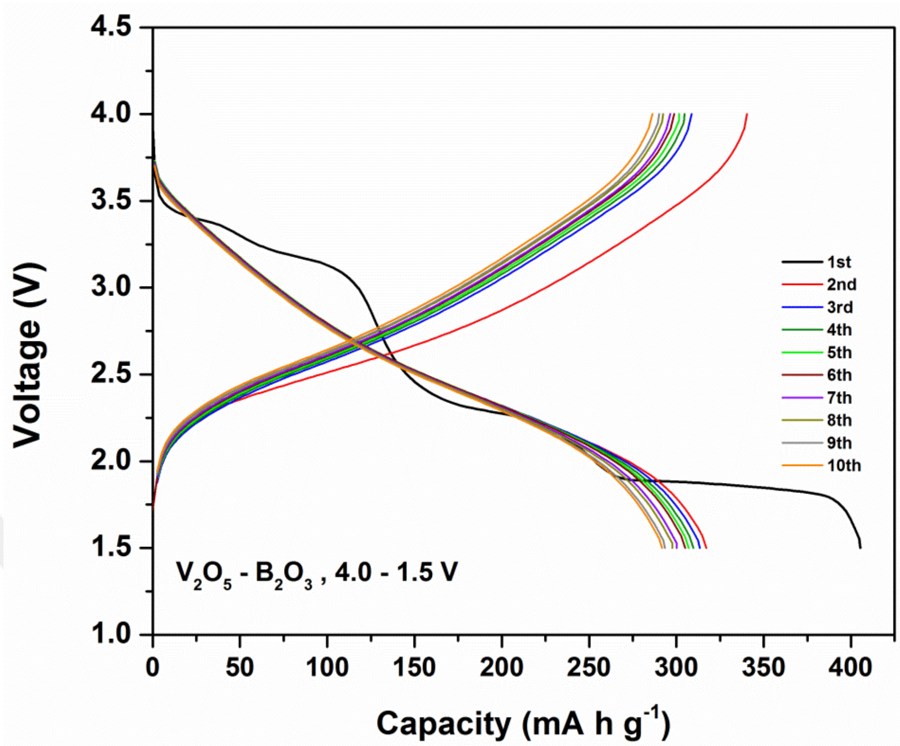

Figure 5.9 The first ten charge/discharge curves of 85:15 wt-% V_2O_5 : B_2O_3 glass ceramics within 1.5 – 4.0 V at 50 mA/g rate

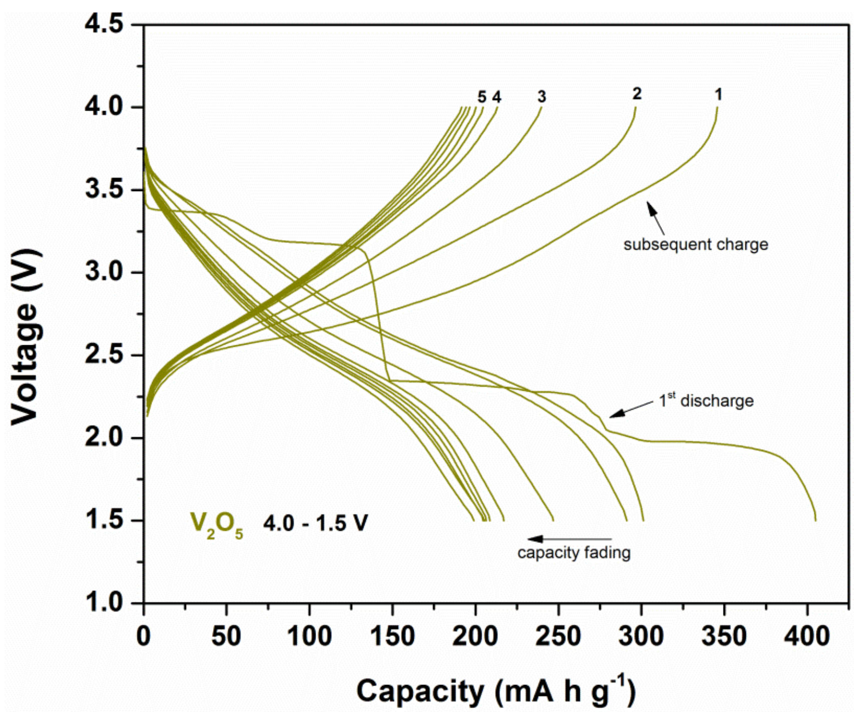

Figure 5.10 Galvanostatic cycling behavior of bulk V_2O_5 (99.2 %, Alfa Aesar) within 1.5 – 4.0 V at 50 mA/g rate.

V_2O_5 transforms into several $Li_xV_2O_5$ phases depending on the amount of lithium inserted, α- (x < 0.01), ε- (0.35 < x < 0.7), δ- (x = 1), γ- (1< x < 2) and ω- (x = 3)[210]. For galvanostatic cycling of 85:15 wt-% V_2O_5 : B_2O_3 glass ceramics, after the first discharge, featureless curves without any distinct plateaus occur comparable to the cycling of the ω-$Li_xV_2O_5$ phase, and this shows a homogeneous phase intercalation/ deintercalation mechanism. However, it should be noted that the first discharge curve of the 85:15 wt-% V_2O_5 : B_2O_3 glass ceramics has a sloppier character. The voltage decreases continuously with lithium insertion between plateaus rather than the distinct steps observed for bulk V_2O_5. This type of change is typical for a homogeneous phase intercalation reaction similar to the behavior of vanadium pentoxide gels. We consider this part to be the contribution of the amorphous region of the glass ceramics to the first discharge profile.

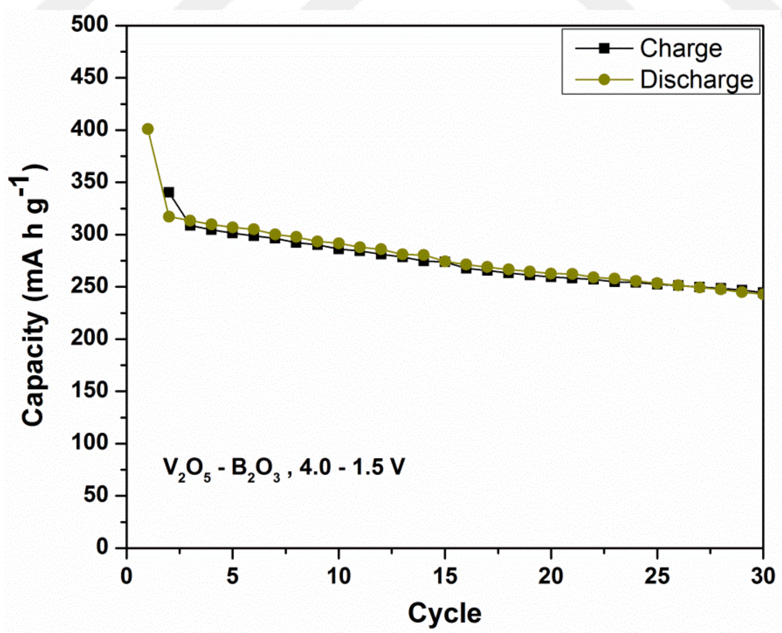

Figure 5.11 Charge/discharge capacity vs. cycle number for 85:15 wt-% V_2O_5 : B_2O_3 glass ceramic.

A high capacity of ~ 405 mAh/g is obtained for the first discharge. The subsequent charge capacity stops at 340 mAh/g, as all of the inserted lithium atoms cannot be extracted again from ω-$Li_xV_2O_5$ phase up to 4.0 V similar to previous reports. The cycling properties are also quite good compared to crystalline phases, but may still be enhanced, with a discharge capacity of ~ 292 mAh/g at the 10th cycle and the retention of 76 % discharge capacity (excluding the initial capacity loss) within the first 30 cycles (**Fig. 5.11)**. It should be highlighted that these capacities refer to the total mass of the V_2O_5 – B_2O_3 composite and corresponding values only for V_2O_5 part are correspondingly higher.

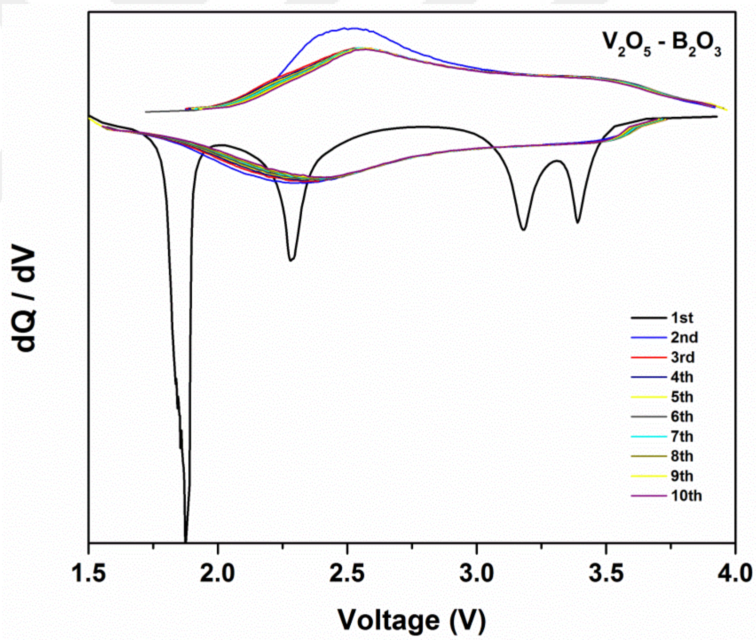

Figure 5.12 The differential capacity plot for the galvanostatic cycling of 85:15 wt-% V_2O_5 : B_2O_3 glass ceramic.

Figure 5.12 shows the differential capacity plot for the galvanostatic cycling of 85:15 wt-% V_2O_5 : B_2O_3 glass ceramics. dQ/dV plots and cyclic voltammetry curves reveal similar information and can be used to study charge/discharge characteristics of an electrochemical system. Plateaus in galvanostatic charge/discharge curves are observed as sharp peaks in dq/dv plots, whereas steady decreases or increases of voltage appear in a featureless fashion or as broad peaks. The change of intensities, positions and shapes of these peaks contain information about charge/discharge mechanisms and electrochemical reactions. In our case, the phase transformation of V_2O_5 to $Li_xV_2O_5$ phases with lithium insertion (α- ($x < 0.01$), ε- ($0.35 < x < 0.7$), δ- ($x = 1$), γ- ($1< x < 2$) and ω- ($x = 3$)) can be very well tracked. The three peaks observed at ~ 3.4, 3.2 and 2.3 V correspond to the two phase regions of α / ε, ε / δ and δ / γ. The sharp peak at ~ 1.9 V shows the formation of ω-phase that further cycles as a single phase in subsequent charge/discharge curves. This cycling is indicated in form of broad oxidation and reduction peaks at ~ 2.6 V and ~ 2.4 V, respectively. The difference in voltage shows a polarization that is slightly reduced upon further cycling via the partial amorphization of the crystalline $Li_xV_2O_5$ particles.

As stated previously, V_2O_5 is thought to be kinetically limited by low ionic and electronic conductivity[218-219]. Not fully reversible delithiation/lithiation after each cycle stemming from this hindrance, especially at high current rates, may be speculated as one of the reasons for capacity fading with cycling. In order to overcome these shortcomings, following a similar route that was successful to improve the electrochemical performance of $LiMnBO_3$, $LiCoBO_3$ and $Li_7Mn(BO_3)_3$, composite electrodes of 85:15 wt-% V_2O_5 : B_2O_3 glass ceramics were designed with reduced graphite oxide (RGO) and Super P®. These composite electrode materials were prepared by ball-milling the glass ceramics with graphite oxide or Super P®. For the composite with graphite oxide, the ball-milled product was further heated at 200-250 ^oC for 8 hours under nitrogen atmosphere to attain reduced graphite oxide (RGO). XRD powder patterns of the composite electrode materials are displayed in **Figure 5.13**.

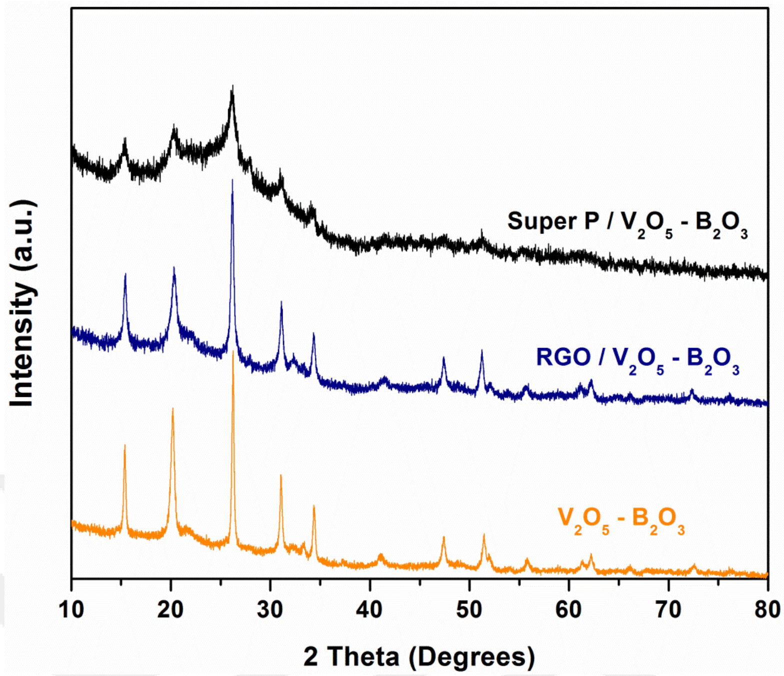

Figure 5.13 XRD powder patterns of 85:15 wt-% V_2O_5 : B_2O_3 glass ceramics (orange), RGO / glass ceramics composite (blue), Super P® / glass ceramics composite (black).

For both of the composites, a reduction in size of V_2O_5 crystallites was evidenced by the broadening of diffraction peaks showing an almost complete amorphization in the case of the Super P® composite. SEM images of the composite samples further support the decrease in size (**Fig. 5.14**). For the RGO composite, micron-sized agglomerates that are cemented with RGO are still observed, but most of the particle agglomerates were ground down to nano size. Consistent with the XRD powder patterns, the Super P® composite contains particles that are smaller than ~ 100 nm, and the large agglomerates are mostly gone. Besides, the porous morphology, which was present before for the plain glass ceramics, is now gone and missing for both composites.

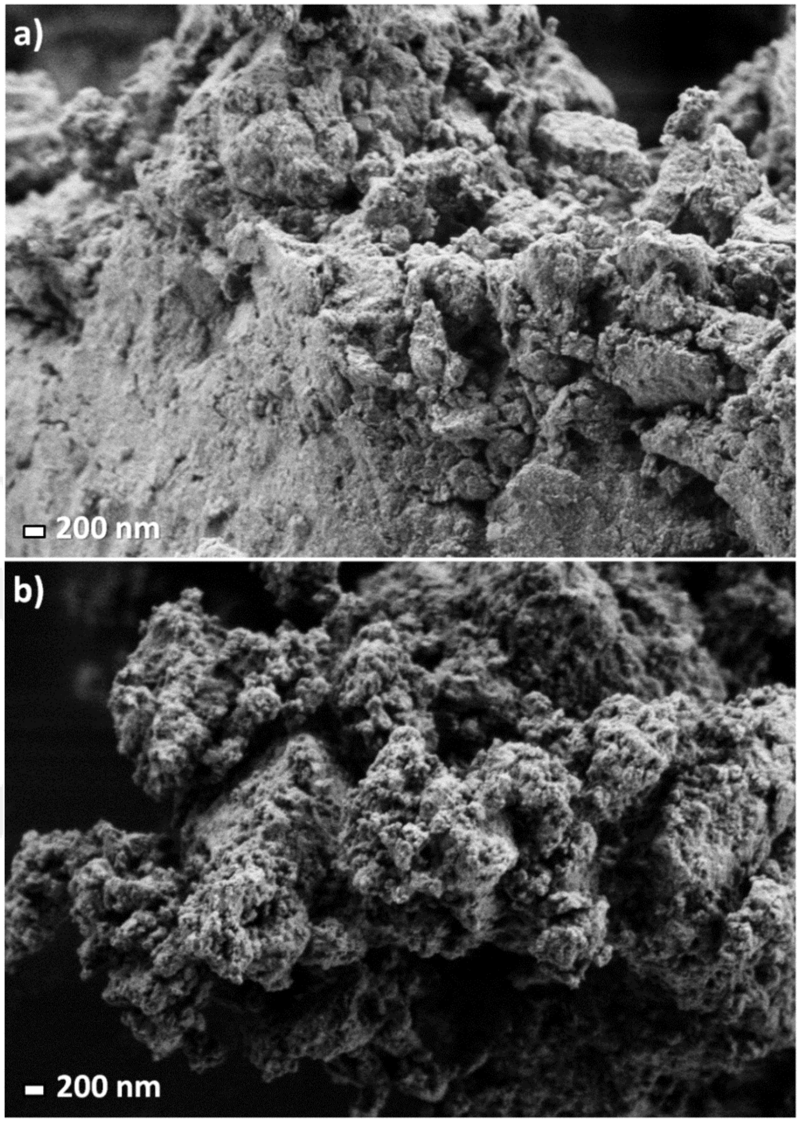

Figure 5.14 Scanning electron microscopy (SEM) images of a) RGO / glass ceramics composite, b) Super P® / glass ceramics composite.

Since further nano-sizing and a possibly better conductive network are achieved for composite electrodes, an improvement of overall electrochemical performance might be expected similar to the previous cases. However, this expectation is not fulfilled for the 85:15 wt-% V_2O_5 : B_2O_3 glass ceramic. Charge/discharge capacities and cycling properties deteriorated for the RGO / 85:15 wt-% V_2O_5 : B_2O_3 glass ceramics and Super P® / 85:15 wt-% V_2O_5 : B_2O_3 glass ceramics composite electrodes compared to the prior described plain glass ceramics electrode as illustrated in **Figure 5.15 & 5.16**. The galvanostatic cycling tests for the composite electrodes were performed within 1.5 – 4.0 V at 50 mA/g rate. The multi-step first discharge curve observed for the plain material changes into a smooth single phase curve for the Super P® composite indicating the conversion from glass ceramic to glass via extensive ball-milling with carbon black (**Fig. 5.15**). A similar result is also found for the RGO composite; though there are still plateaus at ~ 3.1, 2.2 and 1.9 V (**Fig. 5.16**), the contribution of these regions arising from nano-crystalline V_2O_5 to the total capacity has declined.

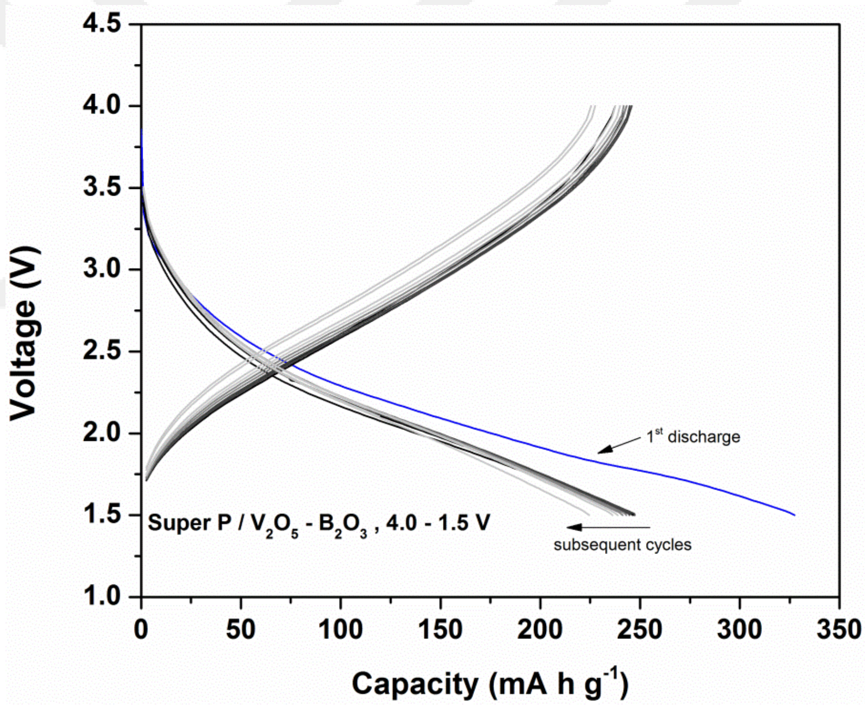

Figure 5.15 Galvanostatic charge/discharge curves for Super P® / 85:15 wt-% V_2O_5 : B_2O_3 glass ceramics composite.

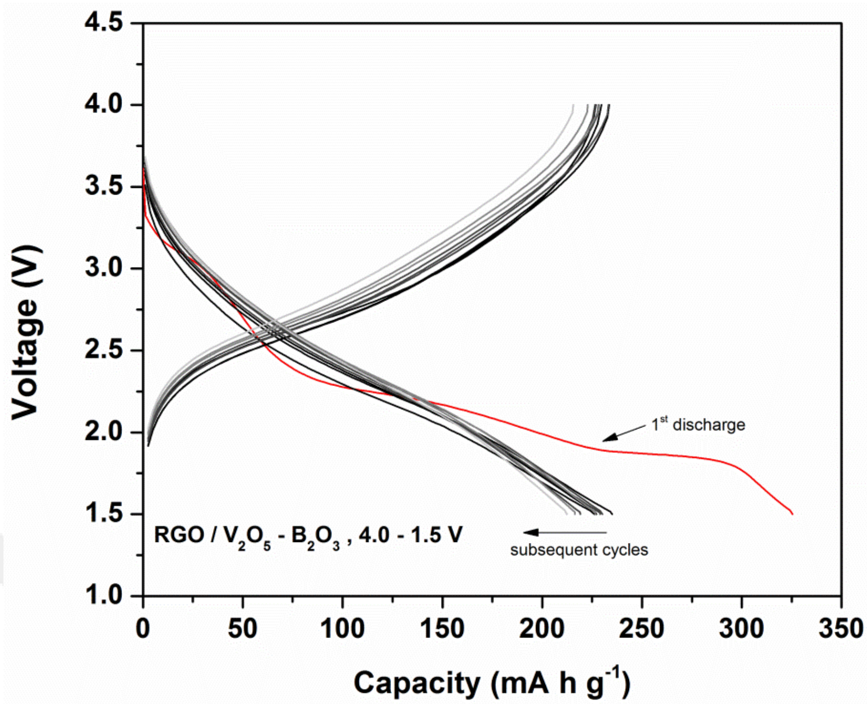

Figure 5.16 Galvanostatic charge/discharge curves for RGO / 85:15 wt-% V_2O_5 : B_2O_3 glass ceramics composite.

The first discharge capacity decreases to ~ 325 mAh/g and ~ 327 mAh/g for the RGO and the Super P® composites, respectively. The capacity losses mostly occurring above 2.5 V with the disappearances of high voltage plateaus indicate a decrease in the initial oxidation state of vanadium, since V^{5+} to V^{4+} reduction is expected in this voltage range. Thus, only a smaller amount of lithium can be inserted into composite materials reducing the achievable theoretical capacity. It can be speculated that V^{5+} species are reduced to lower oxidation states by a partial carbothermal reaction during extensive ball-milling. The cycling stability is also still problematic as the capacities drop to the range of ~ 220 mAh/g at the 10th cycle for both composite electrodes.

Conclusions

85 wt-% V_2O_5 – 15 wt-% B_2O_3 glass ceramic yields a high first discharge capacity of ~ 405 mAh/g at 50 mA/g rate within 1.5 – 4.0 V. A specific capacity of ~ 292 mAh/g is retained at the 10^{th} cycle. 85:15 wt-% V_2O_5 : B_2O_3 glass ceramics show a better electrochemical performance in terms of cycling and charge/discharge capacities compared to bulk and various nano-forms of V_2O_5. Comparable properties were only reported by lengthier approaches, such as fabrication of thin film electrodes and employment of smaller and well-defined nano-particles. The enhanced features of the glass ceramics can be mainly attributed to the employment of amorphous and nano-crystalline V_2O_5 decreasing the diffusion path lengths for Li^+ ions and the volume work upon lithiation/delithiation. In addition, the distinctive porous morphology of the glass ceramics occurring as mesopores in amorphous regions and larger pores in micron-sized agglomerates probably bring about further improvements via soaking of the electrolyte, thus, providing a better access and contact of the electrolyte to the active material and facilitating faster transports of Li^+ ions and electrons. The utilization of carbon composite electrodes, which are normally predicted to improve the capacity retention, resulted in a poorer electrochemical performance in the case of 85:15 wt-% V_2O_5 : B_2O_3 glass ceramics as the cycling stability and delivered capacities largely dropped for the RGO and Super P® composite electrodes compared to the plain electrode. Loss of the porous structure and favorable high oxidation states during the composite formation are thought to be the main reasons of compromised performance.

Further improvements could still be pursued for the V_2O_5 – B_2O_3 system. Glasses in the V_2O_5 – B_2O_3 system could be targeted as cathode materials for lithium batteries. In our study, the complete glass formation couldn't be accomplished due to relatively slow quenching rates. The cooling rate of the glass forming melt to room temperature by quenching between copper plates is estimated to be 10^2 K/s[248]. This rate is not large enough to reach a complete glassy state in the V_2O_5 – B_2O_3 system, so glass ceramics are obtained; however, it was reported that a full vitrification can be achieved by using roller and twin-roller quenching techniques that have cooling rates of ca. 10^{4-5} K/s[249]. If conductive and protective coatings are applied without reducing V^{5+} species, V_2O_5 – B_2O_3 glass ceramics might also be further focused on, even with the absence of a complete glass formation.

5.3.2 V_2O_5 – $LiBO_2$ glass

Alkali oxides are widely used as network modifiers in various glass systems, and they change physical properties of glasses via replacing the bridging network formers. Network modifiers cannot form glasses alone but affect the system through different mechanisms. Specifically, the addition of an alkali metal oxide to borate glasses was discussed to alter the glass network by the conversion of trigonal BO_3 groups from the boroxol rings to BO_4 groups; thus, increasing the number of structural linkages through B – O – B bonds[250-252]. For the Li_2O – B_2O_3 – V_2O_5 glass system, some electrical, mechanical, optical and thermal properties were studied[253-256], but to the best of our knowledge, the utilization in a secondary lithium battery has not been explored much. Moreover, the addition of Li_2O into the V_2O_5 – B_2O_3 system can be expected to increase ionic conductivities, as it was shown already in literature[255, 257]. Thus, a more reversible lithiation/delithiation might be expected for an electrode of Li_2O – B_2O_3 – V_2O_5 glass.

Here, a glassy material from the Li_2O – B_2O_3 – V_2O_5 glass system, which will be stated as V_2O_5 – $LiBO_2$ glass in the further text, is reported as a cathode material for rechargeable lithium batteries. Similar to the synthesis of V_2O_5 – B_2O_3 glass ceramics, a glass forming melt is obtained from 80 wt-% V_2O_5 and 20 wt-% $LiBO_2$ at 900 ^oC that is quenched to room temperature to produce the glass material. The glass material synthesized at 900 ^oC has a greenish-brown color indicating to a lowering of oxidation state of some of the vanadium centers to V^{4+}. Magnetic measurements provide further evidence for this assumption. For V_2O_5 a diamagnetic behavior is expected, yet the V_2O_5 – $LiBO_2$ glass material shows a paramagnetic behavior by a logarithmic decrease of χ (magnetic susceptibility) with increasing temperature (**Fig. 5.17**). Oxygen loss during annealing at high temperatures in an open system could have caused a partial reduction of V^{5+} species to V^{4+} species.

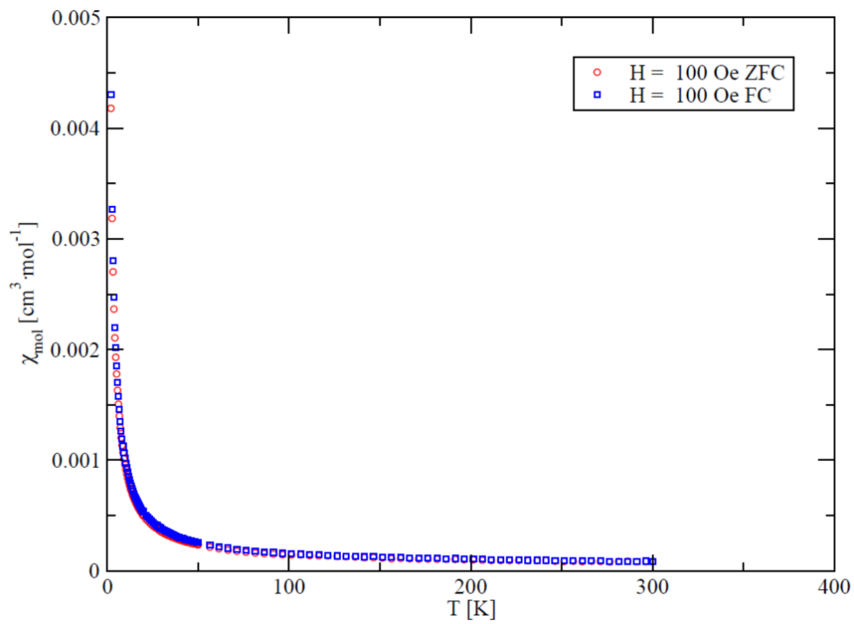

Figure 5.17 Temperature dependence of magnetic susceptibility for the V_2O_5 – $LiBO_2$ glass at a field strength of 100 Oe showing a simple paramagnetic behavior.

The XRD powder pattern of the V_2O_5 – $LiBO_2$ glass material is shown in **Figure 5.18**. The product could be described as glassy with a high background lacking any strong reflections , but very broad diffraction peaks at 2Θ ~ 26.5, 12.2 and 9.3 might be attributed to the trace amounts of $Li_{0.3}V_2O_5$ (ICSD 166482) or $Li_{0.667}V_2O_5$ (ICSD 25383) that have intense reflections in these regions, as well. The presence of $Li_xV_2O_5$ phases further supports the partial reduction to V^{4+} species.

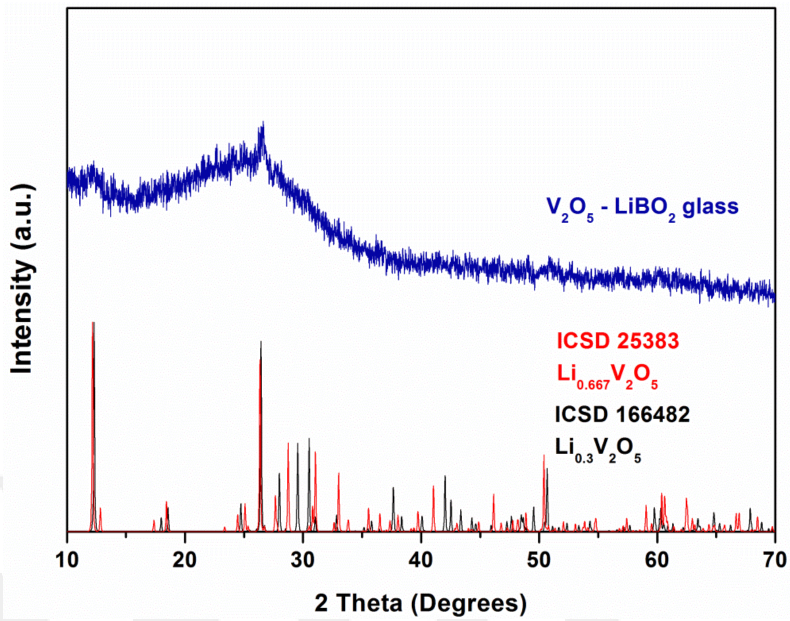

Figure 5.18 XRD powder pattern of the V_2O_5 – $LiBO_2$ glass.

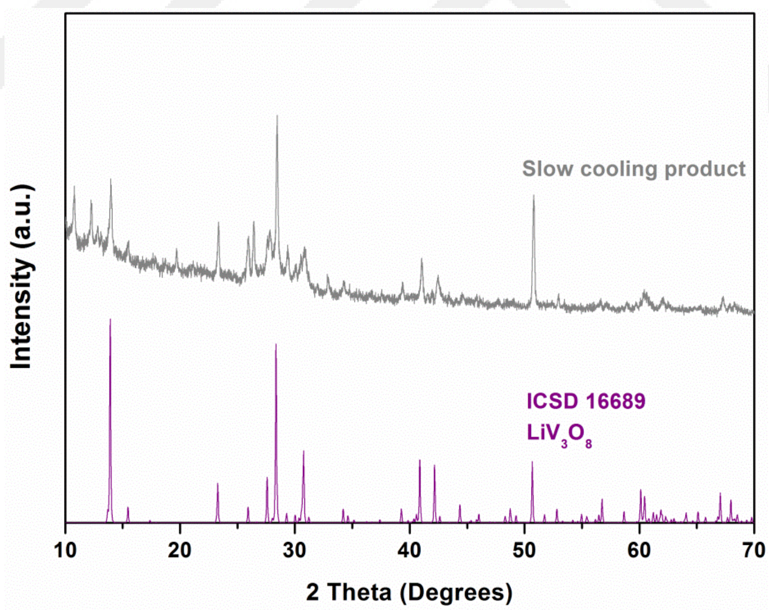

Figure 5.19 XRD powder pattern of a slowly cooled sample containing LiV_3O_8 and $Li_xV_2O_5$ phases.

When the glass forming melt is not quenched by using Cu plates, but rather, cooled down slowly to room temperature by taking out the melt from the hot oven, crystalline phases, LiV_3O_8 and $Li_xV_2O_5$, are found. XRD powder pattern of such a product is displayed in **Figure 5.19**. In addition to the lithiated phases, the formation of boric acid from the glass material is also observed, when the product is exposed to air for 2-3 hours. Therefore, extensive exposure of the glassy material to air should be avoided, especially in humid environments, during handling and fabrication of electrodes.

The differential thermal analysis (DTA) proves the glassy nature of the quenched 80-20 wt-% V_2O_5 – $LiBO_2$ material (**Fig. 5.20**). The endothermic effect at ~ 205 ^oC arises from the glass transition followed by transformations into crystalline phases around 216 ^oC and 322 ^oC that are designated by exothermic peaks. These newly formed phases melt in the range between 560 to 650 ^oC. For the cooling curve obtained at a rate of 10 K/min under air flow (red curve in **Fig. 5.20**), the two exothermic peaks at ~ 580 ^oC and 510 ^oC correspond to crystallizations from the melt.

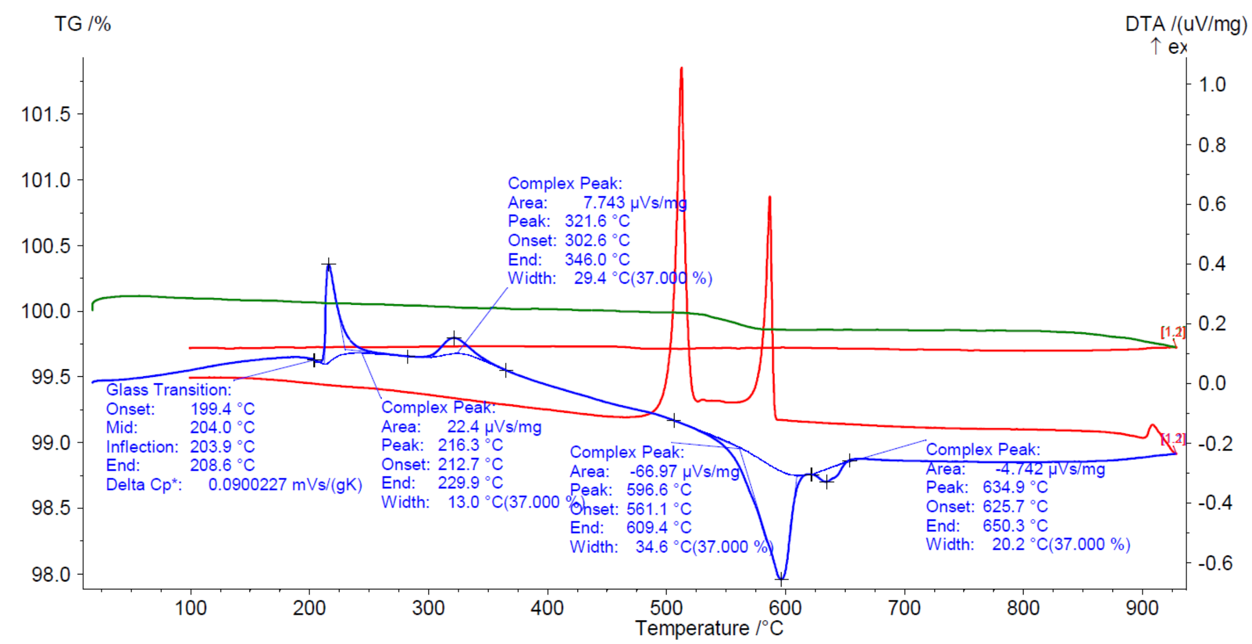

Figure 5.20 Differential thermal analysis (DTA) of the V_2O_5 – $LiBO_2$ glass.

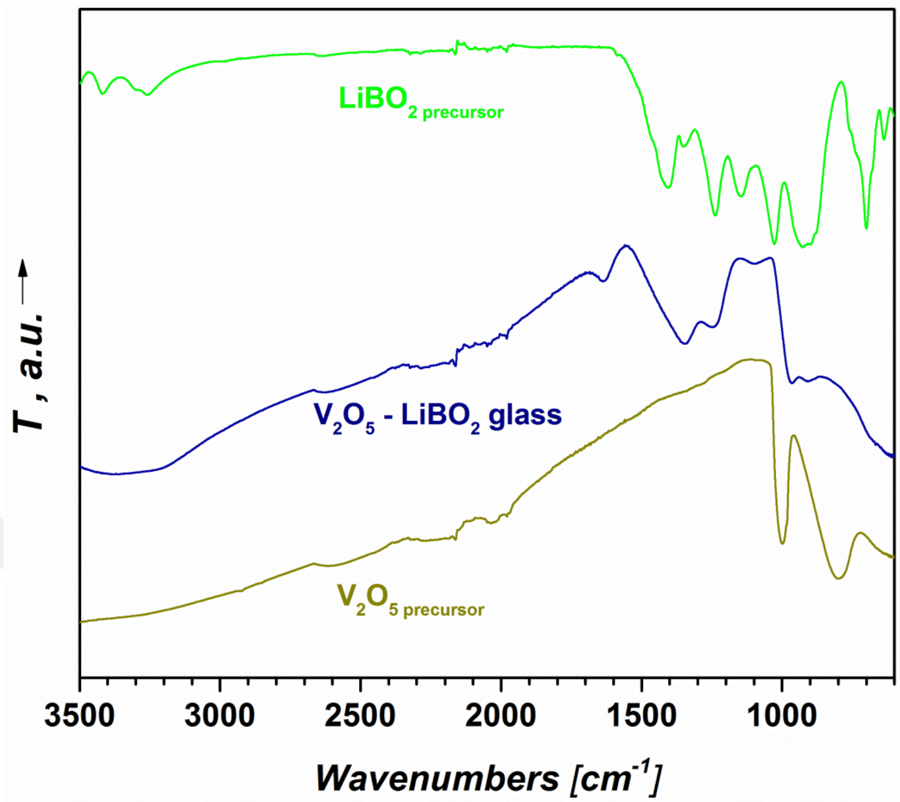

Figure 5.21 Infrared (IR) spectra of the V_2O_5 – $LiBO_2$ glass, and V_2O_5 and $LiBO_2$ precursors.

Figure 5.21 depicts infrared (IR) spectra of the V_2O_5 – $LiBO_2$ glass and the educts, V_2O_5 (99.2 %, Alfa Aesar) and $LiBO_2$ (99.9 %, Alfa Aesar). As presented in the previous section, most of the vibrational characteristics of the V_2O_5 – B_2O_3 glass ceramics closely resemble to the precursor compound spectra except some slight changes. However, the IR spectrum of the V_2O_5 – $LiBO_2$ glass is very different from the spectra of the educts proving the formation of a new kind of material. The strong band observed for V_2O_5 at ca. 1020 cm^{-1} stemming from the stretching of the vanadyl group V = O in the VO_5 square pyramids disappears in the spectrum of the V_2O_5 – $LiBO_2$ glass probably indicating to the loss of the double bond. A weak band emerging at ~ 970-980 cm^{-1} could still be attributed to the stretching of V = O with a decrease in bond order, but this band together with the ones at ~ 890-900 cm^{-1} and ~ 1090-1100 cm^{-1} could also be assigned to the asymmetric stretching vibrations of BO_4 tetrahedral units that are expected to appear between 850 and 1100 cm^{-1}[245, 247, 249, 256]. This finding also fits well with the previously described influence of alkali metal oxide addition into borate glass. Though some BO_3 groups are converted to tetrahedral units, they are still present in the glass network as the bands observed between 1200 and 1600 cm^{-1} are related to the asymmetric stretching modes of BO_3 trigonal units[245, 247]. Bending modes of possible B – O – V – O – B units should be expected in the range of 400 – 750 cm^{-1}[247].

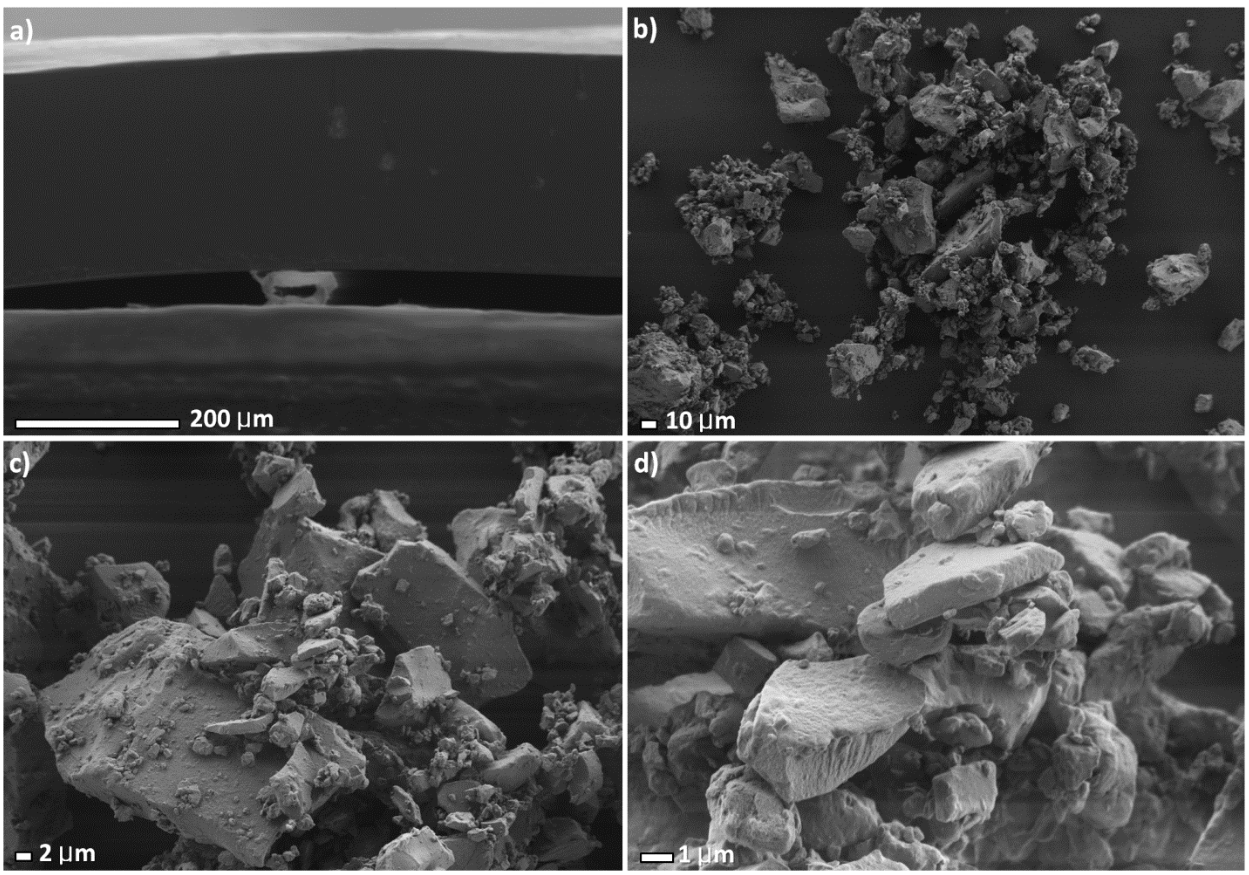

Figure 5.22 Scanning electron microscopy (SEM) images of the V_2O_5 – $LiBO_2$ glass displaying a) a side view of glass disk, b) an overview of a ground sample, c) & d) micron – sub-micron sized glass particles.

Scanning electron microscopy (SEM) images of the V_2O_5 – $LiBO_2$ glass are displayed in **Figure 5.22**. When the glass forming melt is properly quenched in a fast manner, a homogeneous disk of glass is obtained. **Figure 5.22a** depicts a side image of V_2O_5 – $LiBO_2$ glass disk with a thickness of ~ 200 microns. The homogenous nature can also be observed under an optical microscope with a gleaming purple appearance similar to volcanic glass. These large glass pieces have to be grinded in order to make further characterizations and to form electrodes of the material. The particles can be crushed down to a spread between micron and sub-micron size (**Fig. 5.22c & 22d**) in an agate mortar by extensive grinding. Yet, very large pieces of 40-50 microns in size continue to exist (**Fig. 5.22b**).

Figure 5.23 depicts transmission electron microscopy images (TEM) of the V_2O_5 – $LiBO_2$ glass. Micron-sized blocks of the glass material can be seen in **Figures 5.23a & 23c**. As revealed by bulk characterization techniques, the state is mostly amorphous being further verified here with a lack of order even at 5-10 nm resolution for many parts of the sample (**Fig. 5.23b**). However, lattice fringes with a spacing of about 9.5 Å extending into nano-crystallites with sizes in the range of 20-30 nm are also found in some regions (**Fig. 5.23d**). The d-distance (~ 9.5 Å) corresponds to 2Θ = ~ 9.3, where a broad reflection from $Li_xV_2O_5$ phases ($Li_{0.3}V_2O_5$ (ICSD 166482) or $Li_{0.667}V_2O_5$ (ICSD 25383)) appears, in the XRD powder pattern of the V_2O_5 – $LiBO_2$ glass. Thus, it can be concluded that nano-crystallites of $Li_xV_2O_5$ are embedded in the amorphous glass matrix.

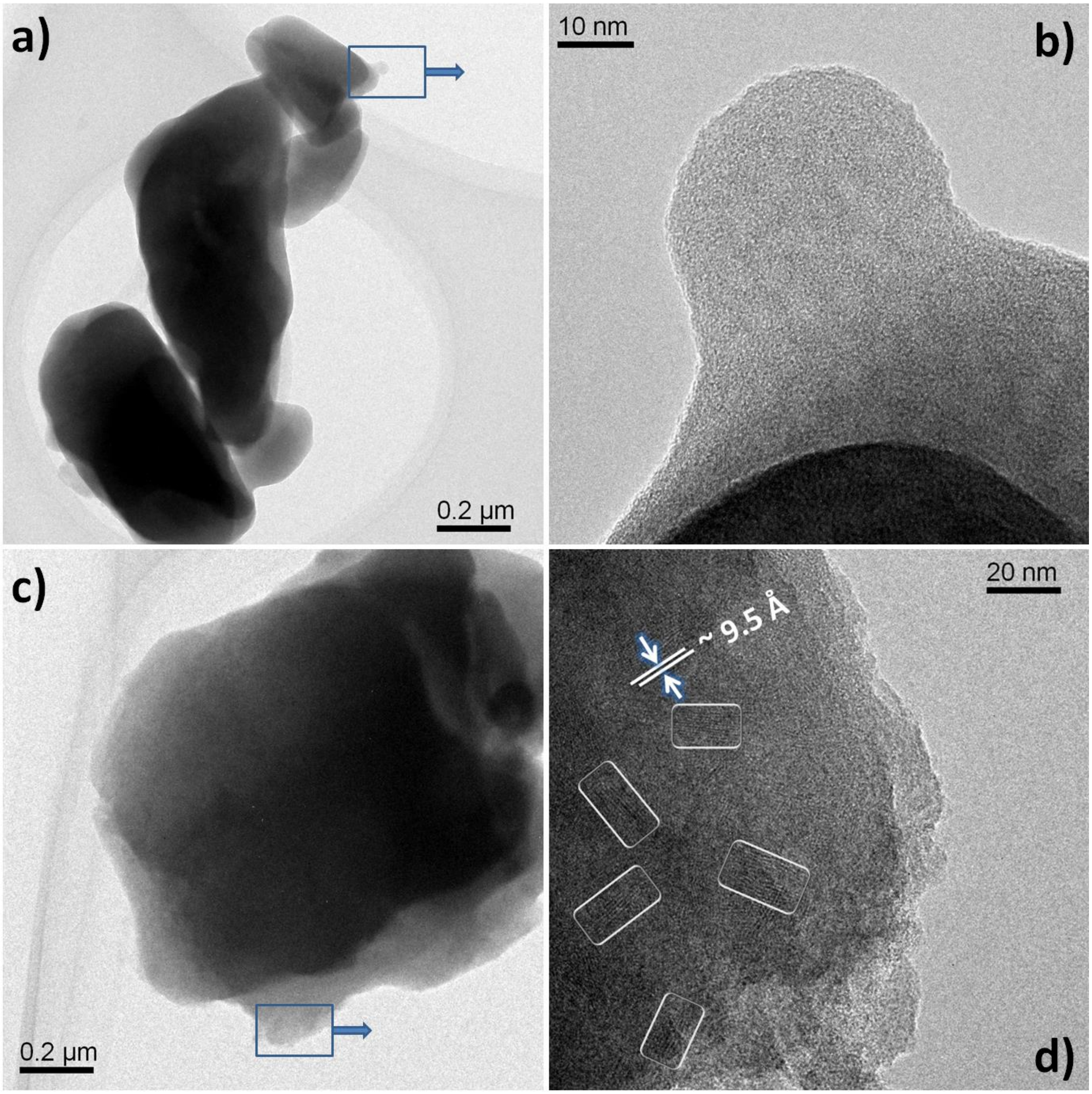

Figure 5.23 Transmission electron microscopy images (TEM) of the V_2O_5 – $LiBO_2$ glass displaying a) an agglomerate of glass particles, b) the amorphous nature of the glass, c) a glass particle block, d) zoomed in image of the marked region in (c) indicating nano-crystallites of $Li_xV_2O_5$ phases embedded in the amorphous glass matrix, and lattice fringes with a spacing of ~ 9.5 Å.

Electrochemical Investigations

For a typical electrode fabrication of the V_2O_5 – $LiBO_2$ glass, (70 wt-%) active material, (20 wt-%) conductive carbon (Super P® Timcal) and (10 wt-%) PVDF binders were manually mixed in an agate mortar without any ball-milling. The cells from such electrodes were tested in a galvanostatic mode by first discharging to 1.5 V and then charging to 4.0 V at a rate of 50 mA/g. The first ten galvanostatic charge/discharge curves of the V_2O_5 – $LiBO_2$ glass are displayed in **Figure 5.24.** The voltage declines continuously with lithium insertion into the material and featureless curves without a multi-step behavior appear that is consistent with the expected homogeneous phase lithiation mechanism of a glass material. As derived from XRD and DTA investigations, the crystalline parts are very small. A first discharge capacity of 327 mAh/g is obtained, and the cell was charged with a capacity of 308 mAh/g in the subsequent cycle. This finding shows that the huge capacity loss associated with irreversible phase transformation of crystalline V_2O_5 materials is largely circumvented for the V_2O_5 – $LiBO_2$ glass. The capacity retention is also improved as 93 % of the initial charge capacity is still available at the 10^{th} cycle.

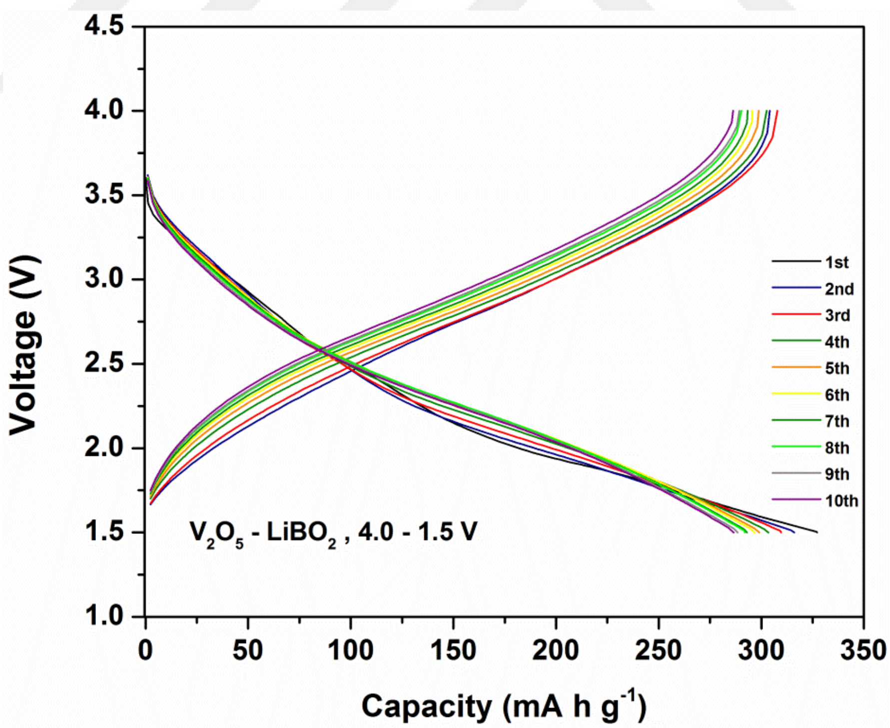

Figure 5.24 The first ten charge/discharge curves of the V_2O_5 – $LiBO_2$ glass within a potential window of 1.5 – 4.0 V at 50 mA/g rate.

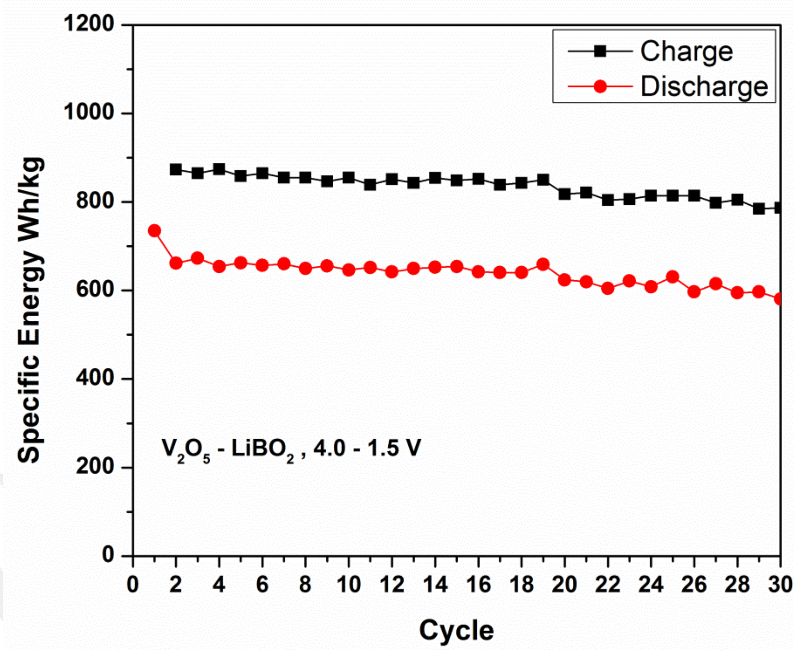

Figure 5.25 Specific energy vs. cycle number for the V_2O_5 – $LiBO_2$ glass in a potential window of 1.5 – 4.0 V at 50 mA/g rate.

The cycling properties in terms of specific energy for the first 30 cycles are illustrated in **Figure 5.25**. Without any optimization of the electrode material, a specific energy of ~ 663 Wh/kg is delivered at the 5th discharge. For this cycle, the specific energy necessary to charge the cell is ~ 859 Wh/kg. The difference of 196 Wh/kg between charge and discharge indicates to a polarization of the system that is also found for other cycles.

Figure 5.26 shows the rate capability for the V_2O_5 – $LiBO_2$ glass within 1.5 – 4.0 V. The capacities in the range of ~ 293, 236 and 180 mAh/g are delivered at rates of 50, 100 and 200 mA/g, respectively. The discharge capacity drastically drops to 125 mAh/g at the 35th cycle, when the rate is increased to 400 mA/g, and recovers to 260 mAh/g at the 45th cycle when the rate is 50 mA/g.

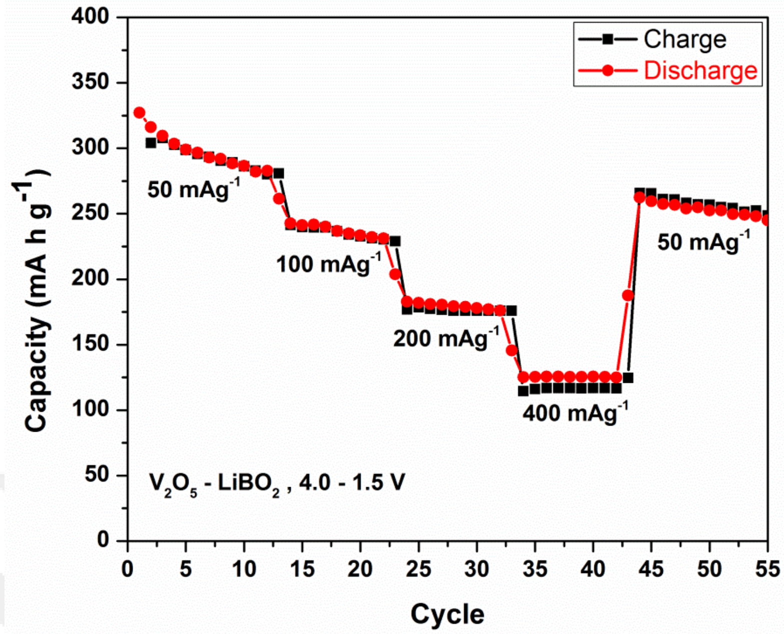

Figure 5.26 The rate capability of the V_2O_5 – $LiBO_2$ glass within 1.5 – 4.0 V at 50, 100, 200 and 400 mA/g rates (at room temperature).

Limited capacities at high rates and relatively high energy differences between charge and discharge cycles are probably caused by poor kinetics of the glassy material, especially for the larger particles of the V_2O_5 – $LiBO_2$ glass that were found to range from 2 to 50 microns in diameter. In order to counter these problems and further improve cycling properties with higher charge/discharge capacities, a composite electrode of the V_2O_5 – $LiBO_2$ glass with reduced graphite oxide (RGO) was employed. The preparation of the composite electrode includes steps of ball-milling the active material with graphite oxide (GO) and reducing GO afterwards at 200 ^{o}C. XRD powder patterns of graphite oxide, the plain V_2O_5 – $LiBO_2$ glass and the RGO / V_2O_5 – $LiBO_2$ glass composite are presented in **Figure 5.27**. The formation of crystalline $Li_xV_2O_5$ phases is promoted as a result of heat treatment that is necessary for the reduction of graphite oxide. The diffraction peaks at 2Θ ~ 26.5, 12.2 and 9.3 become more intense, and new reflections at ~ 30.7, 32.9 and 50.7 emerge that are also belonging to the aforementioned lithium vanadium oxides. As expected, no major diffraction peaks of graphite oxide are detected in the powder pattern of composite material indicating the delamination and partial reduction of graphite oxide.

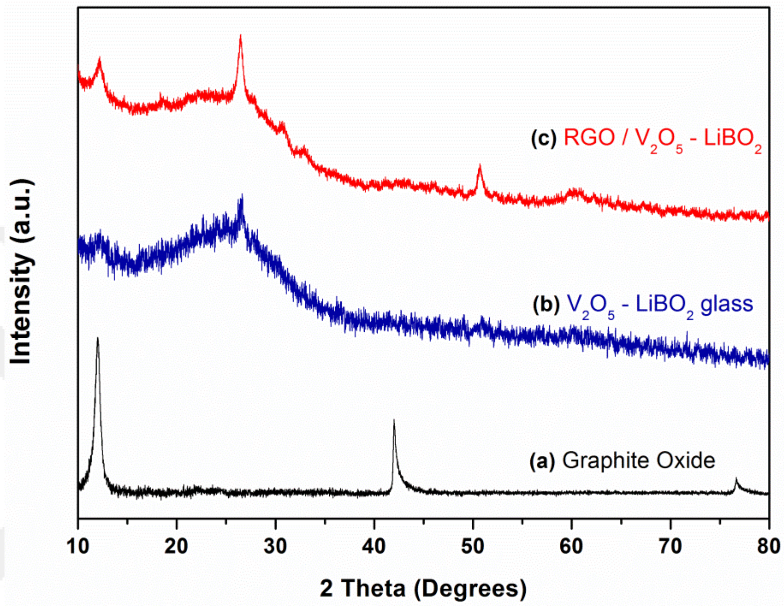

Figure 5.27 XRD powder patterns of a) graphite oxide, b) V_2O_5 – $LiBO_2$ glass, c) RGO / V_2O_5 – $LiBO_2$ glass composite.

Scanning electron microscopy (SEM) images of the RGO / V_2O_5 – $LiBO_2$ glass composite are presented in **Figure 5.28**. The large glass pieces were grinded to sub-micron sizes and a fine mixture with reduced graphite oxide was achieved. However, large flakes of reduced graphite oxide in a wrinkled morphology can also be found at some regions of the composite (**Fig. 5.28b**). The large flakes of RGO may still be useful in terms of providing better long range conduction in the electrode composite.

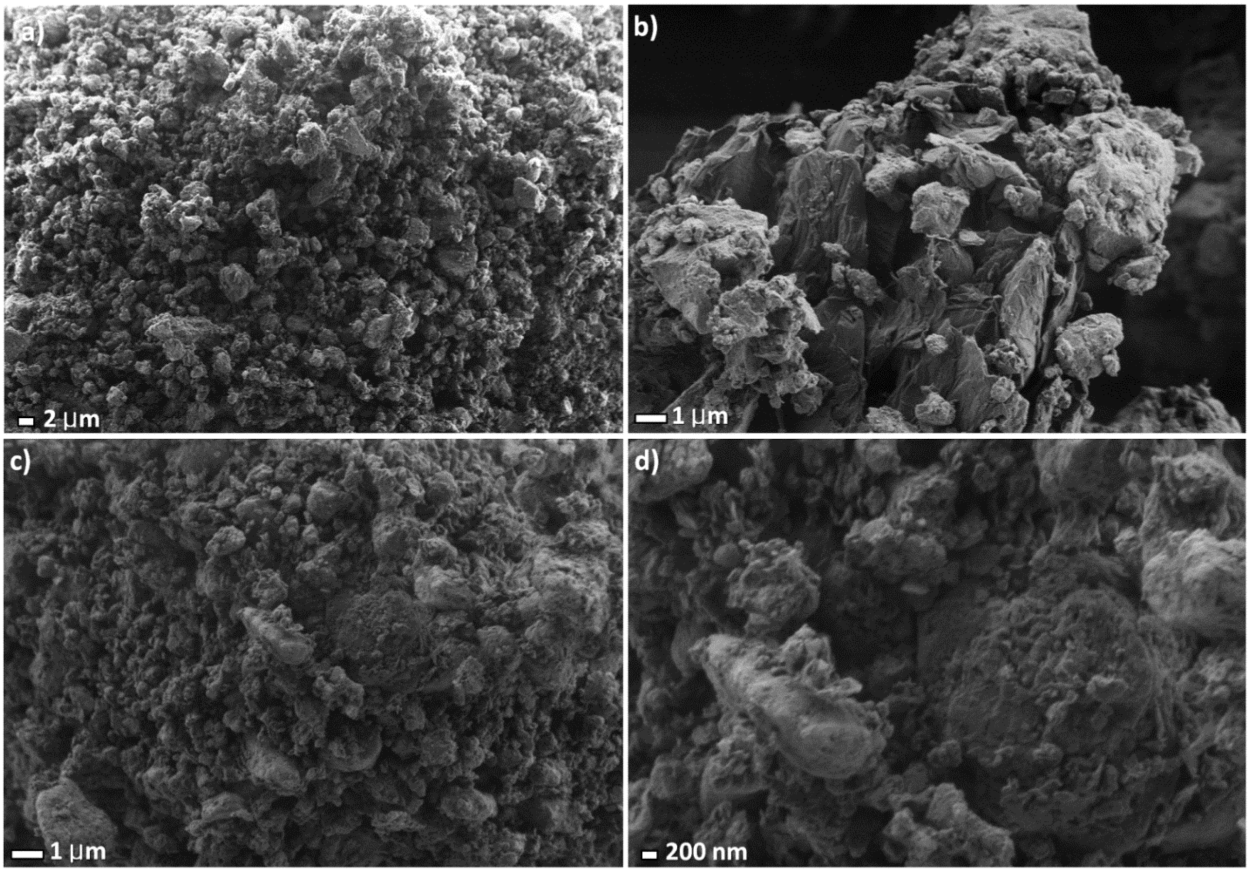

Figure 5.28 Scanning electron microscopy (SEM) images of the RGO / V_2O_5 – $LiBO_2$ glass composite.

Transmission electron microscopy images (TEM) reveal more information on covering and interaction of the V_2O_5 – $LiBO_2$ glass with reduced graphite oxide. Some parts of the glass material are directly coated by only a few layers of RGO as shown in **Figure 5.29**. Also visible in this image are $Li_xV_2O_5$ nano-crystallites embedded in amorphous areas. In accordance with the XRD powder pattern of the annealed sample, it can be concluded that these nano-crystallites grew in number and become more readily noticeable in TEM images. Widespread coating provided by the flocculated RGO is also observed (**Fig. 5.30**). Both the direct RGO coating of the glass surfaces and clustering of RGO between the V_2O_5 – $LiBO_2$ glass particles, respectively, are expected to improve short and long range conductivity within the composite electrode.

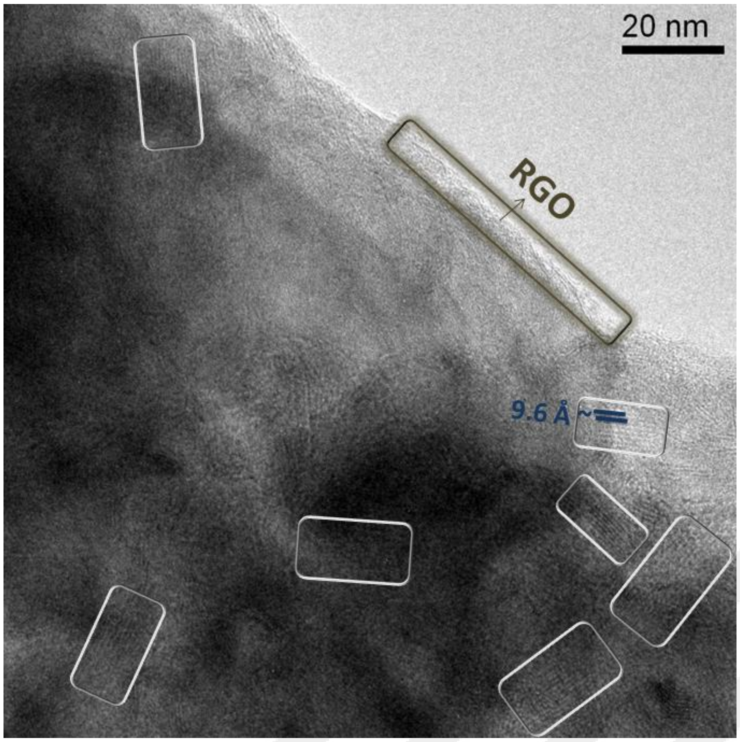

Figure 5.29 Transmission electron microscopy (TEM) image of the RGO / V_2O_5 – $LiBO_2$ glass composite indicating a fine coating of reduced graphite oxide (RGO) and embedded $Li_xV_2O_5$ nano-crystallites.

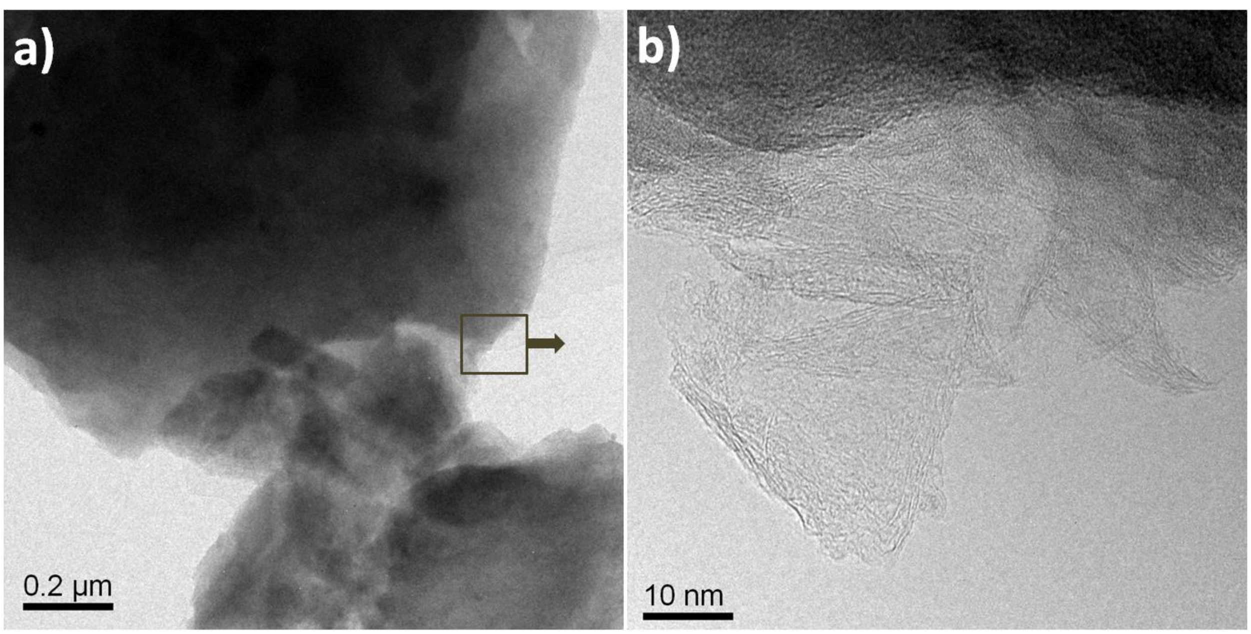

Figure 5.30 Transmission electron microscopy (TEM) images of the RGO / V_2O_5 – $LiBO_2$ glass composite displaying a) particle agglomerates b) RGO flakes on the rim of particles.

The cells with a cathode composition of ~ 74 wt-% active material, ~ 16 wt-% conductive carbon originating from the RGO (no additional carbon black) and ~ 10 wt-% PVDF were cycled between 1.5 V and 4.0 V at a rate of 50 mA/g. The first ten galvanostatic charge/discharge curves of the RGO / V_2O_5 – $LiBO_2$ glass composite are shown in **Figure 5.31.** The first discharge capacity has been raised to ~ 400 mAh/g for the composite electrode. A high capacity of ~ 390 mAh/g is reached in the subsequent charge proving that the RGO / V_2O_5 – $LiBO_2$ glass composite also does not suffer from the irreversible capacity loss associated with the phase transformations of crystalline V_2O_5. This initial charge capacity is largely preserved in the first ten cycles with ~ 96 % retention at the 10th charge. The sloping nature of galvanostatic charge/discharge curves again indicates a homogeneous phase process, and consistent with the existence of crystalline volume fractions, two small plateaus in the first discharge curve around ~ 2.5 V and ~ 2.0 V can be identified as well.

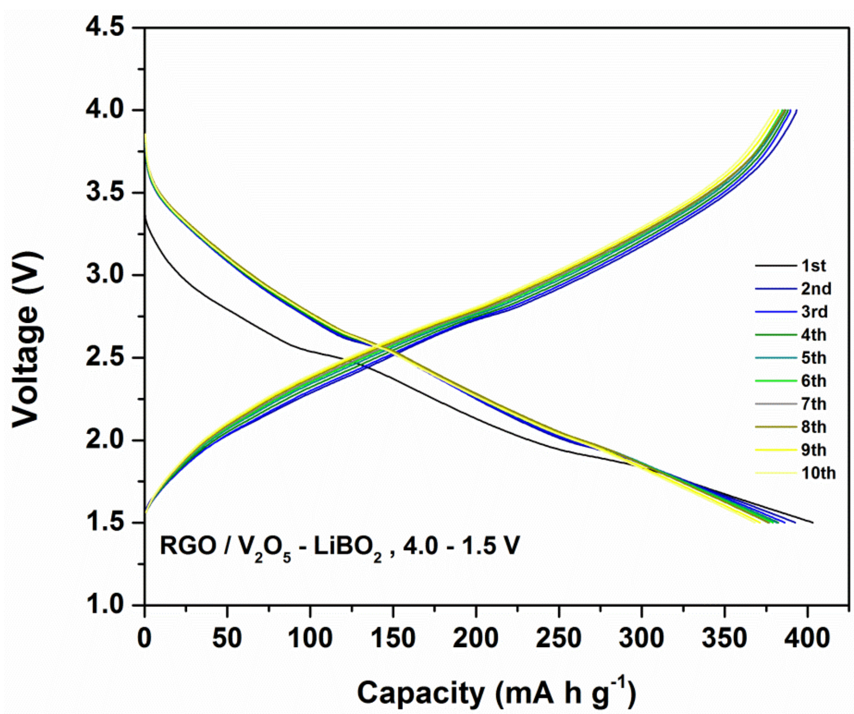

Figure 5.31 The first ten charge/discharge curves of the RGO / V_2O_5 – $LiBO_2$ glass composite in a potential window of 1.5 – 4.0 V at 50 mA/g rate.

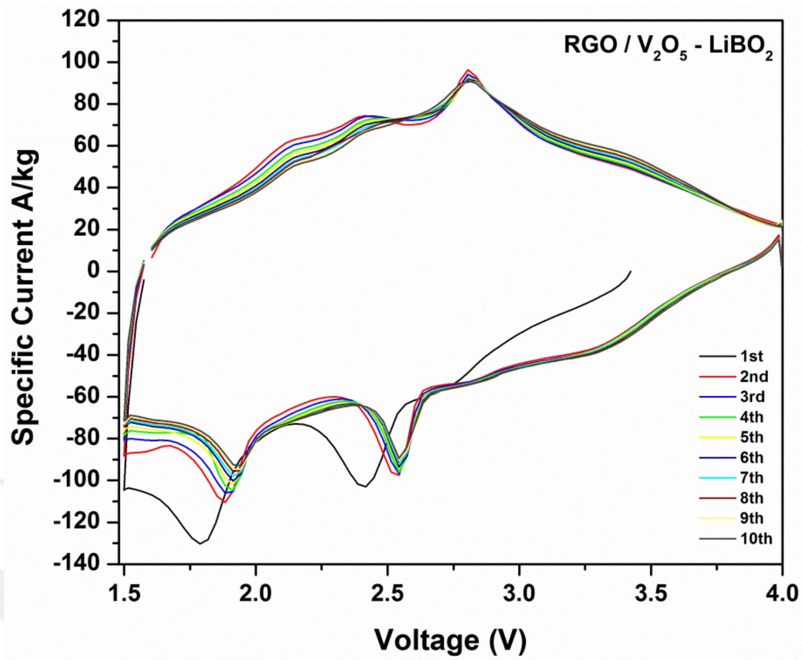

Figure 5.32 The cyclic voltammogram of the RGO / V_2O_5 – $LiBO_2$ glass composite between 1.5 and 4.0 V at a scanning rate of 0.1 mV/s.

Cyclic voltammetry studies should reveal more information about the characteristics of this electrochemical system. The cyclic voltammogram of the RGO / V_2O_5 – $LiBO_2$ glass composite for the potential window, 1.5 – 4.0 V, at a scanning rate of 0.1 mV/s is displayed in **Figure 5.32**. The first reduction cycle starts at ~ 3.4 V and continues as an expanding process in the whole voltage window. The mentioned plateaus in the first galvanostatic discharge curve appear as broad peaks at ~ 2.4 V and 1.8 V. The subsequent oxidation profile also shows peak like features at ~ 2.1, 2.4 and 2.8 V, but, again, their contribution to the total capacity is small. These regions corresponding to small plateaus in galvanostatic charge/discharge profiles can be assigned to the lithiation/delithiation of $Li_xV_2O_5$ phases. Besides, in the first ten cycles, these phases can be cycled in a reversible manner as the peaks continue to reoccur at each oxidation-reduction. On cycling, the oxidation and reduction peaks shift closer to each other, while their shapes and intensities change. These results indicate the amorphization of particles and structural changes of $Li_xV_2O_5$ phases with repeated cycling. However, it should be noted that the major lithiation/delithiation process of the RGO / V_2O_5 – $LiBO_2$ glass composite is still described as a sluggish homogeneous phase reaction with one broad peak for reduction and one broad peak for oxidation, both ranging within the complete voltage window of 1.5 – 4.0 V.

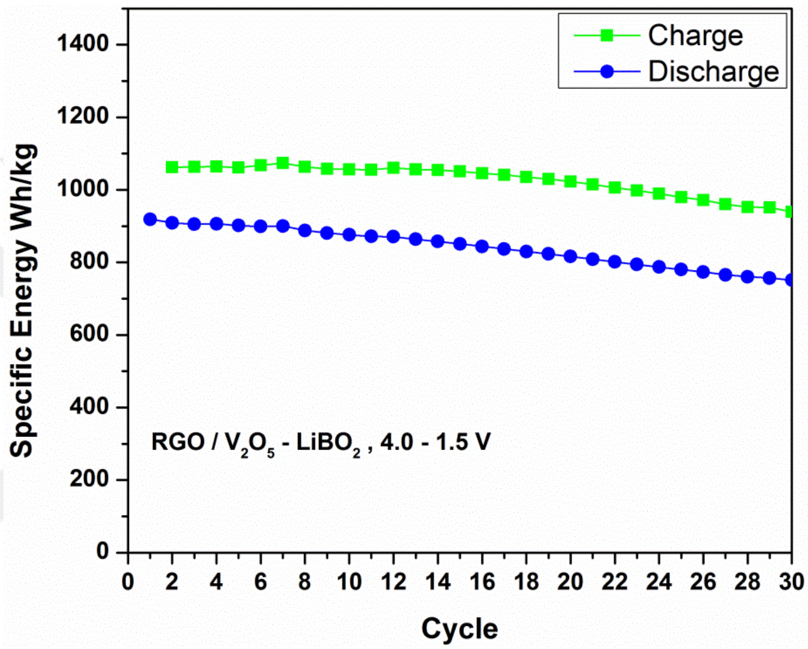

Figure 5.33 Specific energy vs. cycle number for the RGO / V_2O_5 – $LiBO_2$ glass composite in a potential window of 1.5 – 4.0 V at 50 mA/g rate.

The average discharge voltage has been increased by the utilization of the composite electrode; for instance, from ~ 2.33 V to ~ 2.37 V at the 5th galvanostatic cycle. As discharge capacities were also elevated, high specific energies in the range of ~ 900 Wh/kg are delivered within the first ten cycles (**Fig. 5.33**). A specific energy of ~ 752 Wh/kg is still available at the 30th discharge. The kinetic properties are also improved as the energetic difference between charge and discharge decreases. The specific energy for charge and discharge are ~ 1061 Wh/kg and ~ 902 Wh/kg at the 5th cycle for the RGO / V_2O_5 – $LiBO_2$ glass composite, respectively. Thus, the energy difference is decreased compared to the plain V_2O_5 – $LiBO_2$ glass electrode from 196 Wh/kg to 159 Wh/kg. Even though the overpotential still exists, the improvement made with ball-milling and conductive coating is encouraging as it shows that the problem is mainly stemming from the slow kinetics of the larger glass particles. Clearly, further optimization of the electrochemical performance can be expected.

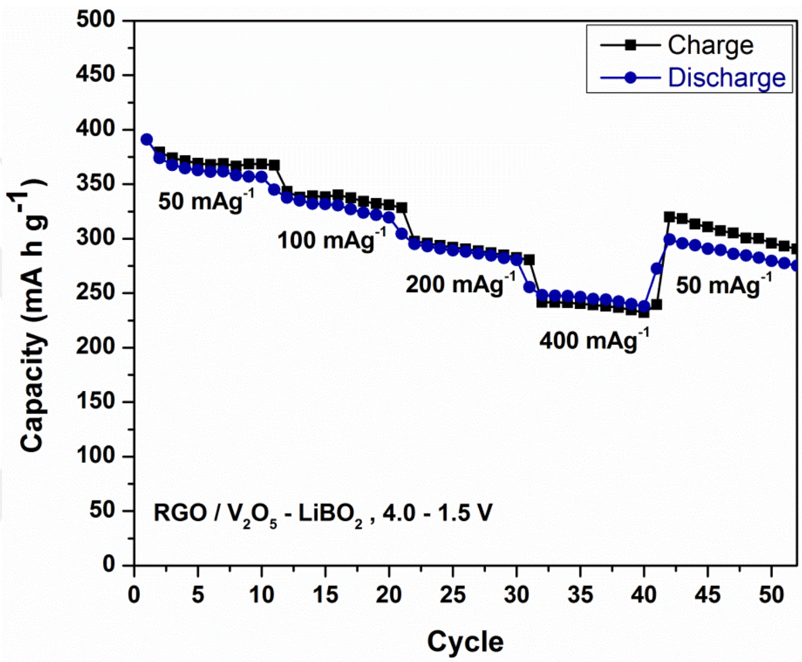

Figure 5.34 The rate capability of the RGO / V_2O_5 – $LiBO_2$ glass composite within 1.5 – 4.0 V at 50, 100, 200 and 400 mA/g rates (at room temperature).

The rate capability for the RGO / V_2O_5 – $LiBO_2$ glass composite has been enhanced as well. **Figure 5.34** shows the rate capability within first 50 galvanostatic cycles between 1.5 V and 4.0 V. For rates of 50, 100, 200 and 400 mA/g, average discharge capacities are ~ 365, 329, 288 and 244 mAh/g, respectively. When the rate is changed back from 400 mA/g to 50 mA/g, the discharge capacity recovers from 244 mAh/g to ~ 300 mAh/g at the 42nd cycle. The response of the electrochemical system to high charge/discharge rates also demonstrates the improvements arising from the composite electrode. The delivered capacity of ~ 244 mAh/g at the highest rate

(400 mA/g) almost doubles the amount obtained for the V_2O_5 – $LiBO_2$ glass electrode without RGO.

Conclusions

Compared to V_2O_5 – B_2O_3 glass ceramics and other forms of V_2O_5, much enhanced cycling properties and charge/discharge capacities were obtained for the V_2O_5 – $LiBO_2$ glass. The absence of a long range order largely circumvents a huge capacity loss in the first cycle related to the irreversible phase transformation of crystalline V_2O_5 to ω-$Li_3V_2O_5$, which cannot be cycled to its full extent within 1.5 – 4.0 V. Different from that, the lithiation/delithiation of the V_2O_5 – $LiBO_2$ glass and its composites are mostly reversible in this voltage window yielding high capacities. Furthermore, the RGO / V_2O_5 – $LiBO_2$ glass composite provides a much enhanced electrochemical performance. This can be attributed to a number of reasons: 1. In comparison to the other borate composites that were discussed in previous chapters, there are common features arising from the reduced graphite oxide network that is expected to facilitate Li^+ ion as well as electron transports, prevent contact losses under extensive cycling and may act as a protective layer against cycling by-products. 2. In addition to common characteristics with previously demonstrated composites, a much finer coating of particles is found for the V_2O_5 – $LiBO_2$ glass with only a few layers of RGO. 3. The direct coating of the surface and the network formation via reduced graphite oxide seemingly improves short and long range conductivity, respectively. 4. Effects of particle size are very prominent for the V_2O_5 – $LiBO_2$ glass system, as noticeably better kinetic properties are attained for smaller particles in terms of a decreased polarization and a better rate capability. The combination of these features of the RGO / V_2O_5 – $LiBO_2$ glass composite leads to higher charge/discharge capacities, specific energies and better capacity retention at high rates. The cycling stability though remains problematic even for the composite electrode with a gradual loss of ~ 1-2 mAh/g at each cycle.

For the RGO / V_2O_5 – $LiBO_2$ glass composite, possible structural changes associated with $Li_xV_2O_5$ phases yielding electrochemically inactive parts upon cycling is one of the reasons for capacity fading. Clearly, preventing the formation of crystalline phases is of major importance. Even though this formation was already well suppressed, the small crystalline ratio, which still exists, can be eliminated by faster quenching rates, for example by roller and twin-roller quenching techniques that may yield cooling rates of ca. 10^{4-5} K/s. Yet, there are more major fading problems that will be discussed later in this work. Nevertheless, the achieved electrochemical properties of the RGO / V_2O_5 – $LiBO_2$ glass composite already make it a competitive cathode material for rechargeable lithium batteries.

5.3.3 V_2O_5 – NiO – $LiBO_2$ glass

The introduction of nickel into mixed layered oxides and lithium manganese spinels, and the use of these compounds as cathode materials for Li-ion batteries have been widely reported in previous investigations. High specific energies stemming from the redox reactions of nickel are obtained for layered oxides like $Li_xMn_{0.5}Ni_{0.5}O_2$[91] and $LiMn_{1/3}Ni_{1/3}Co_{1/3}O_2$[93]. For the spinel compound, $Li_xNi_{0.5}Mn_{1.5}O_4$[113], a relatively high operating potential of ~ 4.80 V is realized compared to that of the pure Mn-based spinel $Li_xMn_2O_4$[101, 258] (~ 3.95 V) due to the high potential redox couple Ni^{2+}/Ni^{3+}. Also improved in this way is the capacity retention during cycling through an enhanced chemical stability with respect to electrolyte decomposition at high potentials and by a structure showing only little volume expansion/contraction and degradation at repeated lithium insertion/ extraction[113-114, 259]. Considering this, to further explore and improve properties of V_2O_5 – $LiBO_2$ glasses as cathode materials for rechargeable lithium batteries, the quaternary Li_2O – B_2O_3 – NiO – V_2O_5 glass system was selected for investigation. A glass forming melt in this system is made with 80 wt-% V_2O_5, 15 wt-% $LiBO_2$ and 5 wt-% NiO at 900 ^{o}C that is quenched to room temperature between two Cu plates. XRD powder pattern of the 80-5-15 wt-% V_2O_5 – NiO – $LiBO_2$ glass is illustrated in **Figure 5.35**. Differing from the V_2O_5 – $LiBO_2$ glass no reflections due to any crystalline $Li_xV_2O_5$ phases are found. A complete vitrification is found in this system.

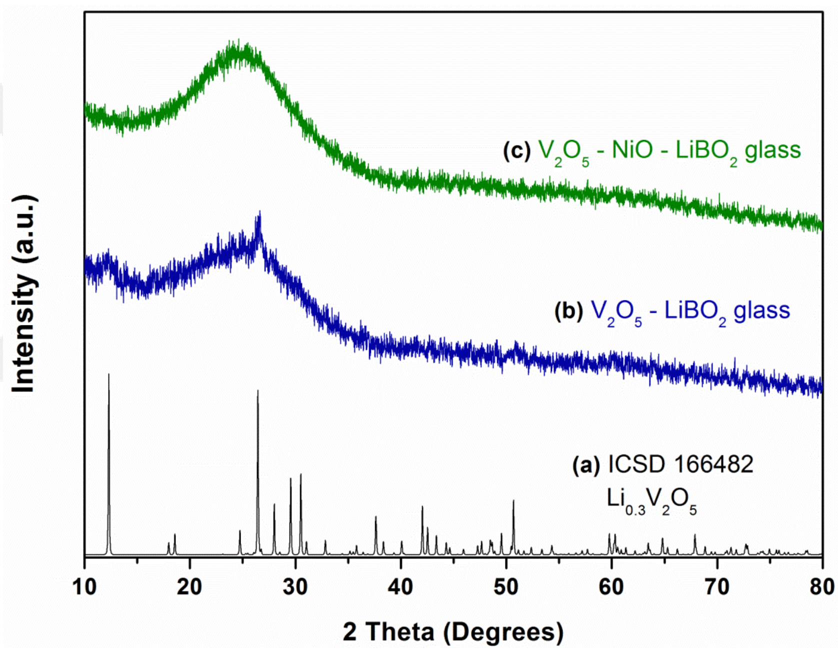

Figure 5.35 XRD powder pattern of (a) $Li_{0.3}V_2O_5$ (theoretical), (b) the Ni-free glass and (c) the V_2O_5 – NiO – $LiBO_2$ glass.

Differential thermal analysis (DTA) also verifies the glass formation. The DTA curve of the 80-5-15 wt-% V_2O_5 – NiO – $LiBO_2$ glass is displayed in **Figure 5.36**. The glass transition starts at ~ 225 ^{o}C and ends at ~ 244 ^{o}C, respectively, followed by exothermic effects that are assigned to the formation of crystalline phases. The melting region for the crystalline phases corresponds to a range of ~ 550-700 ^{o}C, as it can be estimated from the heating curve. In the cooling curve that was obtained at a rate of 10 K/min under air flow (red curve in **Fig. 5.36**), two exothermic peaks are observed indicating the crystallization of two different phases.

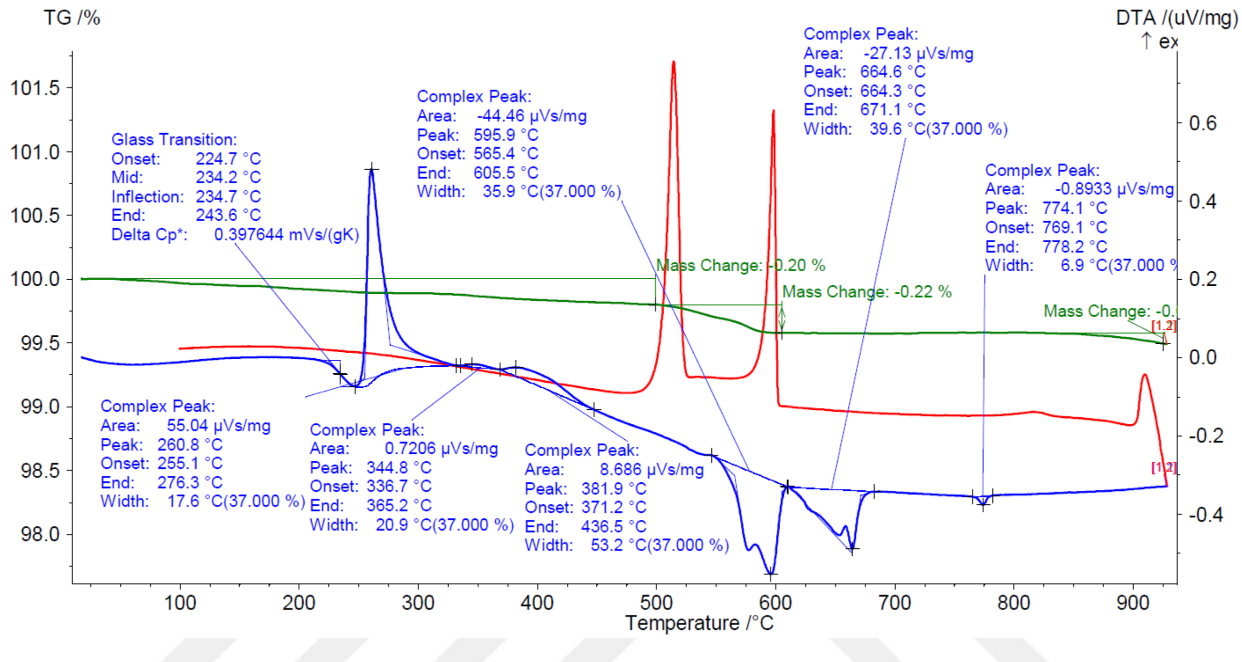

Figure 5.36 Differential thermal analysis (DTA) of the V_2O_5 – NiO – $LiBO_2$ glass.

Changes in the physical properties of the V_2O_5 – $LiBO_2$ glass in terms of an increase in T_g by ~ 30 °C and less tendency for crystalline precipitation should be attributed to the influence of NiO as a network modifier. Network modifiers usually have weaker metal to oxygen bonds and larger coordination numbers compared to network formers, but cannot form glasses by themselves with an absence of bridging polyhedra[252]. If a network modifier is replaced with another one that has greater bond strength, higher coordination number and larger packing density, an elevation of the glass transition temperature (T_g) is expected[248, 260]. In our case, the modification of the V_2O_5 – $LiBO_2$ glass can be explained by the replacement of the network modifier Li_2O by NiO. Bond dissociation energies for Li – O and Ni – O in diatomic molecules are reported to be 340 ± 6.3 kJ/mol and 366 ± 30 kJ/mol, respectively[261], and the coordination in the glass network is expected to be tetrahedral for lithium and octahedral for nickel, respectively. Thus, an increase of cross linking density and bond strength is realized by the introduction of NiO into the V_2O_5 – $LiBO_2$ glass. Accordingly, the 80-5-15 wt-% V_2O_5 – NiO – $LiBO_2$ glass has a glass transition temperature of ~ 235 °C compared to ~ 205 °C for the 80-20 wt-% V_2O_5 – $LiBO_2$ glass, and it lacks any crystalline phases.

The higher T_g also circumvents the formation of crystalline $Li_xV_2O_5$ phases during the heat treatment at 200 °C, which is necessary for the reduction of graphite oxide during the formation of glass composite electrodes. XRD powder patterns of graphite oxide, the plain V_2O_5 – NiO – $LiBO_2$ glass and the RGO / V_2O_5 – NiO – $LiBO_2$ glass composite are displayed in **Figure 5.37**. No reflections indicating crystalline phases are observed. Graphite oxide is partially reduced and delaminated, similar to the previously described composite electrodes.

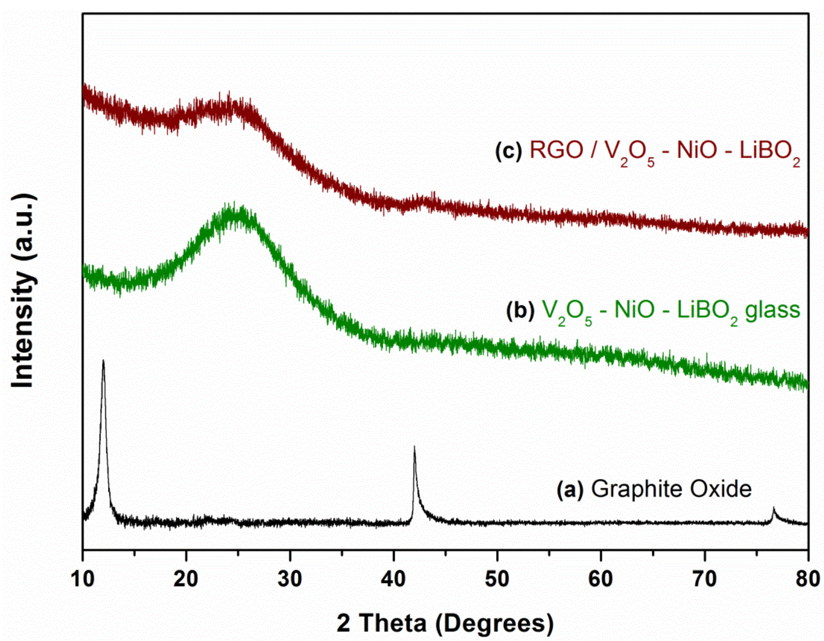

Figure 5.37 XRD powder patterns of a) graphite oxide, b) V_2O_5 – NiO – $LiBO_2$ glass, c) RGO / V_2O_5 – NiO – $LiBO_2$ glass composite.

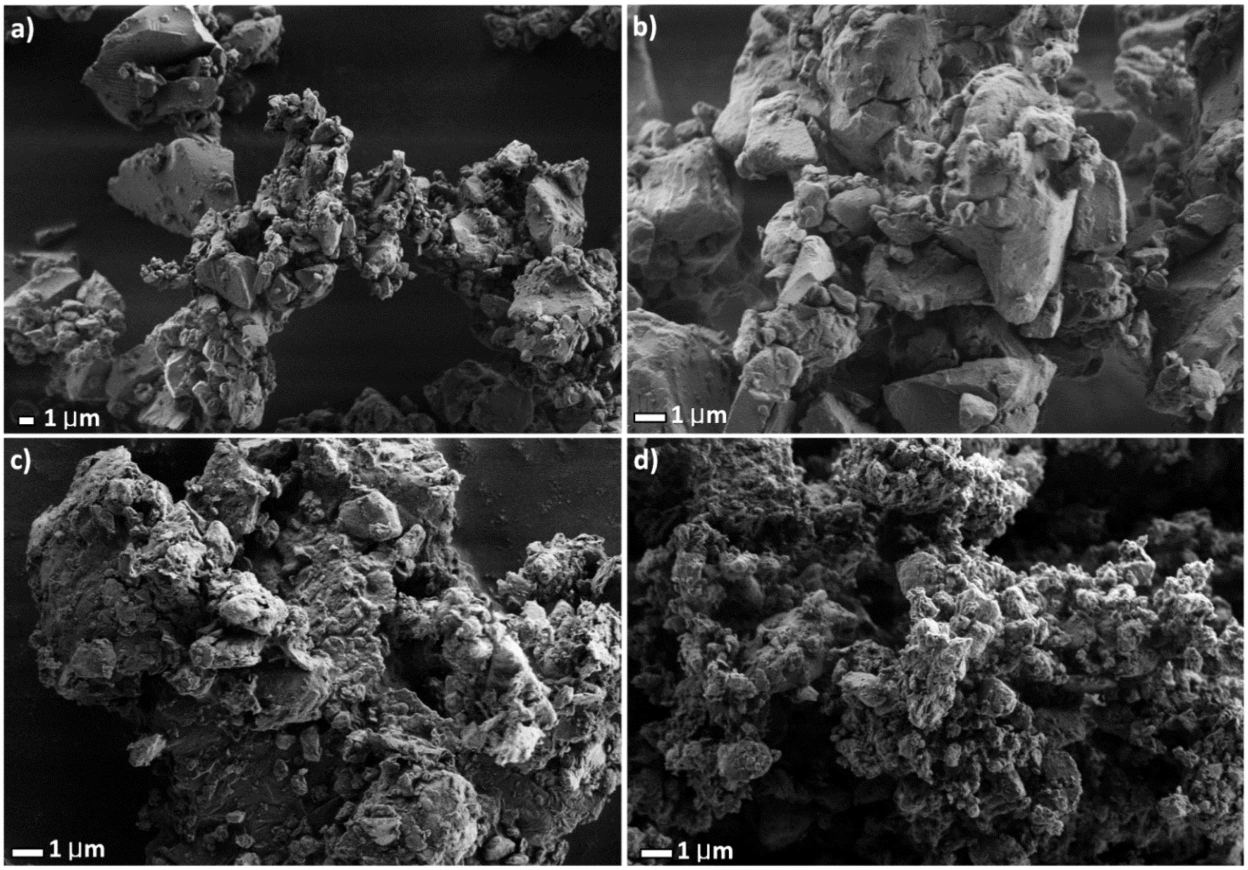

Figure 5.38 Scanning electron micrographs (SEM) of a) & b) the V_2O_5 – NiO – $LiBO_2$ glass, c) & d) the RGO / V_2O_5 – NiO – $LiBO_2$ glass composite.

Consequently, homogenous glass fragments in the micron regime are found in scanning electron microscopy (SEM) images of the V_2O_5 – NiO – $LiBO_2$ glass (**Fig. 5.38a & 38b**). On ball-milling with graphite oxide, these fragments can be ground to sub-micron size, and a well-mixed composite with reduced graphite oxide is achieved after consecutive heat treatment (**Fig. 5.38c & 38d**). In line with the results of X-ray powder diffraction, transmission electron microscopy (TEM) studies verify the glassy nature of V_2O_5 – NiO – $LiBO_2$ glass. The morphology of glass blocks is similar to those of the V_2O_5 – $LiBO_2$ glass with unspecific morphologies (**Fig. 5.39a**). No crystalline regions have been detected even at a scale of 10 nm (**Fig. 5.39b**). Electron diffraction patterns lacking concentric rings further support the absence of nano-crystalline $Li_xV_2O_5$ phases (**Fig. 5.39c**). Agglomerates of sub-micron sized glass particles cemented by the reduced graphite oxide are observed in TEM images of the RGO / V_2O_5 – NiO – $LiBO_2$ glass composite (**Fig. 5.39d**). The rolled flakes of reduced graphite oxide, coating and connecting glass particles can be seen in **Figures 5.39e** and **5.39f**, respectively. The nature of coating and network formation appears to be similar to the previous composites, so a positive influence on the electrochemical performance of the system is expected.

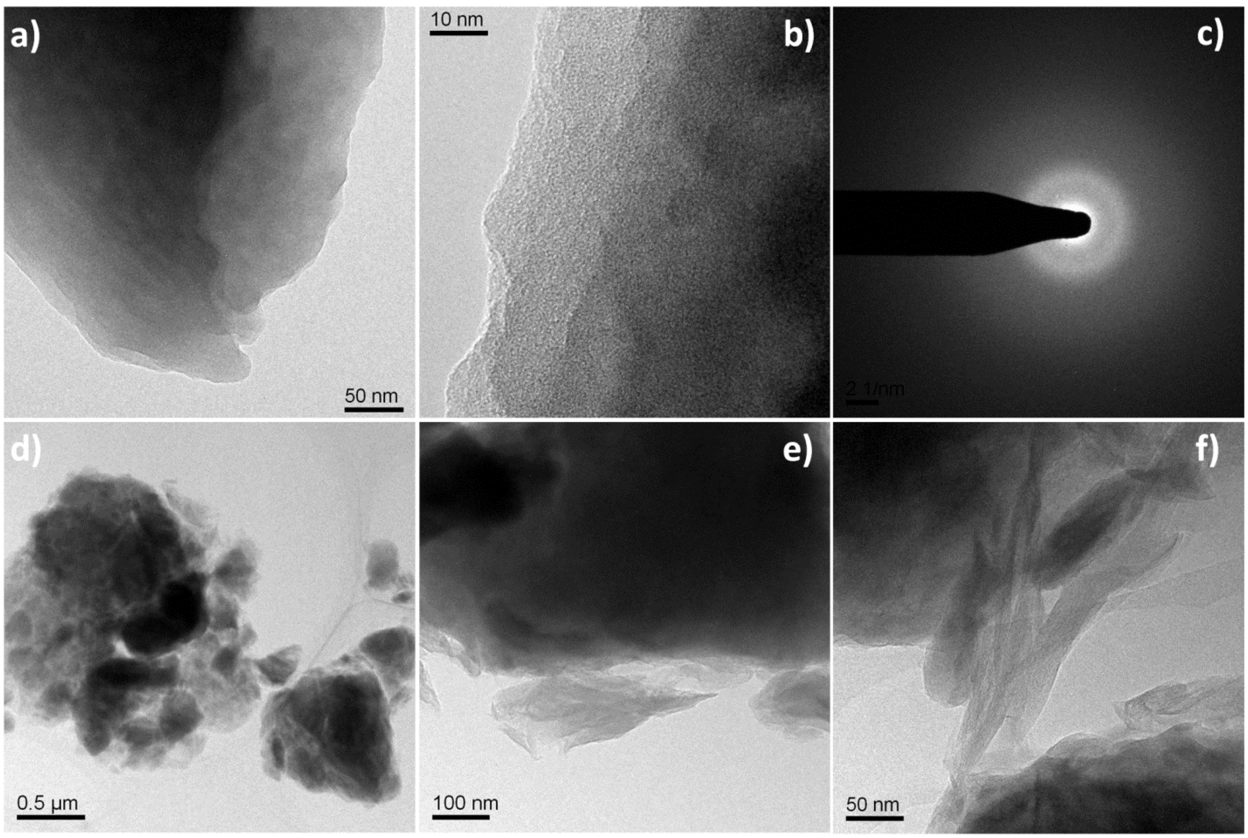

Figure 5.39 Transmission electron micrographs (TEM) of a) the V_2O_5 – NiO – $LiBO_2$ glass showing particle morphology, b) the V_2O_5 – NiO – $LiBO_2$ glass indicating the lack of crystalline regions, c) electron diffraction (ED) pattern of the V_2O_5 – NiO – $LiBO_2$ glass. TEM images of the RGO / V_2O_5 – NiO – $LiBO_2$ glass composite displaying d) particle agglomerates, e) RGO flakes on the rim of glass particles, f) connection of glass particles through RGO flakes.

In order to confirm that NiO is not present in the glass as a separated amorphous phase, high angle annular dark field (HAADF) scanning transmission electron microscopy (STEM) imaging was also employed. The technique is sensitive to the variations of atomic numbers in the sample, so it can be used to track heavier elements in the material. If NiO is not uniformly distributed in the glass matrix, specific brighter regions have to be observed in high angle annular dark field images, since nickel has a larger number of electrons than all other elements of the glass sample. HAADF image of the RGO / V_2O_5 – NiO – $LiBO_2$ glass composite and energy dispersive X-ray (EDX) spectra acquired from different areas in this image are displayed in **Figure 5.40**. No obvious contrast difference is found, and EDX spectra of different glass regions verify the homogeneous distribution of Ni over the glass.

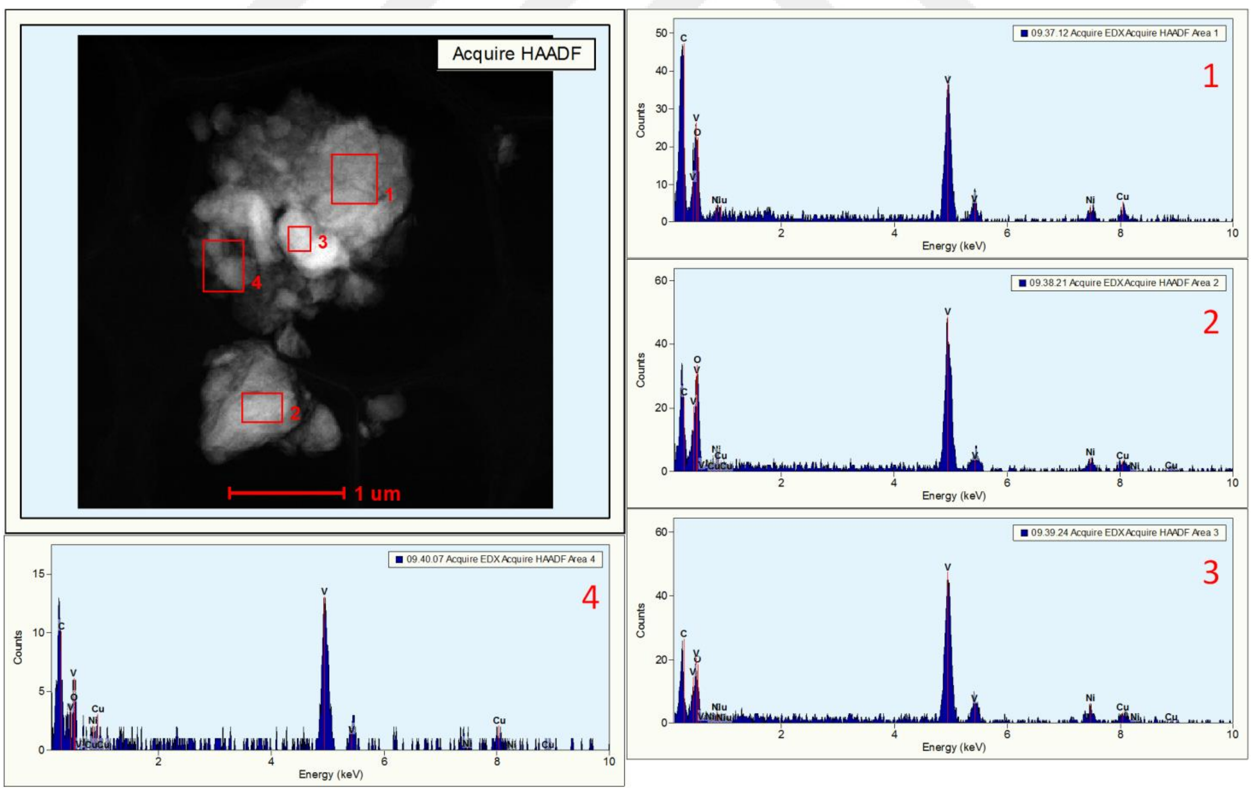

Figure 5.40 High angle annular dark field (HAADF) scanning transmission electron microscopy (STEM) imaging for the RGO / V_2O_5 – NiO – $LiBO_2$ glass composite, and energy dispersive X-ray (EDX) spectra of the marked regions.

Electrochemical Investigations

For the electrochemical characterization, no additional conductive carbon was added into the electrode mixture. Similar to previously investigated cathode composites, cells with a working electrode composition of ~ 74 wt-% active material, ~ 16 wt-% conductive carbon in the form of reduced graphite oxide and ~ 10 wt-% PVDF were assembled to be tested in a galvanostatic protocol within a potential window 1.5 – 4.0 V at a rate of 50 mA/g. **Figure 5.41** shows galvanostatic charge/discharge curves for the RGO / V_2O_5 – NiO – $LiBO_2$ glass composite during the first ten cycles.

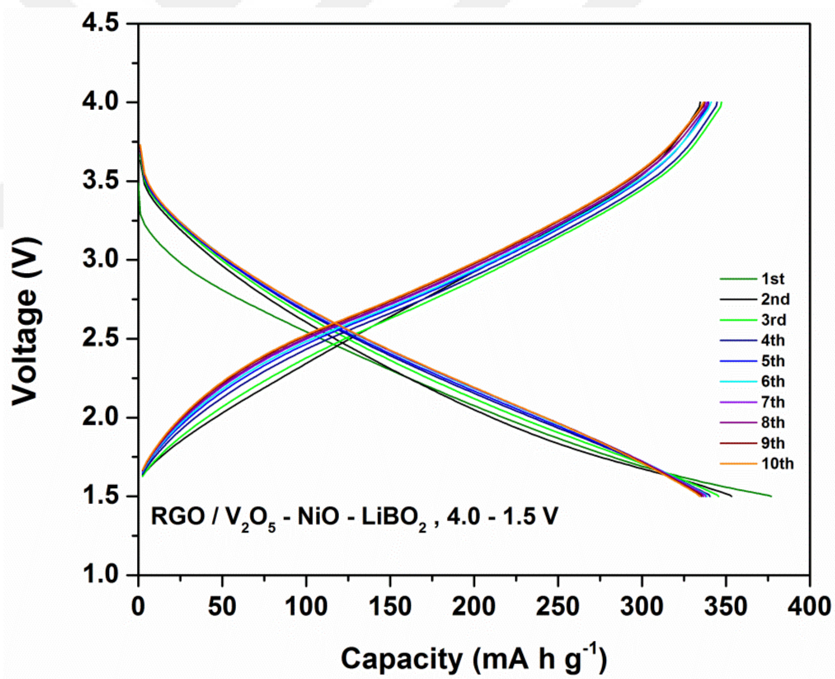

Figure 5.41 The first ten charge/discharge curves of the RGO / V_2O_5 – NiO – $LiBO_2$ glass composite in a potential window of 1.5 – 4.0 V at 50 mA/g rate.

A high discharge capacity of ~ 377 mAh/g is obtained in the first cycle. The capacity remains at ~ 335 mAh/g for the first charge, but it recovers back to ~ 348 mAh/g in the subsequent cycle. The recovery might be explained by the activation of larger glass particles that are reduced in size through mechanical stress upon lithiation/delithiation. The cycling is reversible in subsequent charge/discharge curves, and a capacity of ~ 335 mAh/g is maintained at the 10th galvanostatic discharge. The galvanostatic cycling measurements yield featureless curves with gradual increases-decreases of voltage as expected for glassy material.

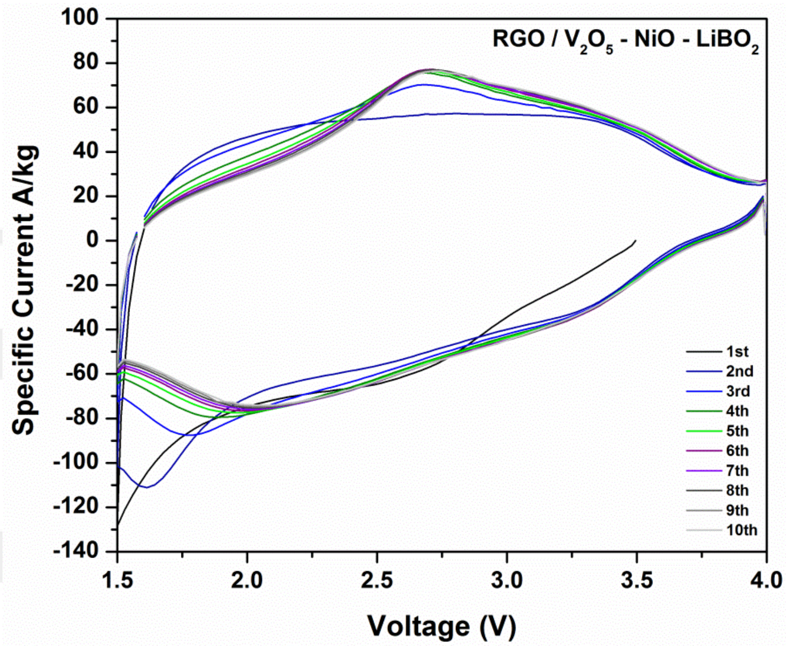

Figure 5.42 The cyclic voltammogram of the RGO / V_2O_5 – NiO – $LiBO_2$ glass composite between 1.5 V and 4.0 V at a scanning rate of 0.1 mV/s.

The cyclic voltammogram of the RGO / V_2O_5 – NiO – $LiBO_2$ glass composite is depicted in **Figure 5.42** for the potential window of 1.5 – 4.0 V at a scanning rate of 0.1 mV/s. The shape of the curves closely resembles to those of the RGO / V_2O_5 – $LiBO_2$ glass composite but with an absence of distinct oxidation-reduction peaks stemming from the nano-crystalline $Li_xV_2O_5$ phases. The broad oxidation and reduction peaks cover the whole voltage range with maxima at ~ 2.7 V and ~ 2.1 V, respectively, in the 10th cycle. The difference between peak positions is larger in the first cycle but decreases with cycling. However, the overall polarization does not disappear, and even slightly increases with ongoing cycling. **Figure 5.43** illustrates this polarization and cycling properties in terms of specific energy within first 30 galvanostatic cycles. Specific energies of ~ 951 Wh/kg and ~ 810 Wh/kg are delivered at the 5th cycle. Thus, with a difference of ~ 141 Wh/kg, the polarization is slightly decreased compared to the RGO / V_2O_5 – $LiBO_2$ glass composite; however, specific capacities are smaller compared to the RGO / V_2O_5 – $LiBO_2$ glass composite. Besides, average discharge voltages (~ 2.37 V at the 5th cycle) in the range of 1.5 – 4.0 V are not raised by the nickel content. The unchanged potential and decreased capacity for the RGO / V_2O_5 – NiO – $LiBO_2$ glass composite are interpreted such that the Ni^{2+}/Ni^{3+} redox couple does not become active in the voltage window of 1.5 – 4.0 V.

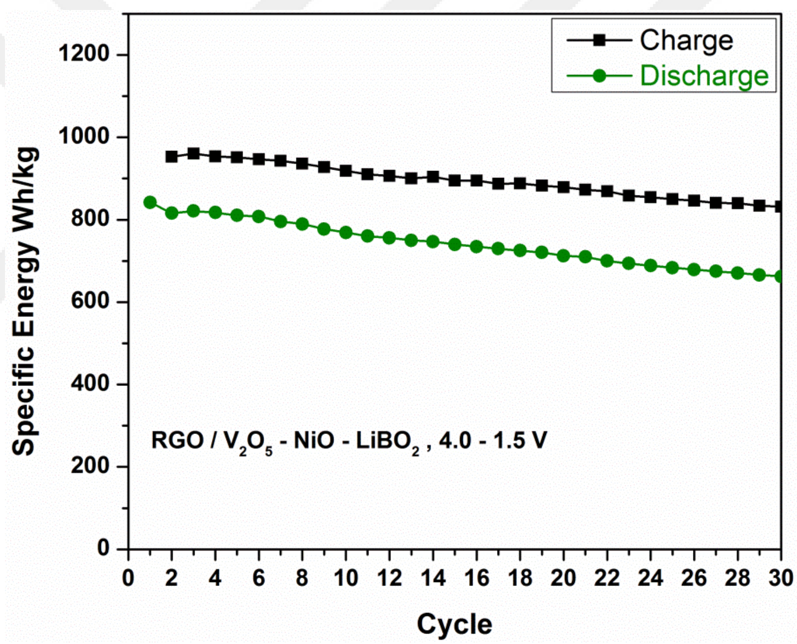

Figure 5.43 Specific energy vs. cycle number for the RGO / V_2O_5 – NiO – $LiBO_2$ glass composite in a potential window of 1.5 – 4.0 V at 50 mA/g rate.

However, when the potential range is expanded to 1.5 – 4.5 V, the RGO / V_2O_5 – NiO – $LiBO_2$ glass composite shows an enhanced cycling stability and an average voltage raise by ca. 0.2 V compared to the RGO / V_2O_5 – $LiBO_2$ glass composite. This hints at an activation of the Ni^{2+}/Ni^{3+} redox couple under these conditions. However, the capacity fades exponentially after 50 cycles for the RGO / V_2O_5 – NiO – $LiBO_2$ glass composite as well (**Fig. 5.44**). The capacity fading for the high potential charge might be explained by the loss of oxygen from the system followed by electrolyte oxidation, as described in the literature for other systems[262-263]. Similar to the case of spinel compounds ($Li_xNi_{0.5}Mn_{1.5}O_4$)[113-114], the introduction of nickel into the glass might be circumventing this problem to some extent, as the electrochemical reaction in the high potential range goes by the oxidation of Ni^{2+} to Ni^{3+} rather than the loss of oxygen from the material.

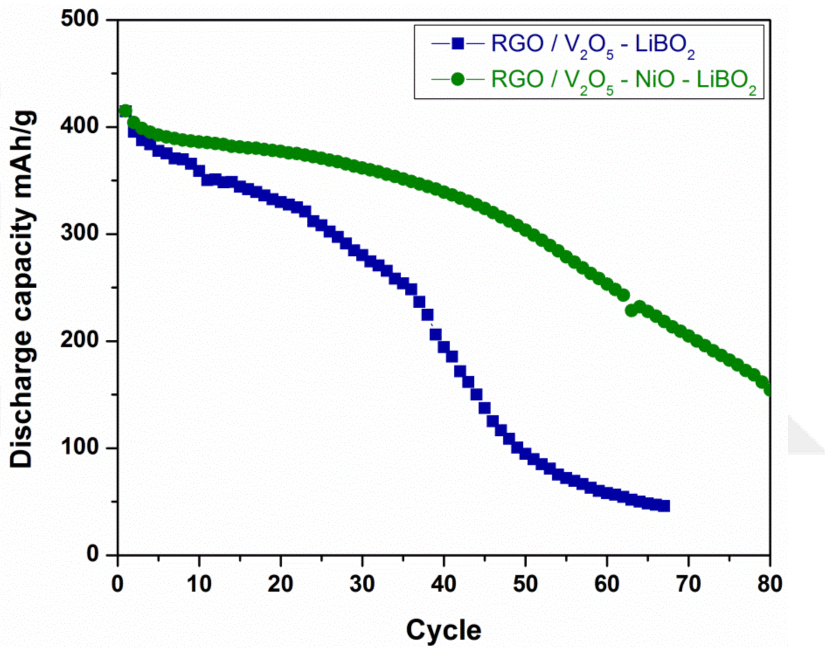

Figure 5.44 Discharge capacity vs. cycle number for RGO / V_2O_5 – $LiBO_2$ glass composite (blue) and RGO / V_2O_5 – NiO – $LiBO_2$ glass composite (green) within 1.5 – 4.5 V at a rate of 25 mA/g.

Figure 5.45 shows the rate capability for the RGO / V_2O_5 – NiO – $LiBO_2$ glass composite within the potential window of 1.5 – 4.0 V. The discharge capacities are in the range of ~ 340, 305, 265 and 220 mAh/g for the rates of 50, 100, 200 and 400 mA/g, respectively. As usual, with increasing rates, the capacities decline at a decrease ratio similar to the RGO / V_2O_5 – $LiBO_2$ glass; however, the capacity retention is slightly enhanced for the NiO glass, with a recovery to ~ 308 mAh/g at the 42nd cycle when the rate is changed back from 400 mA/g to 50 mA/g. After this point, for the next ten cycles, the average discharge capacity loss is only ~ 0.6 % per cycle.

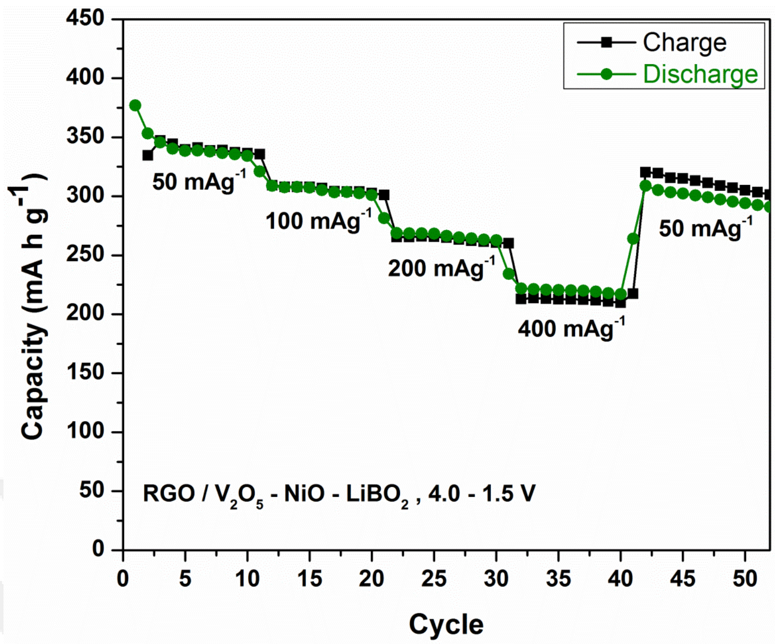

Figure 5.45 The rate capability of the RGO / V_2O_5 – NiO – $LiBO_2$ glass composite within 1.5 – 4.0 V at 50, 100, 200 and 400 mA/g rates (at room temperature).

Conclusions

It can be concluded that for the RGO / V_2O_5 – NiO – $LiBO_2$ glass composite compared to the RGO / V_2O_5 – $LiBO_2$ glass composite within 1.5 – 4.0 V; 1. the initial charge/discharge capacities have slightly decreased, 2. the average charge/discharge voltages have not changed drastically, 3. the cycling stability has been slightly improved. One possible explanation for the improvement of stability could be the cycling of a full glass that is realized by the introduction of NiO into the V_2O_5 – $LiBO_2$ glass as a network modifier enhancing the glassy nature. Thus, capacity losses in the Ni-free system related to structural changes and amorphization of the initially crystalline phases do not show up in the pure glass. However, capacity retention is not considerably better for the RGO / V_2O_5 – NiO – $LiBO_2$ composite, so it could be also claimed that the minor development for the Ni-doped sample stems from the insertion/deinsertion of less lithium compared to the Ni-free glass meaning a reduced electrochemical stress on the system.

Nevertheless, the capacity retention in the range of ~ 300 mAh/g for the first 50 galvanostatic cycles makes the V_2O_5 – NiO – $LiBO_2$ glass an interesting cathode material for rechargeable lithium batteries.

5.3.4 Cycling stability and post-mortem analysis of glass electrodes

Post-mortem analyses of the glass composite electrodes were carried out in order to reveal more information on lithiation/delithiation mechanisms, SEI formation and changes in morphology and linkage properties of electrodes. The primary goal of this is to better understand microscopic changes and gradual composite modifications that would allow to advance electrochemical cycling stability of the V_2O_5 – $LiBO_2$ glass system.

XRD powder patterns of the electrodes of the RGO / V_2O_5 – $LiBO_2$ glass composite in the charged and discharged states are depicted in **Figure 5.46**. For nano-crystalline $Li_xV_2O_5$ phases, it can be seen that the major diffraction peaks slightly shift back and forth, when electrodes are charged and discharged. The broadening and almost disappearance of the major diffraction peaks with extensive cycling indicate the amorphization of the crystalline parts. These results agree well with the results from cyclic voltammetry that prove the reversible cycling and capacity losses, which can be associated with crystalline $Li_xV_2O_5$ phases.

Unexpectedly, the formation of Li_2O_2 was discovered in the first discharge of the RGO / V_2O_5 – $LiBO_2$ glass composite. According to standard knowledge one would expect an SEI layer to be produced in the first discharge; however, lithium peroxide is formed and decomposed in a reversible way in subsequent cycles! Also, to the best of our knowledge, the formation of Li_2O_2 is unusual and has not been reported as a special kind of SEI layer for such cathode materials. Thus, the formation of lithium peroxide might be indicating a partial conversion reaction for the lithiation/delithiation of V_2O_5 – $LiBO_2$ glasses. In a recent study by Lu et al., Li_2O_2 was reversibly cycled on the surface of a $Li_xV_2O_5$ cathode at $p(O_2) = 5 \times 10^{-4}$ atm, but, no lithium peroxide was formed under ultra-high vacuum (~ 10^{-11} atm)[264]. One cannot ultimately rule out that the presence of Li_2O_2 in our experiments might be stemming from environmental oxygen entering into Swagelok-type cells during cycling of batteries. However, in our tested electrodes, Li_2O_2 was formed in substantial amounts because it makes up for quite pronounced diffraction peaks. This makes formation of Li_2O_2 via environmental oxygen less likely. But, still, Li_2O_2 formation by a side reaction is a possibility. Also probable is a direct conversion reaction of incoming Li^+ ions on the surfaces of larger glassy particles due to hindered Li^+ ion mobility into the glass bulk. After ongoing amorphization this kinetically controlled equilibrium state diminishes and enters into more homogeneous uptake of Li into the glass body.

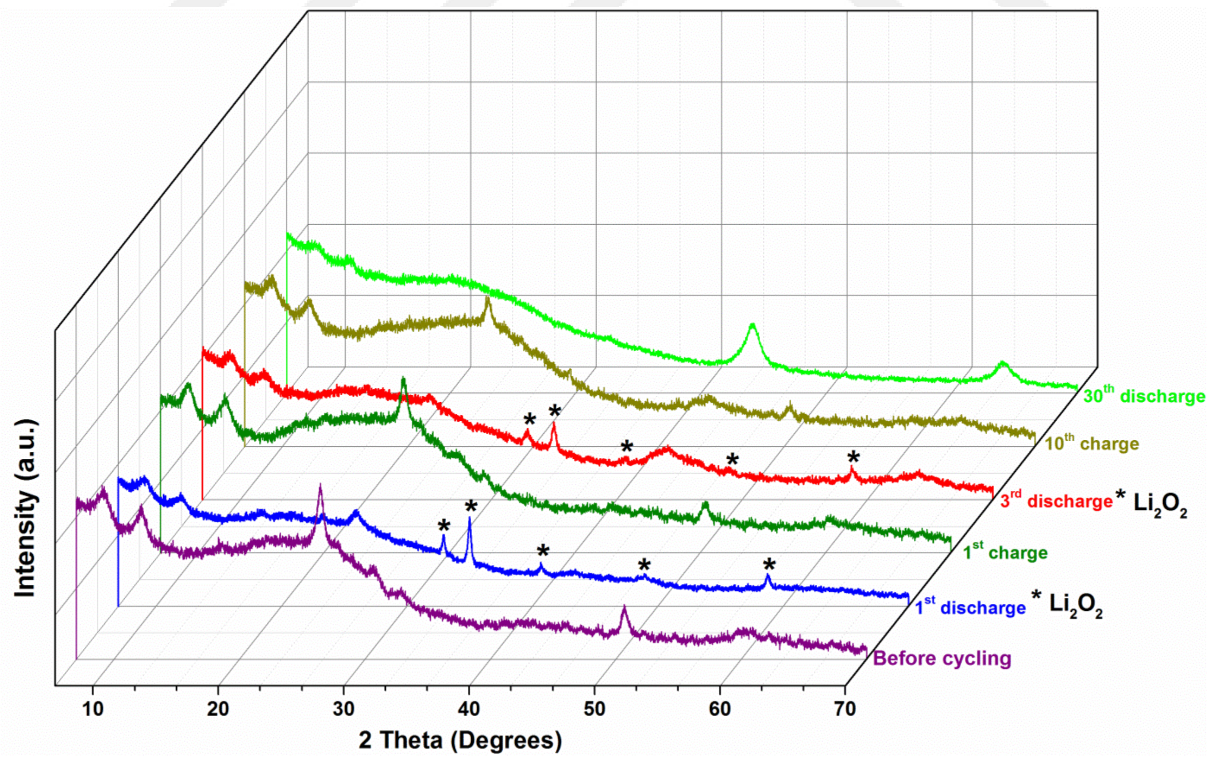

Figure 5.46 XRD powder patterns of the electrodes of the RGO / V_2O_5 – $LiBO_2$ glass composite in the charged and discharged states.

At the 30th discharge, two broad reflections at 2Θ = ~ 44 and ~ 64 can be clearly seen. The same diffraction peaks are already observed in the third cycle, but with smaller intensity. The ω-$Li_3V_2O_5$ phase was reported to have a similar diffraction pattern[210], so some portion of the V_2O_5 – $LiBO_2$ glass particles may have been transformed into this phase upon cycling. Since the $Li_xV_2O_4$ and Li_xVO_2 phases have also major diffraction peaks at the stated values, a phase separation mechanism according to the below reaction (or other possible conversion reactions) may also be possible for a part of the glass in agreement with the formation of Li_2O_2. However, it should be noted that the ex-situ XRD characterization of cycled electrodes based on a few reflections is not sufficient to make definitive conclusions.

$$Li_yV_2O_5 + x\,Li \rightarrow Li_{x+y-z}V_2O_{5-z} + \tfrac{1}{2}\,z\,Li_2O_2$$

Li_2O_2 cannot be found in the XRD powder pattern of the RGO / V_2O_5 – $LiBO_2$ glass composite at the 30th discharge. Similar findings in the ex-situ XRD characterization of electrodes were also reported in the field of Li-O_2 batteries, and they were claimed to be the indications of a decrease in the reversible formation-decomposition of Li_2O_2 and capacity fading with the accumulation of Li_2CO_3, HCO_2Li and CH_3CO_2Li from electrolyte decomposition in the cathode[265]. In our case, if the conversion reaction through the formation of Li_2O_2 is really a part of the lithiation/delithiation mechanism rather than a side reaction, the reversible formation/decomposition of Li_2O_2 could have deteriorated upon cycling similarly to Li-O_2 batteries. Thus, lithium atoms are only intercalated/deintercalated to vanadium oxide phases in the upcoming cycles that would also count for a part of the capacity fading. Nevertheless, further investigations are necessary to reveal the exact source of Li_2O_2 formation and to understand the electrochemical reactions during cycling.

Figure 5.47 Parts of a disassembled RGO / V_2O_5 – $LiBO_2$ glass composite cell after galvanostatic cycling displaying the coloration of electrolyte and separators.

Though one or two problems causing the cycling instability for V_2O_5 based glass electrodes were previously described, the main reasons of capacity fading over extensive cycling are considered to be the vanadium dissolution into the electrolyte and the formation of electrochemically inactive phases and contact losses upon cycling. An inspection of a disassembled RGO / V_2O_5 – $LiBO_2$ glass composite cell after multiple charge/discharge cycles supports this as shown in **Figure 5.47**. The coloration of electrolyte and separators indicate to vanadium transport away from the glass composite. This assumption is further verified by energy-dispersive X-ray spectra of cycled electrode composites. **Figure 5.48** shows the SEM-EDX analysis of the material deposited on the Li anode from a cell of RGO / V_2O_5 – $LiBO_2$ glass composite after 30 cycles. The vanadium signal is found along with other elemental signals corresponding to the electrolyte decomposition products. The vanadium dissolution into the electrolyte is thought to cause capacity fading at each cycle by a combined effect with the loss of active mass on the cathode and the deposition of an insulating layer on the anode. Similar observations and explanations could be also found in the literature about the cycling stability of various forms of V_2O_5[209, 266-267]. The formation of inactive phases after multiple cycles is another explanation[209, 268-270] that should go in line with the dissolution as new phases are supposed to be formed with the loss of vanadium and amorphous layer deposition occurring both on anode and cathode sides.

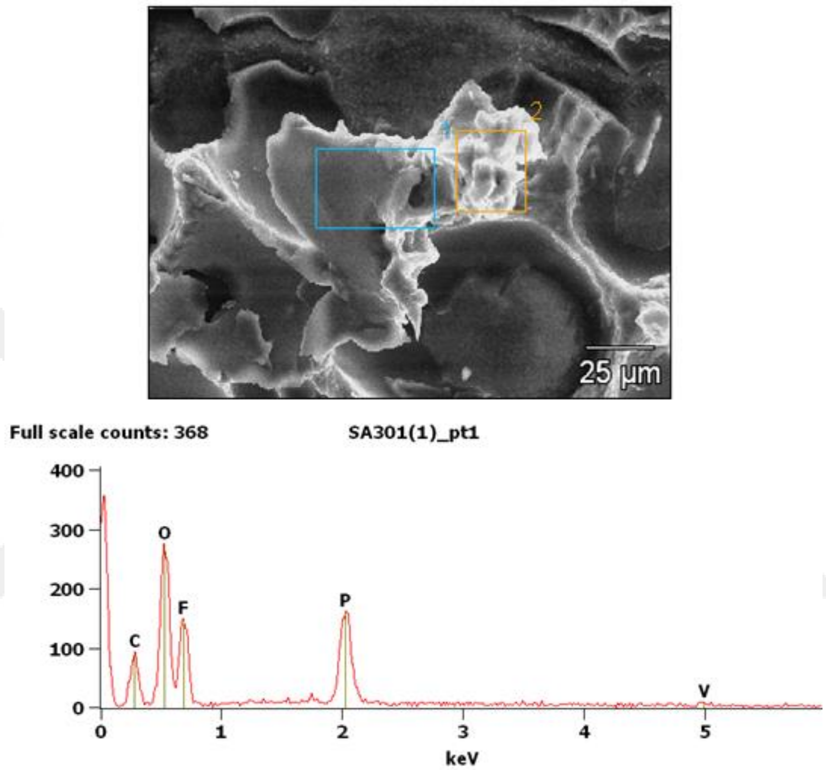

Figure 5.48 Scanning electron microscopy (SEM) image of a deposit on Li anode, and energy dispersive X-ray (EDX) spectrum of the marked region confirming the vanadium dissolution (the deposit taken from a cell of RGO / V_2O_5 – $LiBO_2$ glass composite after 30 cycles).

Scanning electron microscopy images (SEM) of the cycled electrodes of V_2O_5 – $LiBO_2$ glasses that are displayed in **Figure 5.49** verify the presence of these phases. A deposit of an amorphous film can be found on most of the electrodes that are charged/discharged over ~ 50 cycles (**Figure 5.49a & 49b**). The emergence of new crystallites underneath the film and at other regions with various morphologies not belonging to the parent glass is also observed upon extensive cycling (**Figure 5.49b, 49c & 49d**). A loss of contact and deterring linkage in the electrode could be already seen, whether the newly formed phases are electrochemically active or not, since they spike out of the active material (**Figure 5.49c & 49d**).

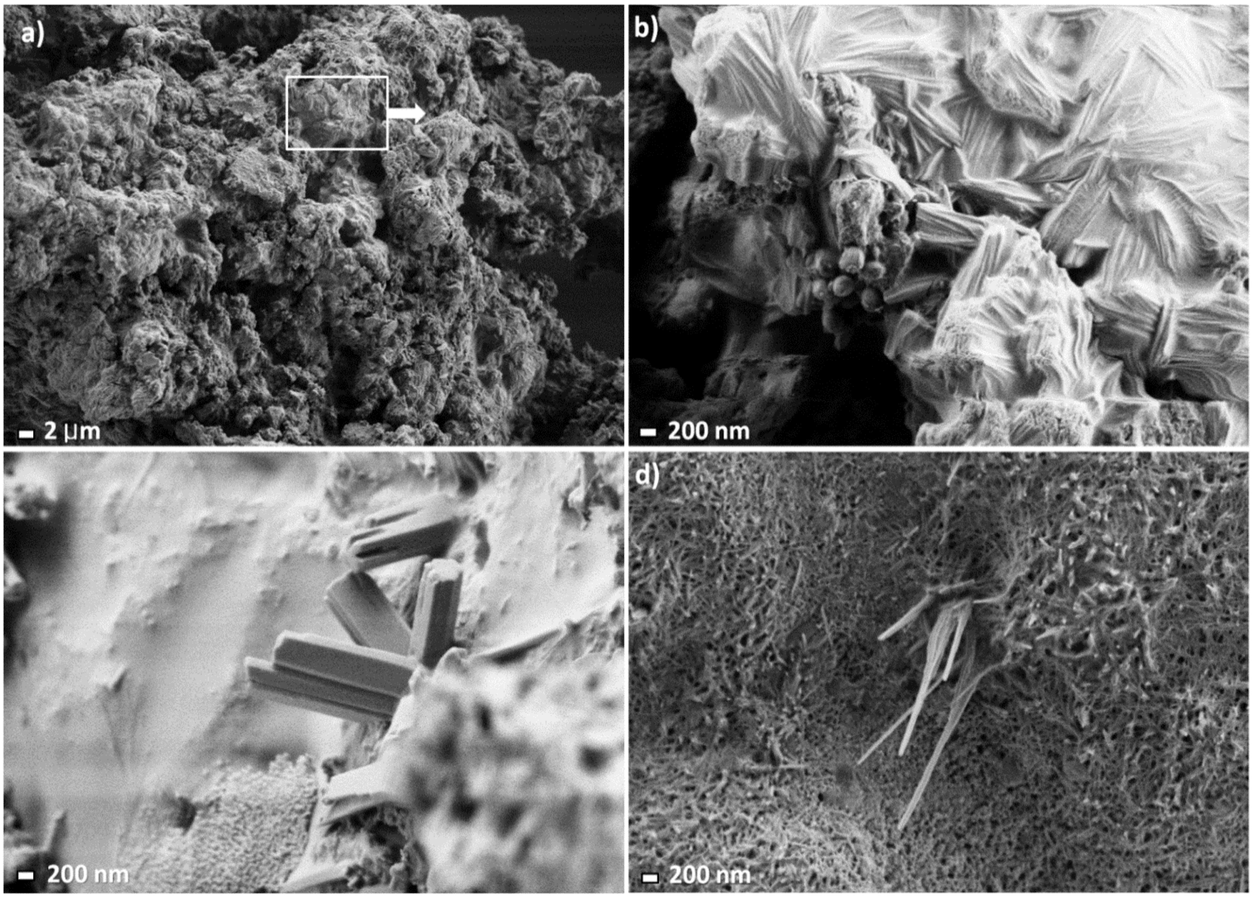

Figure 5.49 Scanning electron microscopy images (SEM) of the cycled electrodes of a) & b) RGO / V_2O_5 – $LiBO_2$ glass composite, c) RGO / V_2O_5 – NiO – $LiBO_2$ glass composite, d) plain V_2O_5 – $LiBO_2$ glass.

Thus, the main reasons of capacity fading for V_2O_5 based glass electrodes have been revealed here. The sources of instable cycling are similar to those reported for crystalline, nano-crystalline and gel-like vanadium oxide cathode materials[209, 266-271]. The side reactions on the electrolyte/electroactive material interface causing the vanadium dissolution and electrolyte decomposition seem to be the most concerning issues that must be prevented to reach a cycling stability over 300 cycles. The problems in the system could be addressed by the employment of more stable electrolytes and protective coatings on active materials.

5.4 Conclusion

In conclusion, novel cathode materials for rechargeable lithium batteries delivering high specific capacities were synthesized, and their electrochemical performances were investigated. 85 wt-% V_2O_5 – 15 wt-% B_2O_3 glass ceramics yielded a first discharge capacity of ~ 405 mAh/g at 50 mA/g rate within 1.5 – 4.0 V, and a specific capacity of ~ 292 mAh/g was still retained at the 10^{th} cycle. The RGO and Super P® composite electrodes of 85:15 wt-% V_2O_5 : B_2O_3 glass ceramics resulted in poorer electrochemical performances as a result of the loss of porous structure and favorable high oxidation states during the composite formation. A glass was obtained from a glass forming melt of 80 wt-% V_2O_5 and 20 wt-% $LiBO_2$. With this glass, huge capacity losses associated with irreversible phase transformation of crystalline V_2O_5 could be prevented, and a first charge capacity of ~ 308 mAh/g was realized with capacity retention of 93 % at the 10^{th} cycle. Similar to previously described borate compounds, further improvements in the electrochemical performance of the glass were accomplished by employing a composite electrode of active material and reduced graphite oxide. The RGO / V_2O_5 – $LiBO_2$ glass composite electrodes delivered first discharge capacities ca. 400 mAh/g until 1.5 V. In a galvanostatic cycling mode within 1.5 – 4.0 V at 50 mA/g rate, these composite electrodes retained capacities in the range of ~ 300 mAh/g for the first 50 cycles. Even when the system was pushed to perform at higher rates, high charge/discharge capacities superior to conventional cathode materials were realized with a discharge capacity of ~ 248 mAh/g (32^{nd} cycle) at 400 mA/g rate. The enhanced electrochemical performance was attributed to the RGO coating and network formation facilitating electron and Li^+ ion transports and acting as a protective layer. A glass of V_2O_5 – NiO – $LiBO_2$ was also synthesized and employed as a cathode material for rechargeable lithium batteries. The composite electrode of this glass with RGO showed a slightly better electrochemical performance in terms of cycling stability compared to the former glass composite that could be ascribed to the advantages coming with the full glass formation. However, the stability over extensive cycling remained to be a problem that was found to be caused by the vanadium dissolution into the electrolyte and the formation of inactive phases, similarly to other V_2O_5-based cathode materials. Nevertheless, V_2O_5 – $LiBO_2$ glasses could be considered as promising cathode materials for rechargeable lithium batteries with high charge/discharge capacities coming from rather simply and cost efficiently produced electrodes.

Summary & Outlook

Li-ion batteries are the most popular and primary choice among secondary batteries for mobile electronics and very likely to power electric vehicles in future. They are considered as energy storage mediums for large scale grid applications too. However, the current positive electrode materials are still not capable enough to provide high practical energy densities that could allow extended driving ranges for electric vehicles or enable the practical implementation of Li-ion batteries for medium to large scale energy storage applications. Therefore, the investigation of novel electrode materials that can enable the operation of batteries with high energy, safety, low cost and robustness, and understanding the principal working mechanisms of these materials in a battery are important both at the fundamental and applied level.

This thesis introduces novel positive electrode materials and their composites for rechargeable lithium batteries, and explores the underlying lithiation/delithiation mechanisms and stability of these materials.

Hexagonal and monoclinic phases of $LiMnBO_3$ were obtained mainly in nano-regime by a sol-gel method. $LiMnBO_3$ crystallites were partially covered with carbon particles that had been achieved by in-situ carbon coating from the precursors during the synthesis. For nano h-$LiMnBO_3$ with an average particle size of ~ 20 nm, a comparatively large first discharge capacity of 136 mAh/g was realized within a window of 4.7 – 1.7 V at C/20 rate. Electrochemical characterizations in this system provided evidence for a solid solution lithiation/delithiation mechanism. The electrochemical performance is considerably improved compared to microcrystalline phases and older investigations, which is ascribed to the small particle size and in situ carbon coating. Further improvement of electrochemical properties in terms of capacity and cycling properties was realized by employing a composite electrode of active material and reduced graphite oxide. The RGO/nano h-$LiMnBO_3$ composite delivered a first discharge capacity of 145 mAh/g and retained most of the capacity over multiple cycles, which is the best electrochemical performance displayed so far for $LiMnBO_3$. Likewise, the composite electrode of the sol-gel synthesized nano-$LiCoBO_3$ with reduced graphite oxide had enhanced electrochemical properties delivering a first charge capacity of ~ 55 mAh/g in a galvanostatic-potentiostatic protocol (within 4.7 - 2.0 V, at C/20 rate) that sets a reasonable example for the electrochemical delithiation of $LiCoBO_3$. The plain electrodes of sol-gel and solid-state synthesized $LiCoBO_3$ delivered very limited charge/discharge capacities, which is not surprising for non-conducting materials. The improvements realized for $LiMnBO_3$ and $LiCoBO_3$ are attributed to RGO composite formation facilitating electron transport and acting as a protective layer.

The advances made on lithium transition metal borates are encouraging not only for the use of these compounds, but also other materials of low transport kinetics, as high energy cathodes for Li-ion batteries. In this respect, the present investigations have a very general scope in battery research. Future investigations of favorable compounds should aim at developing a stable cycling and reducing polarizations. Investigations on high-voltage stable electrolytes exploring upper voltage limits are also very important in order to provide more stable cycling and enable the exchange of more electrons per formula unit, specifically for $LiCoBO_3$.

The novel lithium-rich compound, $Li_7Mn(BO_3)_3$, was demonstrated as a candidate cathode material for Li-ion batteries. The compound is an interesting electrode candidate, as high practical capacities might be achieved for several oxidation state switches of manganese reaching a theoretical capacity of ~ 479 mAh/g at an exchange of 5 Li per formula unit. As already manganese(II) sites are tetrahedrally coordinated, there may be a chance of large redox state changes without too large structural reassembly. Without any conductive composite formation, plain electrodes of the microcrystalline material delivered negligible capacities in the range of ~ 10 mAh/g because of poor conductivity similar to the other poly-anionic positive electrode materials. However, electrochemical activity was realized after nano-sizing and nano-carbon composite formation, so that a high first charge capacity of ~ 280 mAh/g (extraction of ca. 3 Li) and a first discharge capacity of ~ 154 mAh/g were demonstrated in the potential window of 4.7 -1.7 V at 10 mA/g rate. Improvement of capacity and cycling properties may be expected with more sophisticated coating and network formation processes, employment of even smaller nano-particles and limiting potential windows. Further investigations to understand the detailed processes that appear during lithiation/delithiation will be necessary.

Synthesis, characterization and electrochemical properties of vanadate – borate glasses and glass ceramics as promising high capacity cathode materials were displayed in the last chapter of this thesis. Glassy electrode materials were produced in a simple and cost efficient way being an important requirement for practical applications. For vanadate – borate glass ceramics, multi-phase lithium insertion reactions were found to occur during the first discharge similar to the crystalline V_2O_5 materials. 85:15 wt-% V_2O_5 : B_2O_3 glass ceramic still showed a noticeably improved electrochemical performance in terms of cycling and charge/discharge capacities compared to bulk and various nano-forms of V_2O_5, as a discharge capacity of ~ 292 mAh/g was yielded during the 10th cycle. Furthermore, considerably enhanced cycling properties and charge/discharge capacities were accomplished with vanadate – borate glasses (V_2O_5 – $LiBO_2$ and V_2O_5 – NiO – $LiBO_2$) and their composite electrodes delivering first discharge capacities around 360-400 mAh/g and maintaining high capacities in the range of ~ 300 mAh/g for the first 50 cycles (between 1.5 V and 4.0 V at 50 mA/g rate)! The rate capability of the RGO/V_2O_5 –

$LiBO_2$ composite electrode was also notable with a discharge capacity of ~ 248 mAh/g (32nd cycle) at 400 mA/g rate.

The galvanostatic cycling analysis of vanadate – borate glasses shows featureless curves without any distinct voltage plateau starting from the first discharge; this supports the understanding of a glassy material. The enhanced electrochemical properties for vanadate – borate glasses were mainly attributed to the absence of a long range order allowing for subtle structural changes, which cannot occur with crystalline V_2O_5 phases. This is markedly different from the huge capacity loss observed for crystalline V_2O_5 phases in the first cycle related to the irreversible phase transformation to ω-$Li_3V_2O_5$, which cannot be cycled to its full extent within 1.5 – 4.0 V. Though higher charge/discharge capacities and enhanced cycling stabilities compared to bulk and various nano-forms of V_2O_5 have been demonstrated here for vanadate – borate glasses, the overall cycling stability still has to be improved for practical battery applications. Future investigations on vanadate – borate glasses and glass ceramics may include the complete elimination of crystalline segments by realizing faster quenching rates during the synthesis via roller and twin-roller quenching techniques. As the main reasons of capacity fading over extensive cycling are considered to stem from the processes at the electrode/electrolyte interface, the exploration of different protective coatings and stable electrolyte systems are very important to achieve a more stable cycling. Nevertheless, the results obtained for vanadate – borate glasses are very encouraging and will trigger further studies in this and in similar glass systems that could eventually lead to the practical use of glassy materials as next generation electrode materials for rechargeable lithium batteries.

References

[1] M. K. Hubbert, *Drilling and Production Practice (1956) American Petroleum Institute* **1956**, *95*, 1-39.
[2] A. R. Brandt, *Energy Policy* **2007**, *35*, 3074-3088.
[3] M. Šturc, *Eurostat Statistics in Focus* **2012**, *44*, 1-7.
[4] Toyota-Motor, Worldwide Sales of TMC Hybrids, http://www2.toyota.co.jp/en/news/12/05/0522.html, March 2013.
[5] Mitsubishi-motors, Mitsubishi Innovative Electric Vehicle http://www.mitsubishi-motors.com/special/ev/, May 2012.
[6] Nissan, Nissan Leaf Electric Car, http://www.nissan-global.com/EN/NISSAN/LEAF/, May 2012.
[7] Tesla-Motors, Tesla Roadster Electric Car, http://www.teslamotors.com/goelectric, May 2012
[8] P. G. Bruce, S. A. Freunberger, L. J. Hardwick, J. M. Tarascon, *Nat. Mater.* **2012**, *11*, 19-29.
[9] J. L. Sudworth, *J. Power Sources* **1984**, *11*, 143-154.
[10] A. Kita, E. Nomura, *Denki Kagaku* **1987**, *55*, 194-197.
[11] Z. Y. Wen, J. D. Cao, Z. H. Gu, X. H. Xu, F. L. Zhang, Z. X. Lin, *Solid State Ionics* **2008**, *179*, 1697-1701.
[12] R. J. Bones, D. A. Teagle, S. D. Brooker, F. L. Cullen, *J. Electrochem. Soc.* **1989**, *136*, 1274-1277.
[13] J. K. Min, C. H. Lee, *J. Power Sources* **2012**, *210*, 101-109.
[14] J. Fally, C. Lasne, Y. Lazennec, Y. Lecars, P. Margotin, *J. Electrochem. Soc.* **1973**, *120*, 1296-1298.
[15] G. Kear, A. A. Shah, F. C. Walsh, *Int. J. Energ. Res.* **2012**, *36*, 1105-1120.
[16] A. P. Piotto, PhD thesis, ETH Zürich (Zürich), **2004**.
[17] J. Dahn, R. R. Haering, *Mater. Res. Bull.* **1979**, *14*, 1259-1262.
[18] B. V. Ratnakumar, G. Nagasubramanian, S. Distefano, C. P. Bankston, *J. Electrochem. Soc.* **1992**, *139*, 1513-1521.
[19] Campanel.L, G. Pistoia, B. Scrosati, *J. Electrochem. Soc.* **1971**, *118*, C207-&.
[20] N. Kumagai, K. Tanno, T. Nakajima, N. Watanabe, *Electrochim. Acta* **1983**, *28*, 17-22.
[21] K. Mizushima, P. C. Jones, P. J. Wiseman, J. B. Goodenough, *Solid State Ionics* **1981**, *3-4*, 171-174.
[22] B. Banov, J. Bourilkov, M. Mladenov, *J. Power Sources* **1995**, *54*, 268-270.
[23] B. Ammundsen, J. Paulsen, *Adv. Mater.* **2001**, *13*, 943-+.
[24] S. M. Dou, W. L. Wang, *J. Solid State Electr.* **2011**, *15*, 399-404.
[25] C. Julien, G. A. Nazri, A. Rougier, *Solid State Ionics* **2000**, *135*, 121-130.
[26] A. D. Robertson, A. R. Armstrong, P. G. Bruce, *Chem. Mater.* **2001**, *13*, 2380-2386.
[27] B. M. L. Rao, R. W. Francis, H. A. Christopher, *J. Electrochem. Soc.* **1977**, *124*, 1490-1492.
[28] D. W. Murphy, F. J. Disalvo, J. N. Carides, J. V. Waszczak, *Mater. Res. Bull.* **1978**, *13*, 1395-1402.
[29] M. Lazzari, B. Scrosati, *J. Electrochem. Soc.* **1980**, *127*, 773-774.
[30] J. B. Goodenough, Y. Kim, *Chem. Mater.* **2010**, *22*, 587-603.
[31] K. Hayashi, Y. Nemoto, S. Tobishima, J. Yamaki, *Electrochim. Acta* **1999**, *44*, 2337-2344.
[32] K. Hayashi, Y. Nemoto, S. Tobishima, J. Yamaki, *Electroceramics in Japan I* **1999**, *157-1*, 273-279.
[33] X. J. Wang, H. S. Lee, H. Li, X. Q. Yang, X. J. Huang, *Electrochem. Commun.* **2010**, *12*, 386-389.
[34] N. Katayama, T. Kawamura, Y. Baba, J. Yamaki, *J. Power Sources* **2002**, *109*, 321-326.
[35] T. Kawamura, A. Kimura, M. Egashira, S. Okada, J. I. Yamaki, *J. Power Sources* **2002**, *104*, 260-264.

[36] K. Xu, S. S. Zhang, T. R. Jow, *Electrochem. Solid St.* **2003**, *6*, A117-A120.
[37] J. Liu, Z. H. Chen, S. Busking, K. Amine, *Electrochem. Commun.* **2007**, *9*, 475-479.
[38] Y. Qin, Z. H. Chen, J. Liu, K. Amine, *Electrochem. Solid St.* **2010**, *13*, A11-A14.
[39] H. M. Wang, S. Q. Liu, KelongHuang, X. G. Yin, Y. N. Liu, S. J. Peng, *Int. J. Electrochem. Sc.* **2012**, *7*, 1688-1698.
[40] X. H. Yu, J. B. Bates, G. E. Jellison, F. X. Hart, *J. Electrochem. Soc.* **1997**, *144*, 524-532.
[41] Y. Iriyama, T. Kako, C. Yada, T. Abe, Z. Ogumi, *Solid State Ionics* **2005**, *176*, 2371-2376.
[42] R. Kanno, M. Murayama, K. Sakamoto, *Solid State Ionics: Trends in the New Millennium, Proceedings* **2002**, 13-22.
[43] T. Kobayashi, T. Inada, N. Sonoyama, A. Yamada, R. Kanno, *Mater. Res. Soc. Symp. P* **2005**, *835*, 333-345.
[44] Q. W. Lu, J. H. Fang, J. Yang, G. W. Yan, S. S. Liu, J. L. Wang, *J. Membrane Sci.* **2013**, *425*, 105-112.
[45] Y. X. Jiang, J. M. Xu, Q. C. Zhuang, L. Y. Jin, S. G. Sun, *J. Solid State Electr.* **2008**, *12*, 353-361.
[46] M. Egashira, Y. Utsunomiya, N. Yoshimoto, M. Morita, *Electrochim. Acta* **2006**, *52*, 1082-1086.
[47] M. Winter, J. O. Besenhard, M. E. Spahr, P. Novak, *Adv. Mater.* **1998**, *10*, 725-763.
[48] E. Peled, D. Golodnitsky, G. Ardel, *J. Electrochem Soc.* **1997**, *144*, L208-L210.
[49] S. Yamaguchi, H. Asahina, K. A. Hirasawa, T. Sato, S. Mori, *Mol. Cryst. Liq. Crys. A* **1998**, *322*, 239-244.
[50] T. K. Zhao, Y. N. Liu, T. H. Li, X. Zhao, *J. Nanosci. Nanotechno.* **2010**, *10*, 3873-3877.
[51] T. R. Kim, J. N. Lee, Y. S. Lim, M. S. Kim, *Eco-Materials Processing and Design VIII* **2007**, *544-545*, 1029-1032.
[52] F. Bonino, S. Brutti, M. Piana, S. Natale, B. Scrosati, L. Gherghel, K. Mullen, *Electrochim. Acta* **2006**, *51*, 3407-3412.
[53] M. Yoshio, H. Y. Wang, K. Fukuda, T. Abe, Z. Ogumi, *Chem. Lett.* **2003**, *32*, 1130-1131.
[54] K. Tokumitsu, H. Fujimoto, A. Mabuchi, T. Kasuh, *Carbon* **1999**, *37*, 1599-1605.
[55] Toshiba, Super-Charge Ion Battery (SCiB™), http://www.toshiba.com/ind/product_display.jsp?id1=821, March 2013.
[56] C. Lai, Z. Z. Wu, Y. X. Zhu, Q. D. Wu, L. Li, C. Wang, *J. Power Sources* **2013**, *226*, 71-74.
[57] K. Amine, I. Belharouak, Z. H. Chen, T. Tran, H. Yumoto, N. Ota, S. T. Myung, Y. K. Sun, *Adv. Mater.* **2010**, *22*, 3052-3057.
[58] Y. Q. Wang, L. Guo, Y. G. Guo, H. Li, X. Q. He, S. Tsukimoto, Y. Ikuhara, L. J. Wan, *J. Am. Chem. Soc.* **2012**, *134*, 7874-7879.
[59] H. F. Ni, L. Z. Fan, *J. Power Sources* **2012**, *214*, 195-199.
[60] N. Yan, L. Hu, Y. Li, Y. Wang, H. Zhong, X. Y. Hu, X. K. Kong, Q. W. Chen, *J. Phys. Chem. C* **2012**, *116*, 7227-7235.
[61] M. Sathish, T. Tomai, I. Honma, *J. Power Sources* **2012**, *217*, 85-91.
[62] P. Poizot, S. Laruelle, S. Grugeon, L. Dupont, J. M. Tarascon, *Nature* **2000**, *407*, 496-499.
[63] Z. W. Fu, Y. Wang, X. L. Yue, S. L. Zhao, Q. Z. Qin, *J. Phys. Chem. B* **2004**, *108*, 2236-2244.
[64] N. Pereira, L. Dupont, J. M. Tarascon, L. C. Klein, G. G. Amatucci, *J. Electrochem. Soc.* **2003**, *150*, A1273-A1280.
[65] D. C. C. d. S. Gosselink, PhD thesis, University of Waterloo (Waterloo-Ontario), **2006**.
[66] Y. U. Kim, B. W. Cho, H. J. Sohn, *J. Electrochem. Soc.* **2005**, *152*, A1475-A1478.
[67] S. Rangan, R. Thorpe, R. A. Bartynski, M. Sina, F. Cosandey, O. Celik, D. D. T. Mastrogiovann, *J. Phys. Chem. C* **2012**, *116*, 10498-10503.
[68] M. J. Zhou, L. W. Zhao, S. Okada, J. Yamaki, *J. Power Sources* **2011**, *196*, 8110-8115.
[69] Z. W. Fu, C. L. Li, W. Y. Liu, J. Ma, Y. Wang, Q. Z. Qin, *J. Electrochem. Soc.* **2005**, *152*, E50-E55.
[70] E. M. Shembel, I. M. Maksyuta, L. I. Neduzhko, A. I. Belosokhov, A. F. Naumenko, V. V. Rozhkov, *J. Power Sources* **1995**, *54*, 416-420.

[71] M. R. Palacin, *Chem. Soc. Rev.* **2009**, *38*, 2565-2575.
[72] A. Trifonova, M. Wachtler, M. Winter, J. O. Besenhard, *Ionics* **2002**, *8*, 321-328.
[73] X. B. Zhao, G. S. Cao, C. P. Lv, L. J. Zhang, S. H. Hu, T. J. Zhu, B. C. Zhou, *J. Alloy Compd.* **2001**, *315*, 265-269.
[74] C. P. Lu, X. B. Zhao, G. S. Cao, T. J. Zhu, *T Nonferr. Metal. Soc.* **2000**, *10*, 204-208.
[75] C. K. Chan, H. L. Peng, G. Liu, K. McIlwrath, X. F. Zhang, R. A. Huggins, Y. Cui, *Nat. Nanotechnol.* **2008**, *3*, 31-35.
[76] S. C. Jung, J. W. Choi, Y. K. Han, *Nano Lett.* **2012**, *12*, 5342-5347.
[77] B. A. Boukamp, G. C. Lesh, R. A. Huggins, *J. Electrochem. Soc.* **1981**, *128*, 725-729.
[78] H. Wu, G. Chan, J. W. Choi, I. Ryu, Y. Yao, M. T. McDowell, S. W. Lee, A. Jackson, Y. Yang, L. B. Hu, Y. Cui, *Nat. Nanotechnol.* **2012**, *7*, 309-314.
[79] R. Huang, X. Fan, W. C. Shen, J. Zhu, *Appl. Phys. Lett.* **2009**, *95*.
[80] M. H. Park, M. G. Kim, J. Joo, K. Kim, J. Kim, S. Ahn, Y. Cui, J. Cho, *Nano Lett.* **2009**, *9*, 3844-3847.
[81] S. A. Klankowski, R. A. Rojeski, B. A. Cruden, J. W. Liu, J. Wu, J. Li, *J. Mater. Chem. A* **2013**, *1*, 1055-1064.
[82] X. S. Zhou, Y. X. Yin, A. M. Cao, L. J. Wan, Y. G. Guo, *Acs Appl. Mater. Inter.* **2012**, *4*, 2824-2828.
[83] M. Thakur, S. L. Sinsabaugh, M. J. Isaacson, M. S. Wong, S. L. Biswal, *Sci. Rep-Uk* **2012**, *2*.
[84] S. Murugesan, J. T. Harris, B. A. Korgel, K. J. Stevenson, *Chem. Mater.* **2012**, *24*, 1306-1315.
[85] Y. L. Kim, H. Y. Lee, S. W. Jang, S. H. Lim, S. J. Lee, H. K. Baik, Y. S. Yoon, S. M. Lee, *Electrochim. Acta* **2003**, *48*, 2593-2597.
[86] X. L. Yang, Z. Y. Wen, S. H. Huang, X. J. Zhu, X. F. Zhang, *Solid State Ionics* **2006**, *177*, 2807-2810.
[87] Z. H. Chen, Z. H. Lu, J. R. Dahn, *J. Electrochem. Soc.* **2002**, *149*, A1604-A1609.
[88] T. Ohzuku, A. Ueda, *J. Electrochem. Soc.* **1994**, *141*, 2972-2977.
[89] E. Endo, T. Yasuda, A. Kita, K. Yamaura, K. Sekai, *J. Electrochem. Soc.* **2000**, *147*, 1291-1294.
[90] H. F. Wang, Y. I. Jang, B. Y. Huang, D. R. Sadoway, Y. T. Chiang, *J. Electrochem. Soc.* **1999**, *146*, 473-480.
[91] Y. Idemoto, T. Hasegawa, N. Kitamura, Y. Uchimoto, *Electrochemistry* **2011**, *79*, 15-23.
[92] D. Kim, S. H. Kang, M. Balasubramanian, C. S. Johnson, *Electrochem. Commun.* **2010**, *12*, 1618-1621.
[93] N. Yabuuchi, T. Ohzuku, *J. Power Sources* **2003**, *119*, 171-174.
[94] W. S. Yoon, M. Balasubramanian, K. Y. Chung, X. Q. Yang, J. McBreen, C. P. Grey, D. A. Fischer, *J. Am. Chem. Soc.* **2005**, *127*, 17479-17487.
[95] N. Yabuuchi, Y. Makimura, T. Ohzuku, *J. Electrochem. Soc.* **2007**, *154*, A314-A321.
[96] S. C. Yin, Y. H. Rho, I. Swainson, L. F. Nazar, *Chem. Mater.* **2006**, *18*, 1901-1910.
[97] R. Kostecki, F. McLarnon, *Electrochem. Solid St.* **2004**, *7*, A380-A383.
[98] Y. Kim, *Acs Appl. Mater. Inter.* **2012**, *4*, 2329-2333.
[99] M. Broussely, P. Blanchard, P. Biensan, J. P. Planchat, K. Nechev, R. J. Staniewicz, *J. Power Sources* **2003**, *119–121*, 859-864.
[100] Y. K. Sun, S. T. Myung, B. C. Park, J. Prakash, I. Belharouak, K. Amine, *Nat. Mater.* **2009**, *8*, 320-324.
[101] Y. C. Chen, K. Xie, Y. Pan, C. M. Zheng, *J. Power Sources* **2011**, *196*, 6493-6497.
[102] B. Xu, D. N. Qian, Z. Y. Wang, Y. S. L. Meng, *Mat. Sci. Eng. R* **2012**, *73*, 51-65.
[103] M. M. Thackeray, M. F. Mansuetto, J. B. Bates, *J. Power Sources* **1997**, *68*, 153-158.
[104] M. Mohamedi, D. Takahashi, T. Itoh, I. Uchida, *Electrochim. Acta* **2002**, *47*, 3483-3489.
[105] S. Lee, Y. Cho, H. K. Song, K. T. Lee, J. Cho, *Angew. Chem. Int. Edit.* **2012**, *51*, 8748-8752.
[106] J. Cho, *Solid State Ionics* **2001**, *138*, 267-271.
[107] S. T. Myung, H. T. Chung, S. Komaba, N. Kumagai, H. B. Gu, *J. Power Sources* **2000**, *90*, 103-108.

[108] J. T. Son, K. S. Park, H. G. Kim, H. T. Chung, *J. Mater. Sci.* **2004**, *39*, 3635-3639.
[109] K. Y. Chung, K. B. Kim, *Electrochim. Acta* **2004**, *49*, 3327-3337.
[110] S. B. Park, H. C. Shin, W. G. Lee, W. I. Cho, H. Jang, *J. Power Sources* **2008**, *180*, 597-601.
[111] D. Capsoni, M. Bini, G. Chiodelli, V. Massarotti, C. B. Azzoni, M. C. Mozzati, A. Comin, *Phys. Chem. Chem. Phys.* **2001**, *3*, 2162-2166.
[112] B. J. Hwang, R. Santhanam, D. G. Liu, Y. W. Tsai, *J. Power Sources* **2001**, *102*, 326-331.
[113] J. Xiao, X. L. Chen, P. V. Sushko, M. L. Sushko, L. Kovarik, J. J. Feng, Z. Q. Deng, J. M. Zheng, G. L. Graff, Z. M. Nie, D. W. Choi, J. Liu, J. G. Zhang, M. S. Whittingham, *Adv. Mater.* **2012**, *24*, 2109-2116.
[114] L. Zhou, D. Y. Zhao, X. W. Lou, *Angew. Chem. Int. Edit.* **2012**, *51*, 239-241.
[115] A. K. Padhi, K. S. Nanjundaswamy, J. B. Goodenough, *J. Electrochem. Soc.* **1997**, *144*, 1188-1194.
[116] S. Y. Chung, J. T. Bloking, Y. M. Chiang, *Nat. Mater.* **2002**, *1*, 123-128.
[117] K. Striebel, J. Shim, V. Srinivasan, J. Newman, *J. Electrochem. Soc.* **2005**, *152*, A664-A670.
[118] M. M. Doeff, J. D. Wilcox, R. Kostecki, G. Lau, *J. Power Sources* **2006**, *163*, 180-184.
[119] H. B. Gul, D. K. Jun, G. C. Park, B. Jin, E. M. Jin, *J. Nanosci. Nanotechno.* **2007**, *7*, 3980-3984.
[120] Y. S. Hu, Y. G. Guo, R. Dominko, M. Gaberscek, J. Jamnik, J. Maier, *Adv. Mater.* **2007**, *19*, 1963-+.
[121] X. Zhou, X. B. Zhao, H. M. Yu, J. Z. Hu, *J. Inorg. Mater.* **2008**, *23*, 587-591.
[122] D. Kim, J. Lim, V. Mathew, B. Koo, Y. Paik, D. Ahn, S. M. Paek, J. Kim, *J. Mater. Chem.* **2012**, *22*, 2624-2631.
[123] S. Yoon, C. Liao, X. G. Sun, C. A. Bridges, R. R. Unocic, J. Nanda, S. Dai, M. P. Paranthaman, *J. Mater. Chem.* **2012**, *22*, 4611-4614.
[124] D. Lepage, C. Michot, G. X. Liang, M. Gauthier, S. B. Schougaard, *Angew. Chem. Int. Edit.* **2011**, *50*, 6884-6887.
[125] B. Kang, G. Ceder, *Nature* **2009**, *458*, 190-193.
[126] S. Y. Lim, C. S. Yoon, J. P. Cho, *Chem. Mater.* **2008**, *20*, 4560-4564.
[127] H. M. Xie, R. S. Wang, J. R. Ying, L. Y. Zhang, A. F. Jalbout, H. Y. Yu, G. L. Yang, X. M. Pan, Z. M. Su, *Adv. Mater.* **2006**, *18*, 2609-+.
[128] A. S. Andersson, B. Kalska, L. Haggstrom, J. O. Thomas, *Solid State Ionics* **2000**, *130*, 41-52.
[129] G. Kobayashi, S. I. Nishimura, M. S. Park, R. Kanno, M. Yashima, T. Ida, A. Yamada, *Adv. Func. Mater.* **2009**, *19*, 395-403.
[130] A. Yamada, Y. Kudo, K. Y. Liu, *J. Electrochem. Soc.* **2001**, *148*, A747-A754.
[131] N. Sharma, X. W. Guo, G. D. Du, Z. P. Guo, J. Z. Wang, Z. X. Wang, V. K. Peterson, *J. Am. Chem. Soc.* **2012**, *134*, 7867-7873.
[132] D. Choi, D. Wang, I.-T. Bae, J. Xiao, Z. Nie, W. Wang, V. V. Viswanathan, Y. J. Lee, J.-G. Zhang, G. L. Graff, Z. Yang, J. Liu, *Nano Lett.* **2010**, *10*, 2799-2805.
[133] J. Wolfenstine, J. Allen, *J. Power Sources* **2004**, *136*, 150-153.
[134] K. Amine, H. Yasuda, M. Yamachi, *Electrochem Solid St.* **2000**, *3*, 178-179.
[135] S. Nishimura, M. Nakamura, R. Natsui, A. Yamada, *J. Am. Chem. Soc.* **2010**, *132*, 13596-13597.
[136] P. Barpanda, S. Nishimura, A. Yamada, *Adv. Energy Mater.* **2012**, *2*, 841-859.
[137] H. Zhou, S. Upreti, N. A. Chernova, G. Hautier, G. Ceder, M. S. Whittingham, *Chem. Mater.* **2011**, *23*, 293-300.
[138] H. Kim, S. Lee, Y. U. Park, H. Kim, J. Kim, S. Jeon, K. Kang, *Chem. Mater.* **2011**, *23*, 3930-3937.
[139] A. Kokalj, R. Dominko, G. Mali, A. Meden, M. Gaberscek, J. Jamnik, *Chem. Mater.* **2007**, *19*, 3633-3640.
[140] W. H. Chen, M. Lan, D. Zhu, C. L. Wang, S. R. Xue, C. C. Yang, Z. X. Li, J. M. Zhang, L. W. Mi, *Rsc. Adv.* **2013**, *3*, 408-412.
[141] B. Shao, I. Taniguchi, *J. Power Sources* **2012**, *199*, 278-286.
[142] C. Lyness, B. Delobel, A. R. Armstrong, P. G. Bruce, *Chem. Commun.* **2007**, 4890-4892.

[143] R. Dominko, M. Bele, A. Kokalj, M. Gaberscek, J. Jamnik, *J. Power Sources* **2007**, *174*, 457-461.
[144] D. M. Kempaiah, D. Rangappa, I. Honma, *Chem. Commun.* **2012**, *48*, 2698-2700.
[145] D. P. Lv, W. Wen, X. K. Huang, J. Y. Bai, J. X. Mi, S. Q. Wu, Y. Yang, *J. Mater. Chem.* **2011**, *21*, 9506-9512.
[146] N. Recham, J. N. Chotard, L. Dupont, C. Delacourt, W. Walker, M. Armand, J. M. Tarascon, *Nat. Mater.* **2010**, *9*, 68-74.
[147] M. Ati, B. C. Melot, J. N. Chotard, G. Rousse, M. Reynaud, J. M. Tarascon, *Electrochem. Commun.* **2011**, *13*, 1280-1283.
[148] J. Barker, M. Y. Saidi, J. L. Swoyer, *J. Electrochem. Soc.* **2003**, *150*, A1394-A1398.
[149] Y. Makimura, L. S. Cahill, Y. Iriyama, G. R. Goward, L. F. Nazar, *Chem. Mater.* **2008**, *20*, 4240-4248.
[150] B. L. Ellis, W. R. M. Makahnouk, W. N. Rowan-Weetaluktuk, D. H. Ryan, L. F. Nazar, *Chem. Mater.* **2010**, *22*, 1059-1070.
[151] P. Barpanda, J.-N. l. Chotard, N. Recham, C. Delacourt, M. Ati, L. Dupont, M. Armand, J.-M. Tarascon, *Inorg. Chem.* **2010**, *49*, 7401-7413.
[152] S. R. S. Prabaharan, A. Fauzi, M. S. Michael, K. M. Begam, *Solid State Ionics* **2004**, *171*, 157-165.
[153] M. Y. Saidi, J. Barker, H. Huang, J. L. Swoyer, G. Adamson, *Electrochem. Solid St.* **2002**, *5*, A149-A151.
[154] B. L. Cushing, J. B. Goodenough, *J. Solid State Chem.* **2001**, *162*, 176-181.
[155] S. Okada, T. Takada, M. Egashira, J. Yamaki, *Intercalation Compounds for Battery Materials, Proceedings* **2000**, *99*, 237-248.
[156] C. Delmas, F. Cherkaoui, A. Nadiri, P. Hagenmuller, *Mater. Res. Bull.* **1987**, *22*, 631-639.
[157] S. Y. Lim, H. Kim, R. A. Shakoor, Y. Jung, J. W. Choi, *J. Electrochem. Soc.* **2012**, *159*, A1393-A1397.
[158] K. D. Kreuer, U. Warhus, *Mater. Res. Bull.* **1986**, *21*, 357-363.
[159] J. A. Kafalas, *Abstr. Pap. Am. Chem. S.* **1978**, *176*, 99-99.
[160] A. Jain, G. Hautier, C. Moore, B. Kang, J. Lee, H. L. Chen, N. Twu, G. Ceder, *J. Electrochem. Soc.* **2012**, *159*, A622-A633.
[161] G. Hautier, A. Jain, H. L. Chen, C. Moore, S. P. Ong, G. Ceder, *J. Mater. Chem.* **2011**, *21*, 17147-17153.
[162] X. L. Ji, K. T. Lee, L. F. Nazar, *Nat. Mater.* **2009**, *8*, 500-506.
[163] F. Mizuno, S. Nakanishi, Y. Kotani, S. Yokoishi, H. Iba, *Electrochemistry* **2010**, *78*, 403-405.
[164] S. D. Beattie, D. M. Manolescu, S. L. Blair, *J. Electrochem. Soc.* **2009**, *156*, A44-A47.
[165] S. A. Freunberger, Y. H. Chen, N. E. Drewett, L. J. Hardwick, F. Barde, P. G. Bruce, *Angew. Chem. Int. Edit.* **2011**, *50*, 8609-8613.
[166] H. G. Jung, J. Hassoun, J. B. Park, Y. K. Sun, B. Scrosati, *Nat. Chem.* **2012**, *4*, 579-585.
[167] S. A. Freunberger, Y. H. Chen, Z. Q. Peng, J. M. Griffin, L. J. Hardwick, F. Barde, P. Novak, P. G. Bruce, *J. Am. Chem. Soc.* **2011**, *133*, 8040-8047.
[168] Z. Q. Peng, S. A. Freunberger, Y. H. Chen, P. G. Bruce, *Science* **2012**, *337*, 563-566.
[169] H. Matsui, T. Nakamura, Y. Kobayashi, M. Tabuchi, Y. Yamada, *J. Power Sources* **2010**, *195*, 6879-6883.
[170] V. Legagneur, Y. An, A. Mosbah, R. Portal, A. L. La Salle, A. Verbaere, D. Guyomard, Y. Piffard, *Solid State Ionics* **2001**, *139*, 37-46.
[171] A. Yamada, N. Iwane, Y. Harada, S. Nishimura, Y. Koyama, I. Tanaka, *Adv. Mater.* **2010**, *22*, 3583-+.
[172] O. S. Bondareva, M. A. Simonov, Y. K. E. Tismenko, N. V. Belov, *Kristallografiya* **1978**, *23*, 487-490.
[173] J. C. Kim, C. J. Moore, B. Kang, G. Hautier, A. Jain, G. Ceder, *J. Electrochem. Soc.* **2011**, *158*, A309-A315.

[174] L. Chen, Y. Zhao, X. An, J. Liu, Y. Dong, Y. Chen, Q. Kuang, *J. Alloy Compd.* **2010**, *494*, 415-419.

[175] J. L. Allen, K. Xu, S. S. Zhang, T. R. Jow, *Materials for Energy Storage, Generation and Transport* **2002**, *730*, 9-14.

[176] H. P. Boehm, A. Clauss, U. Hofmann, G. O. Fischer, *Z. Naturforsch. Pt B* **1962**, *B 17*, 150-&.

[177] M. Schmidt, U. Heider, A. Kuehner, R. Oesten, M. Jungnitz, N. Ignat'ev, P. Sartori, *J. Power Sources* **2001**, *97–98*, 557-560.

[178] K.-S. Lee, S.-T. Myung, K. Amine, H. Yashiro, Y.-K. Sun, *J. Mater. Chem.* **2009**, *19*, 1995-2005.

[179] W. Weppner, R. A. Huggins, *B. Am. Phys. Soc.* **1977**, *22*, 284-284.

[180] W. Weppner, R. A. Huggins, *J. Solid State. Chem.* **1977**, *22*, 297-308.

[181] J. S. Chen, L. F. Wang, B. J. Fang, S. Y. Lee, R. Z. Guo, *J. Power Sources* **2006**, *157*, 515-521.

[182] S. Komaba, N. Kumagai, T. Sasaki, Y. Miki, *Electrochemistry* **2001**, *69*, 784-787.

[183] S.-M. Oh, S.-W. Oh, C.-S. Yoon, B. Scrosati, K. Amine, Y.-K. Sun, *Adv. Func. Mater.* **2010**, *20*, 3260-3265.

[184] S. M. Oh, S. T. Myung, Y. K. Sun, *J. Mater. Chem.* **2012**, *22*, 14932-14937.

[185] S. Afyon, D. Kundu, F. Krumeich, R. Nesper, *J. Power Sources* **2013**, *224*, 145-151.

[186] K. R. Yang, Z. H. Deng, J. S. Suo, *J. Power Sources* **2012**, *201*, 274-279.

[187] S. H. Jensen, K. Engelbrecht, C. Bernuy-Lopez, *J. Electrochem. Soc.* **2012**, *159*, A791-A797.

[188] X. L. Ji, S. Evers, R. Black, L. F. Nazar, *Nat. Commun.* **2011**, *2*.

[189] M. S. Whittingham, *J. Electrochem. Soc.* **1976**, *123*, 315-320.

[190] F. W. Dampier, *J. Electrochem. Soc.* **1974**, *121*, 656-660.

[191] Z. H. Wen, Q. Wang, J. H. Li, *J. Nanosci. Nanotechno.* **2006**, *6*, 2117-2122.

[192] I. C. Halalay, G. A. Nazri, Y. T. Cheng, G. L. Eesley, M. S. Meyer, *J. Power Sources* **1995**, *54*, 218-220.

[193] F. Chaput, B. Dunn, P. Fuqua, K. Salloux, *J. Non-Cryst. Solids* **1995**, *188*, 11-18.

[194] H. Hirashima, K. Sudoh, *J. Non-Cryst. Solids* **1992**, *145*, 51-54.

[195] D. B. Le, S. Passerini, J. Guo, J. Ressler, B. B. Owens, W. H. Smyrl, *J. Electrochem. Soc.* **1996**, *143*, 2099-2104.

[196] D. B. Le, S. Passerini, A. L. Tipton, B. B. Owens, W. H. Smyrl, *J. Electrochem. Soc.* **1995**, *142*, L102-L103.

[197] S. Passerini, D. Chang, X. Chu, D. B. Le, W. Smyrl, *Chem. Mater.* **1995**, *7*, 780-785.

[198] S. Passerini, W. H. Smyrl, M. Berrettoni, R. Tossici, M. Rosolen, R. Marassi, F. Decker, *Solid State Ionics* **1996**, *90*, 5-14.

[199] M. Giorgetti, S. Passerini, W. H. Smyrl, M. Berrettoni, *Inorg. Chem.* **2000**, *39*, 1514-1517.

[200] M. Lira-Cantu, P. Gomez-Romero, *J. New Mat. Electr. Sys.* **1999**, *2*, 141-144.

[201] J. Livage, *Chem. Mater.* **1991**, *3*, 578-593.

[202] S. Passerini, D. B. Le, W. H. Smyrl, M. Berrettoni, R. Tossici, R. Marassi, M. Giorgetti, *Solid State Ionics* **1997**, *104*, 195-204.

[203] M. Giorgetti, S. Passerini, W. H. Smyrl, *Intercalation Compounds for Battery Materials, Proceedings* **2000**, *99*, 192-200.

[204] G. G. Amatucci, F. Badway, A. Singhal, B. Beaudoin, G. Skandan, T. Bowmer, I. Plitza, N. Pereira, T. Chapman, R. Jaworski, *J. Electrochem. Soc.* **2001**, *148*, A940-A950.

[205] B. B. Owens, S. Passerini, W. H. Smyrl, *Electrochim. Acta* **1999**, *45*, 215-224.

[206] A. L. Tipton, S. Passerini, B. B. Owens, W. H. Smyrl, *J. Electrochem. Soc.* **1996**, *143*, 3473-3477.

[207] R. Baddour-Hadjean, A. Marzouk, J. P. Pereira-Ramos, *J. Raman Spectrosc.* **2012**, *43*, 153-160.

[208] X. Rocquefelte, F. Boucher, P. Gressier, G. Ouvrard, *Chem. Mater.* **2003**, *15*, 1812-1819.

[209] P. L. Moss, R. Fu, G. Au, E. J. Plichta, Y. Xin, J. P. Zheng, *J. Power Sources* **2003**, *124*, 261-265.

[210] C. Delmas, H. Cognacauradou, J. M. Cocciantelli, M. Menetrier, J. P. Doumerc, *Solid State Ionics* **1994**, *69*, 257-264.

[211] L. L. Liu, X. J. Wang, Y. S. Zhu, C. L. Hu, Y. P. Wu, R. Holze, *J. Power Sources* **2013**, *224*, 290-294.
[212] X. W. Gao, J. Z. Wang, S. L. Chou, H. K. Liu, *J. Power Sources* **2012**, *220*, 47-53.
[213] C. C. Torardi, C. R. Miao, M. E. Lewittes, Z. Li, *J. Solid State Chem.* **2002**, *163*, 93-99.
[214] H. Q. Li, P. He, Y. G. Wang, E. Hosono, H. S. Zhou, *J. Mater. Chem.* **2011**, *21*, 10999-11009.
[215] Z. Y. Huang, H. M. Zeng, L. Xue, X. G. Zhou, Y. Zhao, Q. Y. Lai, *J. Alloy Compd.* **2011**, *509*, 10080-10085.
[216] C. Nethravathi, B. Viswanath, J. Michael, M. Rajamath, *Carbon* **2012**, *50*, 4839-4846.
[217] N. Ganganagappa, A. Siddaramanna, *Mater. Charact.* **2012**, *68*, 58-62.
[218] A. M. Glushenkov, V. I. Stukachev, M. F. Hassan, G. G. Kuvshinov, H. K. Liu, Y. Chen, *Cryst. Growth Des* **2008**, *8*, 3661-3665.
[219] C. Leger, S. Bach, P. Soudan, J. P. Pereira-Ramos, *J. Electrochem. Soc.* **2005**, *152*, A236-A241.
[220] C. M. Ban, N. A. Chernova, M. S. Whittingham, *Electrochem. Commun.* **2009**, *11*, 522-525.
[221] S. T. Lutta, H. Dong, P. Y. Zavalij, M. S. Whittingham, *Mater. Res. Bull.* **2005**, *40*, 383-393.
[222] S. Q. Wang, Z. D. Lu, D. Wang, C. G. Li, C. H. Chen, Y. D. Yin, *J. Mater. Chem.* **2011**, *21*, 6365-6369.
[223] Y. Kim, J. S. Kim, M. T. Thieu, H. C. Dinh, I. H. Yeo, W. Il Cho, S. I. Mho, *B. Kor. Chem. Soc.* **2010**, *31*, 3109-3114.
[224] H. M. Song, D. Y. Yoo, S. K. Hong, J. S. Kim, W. I. Cho, S. I. Mho, *Electroanal.* **2011**, *23*, 2094-2102.
[225] H. H. Yin, K. Yu, H. Peng, Z. L. Zhang, R. Huang, J. Travas-Sejdic, Z. Q. Zhu, *J. Mater. Chem.* **2012**, *22*, 5013-5019.
[226] Y. Y. Liu, M. Clark, Q. F. Zhang, D. M. Yu, D. W. Liu, J. Liu, G. Z. Cao, *Adv. Energy Mater.* **2011**, *1*, 194-202.
[227] M. Inamoto, H. Kurihara, T. Yajima, *Electrochemistry* **2012**, *80*, 421-422.
[228] F. Huguenin, M. Malta, R. Torresi, D. A. Buttry, *Elec. Soc. S.* **2003**, 220-229.
[229] Y. Sakurai, J. Yamaki, *J. Electrochem. Soc.* **1985**, *132*, 512-513.
[230] Y. Sakurai, *Vol. 4675260*, H01M 616; H01M 618 ed. (Ed.: U. P. Office), Nippon Telegraph and Telephone Corporation, **1985**.
[231] Y. Sakurai, J. Yamaki, *J. Electrochem. Soc.* **1988**, *135*, 791-796.
[232] F. Wächter, PhD thesis, ETH Zürich (Zürich), **2013**.
[233] J. J. Shyu, C. H. Yeh, *J. Mater Sci.* **2011**, *46*, 999-1006.
[234] V. V. Brazhkin, J. Akola, Y. Katayama, S. Kohara, M. V. Kondrin, A. G. Lyapin, S. G. Lyapin, G. Tricot, O. F. Yagafarov, *J. Mater. Chem.* **2011**, *21*, 10442-10447.
[235] T. Naitoh, T. Namekawa, A. Katoh, K. Maeda, *Nippon Seram Kyo Gak* **1992**, *100*, 685-690.
[236] T. Naitoh, T. Namekawa, S. Yamada, K. Maeda, *Nippon Seram Kyo Gak* **1989**, *97*, 834-841.
[237] D. Stachel, A. Barz, *J. Phys. Chem. Solids* **2007**, *68*, 1021-1023.
[238] V. Kundu, R. L. Dhiman, D. R. Goyal, A. S. Maan, *Optoelectron Adv. Mat.* **2008**, *2*, 428-432.
[239] K. P. Padmasree, D. K. Kanchan, *Mat. Sci. Eng B-Solid* **2005**, *122*, 24-28.
[240] S. Khasa, V. P. Seth, S. K. Gupta, R. M. Krishna, *Phys. Chem. Glasses* **1999**, *40*, 269-272.
[241] I. Kashif, A. M. Sanad, Y. M. Abozeid, *Phys. Chem. Glasses* **1990**, *31*, 196-198.
[242] E. Culea, A. Nicula, *Solid State Commun.* **1986**, *58*, 545-549.
[243] B. K. Sharma, D. C. Dube, A. Mansingh, *J. Non-Cryst. Solids* **1984**, *65*, 39-51.
[244] S.-i. Tobishima, *Vol. 4737424*, H01M 616 ed. (Ed.: U. P. Office), Nippon Telegraph and Telephone Corporation, **1986**, pp. 1-18.
[245] G. D. Khattak, A. Mekki, *J. Phys. Chem. Solids* **2009**, *70*, 1330-1336.
[246] V. Kundu, R. L. Dhiman, A. S. Maan, D. R. Goyal, *Adv. Cond. Matter Phys.* **2008**.
[247] C. A. Hogarth, M. M. Ahmed, *J. Mater. Sci. Lett.* **1983**, *2*, 649-652.
[248] M. Milanova, R. Iordanova, L. Aleksandrov, M. Hassan, Y. Dimitriev, *J. Non-Cryst. Solids* **2011**, *357*, 2713-2718.
[249] R. Iordanova, Y. Dimitriev, E. Kashchieva, D. Klissurski, *Ceram-Silikaty* **2001**, *45*, 115-118.

[250] I. A. Shkrob, B. M. Tadjikov, A. D. Trifunac, *J. Non-Cryst. Solids* **2000**, *262*, 6-34.
[251] I. A. Shkrob, B. M. Tadjikov, A. D. Trifunac, *J. Non-Cryst. Solids* **2000**, *262*, 35-65.
[252] Kirk-Othmer, *Kirk-Othmer Encyclopedia of Chemical Technology, Vol. 12*.
[253] R. S. Gedam, V. K. Deshpande, *B. Mater. Sci.* **2009**, *32*, 83-87.
[254] C. N. Reddy, R. V. Anavekar, *Mater. Chem. Phys.* **2008**, *112*, 359-365.
[255] Y. I. Lee, J. H. Lee, S. H. Hong, Y. S. Park, *Solid State Ionics* **2004**, *175*, 687-690.
[256] Y. M. Moustafa, A. K. Hassan, G. ElDamrawi, N. G. Yevtushenko, *J. Non-Cryst. Solids* **1996**, *194*, 34-40.
[257] K. Gaur, H. B. Lal, *Z. Naturforsch. A* **1992**, *47*, 1011-1012.
[258] J. Barker, K. West, Y. Saidi, R. Pynenburg, B. Zachauchristiansen, R. Koksbang, *J. Power Sources* **1995**, *54*, 475-478.
[259] E. Lee, K. A. Persson, *Energ. Environ. Sci.* **2012**, *5*, 6047-6051.
[260] B. V. R. Chowdari, K. L. Tan, F. Ling, *Solid State Ionics* **1998**, *113*, 711-721.
[261] CRC-Press, *CRC Handbook of Chemistry and Physics, 93rd Edition*, *Vol. 93*, **2012**.
[262] H. Y. Wang, A. D. Tang, K. L. Huang, *Chinese J. Chem.* **2011**, *29*, 27-32.
[263] P. H. Xiao, Z. Q. Deng, A. Manthiram, G. Henkelman, *J. Phys. Chem. C* **2012**, *116*, 23201-23204.
[264] Y. C. Lu, E. J. Crumlin, G. M. Veith, J. R. Harding, E. Mutoro, L. Baggetto, N. J. Dudney, Z. Liu, Y. Shao-Horn, *Sci. Rep-Uk* **2012**, *2*.
[265] Y. Chen, S. A. Freunberger, Z. Peng, F. Barde, P. G. Bruce, *J. Am. Chem. Soc.* **2012**, *134*, 7952-7957.
[266] G. Sudant, E. Baudrin, B. Dunn, J. M. Tarascon, *J. Electrochem. Soc.* **2004**, *151*, A666-A671.
[267] K. West, B. Zachauchristiansen, T. Jacobsen, S. Skaarup, *Electrochim. Acta* **1993**, *38*, 1215-1220.
[268] F. Tanguy, J. Gaubicher, D. Guyomard, *Electrochim. Acta* **2010**, *55*, 3979-3986.
[269] A. N. Mansour, P. H. Smith, M. Balasubramanian, J. McBreen, *J. Electrochem. Soc.* **2005**, *152*, A1312-A1319.
[270] S. Jouanneau, A. L. La Salle, A. Verbaere, D. Guyomard, *J. Electrochem. Soc.* **2005**, *152*, A1660-A1667.
[271] A. N. Mansour, P. H. Smith, W. M. Baker, M. Balasubramanian, J. McBreen, *J. Electrochem. Soc.* **2003**, *150*, A403-A413.

Appendix

The solution and refinement of the structure for $Li_7Mn(BO_3)_3$

A crystal of $Li_7Mn(BO_3)_3$ of suitable size (0.1 x 0.18 x 0.28 mm) was selected under a microscope using polarized light A data set was collected on a Bruker SMART CCD 1K area detector diffractometer using MoKα-radiation (0.73071 Å). Indexing, data reduction and an empirical absorption correction were performed using the programs CELL_NOW [1], SAINT [2] and TWINABS [3], embedded in the APEX2 [4] software package. Using Olex2 [5], the structure was solved with the XS [6] structure solution program using Direct Methods and refined with the XL [7] refinement package using a Least Squares refinement. The data set turned out to be multiply twinned. Four main individuals and at least two more individuals with much smaller volume contribute to the diffraction pattern. For the data evaluation only the four main individuals with volume ratios of about 0.9:0.9:0.66:1 were considered. In total 21066 reflections (R_{int} = 0.0706 after merging in the point group -1) were collected ($2\theta_{max}$=52.3^{o}) and 6703 absorption corrected reflections involving one domain were used for the refinement, leading to 3191 independent reflections when accounting for the overlaps. The refinement allowed anisotropic displacement parameters for Mn-atoms only. All other atoms were refined isotropically. Crystallographic Details are listed in **Table A1, A2, A3 and A4**.

Table A1: Crystal data and structure refinement for $Li_7Mn(BO_3)_3$ (sample code: SA262).

Empirical formula	$Li_7MnB_3O_9$	
Formula weight	279.95	
Temperature	293(2) K °	
Wavelength	0.71073 Å	
Crystal system	triclinic	
Space group	*P* -1	
Unit cell dimensions	a = 8.3234(15) Å	α= 71.495(4)°.
	b = 9.1952(17) Å	β= 79.525(4)°.
	c = 11.248(2) Å	γ = 71.368(4)°.
Volume	770.5(2) $Å^3$	
Z	4	
Density (calculated)	2.413 Mg/m^3	
Absorption coefficient	1.738 mm^{-1}	
F(000)	532	
Crystal size	0.28 x 0.18 x 0.10 mm^3	
Theta range for data collection	1.92 to 26.17°.	
Index ranges	-9<=h<=10, -10<=k<=11, 0<=l<=13	
Reflections collected	3191	
Independent reflections	3191 [R(int) = 0.0000]	
Completeness to theta = 26.17°	99.2 %	
Max. and min. transmission	0.8451 and 0.6413	
Refinement method	Full-matrix least-squares on F^2	
Data / restraints / parameters	3191 / 0 / 174	
Goodness-of-fit on F^2	1.064	
Final R indices [I>2sigma(I)]	R1 = 0.0543, wR2 = 0.1602	
R indices (all data)	R1 = 0.0728, wR2 = 0.1731	
Largest diff. peak and hole	0.84 and -1.01 e.$Å^{-3}$	

Table A2: Atomic coordinates (x 10^4) and equivalent isotropic displacement parameters ($Å^2$x 10^3) for $Li_7Mn(BO_3)_3$. U(eq) is defined as one third of the trace of the orthogonalized U^{ij} tensor.

	x	y	z	U(eq)
Mn1	2964.5(13)	4732.8(12)	5807.2(9)	12.5(3)
Mn2	4575.7(14)	3932.2(13)	1576.1(10)	17.5(3)
O1	43(6)	342(5)	3648(4)	10.6(9)
O2	163(6)	6811(5)	801(4)	11.6(10)
O3	440(6)	5751(5)	8324(4)	9.2(9)
O4	982(6)	8268(5)	2600(4)	11.5(10)
O5	1156(6)	2549(5)	4781(4)	12.1(10)
O6	1433(6)	3690(5)	7251(4)	10.0(9)
O7	1745(6)	727(5)	1696(4)	11.4(10)
O8	2225(6)	4835(5)	4110(4)	11.7(10)
O9	3187(6)	57(5)	7412(4)	11.8(10)
O10	3308(6)	2741(6)	3081(4)	13.8(10)
O11	3407(6)	3802(5)	158(4)	11.9(10)
O12	4246(6)	6251(5)	1442(4)	12.6(10)
O13	5227(6)	2922(5)	6072(4)	9.9(10)
O14	5554(6)	8352(5)	797(4)	14.1(10)
O15	6283(6)	665(5)	5213(4)	12.7(10)
O16	7081(6)	2586(5)	1532(4)	9.8(9)
O17	7250(6)	2994(5)	4301(4)	12.1(10)
O18	8198(6)	477(5)	541(4)	10.6(10)
B1	560(9)	4231(8)	8266(7)	6.0(14)
B2	916(9)	9723(9)	2643(7)	9.2(14)
B3	2224(10)	3421(10)	3981(8)	16.1(17)
B4	5499(10)	6996(9)	683(8)	12.8(16)
B5	6218(9)	2229(8)	5185(7)	6.8(14)
B6	7304(9)	973(8)	1559(7)	7.4(14)
Li1	144(16)	6534(16)	3869(12)	23(3)
Li2	362(15)	1098(14)	320(11)	17(2)
Li3	551(14)	8472(13)	5137(11)	15(2)
Li4	1112(14)	1654(13)	8090(10)	12(2)
Li5	1520(20)	2980(20)	988(17)	47(4)
Li6	1989(14)	7612(13)	1006(10)	12(2)
Li7	2060(14)	445(13)	5921(11)	14(2)
Li8	2110(20)	1110(19)	3448(15)	37(3)
Li9	3236(15)	6522(14)	3053(11)	15(2)
Li10	3525(15)	123(14)	401(11)	17(2)
Li11	4219(18)	1621(16)	7592(13)	28(3)
Li12	5060(16)	845(15)	3757(12)	21(3)

Li13	8304(14)	4252(14)	402(11)	14(2)
Li14	8454(18)	2623(17)	2744(13)	27(3)

Table A3 : Anisotropic displacement parameters ($Å^2$x 10^3) for $Li_7Mn(BO_3)_3$. The anisotropic displacement factor exponent takes the form: $-2\pi^2[h^2a^{*2}U^{11} + ... + 2 h k a^* b^* U^{12}]$

	U^{11}	U^{22}	U^{33}	U^{23}	U^{13}	U^{12}
Mn1	14.4(5)	10.2(5)	12.2(5)	-2.6(4)	2.3(4)	-4.8(4)
Mn2	17.9(6)	15.6(6)	18.1(6)	-4.2(5)	1.3(4)	-5.4(4)

Table A4. Selected bond lengths [Å] for $Li_7Mn(BO_3)_3$.

Atom	Atom	Length	Atom	Atom	Length
Mn1	O6	2.055(5)	O2	$Li13^3$	1.957(12)
Mn1	O8	2.076(5)	O3	B1	1.391(8)
Mn1	O13	2.072(4)	O3	$Li5^2$	1.877(18)
Mn1	$O17^1$	2.006(5)	O3	$Li13^1$	1.920(12)
Mn1	Li1	3.177(13)	O3	$Li14^1$	1.965(15)
Mn1	$Li1^2$	3.082(13)	O4	B2	1.337(8)
Mn1	Li3	3.304(11)	O4	Li1	1.992(14)
Mn1	Li9	3.017(12)	O4	$Li4^2$	2.005(12)
Mn1	$Li9^1$	3.344(12)	O4	Li6	2.024(12)
Mn1	Li11	2.918(14)	O4	Li9	2.064(13)
Mn1	$Li14^1$	3.153(14)	O5	B3	1.396(10)
Mn2	O10	2.022(5)	O5	$Li1^2$	1.955(14)
Mn2	O11	2.065(5)	O5	$Li3^2$	1.913(12)
Mn2	O12	2.020(5)	O5	Li7	1.949(12)
Mn2	O16	2.058(5)	O5	Li8	2.187(16)
Mn2	Li5	3.175(18)	O6	B1	1.381(8)
Mn2	Li6	3.311(11)	O6	$Li1^2$	2.071(14)
Mn2	Li9	3.133(11)	O6	Li4	1.891(12)
Mn2	Li12	3.074(13)	O6	Li11	2.488(15)
Mn2	Li13	3.210(12)	O7	$B2^4$	1.407(9)
Mn2	$Li13^3$	3.241(11)	O7	Li2	1.975(13)
O1	$B2^4$	1.405(8)	O7	Li5	1.927(18)

O1	Li3^{2}	1.912(12)	O7	Li8	2.198(17)
O1	Li3^{4}	1.977(12)	O7	Li10	1.957(12)
O1	Li7^{5}	2.025(12)	O8	B3	1.353(9)
O1	Li8	2.012(16)	O8	Li1	1.920(14)
O1	Li14^{6}	2.132(15)	O8	Li9	1.957(13)
O2	B1^{2}	1.371(8)	O9	B6^{8}	1.336(9)
O2	Li2^{7}	1.898(13)	O9	Li4	2.081(12)
O2	Li4^{2}	2.087(12)	O9	Li7	1.949(12)
O2	Li5^{7}	2.579(19)	O9	Li11	1.971(15)
O2	Li6	1.964(12)	O9	Li12^{8}	1.941(13)

Symmetry transformations used to generate equivalent atoms:

^{1}1-x,1-y,1-z; ^{2}-x,1-y,1-z; ^{3}1-x,1-y,-z; ^{4}+x,-1+y,+z; ^{5}-x,-y,1-z; ^{6}-1+x,+y,+z; ^{7}-x,1-y,-z; ^{8}1-x,-y,1-z.

The solution and refinement of the structure for $Li_{4.14}Mn_{1.21}(BO_3)_3$

For structure determination, a crystal of $Li_{4.14}Mn_{1.21}(BO_3)_3$ with dimensions, 0.20 x 0.20 x 0.10 mm, was selected under an optical microscope (polarized light). The data set collection was carried out on a Bruker SMART CCD 1K area detector diffractometer using MoKα-radiation (0.73071 Å). Indexing, data reduction and an empirical absorption correction were done with the programs SAINT [1] and APEX2 [2]. The structure was solved by employing Olex2 [3] with the XS [4] structure solution program using Direct Methods, and the refinement was performed with the XL [5] refinement package using a Full Matrix Least Squares refinement. The data set was multiply twinned (4 components including the respective inversion twins). The structure was refined in $P\,3_112$ (No.151) by using a twin matrix (-1 0 0 0 -1 0 0 0 1). The volume ratios of the individual twins were found to be to 1:0.78:0.12:0.10. On the neighboring disordered sites, the total occupancy was constrained to be 100 % and no defects were allowed (Li1/Mn1 and Mn2/Li2A/Li2B, respectively). Crystallographic Details are given in **Table A5, A6, A7 and A8**. All atoms except lithium atoms and the Mn2-site were refined using anisotropic displacement parameters. The isotropic displacement parameters of Mn2, Li2A and Li2B were constrained to be equal.

Table A5: Crystal data and structure refinement for $Li_{4.14}Mn_{1.21}(BO_3)_3$ (sample code: SA158).

Empirical formula	$Li_{2.76}Mn_{0.80}B_2O_6$
Formula weight	180.89
Temperature	293(2) K^o
Wavelength	0.71073 Å
Crystal system	trigonal
Space group	$P\ 3_112$
Unit cell dimensions	a = 4.9741(3) Å
	b = 4.9741(3) Å
	c = 17.7511(19) Å
Volume	380.35(5) Å^3
Z	3
Density (calculated)	2.369 Mg/m^3
Absorption coefficient	2.083 mm^{-1}
F(000)	259
Crystal size	0.20 x 0.20 x 0.10 mm^3
Theta range for data collection	1.15 to 33.99°.
Index ranges	-7<=h<=7, -7<=k<=7, -27<=l<=27
Reflections collected	6031
Independent reflections	983 [R(int) = 0.0529]
Completeness to theta = 33.99°	96.8 %
Max. and min. transmission	0.8188 and 0.6808
Refinement method	Full-matrix least-squares on F^2
Data / restraints / parameters	983 / 1 / 65
Goodness-of-fit on F^2	1.102
Final R indices [I>2sigma(I)]	R1 = 0.0494, wR2 = 0.1295
R indices (all data)	R1 = 0.0630, wR2 = 0.1369
Absolute structure parameter	0.00
Largest diff. peak and hole	0.659 and -0.374 e.Å^{-3}

Table A6 : Atomic coordinates (x 10^4) and equivalent isotropic displacement parameters (Å^{2}x 10^3) for $Li_{4.14}Mn_{1.21}(BO_3)_3$. U(eq) is defined as one third of the trace of the orthogonalized U^{ij} tensor.

	x	y	z	U(eq)	Wyck.	Occ.
B(1)	3254(7)	3205(7)	856(2)	15(1)	6c	1
O(1)	3204(6)	542(5)	1032(1)	23(1)	6c	1
O(2)	516(5)	3126(6)	644(2)	22(1)	6c	1
O(3)	5966(6)	5986(6)	840(3)	41(1)	6c	1
Mn(1)	-21(3)	6709(4)	526(1)	18(1)	6c	0.310(3)
Li(1)	-330(20)	6270(30)	1185(6)	39(2)	6c	1-Mn(1)
Mn(2)	6816(17)	79(15)	1163(4)	27(1)	6c	0.093(2)
Li(2A)	6430(40)	-150(30)	493(7)	27(1)	6c	0.484(15)
Li(2B)	-1700(50)	9150(20)	0	27(1)	3a	0.410(15)

Table A7 : Anisotropic displacement parameters (Å^{2}x 10^3) for $Li_{4.14}Mn_{1.21}(BO_3)_3$. The anisotropic displacement factor exponent takes the form: $-2\pi^2[\ h^2a^{*2}U^{11} + ... + 2\ h\ k\ a^*\ b^*\ U^{12}\ ]$

	U^{11}	U^{22}	U^{33}	U^{23}	U^{13}	U^{12}
B(1)	13(1)	19(2)	13(1)	-1(2)	0(1)	9(1)
O(1)	18(1)	17(1)	33(1)	9(1)	1(1)	8(1)
O(2)	15(1)	26(1)	24(1)	4(1)	0(1)	11(1)
O(3)	17(1)	14(1)	89(2)	3(1)	-1(1)	6(1)
Mn(1)	14(1)	15(1)	24(1)	3(1)	1(1)	6(1)

Table A8. Selected bond lengths [Å] for $Li_{4.14}Mn_{1.21}(BO_3)_3$.

Atom	Atom	Length	Atom	Atom	Length
B(1)	O(1)	1.349(4)	O(3)	Li(2A)#7	1.920(14)
B(1)	O(3)	1.367(3)	O(3)	Mn(1)#3	1.925(4)
B(1)	O(2)	1.394(4)	O(3)	Mn(2)#7	1.947(8)
B(1)	Li(2B)#1	2.736(15)	O(3)	Li(2B)#3	2.054(10)
B(1)	Li(1)#2	2.799(12)	O(3)	Li(1)#2	2.339(12)

B(1)	Li(1)#3	2.824(10)	O(3)	Li(2A)#8	2.382(13)
O(1)	Mn(2)	1.936(7)	Mn(1)	Li(1)	1.185(11)
O(1)	Li(1)#1	1.986(10)	Mn(1)	O(3)#5	1.925(4)
O(1)	Mn(1)#1	1.989(3)	Mn(1)	O(1)#7	1.989(4)
O(1)	Mn(2)#4	2.035(6)	Mn(1)	Li(2B)	2.015(7)
O(1)	Li(2A)	2.039(17)	Mn(1)	O(2)#6	2.100(3)
O(2)	Li(2A)#5	1.884(13)	Mn(1)	Li(2A)#9	2.506(13)
O(2)	Mn(2)#5	1.935(7)	Mn(1)	Mn(1)#6	2.533(5)
O(2)	Mn(1)	1.941(3)	Mn(1)	Li(2A)#7	2.779(16)
O(2)	Li(1)	2.052(13)	Mn(1)	Li(2A)#10	2.885(17)
O(2)	Li(2B)#1	2.063(10)	Mn(1)	Li(2A)#5	2.956(12)
O(2)	Mn(1)#6	2.100(3)	Mn(1)	Mn(2)#10	3.033(6)
O(3)	Li(1)#3	1.876(11)	Mn(2)	O(2)#3	1.935(7)

Symmetry transformations used to generate equivalent atoms:

#1 x,y-1,z #2 -x+y,y,-z+1/3 #3 x+1,y,z #4 -x+y+1,y,-z+1/3 #5 x-1,y,z #6 x,x-y+1,-z #7 x,y+1,z #8 x,x-y,-z #9 x-1,x-y,-z #10 x-1,y+1,z

Appendix References

[1] CELL_NOW - Version 2008-2 Bruker AXS, Madison, Wisconsin, USA

[2] SAINT, Version 7.68A, Bruker AXS, Madison, Wisconsin, USA

[3] TWINABS, Version 2008/4 Bruker AXS, Madison, Wisconsin, USA

[4] APEX2, Version 2012.2-0, Bruker AXS, Madison, Wisconsin, USA

[5] O. V. Dolomanov, L. J. Bourhis, R. J. Gildea, J. A. K. Howard and H. Puschmann, OLEX2: a complete structure solution, refinement and analysis program. J. Appl. Cryst. (2009). 42, 339-341.

[6] XS, G.M. Sheldrick, Acta Cryst. (2008). A64, 112-122

[7] XL, G.M. Sheldrick, Acta Cryst. (2008). A64, 112-122

Experimental Infrastructure

Powder X-Ray Diffraction

- Bruker AXS D8 PD, PSD-50m Detector (M-*Braun), $CuK_{\alpha1}$ = 1.54056 Å, Bragg-Brentano Geometry.
- Stoe STADI P, with Dectris MYTHEN 1k silicon strip Detector, bent Ge-Monochromator, $CuK_{\alpha1}$ = 1.54056 Å.
-

Single Crystal X-Ray Diffraction

- Bruker SMART CCD 1K area detector diffractometer, MoKα-radiation (0.73071 Å).

Electron Microscopy

- Scanning electron microscopy (SEM), Zeiss Gemini 1530 operated at 1 kV.
- (Scanning) transmission electron microscopy ((S) TEM) analysis with a CM30ST (FEI; LaB_6 cathode) and a Tecnai F30 microscope (FEI; field emission gun), both operated at 300 kV, point resolution of ~ 2Å. The F30 microscope is equipped with a high-angle annular dark field detector (HAADF STEM), an energy-dispersive X-ray spectrometer (EDXS; EDAX) and an electron energy-loss spectrometer (EELS; Gatan).

Magnetic measurements

- SQUID magnetometer (MPMS 5S, Quantum Design).

Fourier Transform Infrared Spectroscopy (FTIR)

- Thermo Scientific Nicolet iS10 Smart iTR.

Differential thermal analysis (DTA)

- NETZSCH STA 409 C/CD, in Pt crucibles.

Electrochemical Characterization

- Galvanostatic cycling and Cyclic Voltammetry with Swagelok-type cells using BAT-SMALL potentiostat and ASTROL software package (both acquired from Astrol Electronic AG).

Ball-milling

- Retsch Mixer Mill MM 200
- Fritsch Planetary Mono Mill PULVERISETTE 6 *classic line*

Furnaces

- Heraeus Ro 4/50 resistivity tube furnace (RT-1100 ^oC).
- Nabertherm L 9/11/SKM/P330 muffle furnace (RT-1100 ^oC).

Ultrasonic bath

- Bandelin Sonorex Super 10 P

Curriculum Vitae

SEMIH AFYON

Nationality: Turkish
Date of Birth: 11.11.1982
Cell Phone: +(41)786233832
E-mail: afyon@inorg.chem.ethz.ch
safyon@yahoo.com

EDUCATION

2009-2013 **ETH Zurich, D-CHAB, Switzerland**
Department of Chemistry and Applied Biosciences
Ph.D. studies under the supervision of Prof. Dr. Reinhard Nesper

2007-2009 **Koç University, Istanbul**
Graduate School of Sciences & Engineering
Master of Science (M.Sc.) in Materials Science and Engineering
GPA 3.67/4.00, Department rank: 1st

2001-2006 **Koç University, Istanbul**
College of Arts and Sciences
Scholarship based on national university entrance exam success
B.Sc. Chemistry GPA 3.62/4.00, Chemistry-GPA 3.92/4.00
Department rank: 1st, College rank: 4th

1998-2001 **Meram Fen Lisesi, Konya**
High School Diploma

WORK & RESEARCH EXPERIENCE

Fall 2009-2013 **ETH Zurich, D-CHAB, Switzerland**
Research & Teaching Assistant

July-August 2008 **Max-Planck Institute for Chemical Physics of Solids in Dresden, Germany**
Research Assistant

Fall 2002-2009 **Koç University, Istanbul**
Research & Teaching Assistant

July-August 2004, 2005 **Max-Planck Institute for Chemical Physics of Solids in Dresden, Germany**
Research Assistant

July-August 2003 **Degussa Company in Hanau-Wolfgang, Germany**
Intern & Lab. Assistant

Fall 2002- 2004 **Koç University, Istanbul**
Chem.101 & Chem 102. Lab. Assistant

Fall 2001-2002 **Koç University, Istanbul**
Part time assistant in library
Work on cataloguing and processing systems.

PUBLICATIONS

[1] S. Afyon, D. Kundu, F. Krumeich, R. Nesper, *J. Power Sources* **2013**, *224*, 145-151.
[2] S. Afyon, M. Hagemann, M. Somer, C. Schulze Isfort, *Solid State Sci.* **2013**, *18*, 91-97.
[3] S. Afyon, P. Hohn, M. Somer, *Z. Anorg. Allg. Chem.* **2010**, *636*, 1301-1306.
[4] S. Afyon, P. Hohn, M. Armbruster, A. Baranov, F. R. Wagner, M. Somer, R. Kniep, *Z. Anorg. Allg. Chem.* **2006**, *632*, 1671-1680.
[5] Manuscripts based on this thesis have been submitted to peer-reviewed journals.

PATENT PUBLICATIONS

[1] R. Nesper, S. Afyon, M. D. Wörle, J Gonzales, Transition metal borate comprising cathode for rechargeable battery. WO2011128343A1, 2011.
[2] Further patent applications have been filed based on this thesis.

HONORS AND AWARDS

-Research scholarship given by Tubitak (The Scientific and Technological Research Council of Turkey) during M.Sc. studies
-Full scholarship given by Koç University during B.Sc. studies
- Vehbi Koç Scholar: Spring 2004,-2005-2006, Fall 2004-2005
-Dean’s Honor Roll: Fall 2002, Spring 2003, Fall 2003
-Top Ranking Student Award by Koc University